Doctoral Dissertation
Doctoral Program in Metrology (38th Cycle)

Research on Vibration-AE Fusion Detection Technology for Metal Particle Defect in GIS under Electromechanical Coupling Condition

By

Zhaoyu Zhang
******

Supervisor(s):
Prof. Marco. Parvis and Prof. Junhao. Li, Supervisor

Doctoral Examination Committee:
Prof. Yanzhao Xie, Referee, Xi 'an Jiaotong University (Chairman)
Prof. Shengchang Ji, Referee, Xi 'an Jiaotong University
Prof. Hongjie Li, Referee, Xi 'an Jiaotong University
Prof. Qingquan Li, Referee, Shandong University
Prof. Shulin Liu, Referee, Xi`an University of Science and Technology
Prof. Alberto Vallan, Referee, Politecnico di Torino
Prof. Luca Lombardo, Referee, Politecnico di Torino

Politecnico di Torino

2025

Declaration

I hereby declare that, the contents and organization of this dissertation constitute my own original work and does not compromise in any way the rights of third parties, including those relating to the security of personal data.

Zhaoyu Zhang
2025

* This dissertation is presented in partial fulfillment of the requirements for **Ph.D. degree** in the Graduate School of Politecnico di Torino (ScuDo).

To all of you, my love.

Acknowledgment

Five fleeting years, twenty-three years of learning. From the sleepless nights before the college entrance exam to the tireless striving of my undergraduate days, from my first steps into research as a master's student to the unwavering resolve of my doctoral journey—I have grown from a young dreamer into a budding researcher. The path was steep, the struggles unforgettable, yet with every stumble, I found guiding hands. To the mentors and friends who lit my way like sunlight, I offer my deepest gratitude as this thesis comes to a close.

With tireless dedication, my mentor has nurtured me like the spring wind brings life to all things. This dissertation is completed under the careful guidance of Prof. Junhao Li, whose invaluable support shaped every stage of my research—from defining directions and planning work to designing experiments and writing this thesis. Over the past five years, his broad vision, profound knowledge, unwavering optimism, rigorous scholarship, and deep engineering expertise have profoundly influenced my growth. To my mentor, I extend my sincerest gratitude and highest respect. Mountains may part, rivers may diverge, but the bond between teacher and student stands eternal.

Though we may be worlds apart, friendship makes us neighbors at heart. I am deeply grateful to Prof. Xie Yan Zhao for his guidance and support throughout my research journey. His scholarly refinement, visionary international perspective, and unwavering encouragement have been an invaluable source of inspiration. Great thanks to his mentorship, I had the opportunity to study at the Politecnico di Torino in Italy, with the support of the China Scholarship Council. My external supervisors, Prof. Marco Parvis and Prof. Luca Lombardo, have been exceptionally caring, and researchers Leonardo Lannucci and Layla have become

like siblings to me. Their unwavering dedication to research, combined with their optimistic outlook on life, has profoundly influenced me, making them my family across the ocean. I would like to express my deepest gratitude to Prof. Xie Yan Zhao and my Italian colleagues. May they enjoy health, longevity, and prosperity, and may their influence continue to shine brightly across the world.

In the prime of youth, full of vitality, the journey of scientific research is never without the companionship of peers. I am deeply grateful to Professors Han Xutao and Zhang Xuanrui for their invaluable guidance and assistance, as well as to Drs. He Cong, Guo Ruocheng, and Meng Xuan, Yidan Hu, Zhou Yang, Wang Haotian, Chen Huan, Shi Tianyi, Niu Lin, and Zhicheng Liu for their collaborative support. I would also like to thank my fellow graduate students, including Yuan Wenze, Cao Zeyao, Cai Jun, Wu Jiushan, Yang Yueping, Zhao Zhuangmin, Shu Ting, Song Yanfeng, Hou Jiachen, Sun Yuan, Gao Yuting, as well as Huang Hengchao, Li Liao, Zhang Qi, Wang Yu'ang, Ding Hongwei, Gao Zhuo, Shi Xinyue, Yan Lin, Qin Yan, Gao Jinpeng, Sun Ce, Yin Lingjun, Xu Limeng, and Song Tianliang, for their friendship. I also cherish the friendship shared with doctoral students Zhao Kun and Huang Song during our time in Italy. I wish all of them a bright and promising future, with endless success ahead.

Are you not battle-dressed? Let's share the armour! My heartfelt gratitude goes to my dear friends—Dr. Yang Xiong, as well as doctoral candidates Zhao Haoxiang and Liu Yuyang. The memories of our shared meals, deep conversations, and countless hours of study will always remain vivid. Zhao’s boldness, Yang’s composure, and Liu’s passion have only deepened the bond we share as brothers. Don't worry about the road ahead without a confidant, for you will be famed worldwide! May we all press forward with unwavering determination and limitless ambition!

A lone traveler through wild mountains—why not journey together on this long road? My deepest gratitude to the wonderful Zhang Wenting for her unwavering support and companionship. Your sweetness has soothed my every anxious night. Loving you is like loving life itself!

As the morning sun rises and the fish feast, laughter fills our home by the southern pond. My family has always been my strongest support, and every moment spent with them brings warmth to my soul. "While my parents live, I shall not wander far"—I hope to have more time to be by their side, to shoulder my part of our family’s world. May my loved ones bask in the joy of spring breezes and find peace in autumn rains, living in harmony like a well-tuned melody, sharing the simple joys of life together.

It is my great fortune to be born in this land and to live in this era. I am grateful for this prosperous and peaceful age, and for my strong motherland-China that has nurtured and protected me. The Great Wall stands eternal, and the heart of patriotism never wavers.

He who has never reached the Great Wall is not true hero. Looking back on a journey of twenty thousand miles, my heart swells with emotion. The path I have walked is filled with trials and triumphs, each step forging who I am today. The radiant years will forever be etched in my heart, and with unwavering resolve, I shall press forward, spurring my steed toward the boundless future.

Abstract

Gas-Insulated Switchgear (GIS) is a critical transformation and switching equipment in power systems, and its operating condition directly affects grid safety and stability. Studies have shown that under high-voltage and high-current conditions, GIS is simultaneously subjected to electric field and mechanical stress, and there is a correlated influence between its insulation and vibration conditions, making insulation defect and mechanical defect the two main causes of GIS failures. For example, metal particle contamination is a typical insulation defect related to mechanical vibration, while AE and vibration signal measurements are effective for detecting insulation and mechanical conditions, respectively. However, traditional single-signal detection fail to capture the correlation and complementarity between Partial Discharge (PD) and mechanical vibration. The lack of data fusion analysis constrains diagnosis efficiency, and the evolution process of defect cannot be researched. Therefore, the optimal design and development of a vibration-AE fusion sensor, the exploration of intelligent sensing technology for GIS condition detection, the investigation of metal particles motion and PD characteristics under combined power-frequency voltage and mechanical vibration, and the proposal of a vibration-AE fusion detection method, together provide both theoretical and technical support for on-site GIS defect detection, offering significant academic and engineering value.

To overcome the limitations of current sensing technologies for detecting mechanical and insulation defects in power equipment, specifically the separation measurement and resulting restricted diagnosis, a vibration-AE fusion sensor is developed which enables synchronous and co-located measurement of mechanical vibration and PDAE signals. An electromechanical-acoustic equivalent model for piezoelectric vibration-AE measurement is established, and a fusion sensing structure is designed. Simulation analysis clarifies the relationships between

structural parameters and measurement performance for both vibration and AE signals. Furthermore, an intelligent structural optimization method based on data augmentation-algorithmic optimization is proposed. A multifunctional embedded circuit is designed, and a prototype fusion sensing device is developed and calibrated. The developed fusion sensor exhibits a vibration sensitivity of 950 mV/g and an average AE sensitivity of 101 dB within the target frequency band, with a resonant frequency of 54 kHz, enabling synchronous detection of vibration and AE signals.

To address the current issues of low intelligence and poor efficiency in power equipment sensing, incorporating the features of low-power wireless communication, edge computing, and self-calibration, an intelligent architecture for fusion sensors is proposed, which enables autonomous enhancement of sensing, storage, computing, and transmission. An integrated intelligent wireless module is designed, developed, and assembled within the fusion sensor. Test results show that in wireless low-power mode, the sensor achieves a data rate above 1 Mbps within 8 meters in substation environment, with a theoretical battery life of up to four years. An edge computing strategy tailored for vibration-AE fusion signal processing is proposed, along with an embedded algorithm that enables signal feature extraction at the sensor level. A novel calibration method based on pseudo-random M-sequence excitation is firstly proposed for efficient impedance and sensitivity calibration of piezoelectric sensors. Simulation and experimental results verify that the method offers high accuracy, low time and power consumption, and stable, reliable operation. This work improves fusion sensing efficiency and lays the foundation for distributed on-site measurement applications.

Given that current studies on metal particle defect detection do not adequately account for the combined effects of mechanical vibration and operating voltage in GIS, this work experimentally investigates the motion and PD characteristics of free metal particles in GIS under simultaneous power-frequency voltage and mechanical vibration. A GIS experimental platform

is constructed to apply synchronized vibration-voltage excitation. The effects of electric field strength and mechanical vibration on typical metal particle are analyzed, revealing the motion and PD characteristics. For spherical and linear particles, both the jumping initiation (E_i) and cessation (E_c) field strength increase with particle mass, while mechanical vibration reduces the thresholds. For flaky particles, the jumping behavior is influenced by both mass and geometry, small, elongated flakes jump more easily, whereas large, square-shaped ones are more stable. Once airborne, flakes and lines exhibit active motion, with heavier particles generating stronger discharges. Under high field strength, firefly phenomenon may occur. Multiple particles in motion may cause chain breakdown, leading to short-circuit fault. Under the same field strength, lighter particles move more actively with lower discharge, while heavier ones move less but generate stronger PD. These findings provide experimental reference for metal particle detection in practical GIS.

Based on the research background and engineering need, the fusion detection technology is proposed for GIS and on-site tests are conducted in substation. Methods are proposed to evaluate the shape, mass, and quantity of metal particles. Shape is infered by flight patterns and discharge rates; mass is estimated from the flight slope; and quantity is assessed from the discharge-mass-quantity correlation. VMD is employed to denoise and separate fusion signal, and signal feature extraction methods are summarized. A vibration-AE fusion measurement and communication framework is proposed, along with a cloud-edge collaborative computing model, offering an innovative strategy for intelligent distributed sensing, processing, and diagnosis in substation. The developed vibration-AE fusion detection system demonstrates efficient signal sensing, processing, storage, and transmission capabilities, and is successfully applied to the condition monitoring of GIS in substation.

Contents

List of Figures

List of Tables

1 Preface

1.1 Research Background and Significance

Large power equipment, such as transformers, Gas-Insulated Switchgear (GIS), electric reactors and motors, are not only complex electrical equipment but also intricate mechanical systems. As a critical transformation and switching equipment in substation, GIS is widely used in high-voltage and ultra-high-voltage substations of 110 kV and above in China[1-3]. As shown in Figure 1-1 (a), GIS utilizes sulfur hexafluoride (SF_6) gas as an insulating medium. Its internal components mainly include circuit breakers, disconnectors, busbars, transformers, and potential/current transformers, among other switching and transformation equipment. GIS features a large physical size, long internal conductors, and a compact yet complex mechanical structure[4,5]. Due to its high reliability and stable operation, GIS has a lower failure rate than traditional electrical equipment and requires relatively longer maintenance intervals. However, due to possible lapses during manufacturing, transportation, and assembly, internal defects are inevitably introduced. Moreover, during operation, GIS is subjected to high-voltage and high-current environment, continuously exposed to the combined effects of electric field and mechanical stress. The interaction between the two factors over time can eventually lead to failures As shown in Figure 1-1(b), statistical data indicate that mechanical defects and insulation defects are the most common causes of GIS failures, accounting for 39.3% and 38.1%, respectively[6-8]. Typical mechanical defects include poor internal electrical contacts, internal metallic foreign objects, and loosened insulation components and fasteners[9,10]. Under the influence of electrodynamic forces, electromagnetic forces, and magnetostrictive effects, such defects generate abnormal vibration signal. Sustained mechanical vibration, under the influence of the strong electric field, can induce insulation defects and trigger PD. The electrical and thermal effects of PD can further loosen mechanical connections, cause burn marks, and induce deformation, thereby exacerbating mechanical defects[11-14]. Mechanical and insulation defects interact during the degradation process, generating correlated mechanical vibration and PD signals.

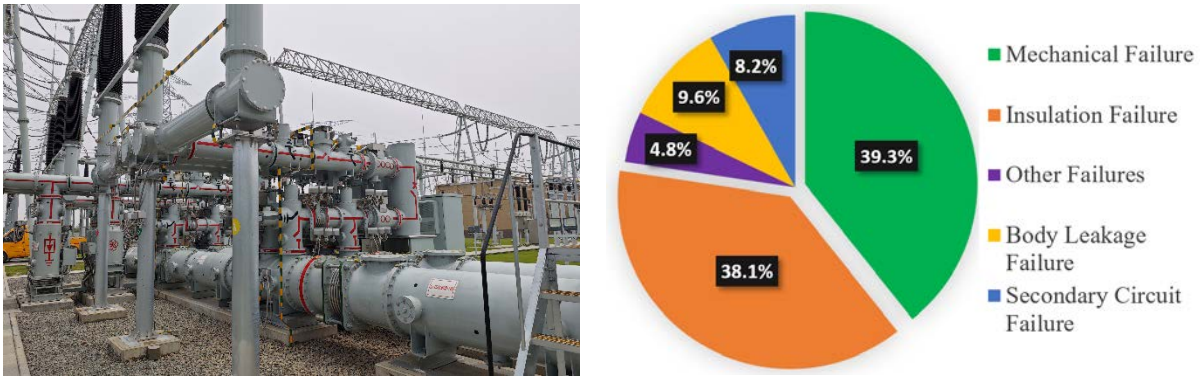

(a) (b)

Figure 1-1 GIS and statistical failure causes. (a) Actual GIS. (b) Proportion of GIS failure categories.

Therefore, conducting synchronous measurement and fusion analysis of the mechanical and insulation states of GIS is essential for the early detection of internal defects, playing a crucial role in ensuring the safety and stability of the power system.

Free metal particles inside GIS are a typical and inevitable insulation defect related to mechanical vibration. The main causes are the processing quality of parts and mechanical vibration friction during operation. The enclosed installation design and complex mechanical structure further complicate the detection of internal metal particles[15]. According to the survey results from the International Conference on Large Electric Networks (CIGRE), the discharge failure rate caused by metal particles and foreign objects in GIS accounts for 21%. The metal particles can severely jeopardize the insulation condition of GIS[16]. Firstly, stationary metal particles may be located at the bottom of the GIS enclosure or adsorbed on the insulators or high-voltage electrodes, causing distortion of the nearby electric field and shortening the discharge distance, which can lead to surface flashover[17,18]. Secondly, when the particles are in motion, the metal particles inside the GIS exhibit complex motion characteristics under the combined effects of the electric field and GIS vibration. These particles can jump and move inside the equipment, significantly increasing the discharge risk and insulation instability, making it easier to trigger air-gap breakdown[19,20]. Figure 1-2 (a) shows the internal structure of GIS disconnector. The metal particles generated by friction at the contact may fall onto the inner wall of the GIS enclosure or attach to the surface of the insulator, triggering PD. Figure 1-2 (b) illustrates an insulation breakdown incident at the busbar connection of a 1100 kV ultra-high-voltage GIS substation, where tiny particles are present at the insulation pot connection gap. When the busbar is re-energized, factors such as residual charges on the pot surface and operation overvoltage induced electric field distortion in the triangular zone of the pot's electrical connection, causing flashover failure at the connection[21]. Currently, research on metal particle defect mainly focuses on high-voltage environment. However, during actual GIS operation, mechanical vibration of varying degrees also occur, which can affect the motion of metal particles. Therefore, it is necessary to study the motion and discharge characteristics of metal particles in GIS under real operating conditions (high voltage combined with mechanical vibration).

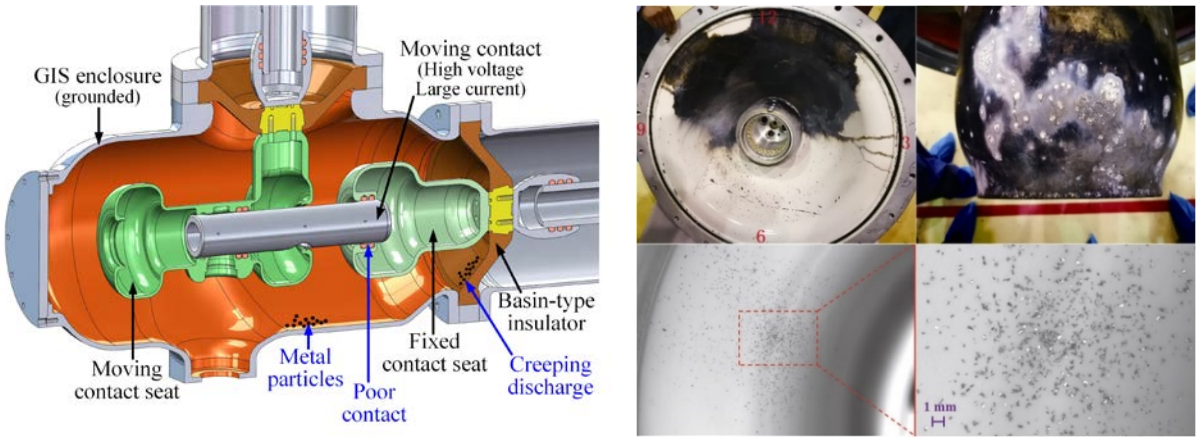

(a) (b)

Figure 1-2 Metal particle defect in GIS equipment. (a) Particle defect at the disconnector. (b) Flashover along the surface of the insulation basin induced by particles.

Vibration acceleration sensors are the most important measurement sensors for detecting mechanical vibration signal on power equipment. Vibration signal reflect the mechanical condition of the equipment and are particularly effective in fault detection for GIS, transformers, motors, and other equipment[22-24]. On the other hand, PD measurement is the most effective and intuitive method for characterizing the insulation performance of equipment. PD is usually detected in the form of sound, light, or electrical signals. Common PD measurement sensors include current sensor, Acoustic Emission (AE) sensor, optical sensor, and Ultra-High-Frequency (UHF) sensor. Among these, optical and UHF sensors are typically built-in, while the current sensor has a different measurement principle with vibration measurement. Thus, only the AE sensor can be effectively integrated with vibration measurement. The sensitivity of different PD sensors varies for different types of insulation defects[25,26]. Currently, the detection of power equipment status is limited by the single detection function of sensors, which can only detect vibration signal or PD signal separately. This limitation hinders the simultaneous, co-located, and synchronized acquisition of both mechanical vibration and PD signals, which is essential for accurately analyzing the correlation between the mechanical and insulation states of GIS equipment. Without this capability, it is difficult to capture the dynamic interaction between mechanical defects and insulation degradation under real operating condition. Furthermore, the single-type sensing approach results in incomplete diagnostic information, increasing the possibility of false alarms or missed fault detection. This not only reduces the reliability of condition monitoring systems but also limits the ability to comprehensively understand and track the progression of faults, thereby affecting timely maintenance decisions and overall system reliability.

Fusion signal detection and analysis for power equipment defects is a key research focus. Economically, Fusion sensors can measure multiple signals, offering more functions, broader detection coverage, fewer required devices, and lower costs, making them suitable for large-scale substation applications. In terms of efficiency, traditional sensors can only detect a single physical signal, whereas fusion sensors can simultaneously detect multiple signals, simplifying the detection process and reducing time costs. For technical aspect, the synchronized detection of multi-physical signals in both time and space enables multi-signal fusion analysis of power equipment defects, improving defect detection efficiency[27-29]. Currently, most research on fusion sensors focuses on specific defects. However, in addition to improving detection accuracy, it is equally important to enhance the detection scope and comprehensiveness. Nowadays, no studies have reported the development of fusion sensing devices capable of simultaneously detecting both mechanical vibration and PD.

In summary, this study focuses on the optimized design and development of a vibration-AE fusion sensor, explores intelligent sensing technology for GIS equipment condition detection, investigates the motion and PD characteristics of metal particles in GIS under real operating conditions with power-frequency voltage and mechanical vibration, and proposes a fusion detection method based on mechanical vibration and Partial Discharge Acoustic Emission (PDAE) signals, providing theoretical and technical support for on-site GIS defect detection experiments, which holds significant academic and engineering value.

1.2 Research Status at Home and Abroad

1.2.1 Piezoelectric Vibration and AE Sensors and the Applications in Power Equipment Defect Detection

1) Research on Piezoelectric Vibration Sensors

Vibration acceleration sensor is used to measure the vibration acceleration of an object's surface. Within its linear operating range, the output electrical signal is proportional to the measured acceleration value[30]. Based on the type of sensing element, common vibration sensors can be categorized into piezoelectric, capacitive, piezoresistive, magnetic induction, and fiber-optic types[31]. Among them, piezoelectric vibration sensors exhibit excellent dynamic response and linearity, a wide frequency range, high sensitivity, suitability for various temperature environments and reliable performance, making them the predominant choice in vibration sensing. Researchers have conducted extensive studies on the design, optimization, and development of vibration sensors.

In the 1940s, with the development of piezoelectric materials, researchers began exploring their applications in vibration measurement. The work of D.E. Weiss in the US on piezoelectric sensor technology contributed to its early commercialization[32]. Subsequently, more companies recognized the significant advantages of piezoelectric materials in sensor applications, leading to the continuous development of new piezoelectric sensors. In 1943, the Brüel & Kjær company developed the world's first commercially available piezoelectric accelerometer. In the early 1950s, the company further advanced accelerometer technology by utilizing piezoelectric ceramics as sensing elements[33]. In 1972, Brüel & Kjær introduced the shear-type piezoelectric accelerometer, which offered improved low-frequency response and static characteristics. This design prevented direct contact between the sensing element and the base, effectively reducing the influence of base strain interference on measurements and minimizing thermal coupling effects, thereby significantly enhancing the overall sensor performance. This technological innovation played a crucial role in the development of piezoelectric accelerometers[34]. Figure 1-3 illustrates the structures of typical compression-type and shear-type sensors.

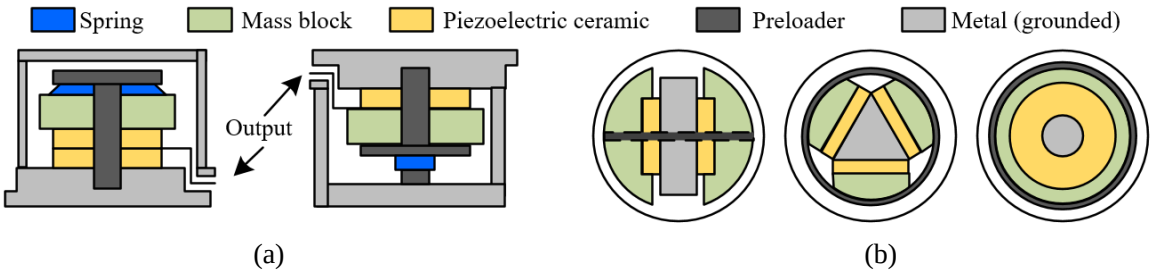

Figure 1-3 Compression-type and shear-type structures of vibration sensor. (a) Central and inverted compression type (cross-sectional). (b) Planar, triangular, and annular shear type (top view).

American Endevco company primarily develops miniature, high-g acceleration sensors. In the 1960s, they developed a sensor weighing only 1.3 g with a measurement range of up to 10,000 g (1 g = 9.8 m/s²)[35]. In the 1950s, Swiss company Kistler pioneered the charge-output piezoelectric sensor, which featured high sensitivity and anti-interference

characteristics. It required an external charge amplifier to convert the signal, and is used to measure dynamic forces, pressures, and accelerations[36]. Founded in 1967, American company PCB played an important role in the development and promotion of built-in circuitry technology for sensors. They are the first to develop acceleration sensors with built-in amplification circuits and later introduced Integrated Electronics Piezo-Electric (IEPE) technology to the industrial market[37]. In 1973, PCB introduced the first industrial IEPE acceleration sensor, and now, the built-in amplification circuit technology continues to play a key role in dynamic measurement fields. Figure 1-4 shows the structure of the IEPE shear-type vibration acceleration sensor.

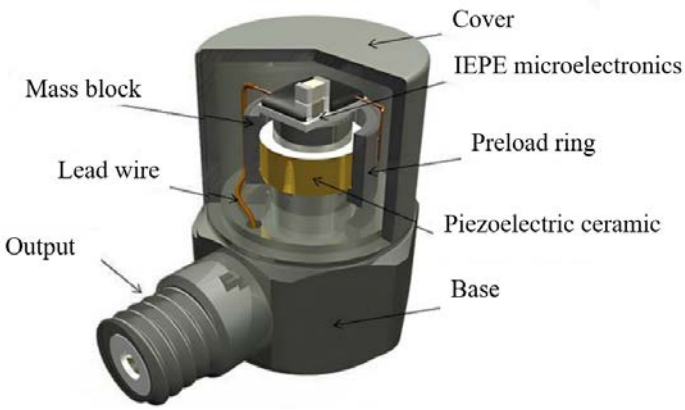

Figure 1-4 IEPE shear-type acceleration sensor

The development of piezoelectric vibration sensors in China has gone through a process from basic research to independent innovation, and then to industrial application. Around the 1960s, research on domestic vibration acceleration sensors began, and the Wuhan radio components factory successfully produced the first batch of barium titanate piezoelectric ceramics. With continuous technological advancements, domestic PZT series piezoelectric ceramics are successively introduced, laying a solid foundation for the development of domestic piezoelectric technology[38]. Subsequently, domestic research institutions and universities achieved independent research and development of piezoelectric acceleration sensors, which are gradually applied in fields such as aerospace, weaponry, and industrial monitoring. Meng Yuanbo from Harbin Institute of Technology analyzed the mechanism of piezoelectric sensors, designing the structure, conditioning circuits, and sensitive elements, and researched a piezoelectric vibration sensor for monitoring petroleum pipelines[39]. Zhu Ruihao from the University of Electronic Science and Technology designed and built a high-temperature piezoelectric acceleration sensor[40]. Chen Yiqiang from Yanshan University developed an IEPE piezoelectric acceleration sensor and studied its low-noise characteristics, establishing a noise model, optimizing the design, and improving the measurement accuracy of low-frequency weak vibration signals[41]. Currently, foreign companies have launched MEMS-based precision portable, fiber-optic digital, and electromagnetic vibration sensors. Domestic universities (such as Tsinghua University, Shanghai Jiao Tong University), research institutions (such as the Chinese Academy of Sciences, Aerospace Fifth Academy), and enterprises (such as Wuhan Ulik Technology,

LITAI Technology) have also successfully developed a series of diversified, high-performance vibration acceleration sensors. However, China's vibration sensor technology still lags behind that of foreign countries, particularly in terms of sensor intelligence, product variety, and specifications.

2) Research on piezoelectric AE sensors

AE is a mechanical wave with frequencies above 20 kHz, characterized by high frequency, short wavelength, and good directionality. AE sensors convert AE signal into electrical signal and are widely used in distance measurement, flow measurement, liquid level detection, nondestructive testing, and medical imaging. Based on working principles, AE sensors are classified into capacitive, electromagnetic, fiber-optic, and piezoelectric types[42-45]. Capacitive AE sensors measure by converting AE signals into capacitance but require DC bias voltage and have poor noise resistance. Electromagnetic AE sensors use eddy currents and Lorentz forces to excite and receive AE waves on conductive surfaces, but they have high power requirements, high costs, and low sensitivity. Fiber-optic AE sensors detect changes in light parameters to sense AE signals, offering high sensitivity and small size, though they are susceptible to external interference. Piezoelectric AE sensors, which convert AE signals into electrical signals via the piezoelectric effect, are the most widely used due to their high sensitivity, wide bandwidth, and stability, making them a focus of extensive research.

In the 1930s, the Massachusetts Institute of Technology applied quartz piezoelectric sensors to underwater sonar, but the low mechanical strength and charge constant made them inadequate for high-sensitivity applications. In the early 1940s, American researchers successfully developed Barium Titanate ($BaTiO_3$) ceramics with piezoelectric properties, which are used to develop ultrasonic Non-Destructive Testing (NDT) transducers. In the 1950s, B. Jaffe and others invented PZT (lead zirconate titanate) ceramics, which significantly outperformed barium titanate and became the dominant material[46]. Companies such as Kistler, Brüel & Kjær, and PCB are pioneers in the commercial production of piezoelectric sensors based on PZT. These sensors are then widely applied in medical ultrasound imaging and industrial NDT. In the 1980s, PCB incorporated IEPE technology into piezoelectric AE sensors, solving the impedance matching issues of traditional sensors with built-in signal conditioning modules, thus improving the signal-to-noise ratio in industrial testing. Piezoelectric AE sensors are widely used, and selecting the appropriate piezoelectric material and designing the structure according to the specific application scenario is critical. Vivek T. Rathod summarized recent research on acoustic impedance matching techniques for piezoelectric sensors, providing technical references for selecting and manufacturing acoustic matching layers[47]. C.S. Desilets and others proposed a design method for high-efficiency, broadband, and good pulse response acoustic disc transducers based on quarter-wave theory and the KLM model, offering new ideas for AE sensor design[48]. Martin A. Aulestia Viera and others developed a closed PZT sensor to improve the durability of low-cost piezoelectric sensors for repeated use, with experimental results showing response characteristics close to commercial AE sensors[49]. Three typical structures

of piezoelectrical AE sensor are shown in Figure 1-5. The resonant type obtains enhanced sensitivity at the resonant frequency by utilizing the mechanical resonance of the piezoelectric ceramic. The broadband type achieves a more uniform AE frequency response by incorporating a backing material. The IEPE type enhances output sensitivity and interference resistance by integrating a signal conditioning circuit.

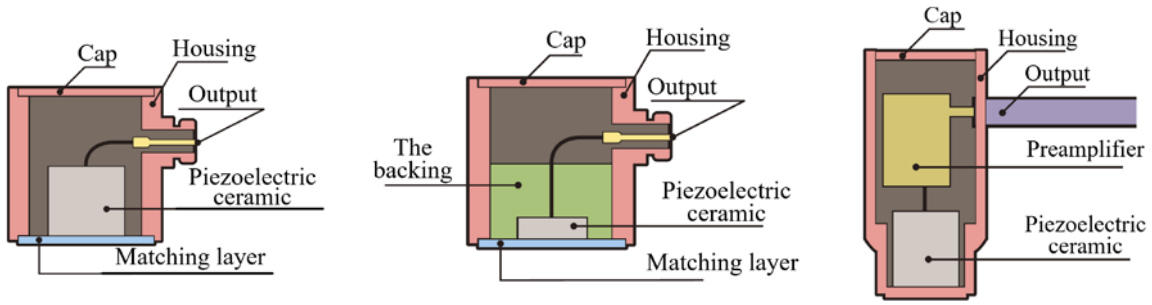

(a) (b) (c)

Figure 1-5 Three typical structures of AE sensor. (a) Resonant type. (b) Broadband type. (c) IEPE type.

Research on piezoelectric ultrasonics in China began in the 1950s-1970s, driven by the efforts of Academician Chong Fu, who laid the theoretical foundation for the field of ultrasonics in China[50]. Shuyu Lin from Shaanxi Normal University summarized the working principle, dynamic characteristics, and key parameters of piezoelectric ultrasonic sensors, establishing electrical and acoustic matching for AE measurements, thus providing a theoretical and design basis for sensor research. In the area of AE sensors for power equipment defect detection, Rong Liu from Northwestern Polytechnical University developed a PD ultrasonic and ultra-high-frequency signals detection and identification system for cross-linked polyethylene (XLPE) cable insulation defects [51]. Yu Yan and others from Xi'an Jiaotong University designed and fabricated a high-sensitivity flexible AE sensor based on PZT piezoelectric films for cable partial discharge detection[52]. Wang Yan and colleagues from the global energy interconnection research institute studied the effects of material and structure on the sensitivity of contact-type piezoelectric AE sensors using finite element simulation and proposed optimization methods for sensor structures[53].

Currently, companies like Physical Acoustics Corporation (PAC) in the United States, Vallen Systeme in Germany, and Fuji Ultrasound in Japan have launched microelectronic integrated AE sensors and portable AE detection systems. In China, companies such as Qingcheng Acoustic Emission and Pengxiang have developed PVDF film-based and MEMS micro AE sensors. However, China's AE sensors still lag behind those from abroad, mainly in terms of lower sensitivity and a limited variety of sensor specifications.

3) Application of Mechanical Vibration and AE Signals in GIS Defect Detection

Large GIS equipment operates under high voltage and high current conditions, creating strong electromagnetic fields and complex mechanical vibration. In this condition, the presence of certain defects can lead to abnormal vibration and PD. The PD causes charge neutralization, resulting in a steep current pulse that leads to rapid local heating and expansion, producing an explosion-like effect. The region then quickly returns to its original volume. This rapid expansion and contraction causes the transient volume change that

generates the acoustic emission of PD. In GIS, the resonant frequency of acoustic emission signals from partial discharge is typically around 25 kHz, with a range of 20~100 kHz. Studies have shown that vibration and AE sensoring technologies are effective ways for detecting mechanical defects and insulation defects, respectively[54,55]. As a result, both domestic and international researchers have conducted extensive studies in this field.

The research group of Junhao Li at Xi'an Jiaotong University has conducted extensive studies on the mechanical vibration characteristics and defect diagnosis methods for GIS equipment. Their work investigates the vibration characteristics of typical mechanical defects inside GIS, such as poor contact, loose components, busbar misalignment, and internal foreign objects. They proposed a GIS mechanical defect diagnosis method based on EMD-FFT feature extraction[56-58]. Dengwei Ding and his team at the Tsinghua Sichuan Energy Internet Research Institute successfully quantified the severity of GIS disconnector mechanical defects by analyzing three characteristic parameters: waveform amplitude, spectral distribution, and waveform distortion rate[59]. Ying Feng and colleagues at Beihang University introduced a method based on harmonic energy ratio features, effectively distinguishing between normal GIS operation, disconnector faults, and loose flange bolts—three typical mechanical defects[60]. Yao Zhong at Chongqing University characterized the nonlinear vibration behavior of GIS mechanical defects using key parameters such as centroid frequency, harmonic distortion rate, energy, chaos index, and kurtosis, extracted through Gaussian threshold filtering, Poincaré mapping, and composite feature analysis. The proposed load ratio-based grading diagnosis algorithm enables accurate identification of defect types and severity under varying load conditions[61].

The PDAE detection method for power equipment offers high sensitivity and strong anti-interference capability. Studies have shown that it can detect internal insulation defects in power equipment, with AE signals exhibiting distinct time-domain and frequency-domain characteristics under different defect conditions. Currently, AE detection technology is widely applied in PD detection in laboratories and substations. Yanpeng Hao et al. at South China University of Technology systematically reviewed the research progress of multiple AE detection techniques for GIS insulators, addressing issues such as stress concentration, density non-uniformity, and internal defects. They also highlighted key technical and theoretical challenges that need to be resolved[62]. Wenrong Si from East China Electric Power Test & Research Institute introduced a GIS insulation defect identification technique based on AE detection, where amplitude, time-of-flight, and phase patterns are used to distinguish different types of PD[63]. H. D. Ilkhechi et al. summarized the key characteristics of AE technology and sensors, comparing acoustic and electrical PD measurement methods. Their study analyzed PD detection applications in transformers and GIS, reviewed AE signal processing techniques, and emphasized the low cost of AE detection, which enables measurement, identification, and localization of PD in various power equipment, making it suitable for online monitoring[64]. Zulbirri Faizol et al. reviewed and compared existing PD signal detection and localization methods for high-voltage equipment, summarizing future research directions in PD detection. They pointed out that AE-based PD detection has

become the preferred technology for power equipment due to its effectiveness, low cost and interference immunity[65].

Existing GIS defect detection studies have primarily focused on either vibration or AE signal analysis alone. However, increasing attention is now being given to multi-signal fusion for comprehensive defect detection. A. Stief et al. analyzed acoustic, electrical, and vibration signals collected from induction motors operating under different conditions. They employed a fusion method combining a two-stage Bayesian approach and Principal Component Analysis (PCA) to diagnose electrical and mechanical faults[66]. Jian Hao et al. at Chongqing university conducted joint AE and vibration detection for a 550 kV GIS busbar base with looseness and foreign object defects. They analyzed the PD and vibration characteristics of the defect under different voltage and current conditions. Additionally, they made joint detection on both normal and abnormal disconnector and voltage transformer chambers, comparing signal differences in the time domain, frequency domain, and generation mechanism[67,68].

In summary, significant progress has been made in the research of piezoelectric vibration acceleration sensors and AE sensors, both of which have been effectively applied to GIS mechanical and insulation conditions detection[69]. In recent years, studies on multi-signal joint detection have demonstrated that comprehensive analysis of multiple physical signals enables faster and more accurate diagnosis of a wider range of fault modes. However, existing sensors remain limited by their single-function design, low intelligence, and constrained measurement range, making it difficult to enhance fusion detection efficiency. To date, there has been no systematic research on the design, fabrication, testing, and application of vibration-AE fusion sensor.

1.2.2 Research on Intelligent Sensor Technology for Power Equipment Condition detection

Sensor technology is a multidisciplinary and cross-technology research field, serving as a key approach to achieving intelligent and digitalized condition detection of power equipment[70,71]. Initially, sensors consisted solely of sensing elements, later evolving into basic sensors incorporating analog-to-digital conversion and signal processing units. Modern intelligent sensors now integrate perception, storage, computation, and communication capabilities. Researchers continue to advance sensor intelligent optimization and improvement, driving the application in the field of power equipment measurement[72-76].

Currently, common wireless transmission technologies have distinct characteristics. Table 1-1 compares four widely used wireless transmission technologies[77,78]: Wi-Fi offers the highest throughput (0.6–7 Gbps) with a communication range of 30-100 meters. However, it has high power consumption and cost, making it suitable for applications requiring stable power supply, such as public networks (entertainment or office use) and video streaming. Bluetooth Low Energy (BLE) provides moderate throughput (1–3 Mbps) with a range of 10-50 meters. It features low power consumption, low cost, and low latency, making it ideal for home automation, Personal Area Networks (PAN), and positioning

applications. LoRa is characterized by ultra-low power consumption and long transmission distances (up to 10 km). However, it has low throughput (0.3-50 kbps) and communication latency, making it suitable for applications requiring large coverage but low data volume, such as environmental monitoring, smart cities, and agriculture. ZigBee supports scalable mesh networking between devices but has relatively low throughput (20–250 kbps). It is well-suited for low-data communication across numerous devices in a limited area, such as IoT, building automation, and energy management (smart meters).

Table 1-1 Comparison of four major wireless technologies

Protocol	Wi-Fi	BLE	LoRa	ZigBee
Throughput	0.6~7 Gbps	1~3 Mbps	0.3~50 kbps	20~250 kbps
Range/m	30~100	10~50	100~10000	10~75
Power consumption	High	Low	Very Low	Low
Scalability	Middle	Middle	Middle	High
Cost	High	Low	Middle	Middle
Latency	Low	Low	Middle	Low

Yu BoNing et al. from Xi'an Jiaotong university proposed a LoRa-based distributed Wireless Sensor Network (WSN) for PD detection and early warning in power distribution equipment. They designed Transient Earth Voltage (TEV) and High-Frequency Current Transformer (HFCT) sensor nodes for switchgear and cable accessories, utilizing a Low Power Wide Area Network (LPWAN) for data transmission and management. Energy consumption measurements and evaluations verified the feasibility of this approach, and insulation condition assessment and early warning strategies suitable for WSNs are explored[79]. Annalisa Liccardo et al. from the University of Naples Federico II developed an IoT-enabled LoRa wireless sensor for PD monitoring in underground substations. The system includes an AE sensor for PD measurement, a programmable signal conditioning circuit, and a digital signal transmission module. Experimental results demonstrated that the sensor reliably detects PD, and the LoRaWAN transmission remains highly reliable even in underground environments characterized by thick concrete walls and strong electromagnetic interference[80]. Shi Dawei et al. from the University of Huddersfield proposed a Wireless Rotor Sensing (ORS) method for motor condition monitoring. An embedded MEMS accelerometer measures rotor vibration, while BLE 5.0 enables efficient wireless data transmission. The ORS node is directly mounted on the motor shaft, close to the vibration source, significantly improving the signal-to-noise ratio and enhancing fault detection capability[81].

Edge computing is a key feature of intelligent sensors. Since the concept of cloud computing was introduced in 2005, its widespread adoption has profoundly impacted human society. From 2005 to 2015, centralized big data processing is the dominant model globally. However, with the explosive growth of data (especially edge data) in everyday applications, cloud computing has increasingly revealed efficiency bottlenecks. The rising number of

client devices, along with growing data volume and transmission costs, are the primary factors reducing cloud computing efficiency. The emergence of the Internet of Things (IoT) has provided an effective solution to this challenge[82]. Edge computing is particularly crucial in industrial measurement. For example, a Boeing 787 generates over 5 GB of data per second, while an autonomous vehicle produces more than 1 GB per second. Due to internet bandwidth limitation, transmitting such massive data volumes to the cloud would lead to significant latency. To reduce transmission costs and improve processing efficiency, these edge data must be processed locally through edge computing[83].

Zhao Chunhua et al. from Chongqing University conducted a series of studies on intelligent edge computing for wireless sensor nodes used in monitoring mechanical defects in equipment. They embedded self-developed acquisition and computing nodes into wireless sensors, addressing issues such as large data transmission volumes and limited storage and computing resources in wireless sensor networks. By optimizing acquisition and reconstruction algorithms, the data transmission is significantly reduced (by 70%) while maintaining high-accuracy fault detection efficiency[84,85]. Figure 1-6 (a) illustrates the developed wireless edge computing node. Peter Luong et al. from Lakehead university, Canada, proposed an intelligent sensor for detecting rotor bar faults in induction motors by combining vibration and current harmonic signals. This sensor enables low-cost installation through a non-intrusive wireless sensor system and uses Signal-to-Noise Ratio (SNR) analysis to generate fault diagnosis indicators. Experimental results validated the method's advantages in fault detection accuracy and diagnostic capability under no-load conditions[86]. Figure 1-6 (b) shows the developed wireless intelligent sensor node.

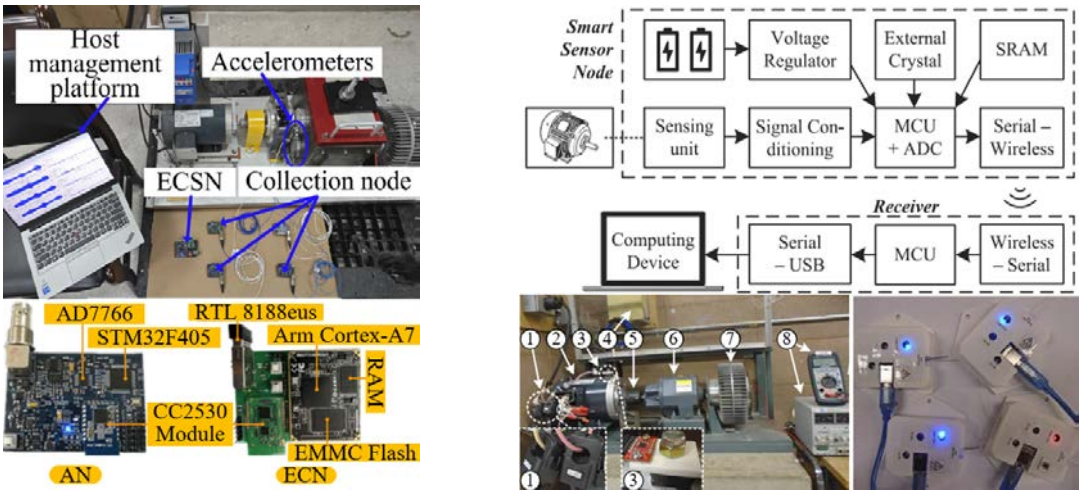

(a) (b)

Figure 1-6 Intelligent wireless sensor (a) Wireless edge computing node (b) Wireless intelligent sensing node for induction motors.

Jiang Yi et al. from NARI Group developed an edge-cloud collaborative service architecture to address the challenges in monitoring multiple status variables of substation equipment, such as difficulties in integrating heterogeneous sensors, large data processing delays, and high data transmission bandwidth utilization. They designed an edge computing device that supports multi-sensor protocol parsing, data acquisition, and processing, enabling

status evaluation and edge services for substation equipment at the edge side[87]. Jinsheng Ji et al. from Nanyang Technological University, Singapore, improved the efficiency and accuracy of PD detection by combining edge computing with Knowledge Distillation (KD) and Multi-Task Learning (MTL). They optimized feature extraction through energy-adaptive sampling and spatial information distillation, and used k-means clustering to separate PD signals from noise. Experimental results showed that the integrated KD and MTL model outperforms baseline methods, fully showing the advantages of edge computing[88].

Piezoelectric elements, such as lead zirconate titanate (PZT) and piezoelectric polymers, form the core components of piezoelectric sensors. Their performance is influenced by environmental factors, service life, and the structural characteristics of the sensor itself. Since any variation in the performance parameters of piezoelectric sensors can lead to measurement errors, periodic calibration is essential. The impedance curve and sensitivity response curve are two critical parameters of piezoelectric sensors, representing electrical and mechanical responses, respectively. Both parameters require regular calibration during operation[89,90]. However, calibration experiments for piezoelectric sensors are not only time-consuming and costly but also depend on bulky specialized equipment, which restricts calibration to laboratory settings.

To enhance the efficiency of on-site calibration for piezoelectric sensor sensitivity, Hualan et al. proposed a face-to-face method (as shown in Figure 1-7 (a)), which determines the sensitivity response of AE sensors point by point. The results are generally consistent with ISO standard measurements. However, this method requires bulky experimental equipment, such as signal generators and oscilloscopes, making it unsuitable for field testing[91]. Zhang Lu et al. combined a multi-physics coupled numerical model and an experimental model to achieve absolute calibration of piezoelectric AE sensors. However, obtaining the actual parameters of the electrical model is challenging, and the accuracy of the results needs further improvement[92]. Therefore, existing calibration methods for piezoelectric sensors remain inconvenient and inefficient, particularly in multi-sensor calibration, emergency scenarios, or field applications.

As one of the fundamental characteristics of intelligent sensors, self-calibration has increasingly attracted the attention of researchers. Michiel Pertijs defined self-calibration as the process by which a sensor establishes the relationship between the measured physical quantity (input) and the corresponding indication quantity (output) through its internal system configuration in the field of application[93]. Although achieving absolute self-calibration is extremely challenging and cannot fully replace international standards, conditional self-calibration can effectively reflect changes in sensor performance and extend the interval between laboratory calibrations or recalibrations. From an economic perspective, self-calibration significantly reduces calibration costs and enables rapid and efficient sensor calibration, with each sensor capable of self-calibration through embedded devices. Technically, self-calibration methods can monitor the state of measuring equipment in real time, ensuring measurement accuracy. Current research generally integrates an internal actuator within the sensor to achieve self-calibration (as shown in Figure 1-7 (b)). However,

these methods often rely on external power supplies and data acquisition systems, which are not only expensive and inconvenient to use but also susceptible to accuracy degradation due to variations in the performance of the internal actuator[94]. In the field of piezoelectric sensors, research on the application of self-calibration technology remains limited.

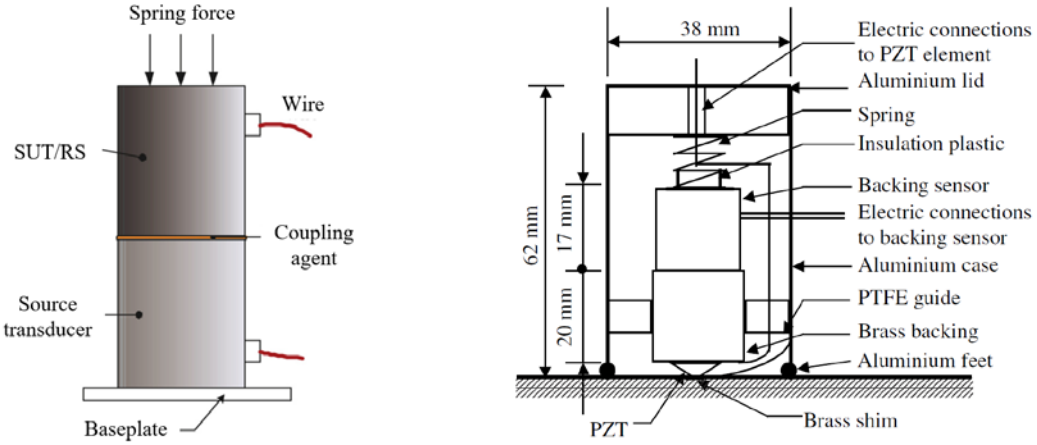

(a) (b)

Figure 1-7 Self-calibration methods for piezoelectric sensors. (a) Face-to-face calibration. (b) Self-calibration of conical piezoelectric sensors.

In summary, current intelligent sensors perform well in laboratory measurements for defect detection in power equipment, with research primarily focusing on key technologies such as wireless sensor networks, edge computing, compressed sensing, and self-calibration. However, some challenges still exist, including the lack of fusion measurement capabilities, low system integration, and high complexity in self-calibration. Furthermore, while research efforts have advanced sensor intelligence, they have yet to fully address practical implementation, which limits their engineering applications.

1.2.3 Research on Detection of Metal Particle Defects in GIS Equipment

The components of GIS are processed in factories and assembled on-site at substations. During the processing, transportation, assembly and operation, mechanical factors such as internal component collisions, friction, cylinder vibration, and thermal expansion and contraction can inevitably lead to metal particles generation inside the equipment. Moreover, due to the large length of GIS, ranging from tens to hundreds of meters, long cables and complex structures increase the probability of metal particle generation[95]. Furthermore, GIS equipment is completely sealed with SF_6 gas at approximately 0.4 MPa pressure inside, making periodic disassembly, inspection, and maintenance impossible. Although some critical areas within the GIS are equipped with particle collectors, the results are limited, and metal particles are difficult to be detected and completely eliminated in time. Many scholars have researched on this complex practical issue.

In the last century, foreign scholars such as NITTA T and DOEPKEN H C researched on the impact of metal particle materials inside GIS equipment on breakdown voltage, including copper, aluminum, epoxy resin, carbon, and fluorite. The results show that conductive particles have a significant impact on insulation, while insulating particles have a

few effect. Therefore, conductive metal particles became the focus of research[96,97]. Scholars have statistically analyzed the actual metal particles in GIS, finding that the shapes are mainly spherical, linear, and flaky[98-101]. Sakai et al., based on wedge-shaped plate tests, summarized that linear particles in an AC electric field exhibit three behaviors: stationary, lifting, and jumping, and particles are likely to move toward high-field regions and cause breakdown[102]. Asano K et al., using parallel plate and inclined electrode models, calculated the critical voltage at which spherical particles begin to move and stop. They also verified the results using high-speed images of particle motion[103]. Li Chengrong's team at North China electric power university researched on spherical, flaky, and linear particles, finding that the motion of flaky and linear particles mainly involves stationary standing, small amplitude jumping, large amplitude jumping, and penetrating jumping. Increasing the number of adjacent linear and flaky particles leads to a decrease in the initiation voltage, while the initiation voltage of spherical particles is almost unaffected by particle quantity. As shown in Figure 1-8, under the same parameters, plate-shaped particles carry more charge than linear ones and are more likely to jump and cause PD[104,105].

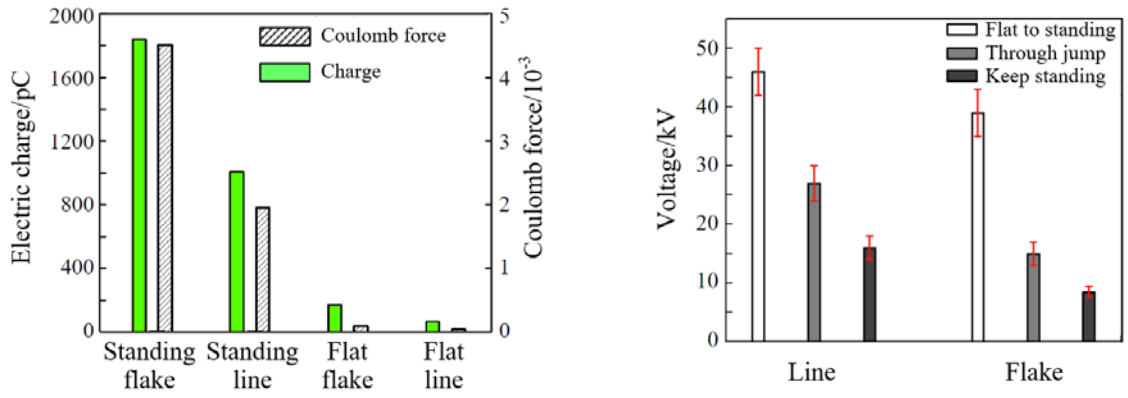

(a) (b)

Figure 1-8 Comparison of PD characteristics between flaky and linear metal particles of the same size. (a) Coulomb force and charge comparison. (b) State maintenance voltage comparison.

The study of the size and quantity of metal particles has also received considerable attention. Ma Hongzhong et al. at Hohai university researched on the motion of metal particle contaminant and insulation cracking caused by abnormal PD inside Gas Insulated metal enclosed transmission Line (GIL). Using UHF phase-resolved partial discharge (PRPD) patterns, they analyzed the PD behavior of single and multiple metal particles[106]. It is found the motion of multiple metal particles in an electric field exhibits significant disorder, with frequent charge exchange between them. The presence of particle clusters significantly reduces the partial discharge inception voltage (PDIV) and increases the discharge amplitude. Ji Hongxin' et al. at North China electric power university studied the motion behaviors and PD characteristics of different metal particles under high voltage. It is found the free jumping of single linear and flaky particles under high-voltage busbars and shielding rings poses relatively little threat to GIS, but the threat increases significantly as the number of particles increases[107]. Zhan Zhenyu compared the motion characteristics of different types of particles (including metal, semiconductor, and insulating powders) inside the GIL model.

The results show that large-sized metal particles significantly reduce the surface flashover voltage of insulation materials[108]. Kuwahara et al. studied the effect of metal particle size on insulation strength, finding that a small number of particles with diameters less than 30 μm do not significantly affect the breakdown voltage, but as the number and size of particles increase, the insulation strength of GIL devices significantly decreases[109]. Alan H. Cookson's research indicated that, in coaxial structure electrodes, the longer the linear particle, the lower the breakdown voltage, while the particle width has a smaller effect. Additionally, the breakdown voltage is unstable[110].

The PDAE detection method is highly sensitive to metal particle defects inside GIS equipment, and scholars mainly focus on analysis using AE signals. L.E. Lundgaard et al. proposed an AE flight spectrogram for PD detection, as shown in Figure 1-9 (a). This method can be used to assess the severity of PD and has been found that the amplitude of AE signals generated by PDs is linearly related to the particle's momentum, as shown in Figure 1-9 (b)[111-113].

Magne Runde et al. investigated the relationship between the amplitude-suspension time characteristic spectrogram of AE signal and particle length, proposing that the maximum flight time and maximum AE amplitude can be used to assess whether particles trigger breakdown[114]. Schlemper et al. analyzed the discharge amplitude-suspension time characteristic spectrogram of particles and examined the influence of the charge-to-mass ratio on particle suspension time. The results indicate that this ratio determines the flight duration of particles[115]. Li Dajian et al. from Xi'an Jiaotong university studied the AE signal characteristics of freely moving metal particles under high electric field strength. They found that the flight spectrogram of metal particle defects exhibits a distinct "hump" feature, which is absent in other defect types[116]. Additionally, the AE signal of stationary particles is relatively weak with strong phase correlation, whereas after jumping, the amplitude increases, and phase correlation decreases.

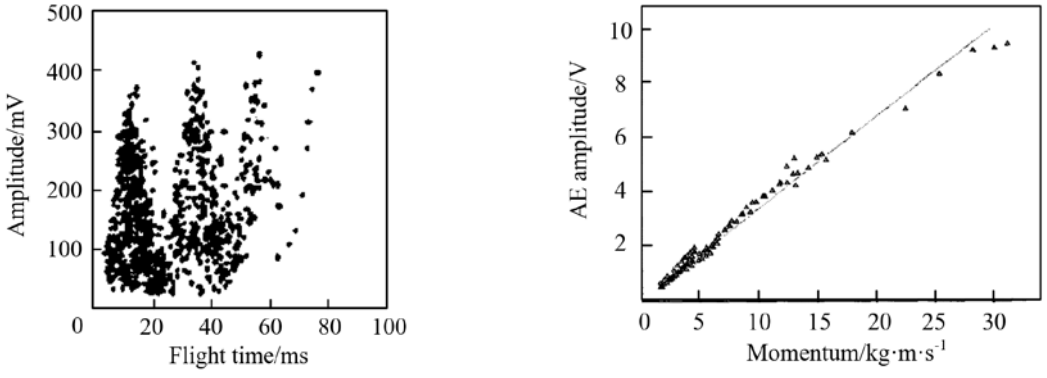

(a) (b)

Figure 1-9 AE detection of metal particle PD. (a) Typical flight pattern of aluminum linear particles. (b) Relationship between particle momentum and AE amplitude.

The above studies have provided a detailed investigation into the behavior and patterns of metal particles under the influence of AC electric fields. However, the mechanical vibration of GIS enclosure’s impact on particle state cannot be ignored. Li Xing et al. from

Tsinghua University studied the impact of shock vibration on the motion-induced insulation surface flashover process of metal particles based on an electric field superimposed shock vibration experimental platform. The experiment show that shock vibration can induce metal particles to take off and continue to jump under the influence of the electric field[117]. Li Xiaoang et al. from Xi'an Jiaotong university established a simulation model for the charging, force, and motion of free metal particles under the condition of superimposed power frequency voltage and sinusoidal vibration in GIS. They investigated the effects of different external voltages and vibration parameters on the motion characteristics of spherical particles and obtained AE flight time spectrograms under different conditions. The results indicate that the vibration reduces the electric field strength required for particle jumping and causes the flight spectrograms to present a peaked shape. Moreover, the maximum flight height between two consecutive collisions of particles is related to the instantaneous voltage phase at the moment of collision and the recovery speed of the collision[118,119].

In summary, the researches on metal particle defect inside GIS are mainly conducted under high-voltage conditions, overlooking the influence of mechanical vibration. However, the vibration of GIS enclosure does have a certain effect on metal particle defects. Enclosure vibration includes both steady-state and transient vibrations, with more research focused on the latter. The actual operating conditions of high voltage combined with steady-state vibration (caused by current) are difficult to simulate, and the related studies are still at the theoretical and simulation stages, lacking corresponding experimental research. Therefore, further study is needed on the motion and PD characteristics of different metal particles inside GIS under power frequency voltage combined with steady-state vibration.

1.3 Main Research Content of This Dissertation

To address the challenges of synchronously detecting and efficiently diagnosing mechanical and insulation defects in GIS, this dissertation proposes the theoretical design, intelligent optimization, and development of a vibration-AE fusion sensor. On this basis, the study further explores sensor intelligence, including wireless module design, edge computing strategies, and self-calibration method. The developed sensor is used to investigate the motion and PD characteristics of free metal particles in GIS under combined power-frequency voltage and mechanical vibration. Furthermore, an evaluation method for metal particle defects in GIS is proposed, along with a summary of vibration and AE fusion detection method. The developed system has been successfully applied in a substation field test. The research framework of this dissertation is illustrated in Figure 1-10, with the main content outlined as follows:

1) A theoretical model for piezoelectric vibration acceleration-AE fusion measurement is proposed, and a fusion sensing structure is designed. The influence of six key structural parameters on the measurement performance is analyzed through simulation. A bidirectional fitting method is employed to expand the simulation dataset, based on which an intelligent algorithm-driven optimization method is developed to determine the optimal structural parameters. The fusion sensing device is fabricated and tested on the established calibration

platforms for vibration and AE measurement.

2) An intelligent upgrade framework for the fusion sensor is established and implemented. A smart wireless sensing module is designed and embedded into the sensor, and its wireless transmission performance and power consumption are tested. Based on the integrated SoC platform, an edge computing strategy is developed for feature extraction of vibration, AE, and fusion signals. Furthermore, a fast calibration method for piezoelectric sensors is proposed, using pseudo-random M-sequence excitation, enabling efficient calibration of impedance and sensitivity curves.

3) A scaled-down experimental platform of a practical 330kV GIS is constructed, capable of simultaneously applying power-frequency voltage and mechanical vibration excitations. The platform is used to experimentally investigate the motion behavior and discharge characteristics of metal particles with varying shapes, masses, and quantities under combined electromechanical conditions. Relevant patterns are analyzed and summarized through theoretical calculation and experiment.

4) An evaluation method for metal particle defect in GIS is explored. Feature extraction approaches for mechanical vibration, PDAE, and fusion signals are summarized, and an intelligent distributed sensing and computing architecture suitable for substation equipment monitoring is proposed. Furthermore, A vibration-AE fusion detection system is developed and successfully applied to GIS condition detection in substation.

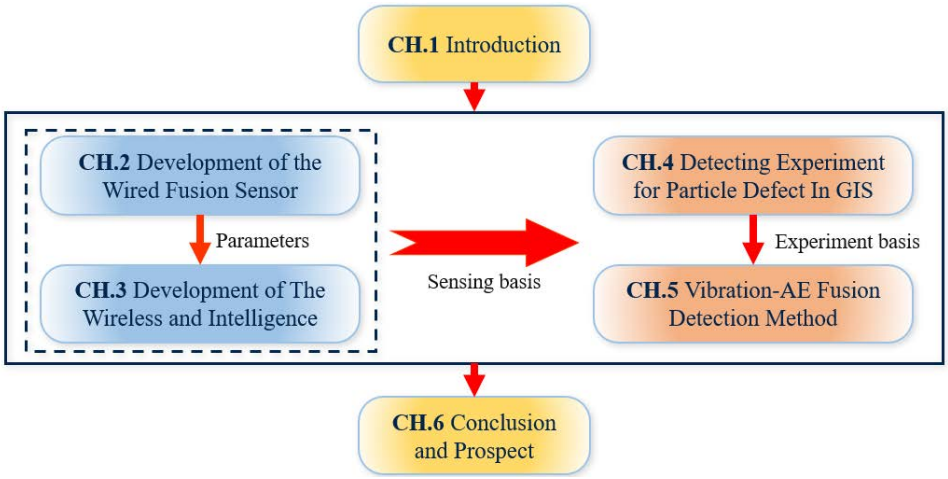

Figure 1-10 Chapter Research Framework

2 Design and Performance Optimization of the Vibration-AE Fusion Sensor

To address the limitations of existing sensor technologies for independent detection and diagnosis of mechanical and insulation conditions of power equipment, this chapter focuses on the design, optimization, and development of vibration-AE fusion sensor to enable synchronized and co-located measurement. First, based on the basic structure and working principle of piezoelectric sensors, an electro-acoustic-mechanical equivalent model is proposed, and the sensing structure of the fusion sensor is designed. Finite element simulations are then conducted to analyze the influence of six key structural parameters on the sensor's vibration and AE measurement performance. A combination of numerical expansion and intelligent algorithms is used to determine the optimal configuration of the structural parameters. Finally, a vibration-AE fusion sensing device is developed and calibrated according to national standards. The developed sensor exhibits good sensitivity in both vibration and AE.

2.1 Measurement Principle and Structural Design of the Vibration-AE Fusion Sensors

2.1.1 Measurement Principles of Piezoelectric AE and Vibration Sensors

1) Piezoelectric Vibration Sensor

Currently, piezoelectric vibration sensors are mainly categorized into compression-type and shear-type. Compression-type sensors utilize the thickness piezoelectric effect (piezoelectric constant: d_{33}), whereas shear-type sensors employ the tangential piezoelectric effect (piezoelectric constant: d_{31}). Depending on specific application requirements, both types are widely used in various measurement fields. Table 2-1 compares their characteristics. The compression-type vibration sensor features a wide bandwidth, high sensitivity, and low cost, making it more suitable for AE-vibration fusion sensor research. Therefore, this section primarily focuses on compression-type piezoelectric vibration sensors.

Table 2-1 Comparison of compression-type and shear-type piezoelectric sensors

Item	Complexity	Cost	Sensitivity	anti-interference	Bandwidth
Compression	Low	Low	High	Middle	Broad
Shear	High	High	High	High	Narrow

Figure 2-1 (a) illustrates the basic structure and measurement principle of a compression-type piezoelectric vibration sensor, which primarily consists of a mass block, a piezoelectric element, and a steel base. The base serves to support and stabilize the entire sensor, while the piezoelectric element converts vibration signals into electrical signals. The mass block provides inertial force to the piezoelectric element, enhancing its deformation

during operation to improve electromechanical conversion efficiency. Figure 2-1(b) shows the mechanical model of the compression-type piezoelectric vibration sensor, where the piezoelectric element is regarded as an elastic medium characterized by a stiffness coefficient k and a damping coefficient c. This model can be used to describe the vibration measurement principle[120].

When vibration signal occurs on the sensor base, it induces a displacement $x(t)$. Due to inertial force, the mass block has a displacement $y(t)$. Consequently, the relative displacement $z(t)$ between the base and the mass block can be given by Equation (2-1).

$$z(t) = y(t) - x(t) \tag{2-1}$$

Under the action of the piezoelectric element, which is considered an elastic medium, the motion equation of the mass block is given by:

$$m\frac{\mathrm{d}^2 y(t)}{\mathrm{d}t^2} + kz(t) + c\frac{\mathrm{d}z(t)}{\mathrm{d}t} = 0 \tag{2-2}$$

Therefore, it can be obtained that:

$$m\frac{\mathrm{d}^2 z(t)}{\mathrm{d}t^2} + kz(t) + c\frac{\mathrm{d}z(t)}{\mathrm{d}t} = -m\frac{\mathrm{d}^2 x(t)}{\mathrm{d}t^2} \tag{2-3}$$

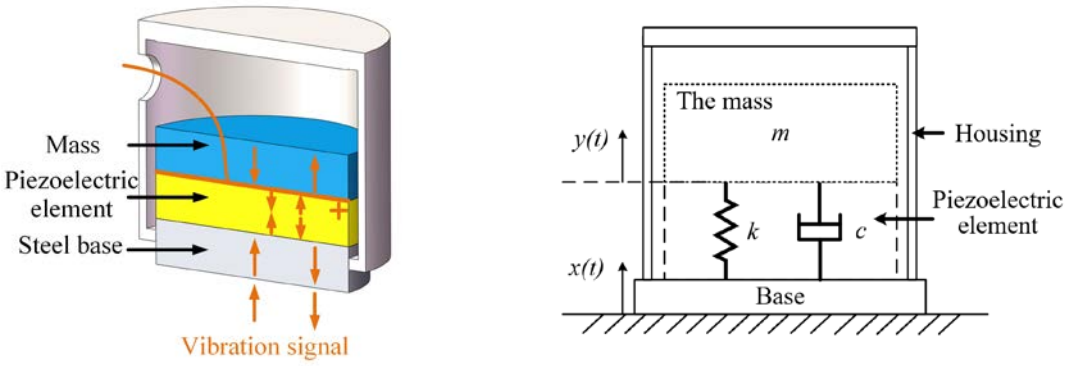

(a) (b)

Figure 2-1 The measurement principle of the piezoelectric vibration acceleration sensor. (a) Basic structure. (b) Mechanical model.

The undamped resonant frequency ω_n and the dimensionless damping ratio ξ are:

$$\omega_n = \sqrt{\frac{k}{m}} \tag{2-4}$$

$$\xi = \frac{c}{2\sqrt{km}} \tag{2-5}$$

The Equation (2-3) can be expressed as:

$$m\frac{\mathrm{d}^2 z(t)}{\mathrm{d}t^2} + 2\xi\omega_n\frac{\mathrm{d}z(t)}{\mathrm{d}t} + \omega_n^2 z(t) = -\frac{\mathrm{d}^2 x(t)}{\mathrm{d}t^2} \tag{2-6}$$

since $m<<k$, $c<<k$, then $\xi<<\omega_n$. The first two terms in Equation (2-6) can be neglected, thus:

$$z(t) = -\frac{1}{\omega_n^2} \cdot \frac{\mathrm{d}^2 x(t)}{\mathrm{d}t^2} \tag{2-7}$$

as ω_n tends to infinity, $z(t)$ tends to 0 ($x(t) \approx y(t)$), meaning the vibration of the base and the mass block are approximately equal, so:

$$\boldsymbol{a} = \frac{\mathrm{d}^2 x(t)}{\mathrm{d}t^2} = \frac{\mathrm{d}^2 y(t)}{\mathrm{d}t^2} = -\frac{kz(t)}{m} \tag{2-8}$$

Equation (2-8) describes the relationship where the stress on the piezoelectric element from the base is equal to the stress applied by the mass block to the piezoelectric element. So the force applied by the mass block on the piezoelectric element can be expressed as:

$$\boldsymbol{F} = kz(t) \tag{2-9}$$

According to the piezoelectric equation[121], the charge Q generated on the piezoelectric element and the force $\boldsymbol{F}$ exerted on the piezoelectric element can be described by the electromechanical conversion Equation (2-10), while the conversion between charge and voltage can be represented by Equation (2-11).

$$Q = d_{33}\boldsymbol{F} \tag{2-10}$$

$$Q = UC \tag{2-11}$$

Therefore, the acceleration of the mass block can be expressed by:

$$\boldsymbol{a} = \frac{\mathrm{d}^2 x(t)}{\mathrm{d}t^2} = \frac{1}{md_{33}} Q = \frac{UC}{md_{33}} \tag{2-12}$$

where the mass m, capacitance C, and piezoelectric constant d_{33} are constants. So the vibration acceleration $\boldsymbol{a}$ is proportional to the charge Q and the voltage U. After the charge is converted into voltage signal by subsequent circuit, it can be measured by the acquisition device. The above describes the measurement principle of the compression-type piezoelectric vibration sensor.

2) Piezoelectric AE sensor

Figure 2-2 (a) shows the basic structure of the piezoelectric AE sensor, which consists of three components: the backing layer (green), the piezoelectric element (yellow), and the acoustic matching layer (red). The measured AE waves pass through the matching layer and piezoelectric element before reaching the backing layer. The function of the matching layer is matching the acoustic impedance difference between the piezoelectric element and the measured object to improve AE transmission efficiency. The piezoelectric element converts the mechanical deformation caused by the AE signal into electrical signal. The backing layer effectively absorbs the AE signal that penetrates the piezoelectric element, reducing the interference from reflections, improving detection resolution and extending frequency response range[122].

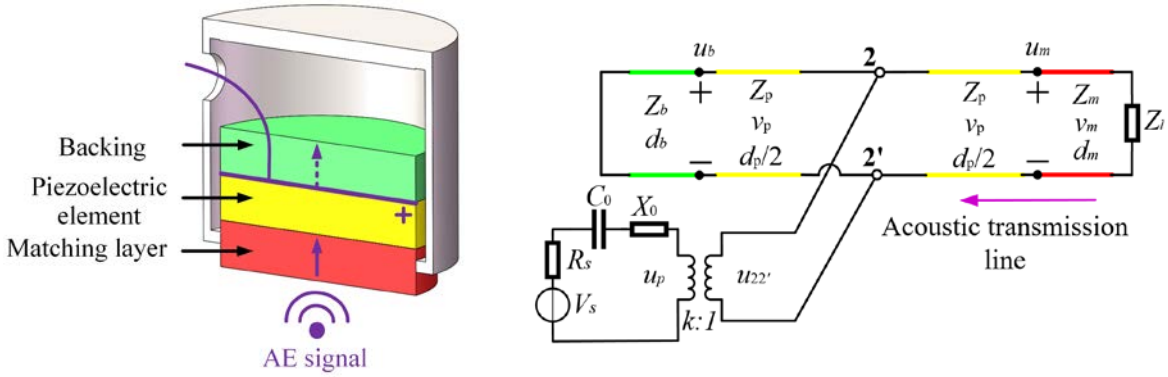

(a) (b)

Figure 2-2 The measurement principle of piezoelectric AE Sensor. (a) Basic structure. (b) KLM model.

Table 2-2 Parameters of KLM model

Parameters	Description	Parameters	Description
Piezoelectric Element Area	S	Clamped Static Capacitance	$C_0 = \frac{\varepsilon_{33}^S S}{d_p}$
Piezoelectric Element Thickness	d_p	Compressional Electromechanical Coupling Coefficient	$M^2 = \frac{e_{33}^2}{c_{33}^D \varepsilon_{33}^S}$
Piezoelectric Element Elastic Constant	c_{33}^D	Open-Circuit Anti-Resonant Frequency	$\omega_0 = \frac{2\pi v_p}{d_p}$
Piezoelectric Element Sound Velocity	v_p	Turns Ratio	$k = M\sqrt{\frac{\pi}{\omega_0 C_0 Z_p}}\sin c(\frac{\omega}{2\omega_0})$
Piezoelectric Layer Acoustic Impedance	Z_p	Equivalent Reactance	$X_0 = -\frac{C_0}{M^2}(\sin c(\frac{\omega}{\omega_0}))^{-1}$
Clamped Dielectric Constant	ε_{33}^S		

The piezoelectric AE sensor can be analyzed with the wave equation in continuous media, but the equivalent circuit method simplifies the acoustic model into an electrical model, making it more convenient and intuitive. This provides an effective approach for analyzing the sensor's frequency response characteristics. There are two classic theoretical models for piezoelectric AE sensors. The Mason model is widely known because it introduces a transformer to link the mechanical and electrical characteristics, while the KLM model is more advantageous in analyzing cascaded acoustic characteristics, as it can easily calculate the electrical input admittance of any acoustic load[123]. In the transmit state, the KLM equivalent circuit for the compression-type piezoelectric transducer is shown in Figure 2-2 (b). It divides the piezoelectric element into acoustic and electrical ports. For the acoustic port, the section from the matching layer to the piezoelectric element is the acoustic front end, and the section from the backing layer to the piezoelectric element is the acoustic rear end. The acoustic transmission line is connected to the power supply port through a transformer (k:1) to represent the electromechanical conversion relationship. In the receive

state, the power supply port is open circuit. The involved parameters and related calculations are shown in Table 2-2. Specific parameter information can be referenced from[124].

The transfer matrix is commonly used to describe two-port networks. The transfer matrix coefficients of a piezoelectric transducer can be obtained through circuit analysis by decomposing the equivalent circuit into a set of simple cascaded networks:

$$\begin{bmatrix} A_s & B_s \\ C_s & D_s \end{bmatrix} = \begin{bmatrix} 1 & j\left(\dfrac{\bar{h}_{33}^2 \sin(k_p d_p)}{\omega^2 Z_p S} - \dfrac{1}{\omega C_p^S}\right) \\ 0 & 1 \end{bmatrix} \begin{bmatrix} \dfrac{1}{k} & 0 \\ 0 & k \end{bmatrix} \cdot \begin{bmatrix} 1 & 0 \\ \dfrac{Z_p + jZ_b \tan(k_p d_p / 2)}{Z_p S(Z_b + jZ_p \tan(k_p d_p / 2))} & 1 \end{bmatrix} \begin{bmatrix} \cos(k_p d_p / 2) & jZ_p S \sin(k_p d_p / 2) \\ \dfrac{j \sin(k_p d_p / 2)}{Z_p S} & \cos(k_p d_p / 2) \end{bmatrix} \cdot \begin{bmatrix} \cos(k_p d_p) & jZ_p S \sin(k_p d_p) \\ j \sin(k_p d_p) / Z_p S & \cos(k_p d_p) \end{bmatrix} \tag{2-13}$$

where $\bar{h}_{33}$ is the equivalent piezoelectric constant; k is the transformer ratio; k_p is the wavenumber of the piezoelectric layer. The right side of Equation (2-13) corresponds to the power source terminal of the equivalent circuit, the transformer, the transmission line of the acoustic rear end, the transmission line of the acoustic front end, and the matching layer itself[125]. Then, the transfer functions for transmission and reception can be calculated as:

$$\frac{F_L}{V_G} = \frac{Z_L}{(A_s Z_L + B_s) + Z_G (C_s Z_L + D_s)} \tag{2-14}$$

$$\frac{V_r}{F_L} = \frac{2Z_r}{(A_s Z_L + B_s) + Z_r (C_s Z_L + D_s)} \tag{2-15}$$

where F_L and V_G represent the force of the load and the voltage source applied to the piezoelectric element, respectively (generally, Z_G equals around 0). V_r,、 Z_r and Z_L denote the received voltage of the piezoelectric element, the impedance of the equivalent circuit, and the acoustic impedance, respectively[126]. This study focuses on the receiving sensor. Since velocity is related to force, the transfer function for velocity with respect to the load can be expressed as:

$$H_r(j\omega) = \frac{V_r}{v_L} = \frac{2Z_r Z_L}{(A_s Z_L + B_s) + Z_r (C_s Z_L + D_s)} \tag{2-16}$$

According to Equation (2-16), the frequency response of the AE transducer can be obtained, and the time-domain response can also be calculated via inverse FFT. Simulation software developed based on the KLM model is widely used.

2.1.2 Structural Design of the Piezoelectric Vibration–AE Fusion Sensor

The measurement principle of the vibration-AE fusion sensor proposed in this study is based on the fundamental principles of piezoelectric AE and vibration acceleration sensors.

Figure 2-3 (a) illustrates the basic structure of the vibration-AE fusion sensor, which consists of a piezoelectric element, a matching layer, and a mass backing block.

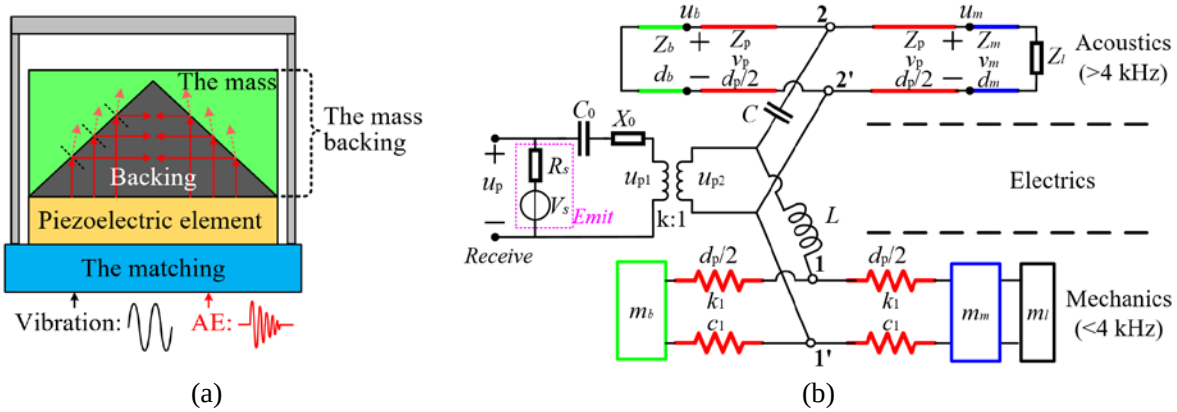

(a) (b)

Figure 2-3 The measurement principle of the Vibration-AE fusion sensor. (a) Basic structure. (b) Equivalent electromechanical model.

The piezoelectric element can convert both AE and vibration acceleration into electrical signals. PZT-5 piezoelectric ceramic is widely used due to its high piezoelectric coefficient, high mechanical strength, excellent and stable performance, and broad-band electromechanical response. The fundamental parameters of PZT-5 piezoelectric ceramic are listed in Table 2-3.

Table 2-3 Basic parameters of PZT-5

Name	Value	Name	Value
Diameter/mm	20	Thickness/mm	4
Resonant frequency/kHz	500	Young modulus/GPa	51
Coupling coefficient	k_{33}=0.59 k_{31}=0.55	Relative dielectric constant	1730
Mechanical constant Q	64	Dielectric loss/%	2~2.5
Piezoelectric coefficients/pC/N	d_{33}=460~600	Curie point/℃	240

The mass backing block is a key component of the fusion sensor. The outer shell is made of high-density stainless steel, which provides good electrical conductivity and allows the mass backing to function as the mass block in vibration detection. On the other hand, the interior of the conical mass backing is embedded with a tungsten and epoxy resin mixture using casting method, enabling direct contact with PZT-5 to absorb transmitted AE waves and significantly reduce echo interference. The matching layer is used to support and stabilize the sensor while achieving acoustic impedance matching. Since the acoustic impedance difference between PZT-5 (approximately 29.2 MRayl) and the measured object is inversely proportional to AE transmission efficiency, achieving acoustic impedance matching enhances AE detection performance.

For low-frequency vibration signal, the mass backing block enhances the inertia effect, improving sensitivity and stability in the thickness direction of vibration, as well as adjusting

the resonant frequency. For high-frequency AE signals, the conical backing block reduces back-reflection to improve time-domain resolution, matches the impedance to optimize energy transfer, and adjusts the sensor's operating frequency and bandwidth. Both signals are converted into electrical signals by the piezoelectric element, but their transmission processes and principles are different. Vibration signal transmission generally uses mechanical analysis, while AE signal transmission relies on acoustic analysis. The proposed fusion sensor's equivalent circuit model, shown in Figure 2-3 (b), describes the energy conversion between electrical, acoustic, and mechanical domains. In the electrical domain, u_p represents the voltage generated by the PZT-5 in the receiving mode, while *R*s and *V*s represent the internal resistance and voltage signal of the external power source in the transmitting mode. In the receiving mode, the voltage signal from the acoustic model is passed through the coupling capacitor *C* (cutoff frequency > 4 kHz) and then converted to the output voltage u_{p1} via the transformer (*k*:1) equivalent circuit. The voltage signal generated by the mechanical model is passed through the coupling inductor *L* (cutoff frequency < 4 kHz) and then converted to the output voltage u_{p1} via the transformer (*k*:1) equivalent circuit. In the equivalent model, the green, red, and blue lines represent the mass backing block, piezoelectric element, and matching layer, respectively. The acoustic model is mainly analyzed based on acoustic impedance theory, while the mechanical model is analyzed based on elastic theory. Based on the above piezoelectric AE and vibration principles, the transfer function $H(j\omega)$ of the fusion sensor can be derived as:

$$H(j\omega)=\left[\frac{m_b d_{33} d_p}{\varepsilon_0 \varepsilon_r S}\times\frac{Z_r}{Z_r+j\omega L}\right]+\left[\frac{2Z_r Z_L}{(A_s Z_L+B_s)+Z_r(C_s Z_L+D_s)}\times\frac{j\omega C Z_L}{1+j\omega C Z_L}\right] \quad (2\text{-}17)$$

The performance of sensors is commonly described by input-output frequency response curves. The definitions of vibration acceleration sensitivity response $S_V(f)$ and AE sensitivity response $S_A(f)$ are given as follows:

$$S_V(f)=\frac{U(f)}{A(f)} \quad (2\text{-}18)$$

$$S_A(f)=20*\log_{10}\frac{U(f)}{X(f)} \quad (2\text{-}19)$$

where $U(f)$ represents the amplitude of the sensor output voltage (unit: V), $A(f)$ denotes the amplitude of vibration acceleration (unit: *g* or m/s²), and $X(f)$ refers to the amplitude of surface acoustic pressure (unit: bar) or velocity (unit: m/s).

Figure 2-4 shows the typical frequency response curve of a piezoelectric sensor. The low-frequency vibration response (F_L~F_H) is relatively smooth, while the high-frequency AE response exhibits resonance at F_R with a significant amplitude. Generally, F_H should be at least one-fifth of the resonance frequency F_R. The material and structure of the piezoelectric sensor affect its detection performance, so the designed vibration-AE fusion sensor should demonstrate a favorable frequency response curve in both vibration and AE sensitivity.

As previously mentioned, existing studies have shown that the frequency range of AE

excited by PD in GIS is 20 kHz~100 kHz[127], while the frequency range of vibration signal in the presence of mechanical defects is 100 Hz~4 kHz[128]. This study is conducted based on this research background to develop vibration-AE fusion sensor.

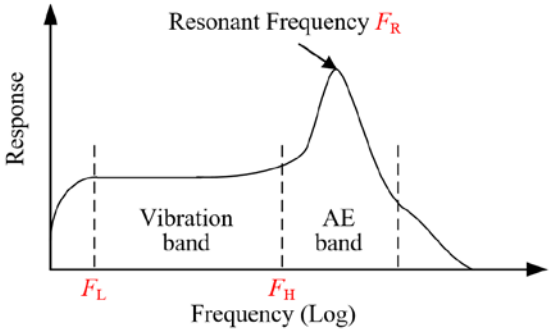

Figure 2-4 Typical frequency response of piezoelectric sensors

2.2 Analysis of the Influence of Structural Parameters on Fusion Sensor Measurement Performance

2.2.1 Simulation Modeling

This section investigates the influencing factors of fusion sensor measurement performance using multiphysics coupled simulation. In fusion sensing research, it is essential to consider electrical, vibration, and AE signals while addressing the effects of material properties, geometric structures, and external environmental factors. Multiphysics coupled simulation software, with its flexible modular design, enables multi-physics field simulation within a single model, effectively enhancing simulation accuracy and computational efficiency. Based on the theoretical analysis and structural design of the fusion sensor, the primary influencing factors originate from the piezoelectric element, the mass backing block, and the matching layer. The study explores these factors from the aspects of dimension, mass, and acoustic impedance. The developed simulation model for the vibration-AE fusion sensor is shown in Figure 2-5, with *r*=0 representing its rotational axis.

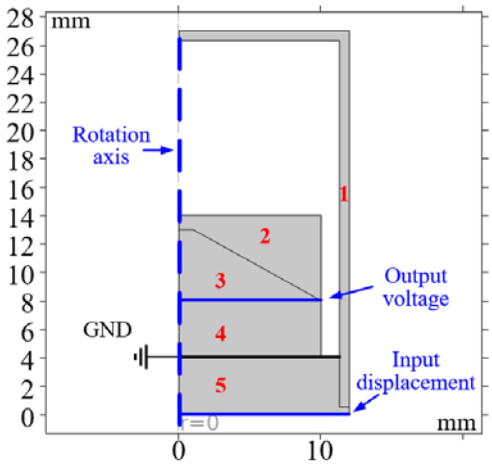

Figure 2-5 Fusion sensor FEA simulation model

The corresponding material properties used in the simulation, indexed in the figure, are

listed in Table 2-4, including relative permittivity, density, Young's modulus, and Poisson's ratio. Additionally, the piezoelectric material properties include mechanical damping and dielectric loss (referencing the software library). The simulation employs the solid mechanics, electrostatics, and piezoelectric effect multiphysics modules. The simulation type is frequency-domain analysis, and the meshing scheme utilizes free triangular elements.

Table 2-4 Material properties in simulation

Number	Material	Relative Dielectric Constant	Density /kg·m^{-3}	Young's Modulus/GPa	Poisson ratio
1	Stainless steel	1	7870	210	0.29
2	Copper	1	8930	132	0.34
3	Solid epoxy resin	3	1673	6.12	0.38
4	PZT-5	1730	7750	60	0.36
5	Zinc alloy	1	6580	83	0.3

The sensitivity response curve can be used to characterize the measurement performance of the sensor. Both the vibration and AE sensor sensitivity responses have voltage signal as output; however, their input physical references are different. The input parameter for vibration sensing is surface acceleration, whereas for AE sensing, it is surface velocity or acoustic intensity. To standardize the input conditions in the simulation, a sinusoidal surface displacement with an amplitude of 1 μm is applied. The frequency sweep ranges are set to 100 Hz-18 kHz (step size: 300 Hz) for vibration sensing and 20 kHz-100 kHz (step size: 1 kHz) for AE sensing. During post-processing, the extracted input parameter for vibration measurement is surface acceleration within the 100 Hz-4 kHz range, while for AE measurement, it is surface velocity within the 20 kHz-100 kHz range. Finally, the vibration and AE sensitivity curves are calculated with Equation (2-18), (2-19), respectively.

Key characteristic parameters are extracted from the computed vibration and AE sensitivity curves to quantitatively describe them. For the vibration sensitivity curve, the extracted parameters include: *SV* (Sensitivity-Vibration): average sensitivity; *MV* (sMooth-Vibration): standard deviation. For the AE sensitivity curve, the extracted parameters include: *SA* (Sensitivity-AE): average AE sensitivity; *Fr* (Frequency-response): resonant frequency; *FrA* (Frequency-response Amplitude): resonant amplitude; *MA* (sMooth-AE): standard deviation.

2.2.2 Influence of the Piezoelectric Element on Fusion Measurement Performance

The piezoelectric element of the proposed fusion sensor is PZT-5, whose intrinsic properties are predetermined. Therefore, dimension and mass are two critical factors affecting the measurement performance of the fusion sensor.

1) Influence of the piezoelectric element mass

The mass variation range of PZT-5 is set between 5.74 g and 12.74 g with a step size of 1 g, ensuring that the aspect ratio (Φ=Hight: Dimension) remains constant at 1:5.

Additionally, other parameters must remain unchanged. In particular, to maintain the mass (volume) of the mass backing block constant, it is necessary to adjust the base area and height of the mass backing block accordingly. Table 2-5 presents the dimensional parameters of PZT-5, while Figure 2-6 illustrates the cross-sections of PZT-5 with different dimensions as the mass increases.

Table 2-5 Mass setting of piezoelectric element

m/g	5.74	6.74	7.74	8.74	9.74	10.74	11.74	12.74
H/mm	3.35	3.54	3.7	3.86	4	4.13	4.26	4.37
D/mm	16.75	17.7	18.5	19.3	20	20.65	21.3	21.85

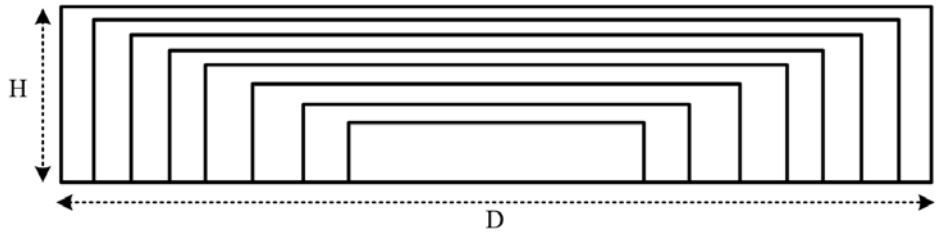

Figure 2-6 PZT-5 cross-sections of different masses (height-to-diameter ratio Φ=1:5)

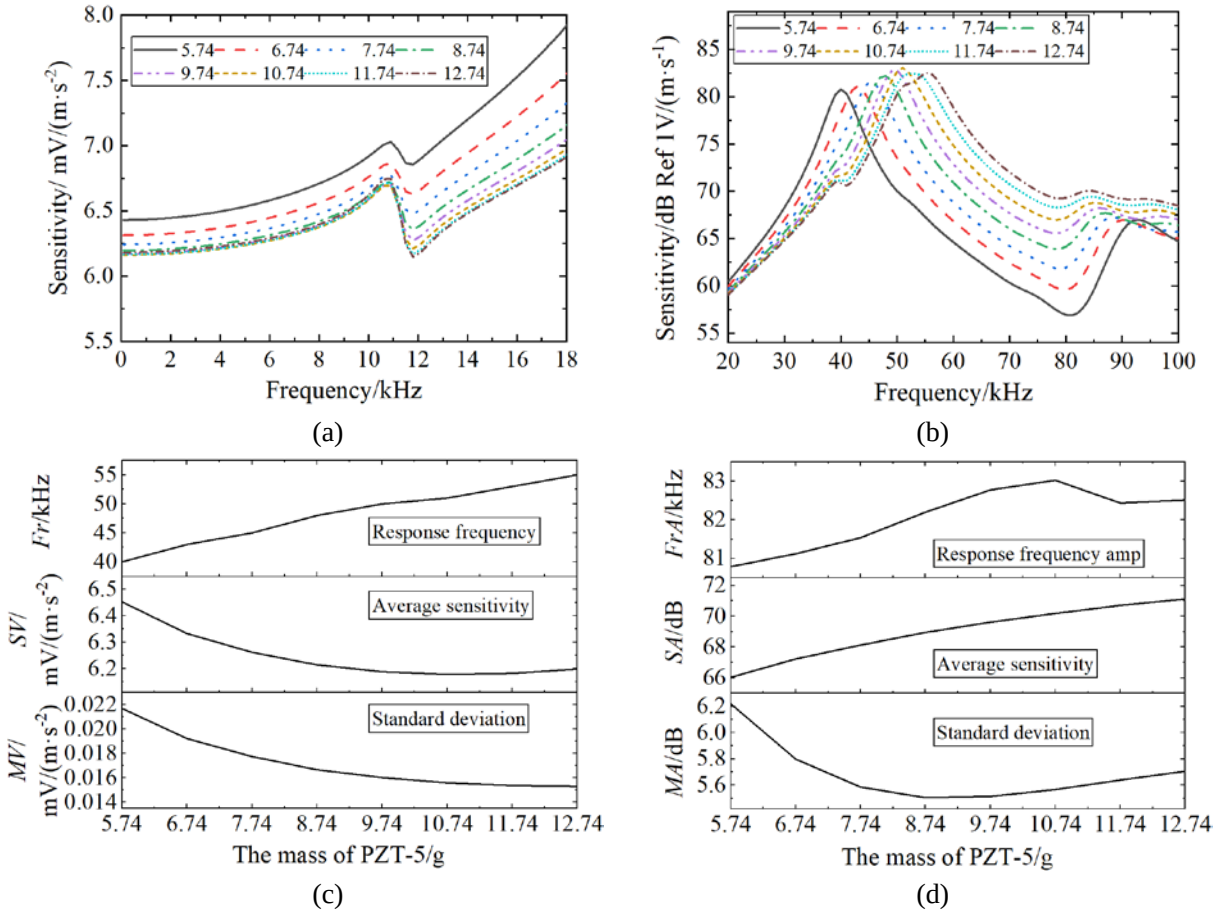

Figure 2-7 The influence of piezoelectric element mass on the fusion sensor measurement. (a) Vibration response. (b) AE response. (c) *Fr*, *SV*, *MV* parameters (d) *FrA*, *SA*, *MA* parameters.

The simulation results are shown in Figure 2-7. Figure (a) and (b) represent the

sensitivity curves for vibration and AE, respectively, while (c) and (d) describe the changes of six parameters. It can be seen that with the increase in PZT-5 mass, the resonance frequency increases from 40 kHz to 55 kHz; the average vibration sensitivity decreases from 6.45 mV/(m/s²) to 6.2 mV/(m/s²); the resonance amplitude increases from 80.6 dB to about 82.5 dB; the vibration standard deviation decreases from approximately 0.022 mV/(m/s²) to 0.016 mV/(m/s²); the average AE sensitivity increases from 66 dB to 71 dB; the AE standard deviation decreases from 6.2 dB to a minimum of 5.5 dB and then rises to 5.7 dB.

Theoretically, the resonant frequency of a sensor can be estimated by Equation (2-20):

$$f_r = f_{er}\sqrt{\frac{m_{eff}}{m_{eff}+M}} \tag{2-20}$$

where f_r represents the sensor's resonant frequency. The intrinsic resonant frequency of the piezoelectric ceramic, f_{er}, is primarily determined by its thickness and diameter. When the ratio of these two parameters remains constant, f_{er} remains nearly unchanged. The term m_{eff} refers to the effective mass of the piezoelectric ceramic, while M denotes the mass of the sensor excluding the piezoelectric ceramic. Based on the analysis in this section, when the height-to-diameter ratio of the piezoelectric ceramic is fixed, an increase in m_{eff} leads to an increase in f_r, a decrease in vibration sensitivity, and an improvement in signal smoothness.

2) Influence of the piezoelectric element dimension

Define the height-to-diameter ratio Φ of the piezoelectric element to describe dimensional variations, which is set in Table 2-6 within the range of 0.15 to 0.5 (step: 0.05). Additionally, the mass of PZT-5 is maintained at 9.74 g, and other parameters remain unchanged. Figure 2-8 illustrates the cross-sections of PZT-5 with increasing dimensions.

Table 2-6 Dimension setting of piezoelectric element

H:D=Φ	0.15	0.2	0.25	0.3	0.35	0.4	0.45	0.5
H/mm	3.3	4	4.64	5.24	5.80	6.34	6.86	7.36
D/mm	22	20	18.56	17.47	16.6	15.87	15.26	14.73

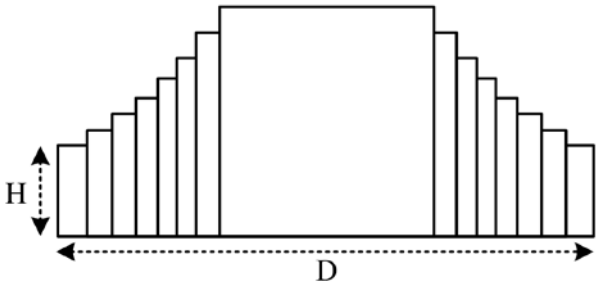

Figure 2-8 Cross-section of PZT-5 with different dimensions (mass=9.74 g).

Simulation results are shown in Figure 2-9, where (a) and (b) represent the sensitivity curves for vibration and AE, respectively, while (c) and (d) depict variations in the six parameters. As the aspect ratio Φ increases, the resonance frequency decreases from 59 kHz to 31 kHz; the average vibration sensitivity increases from 5 mV/(m/s²) to 19 mV/(m/s²); the vibration standard deviation rises from 0.011 mV/(m/s²) to 0.1 mV/(m/s²); the resonance

peak increases from 79 dB to 89 dB; the average AE sensitivity first rises from a peak of 50.5 dB to 52.7 dB, then decreases to 51 dB, and finally stabilizes at 51.5 dB; the AE standard deviation increases from approximately 26.5 dB to 31 dB.

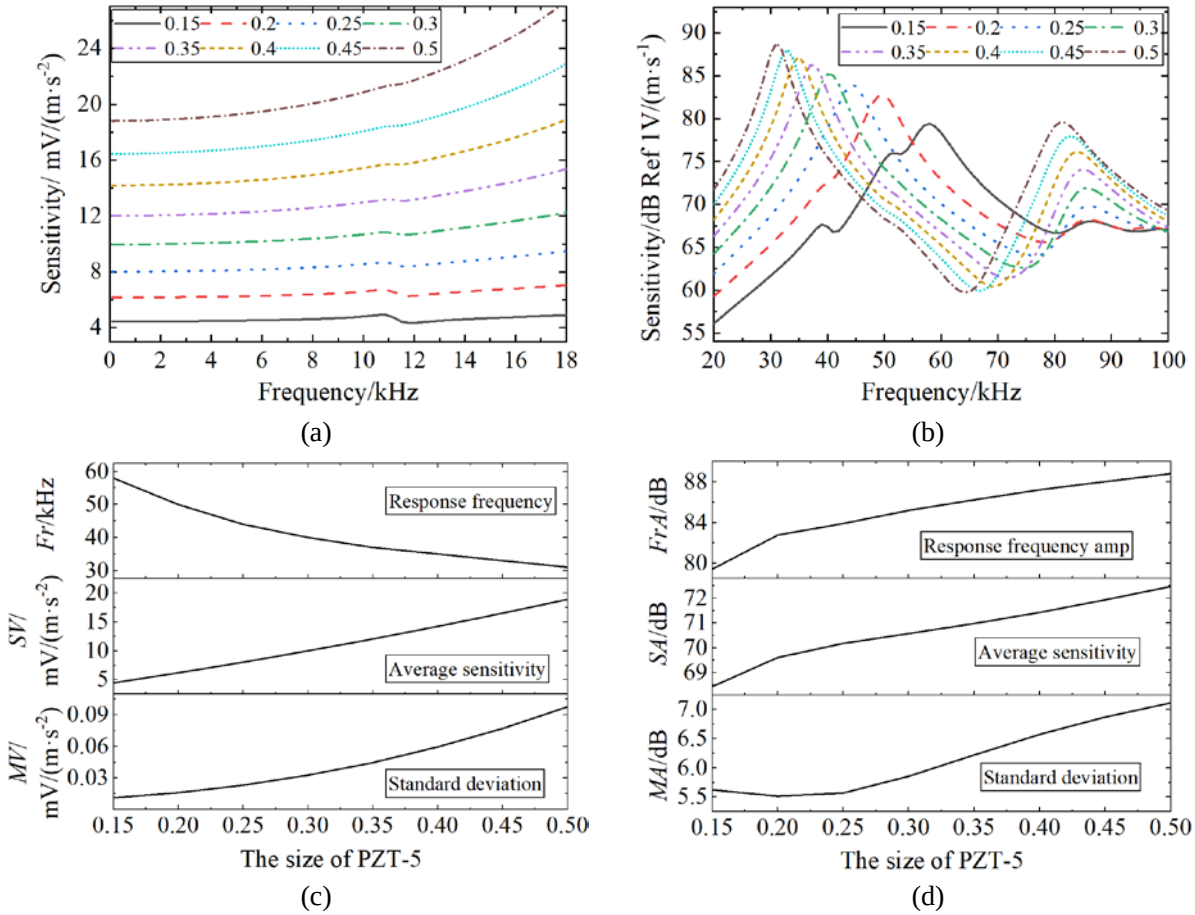

Figure 2-9 The influence of PZT-5 dimension on the fusion sensor measurement. (a) Vibration response. (b) AE response. (c) *Fr*, *SV*, *MV* parameters (d) *FrA*, *SA*, *MA* parameters.

When other parameters remain constant, the relationship between the piezoelectric ceramic thickness and the resonance frequency f_r can be estimated by Equation (2-21), where N_T is the frequency constant. Different piezoelectric materials have different frequency constants, with N_T for PZT-5 typically being 2000. h represents the height of the piezoelectric element. As h increases, the resonance frequency decreases, the structural stability of the piezoelectric module deteriorates, and vibration mode interference increases, leading to reduced smoothness in the vibration and AE sensitivity curves. Furthermore, as the thickness increases, the diameter of piezoelectric element declines, increasing the force per unit area and consequently enhancing the sensor sensitivity.

$$f_r = \frac{N_T}{h} \tag{2-21}$$

2.2.3 Influence of the Mass Backing on Fusion Measurement Performance

1) Influence of the mass backing acoustic impedance

The acoustic impedance of the backing layer serves the opposite function of the

acoustic matching layer. The purpose of the acoustic matching layer is to improve the efficiency of AE transmission to the piezoelectric element, whereas the backing layer attenuates AE penetrating through the piezoelectric element to reduce echo interference. The backing layer is typically made by tungsten powder and epoxy resin, with an acoustic impedance generally ranging from 2 to 10 MRaly. As a material property, acoustic impedance (Z) is related to density (ρ), Young's modulus (E), and sound velocity (c), and it can be described by the following Equation:

$$Z = \rho \cdot c = \sqrt{\rho \cdot E} \tag{2-22}$$

Since changes in density affect mass, leading to non-uniqueness of variables in the simulation, this study modifies the material's Young's modulus to adjust its acoustic impedance. Young's modulus is a key physical parameter that measures a material's resistance to deformation, indicating the degree of deformation under stress and reflecting the material's stiffness. In the simulation, the acoustic impedance of the mass backing block is set to range from 3.2 to 10.2 MRaly, with a step size of 1 MRaly, as shown in Table 2-7.

Table 2-7 Acoustic impedance setting of the mass backing block

Acoustic impedance /MRaly	3.2	4.2	5.2	6.2	7.2	8.2	9.2	10.2
Young's modulus /GPa	6.12	10.54	16.16	22.98	30.97	40.19	50.59	62.19

The simulation results are shown in Figure 2-10. (a) and (b) represent the sensitivity curves for vibration and AE, respectively, while Figures (c) and (d) describe the changes in the six parameters. It can be observed that as the acoustic impedance of the mass backing block increases, the sensor's resonant frequency rises from 50 kHz to 63 kHz; the resonant amplitude increases from 82.5 dB to 88.5 dB; the average vibration sensitivity decreases from 6.2 mV/(m/s²) to 5.8 mV/(m/s²); the vibration standard deviation decreases from approximately 0.016 mV/(m/s²) to 0.011 mV/(m/s²); the average AE sensitivity increases from 69.6 dB to 72.5 dB; and the AE standard deviation rises from 5.5 dB to 7.5 dB.

The acoustic impedance of the backing is exponentially proportional to the Young's modulus. The relationship between the Young's modulus E and the resonant frequency of the piezoelectric element can be qualitatively expressed by formula (2-23). Here, ρ is the material density, and k_b is the shape constant of the backing. It can be observed that as the Young's modulus of the backing increases, its acoustic impedance also increases, leading to a rise in the resonant frequency.

$$f_{\mathrm{r}} = \frac{1}{2\pi}\sqrt{\frac{E}{\rho}} \times k_b \tag{2-23}$$

The backing can reduce echo interference and improve the efficiency of AE signal propagation, which can be explained from the perspective of acoustic impedance matching. The acoustic impedance of piezoelectric ceramics typically ranges from 28 to 34 MRayl. Without the backing material, air serves as the backing, with a much lower acoustic

impedance of only 0.415 MRayl. This large difference in acoustic impedance between the piezoelectric ceramic and air results in low transmission efficiency, with most of the signal being reflected. By adding backing material, its acoustic impedance is between 0.438 and 33 MRayl, which effectively matches the acoustic impedance. Moreover, the particles within the backing help attenuate the AE signal, which, after passing through the piezoelectric ceramic, is further transmitted into the backing where it is absorbed and dampened.

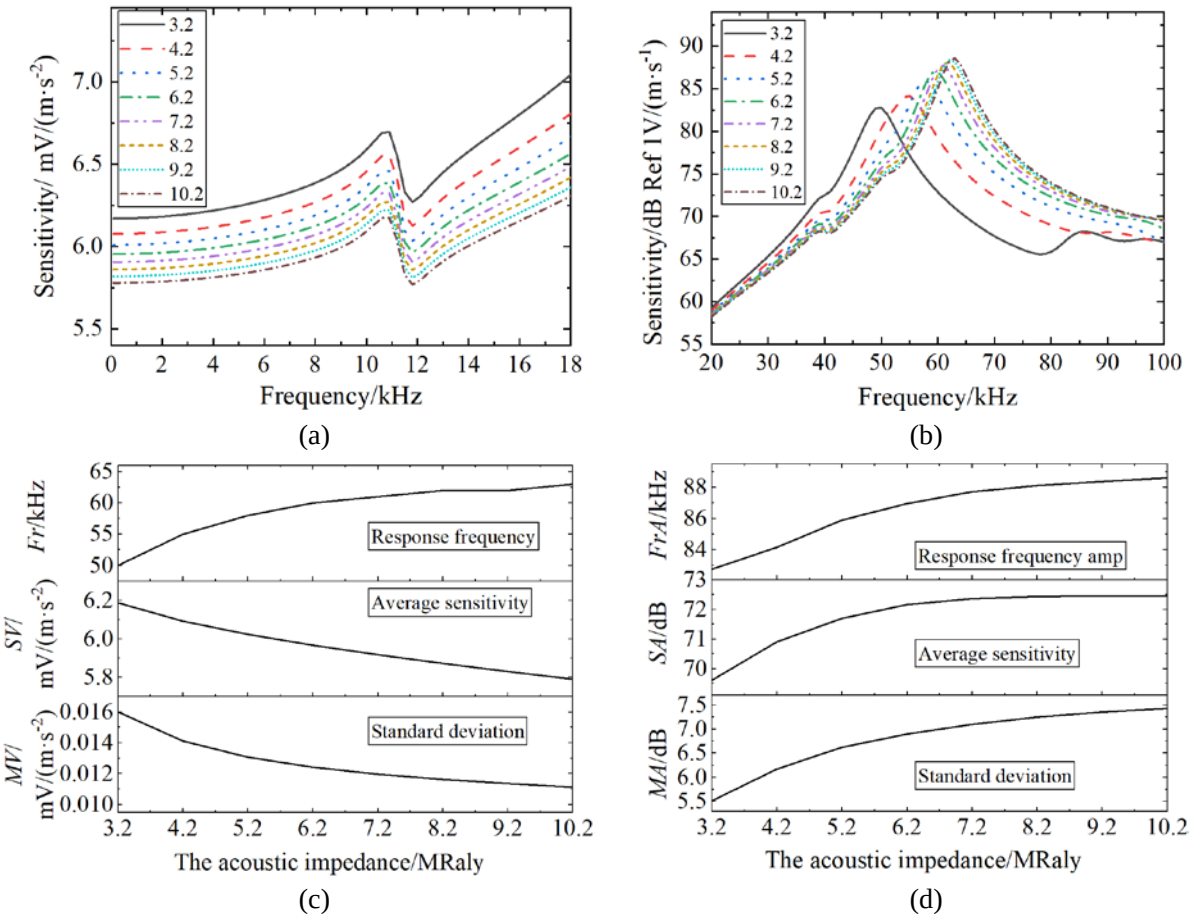

Figure 2-10 The influence of mass backing block acoustic impedance on the fusion sensor measurement. (a) Vibration response. (b) AE response. (c) *Fr*, *SV*, *MV* parameters (d) *FrA*, *SA*, *MA* parameters.

2) Influence of the mass of the mass backing block

The mass of the backing block has a significant impact on sensitivity. In the simulation, the density of the backing block is adjusted, so the mass vary from 9.61 g to 16.61 g by 1 g increments. The specific setting are shown in Table 2-8

Table 2-8 Mass setting of the mass backing block

Density/g·cm^{-3}	6.63	7.397	8.164	8.93	9.698	10.465	11.233	12
Mass/g	9.61	10.61	11.61	12.61	13.61	14.61	15.61	16.61

The simulation results are shown in Figure 2-11, where (a) and (b) represent the sensitivity curves for vibration and AE, respectively, and (c) and (d) describe the changes in the six parameters. It is found that as the mass of the mass backing block increases, the resonant frequency decreases from 56 kHz to 44 kHz; the average vibration sensitivity

increases from 5.1 to 7.5 mV/(m/s²); the vibration standard deviation increases from 0.012 mV/(m/s²) to 0.023 mV/(m/s²); the resonant amplitude increases from 82 dB to 82.8 dB; the average AE sensitivity remains stable at 69.55 dB; and the AE sensitivity standard deviation decreases from 5.3 dB to 5.89 dB.

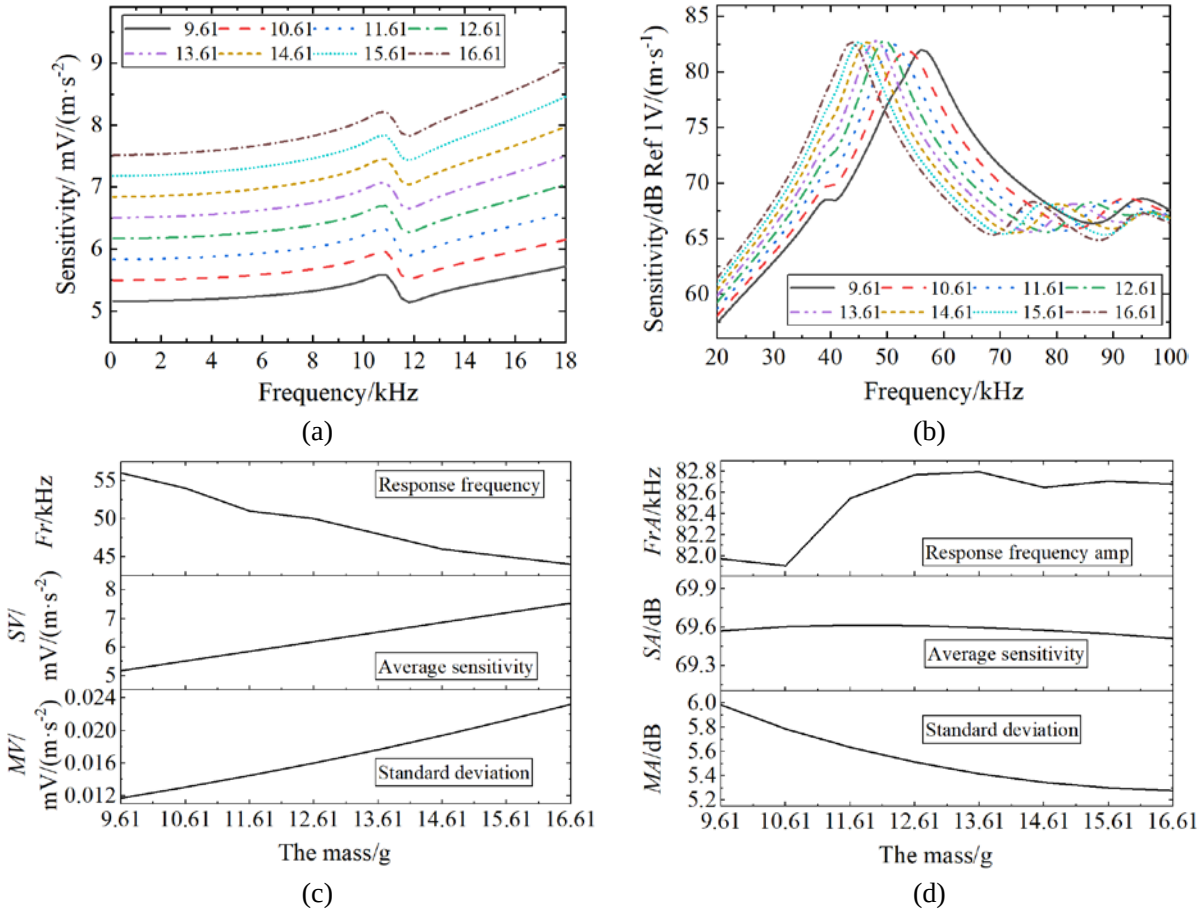

Figure 2-11 The influence of the mass backing block mass on the fusion sensor measurement. (a) Vibration response. (b) AE response. (c) *Fr*, *SV*, *MV* parameters (d) *FrA*, *SA*, *MA* parameters.

The role of the mass of the mass backing block in the sensor is shown in Figure 2-1. The resonant frequency ω_n, damping ratio λ, and mechanical sensitivity S_m of the entire structure can be qualitatively expressed by Equation (2-24), where m is the mass of the mass backing block, k is the stiffness coefficient, and c is the damping coefficient. It can be observed that as the mass of the mass backing block increases, the resonant frequency decreases, but the mechanical sensitivity increases.

$$\omega_n = \sqrt{\frac{k}{m}}, \lambda = \frac{c}{2\sqrt{km}}, S_m = \frac{m}{k} \tag{2-24}$$

2.2.4 Influence of the Acoustic Matching Layer on Fusion Measurement Performance

1) Influence of matching layer acoustic impedance

The acoustic impedance of the matching layer directly affects the efficiency of AE transmission. According to conventional theory, the optimal acoustic impedance of the

matching layer can be calculated by:

$$Z_m = \sqrt{Z_p \times Z_o} \tag{2-25}$$

where Z_m, Z_p , and Z_o represent the acoustic impedances of the matching layer, PZT-5, and the measured object, respectively. In this study, Z_p is set as 29.2 MRayl and Z_o is set as 17.06 MRayl. Theoretically, to achieve good acoustic impedance matching, Z_m should be 22.32 MRayl. The acoustic impedance values for the matching layer in the simulation are listed in Table 2-9. The impedance values are adjusted by modifying the Young's modulus E (as shown in Equation (2-22)), with Z_m increasing from 17.4 MRayl to 44.4 MRayl in increments of 3 MRayl.

Table 2-9 Acoustic impedance setting of the matching layer

Acoustic impedance /MRaly	17.4	20.4	23.4	26.4	29.4	32.4	35.4	38.4	41.4	44.4
Young's modulus /GPa	45.8	63	83	105.6	131	159	190	223	260	299

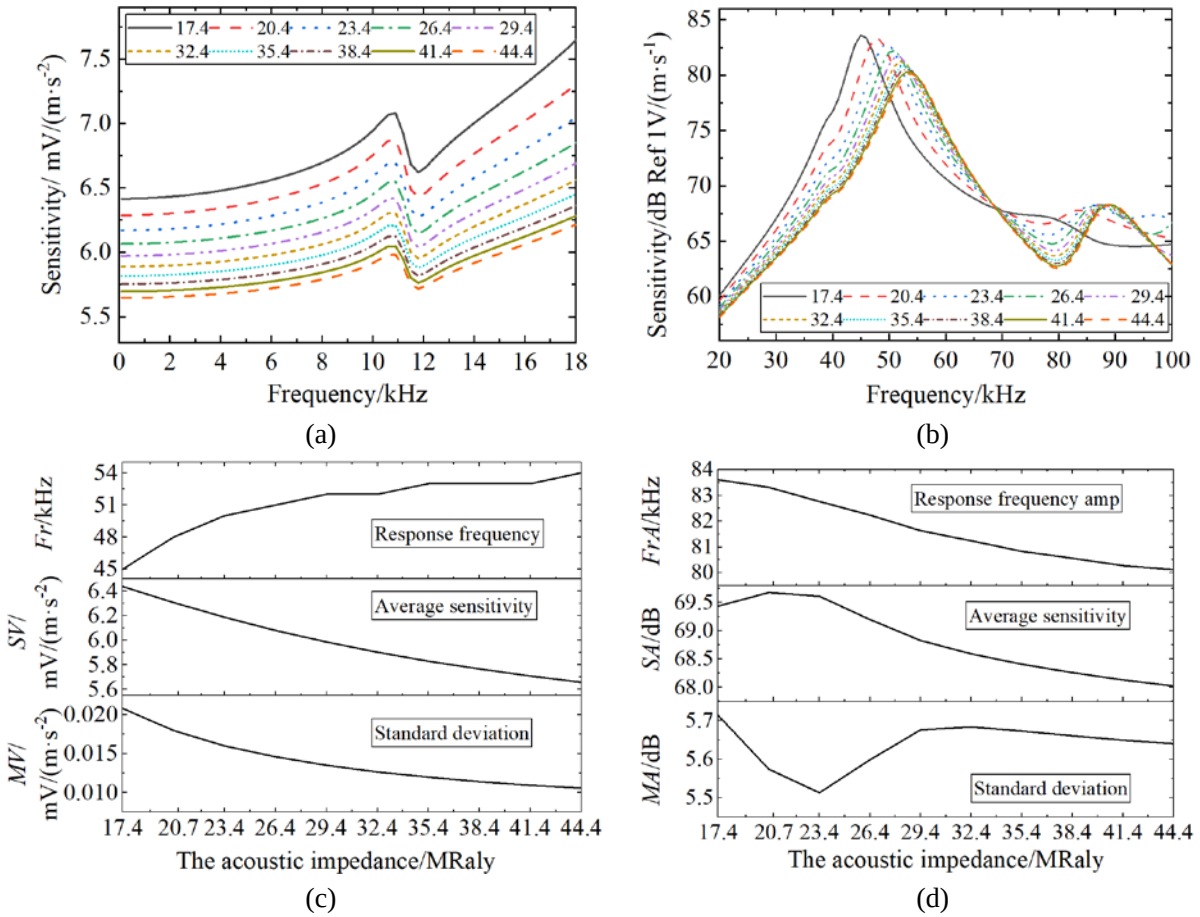

Figure 2-12 The influence of matching layer acoustic impedance on the fusion sensor measurement. (a) Vibration response. (b) AE response. (c) *Fr*, *SV*, *MV* parameters (d) *FrA*, *SA*, *MA* parameters.

The simulation results are shown in Figure 2-12, where (a) and (b) represent the sensitivity curves for vibration and AE, respectively, while (c) and (d) illustrate the

variations of six measurement performance parameters. It can be observed that as the acoustic impedance of the matching layer increases, the resonance frequency rises from 45 kHz to 54 kHz; the average vibration sensitivity decreases from 6.42 mV/(m/s²) to 5.67 mV/(m/s²); the standard deviation of vibration sensitivity decreases from 0.021 mV/(m/s²) to 0.011 mV/(m/s²); the resonance peak drops from 83.5 dB to 80 dB; the average AE sensitivity initially increases from 69.4 dB to 69.7 dB and then declines to 68 dB; and the standard deviation of AE sensitivity decreases from 5.7 dB to 5.5 dB before stabilizing at approximately 5.65 dB.

As the acoustic impedance of the matching layer increases, its Young's modulus E also increases, which means the matching layer becomes stiffer and less deformable. Since the average vibration sensitivity SV follows the relationship $SV \propto d_{33}/E$, an increase in E leads to a slight decrease in vibration sensitivity. According to Equation (2-23), an increase in Young's modulus E results in a higher resonance frequency of the sensor, which in turn affects the AE sensitivity.

2) Influence of matching layer thickness

The thickness of the matching layer is a critical factor influencing the sensitivity of an AE sensor, as it affects the reflection, transmission, and interference characteristics of acoustic waves. Traditional theory suggests that the matching layer thickness should be designed as one-quarter of the acoustic wavelength to maximize transmission efficiency. However, for relatively low-frequency AE signal (20 kHz~100 kHz), the calculated matching layer thickness reaches the centimeter scale, which is impractical for sensor applications. In this study, simulations are conducted with the matching layer thickness varying from 0.5 mm to 4 mm in increments of 0.5 mm.

The simulation results are shown in Figure 2-13, where figures (a) and (b) represent the sensitivity curves for vibration and AE, respectively, while figures (c) and (d) illustrate the variations of six key parameters. It is observed that as the matching layer thickness increases, the resonant frequency decreases from 55 kHz to 50 kHz; the average vibration sensitivity increases from 5.95 mV/(m/s²) to 6.2 mV/(m/s²); the standard deviation of vibration sensitivity rises from 0.01 mV/(m/s²) to 0.016 mV/(m/s²); the resonance peak increases from 80.6 dB to 82.7 dB; the average AE sensitivity increases from 67.5 dB to 69.5 dB; and the standard deviation of AE sensitivity decreases from 6.3 dB to 5.5 dB.

Overall, the influence of matching layer thickness on vibration and AE measurement performance is relatively minor. The primary reason is that impedance matching effects are weaker at low frequencies, and the thickness increments of the matching layer are small relative to the wavelength of acoustic waves in this frequency range, resulting in gradual changes in transmission and interference characteristics. Additionally, in the low-frequency AE range, the multiple reflection and absorption effects within the matching layer are less pronounced, with most of the energy concentrated in the primary transmission path. As a result, variations in AE sensitivity response remain limited. Furthermore, vibration measurement sensitivity is primarily influenced by the mechanical properties of the matching layer material, while the direct effect of thickness is relatively small.

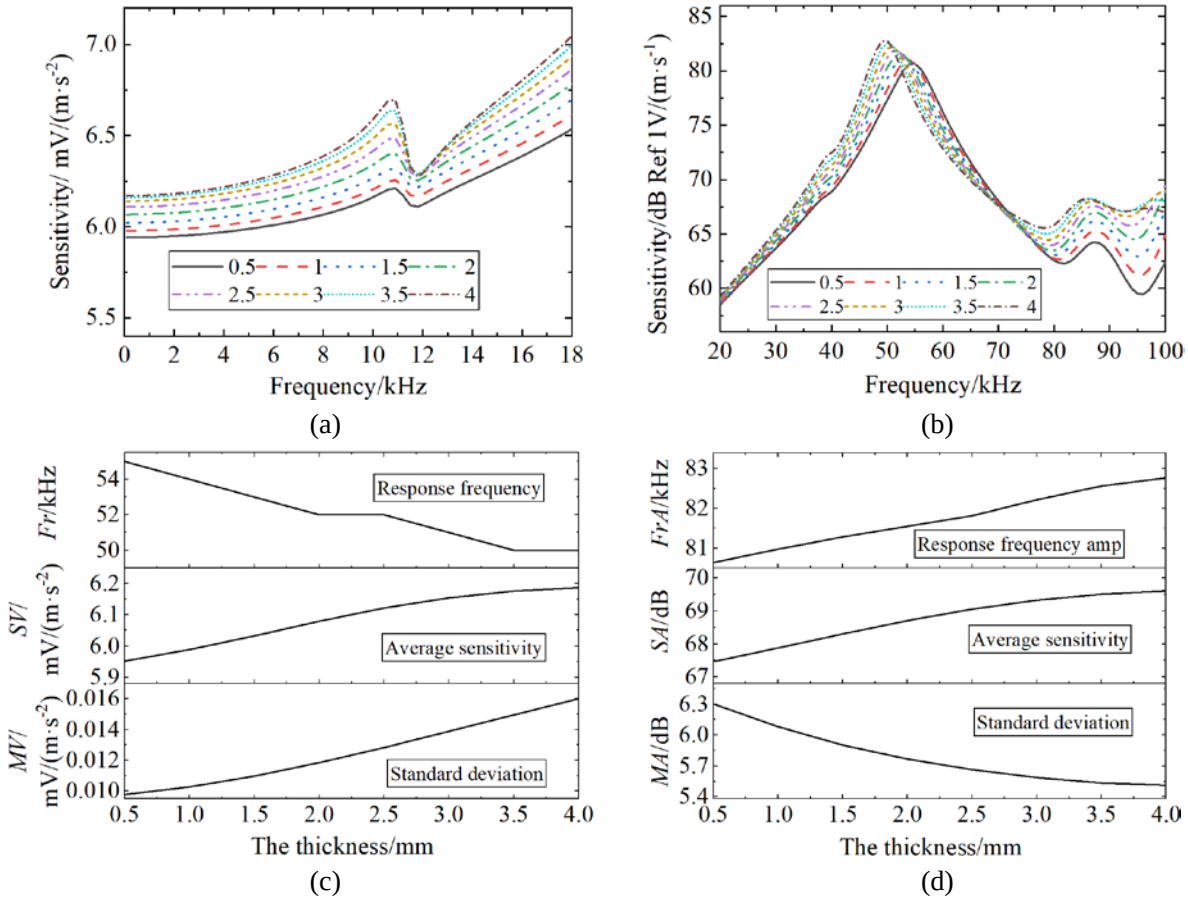

Figure 2-13 The influence of matching layer thickness on the fusion sensor measurement. (a) Vibration response. (b) AE response. (c) *Fr*, *SV*, *MV* parameters (d) *FrA*, *SA*, *MA* parameters.

2.3 Fusion Sensor Optimization Method Based on Data Expansion and Algorithm Optimization

Based on the above research results, the six fundamental variables have different effects on the measurement performance of the fusion sensor. However, the existing simulation data is limited and discrete, necessitating an expansion of the simulation results to facilitate parameter optimization. In this section, a neural network approach is employed to extend the simulation data, further clarifying the influence of each variable on the sensitivity performance of the fusion sensor. Ultimately, the optimal sensor parameter configuration is determined through optimization criteria and the particle swarm optimization algorithm.

2.3.1 Expansion of Simulation Results for Fusion Sensor Influence Factors

Taking the piezoelectric element dimension as an example, the principle of extending the simulation results is illustrated. Figure 2-14 compares the effects of different piezoelectric element dimensions on the AE sensitivity response of the fusion sensor. The x-axis represents frequency, the y-axis represents the dimension variable, and the z-axis represents sensitivity amplitude. For the x-axis (with frequency as the independent variable), a BackPropagation (BP) neural network is employed for fitting due to the large data volume

and nonlinearity. For the y-axis (with the dimension variable as the independent variable), an equivalent polynomial fitting method is used to achieve efficient fitting, given the relatively small data volume. Ultimately, based on simulation data, this method enables the generation of a complete dataset for all optimization parameter variables within the specified range.

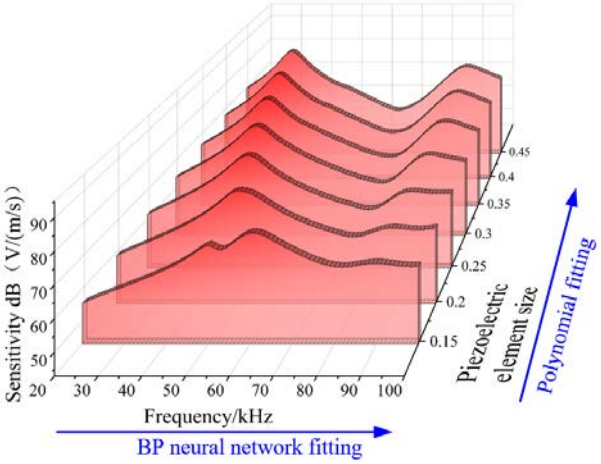

Figure 2-14 Neural network–polynomial fitting for extended data.

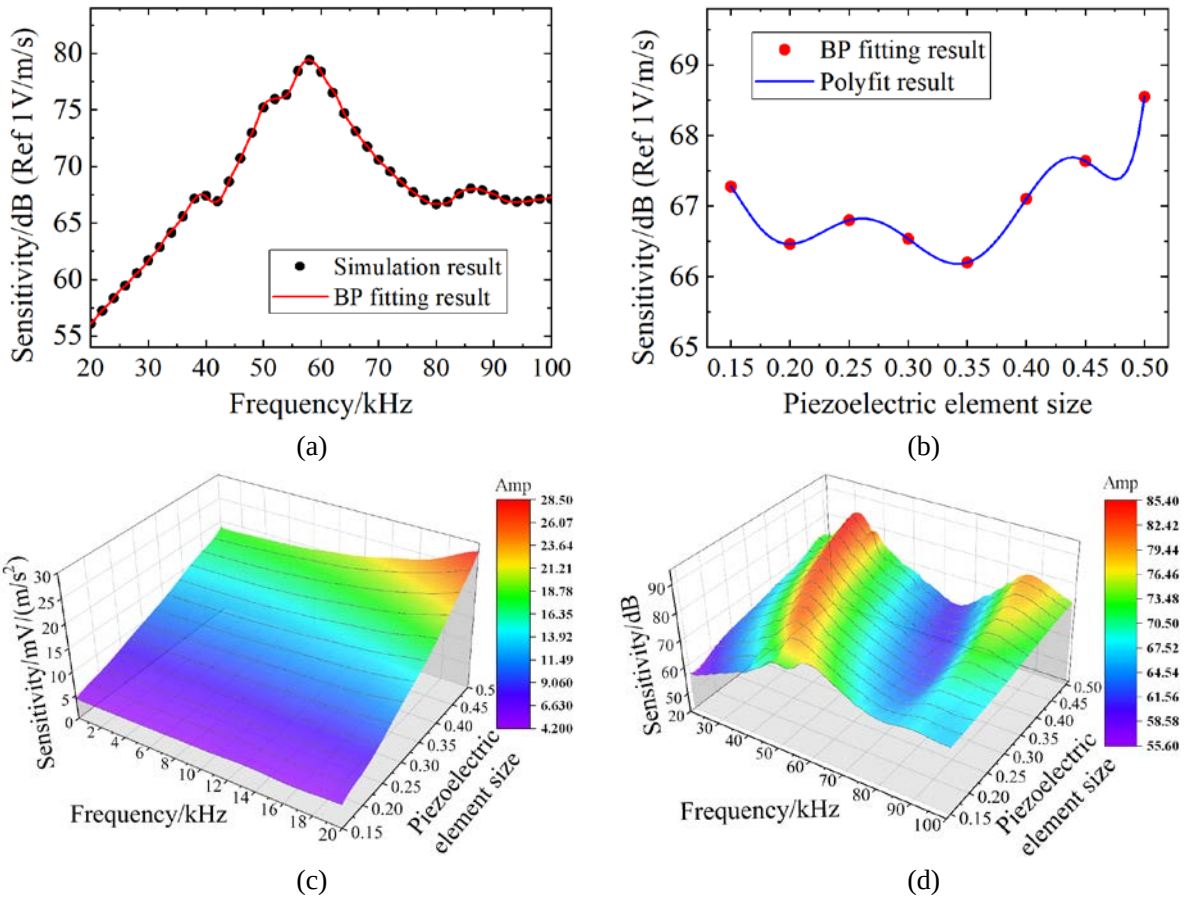

Figure 2-15 Neural network-polynomial fitting results. (a) BP neural network fitting. (b) Polynomial fitting. (c) Extension of vibration response. (d) Extension of AE response.

For the x-axis data fitting, the BP neural network created in this study consists of 25 hidden neurons, which allows it to capture complex nonlinear relationships while avoiding overfitting caused by excessive network complexity. A random seed of 0 is set to ensure

reproducibility of the results. The maximum number of iterations is set to 1000 to allow the network to fully learn the data characteristics, and the learning rate is set to 1 to improve convergence efficiency. For the y-axis data fitting, the least squares method is used to determine the polynomial coefficients for data fitting. The polynomial order matches the number of data points to be fitted. The polynomial fitting model is expressed as follows:

$$P(x) = p_1 x^n + p_2 x^{n-1} + \cdots + p_n x + p_{n+1} \tag{2-26}$$

The simulation results and BP neural network fitting results are shown in Figure 2-15 (a). The data expanded using the BP neural network and subsequently fitted with polynomial are shown in figure (b). Through this, the simulation data can be effectively extended. The extended results are then visualized as three-dimensional plots of frequency, parameter variables, and sensitivity. The vibration and AE sensitivity distributions are shown in Figure 2-15 (c) and (d), respectively.

2.3.2 Optimization Method for Vibration-AE Fusion Sensor Based on Intelligent Algorithm

The optimization process for the vibration-AE fusion sensor based on intelligent algorithms proposed in this study is illustrated in Figure 2-16：

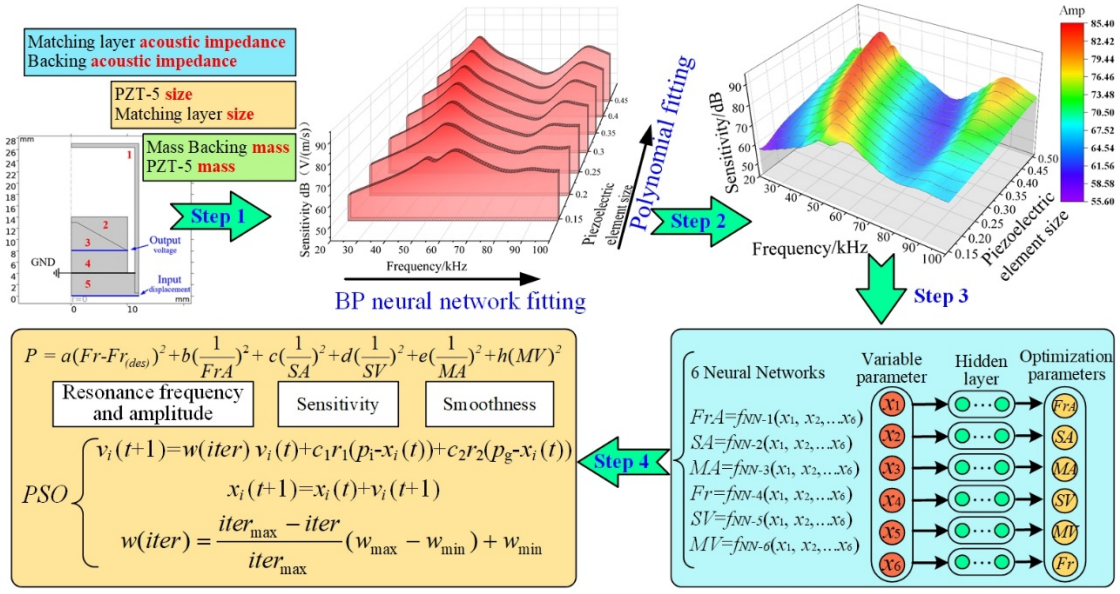

Figure 2-16 Optimization method of vibration-AE fusion sensor based on intelligent algorithm.

It mainly consists of the following four parts:：

1) Single variable sweep simulation

First, based on the established fusion sensor model, a single-variable sweep simulation is performed for the six fundamental variables to obtain simulation results (AE and vibration sensitivity curves). Additionally, some optimized characteristic parameters, such as sensitivity, smoothness, and resonance frequency, can be extracted. This step has already been completed in Section 2.2.

2) Data expansion based on bidirectional fitting

The simulation results of each variable obtained in Step 1 are arranged in ascending

order, forming a 3D distribution where the x-axis represents frequency, the y-axis represents the variable value, and the z-axis represents the sensitivity amplitude. To expand the data, the fitting approach is selected based on the data characteristics: For the x-direction, due to the large data volume and strong nonlinearity, BP neural network fitting is applied. For the y-direction, since the data volume is small and nonlinearity is weak, an equivalent polynomial fitting method with the same number of points is used. By fitting in both directions, a fitted surface is obtained, making the relationship between the six fundamental variables and the fusion sensor's performance more intuitive.

3) Establishing the relationship between sensor variables and measurement performance parameters based on BP neural network

After obtaining a large dataset, it is necessary to establish the relationship between the sensor variables and the measurement performance parameters. First, six performance parameters are extracted from the obtained sensitivity curves: *SA* for average AE sensitivity; *MA* for AE sensitivity curve smoothness; *SV* for average vibration sensitivity; *MV* for vibration sensitivity curve smoothness; *Fr* for resonance frequency; *FrA* for resonance frequency amplitude. Based on these parameters, a BP neural network is used to establish the implicit functional relationships between the variables and the performance parameters.

4) Acquiring optimization result based on the established criteria and PSO algorithm

The optimization evaluation criterion *P* is established, which includes the optimization standards for the above six performance parameters. The minimum value of *P* is then computed through the PSO algorithm to obtain the optimized result. The established optimization evaluation criterion *P* is as follows:

$$P = a(Fr\text{-}Fr_{(des)})^2 + b(\frac{1}{FrA})^2 + c(\frac{1}{SA})^2 + d(\frac{1}{SV})^2 + e(MA)^2 + h(MV)^2 \tag{2-27}$$

where *a*, *b*, *c*, *d*, *e,* and *h* are the weight coefficients for the six measurement performance parameters, and $Fr_{(\mathrm{des})}$ is the set resonance frequency. Under the influence of the weights, by calculating the minimum value of *P*, it is possible to make *Fr* approach the set value $Fr_{(\mathrm{des})}$, maximize the sensitivities *SA*, *SV*, *FrA*, and minimize the smoothness values *MA* and *MV*.

The PSO algorithm combines both local and global search capabilities. By using the Linearly Decreasing Weight (LDW) strategy, it emphasizes local search in the early stages and global search in the later stages, providing high accuracy and efficiency. The standard PSO optimization algorithm is as follows:

$$v_i(t+1) = w(iter)v_i(t) + c_1r_1(p_i - x_i(t)) + c_2r_2(p_g - x_i(t)) \tag{2-28}$$

$$x_i(t+1) = x_i(t) + v_i(t+1) \tag{2-29}$$

$$w(iter) = \frac{iter_{\max} - iter}{iter_{\max}}(w_{\max} - w_{\min}) + w_{\min} \tag{2-30}$$

where $v_i(t)$ and $x_i(t)$ represent the velocity and position of the i-th particle, $w(iter)$ represent the inertia factor, c_1 and c_2 denote the learning factors, p_i and p_g are the individual best

position and global best position, and r_1 and r_2 are random numbers. The particle velocity for the next iteration is obtained thtough Equation (2-28), and the particle position for the next iteration is obtained using Equation (2-29). Equation (2-30) represents the linearly decreasing formula for the inertia factor. Table 2-10 shows the primary parameter settings for the intelligent optimization algorithm.

Table 2-10 Parameter setting of intelligent optimization algorithm

Parameters	Value	Parameters	Value
Weight factor *a*	0.2	Learning factor c_1	2
Weight factor *b*	0.2	Learning factor c_2	2
Weight factor *c*	0.2	Inertia factor w_{min}~w_{max}	[0.4, 0.9]
Weight factor *d*	0.2	Resonant frequency set value $Fr_{(des)}$	60
Weight factor *e*	0.2	Number of particles	100
Weight factor *h*	0.2	Particle velocity range	[-0.05, 0.05]
Mass backing block acoustic impedance x_1	[3.2, 10.2]	PZT-5 dimension x_4	[0.15, 0.5]
Matching layer acoustic impedance x_2	[17.4, 44.4]	PZT-5 mass x_5	[5.74, 12.74]
Matching layer dimension x_3	[0.5, 4]	Mass backing block mass x_6	[9.61, 16.61]

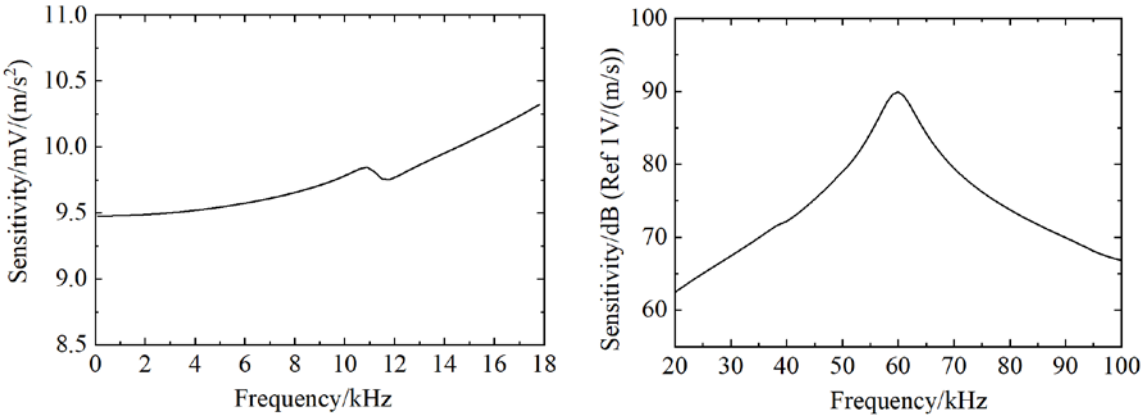

(a) (b)

Figure 2-17 Optimized results. (a) Optimized vibration response. (b) Optimized AE response.

The minimum value of *P* obtained through calculations is 0.00526, with the following variable values: mass backing acoustic impedance of 7.93 MRaly, matching layer acoustic impedance of 28.58 MRaly, matching layer thickness of 1.7 mm, PZT-5 dimension of 0.255, piezoelectric mass of 9.88 g, and mass backing block mass of 12.11 g. The optimization results obtained are as follows: resonance frequency of 60 kHz, AE resonance peak of 88.87 dB, average AE sensitivity of 77.55 dB, AE smoothness of 7.33 dB, vibration sensitivity of 9.73 mV/(m/s²), and vibration smoothness of 0.0091. Finally, the optimized variable values obtained from the calculation are input into the simulation model, and the optimized sensor vibration and AE sensitivities are shown in Figure 2-17. It can be observed that the

simulation results are in good agreement with the optimization calculation results.

2.4 Assembly Design and Performance Calibration of the Fusion Sensor

Based on the optimization results of the fusion sensor described in above sections, this section introduces the assembly and calibration processes of the sensor. Firstly, a two-wire signal processing PCB based on a field-effect transistor (FET) is designed. The built-in circuit realizes impedance conversion, amplification, and noise reduction functions. Additionally, the process of manufacturing the piezoelectric module of the sensor is introduced. Finally, a fusion sensor measurement device is assembled, including the sensor, portable oscilloscope, and PC. Furthermore, AE and vibration calibration platforms are established respectively based on national standards to accurately obtain the AE and vibration measurement sensitivities of the fusion sensor.

2.4.1 Assembly Design of the Fusion Sensor

The piezoelectric element can be approximated as a capacitor, and its output voltage signal requires preprocessing to improve transmission efficiency. Due to the high output impedance of PZT-5 (reaching the MΩ level), voltage acquisition is challenging, and high-frequency electromagnetic noise surrounding the wiring can interfere with the signal transmission of the fusion sensor. Therefore, the built-in PCB must not only convert the high output impedance to a low impedance but also achieve signal amplification and filtering, thereby enhancing sensitivity and reducing noise.

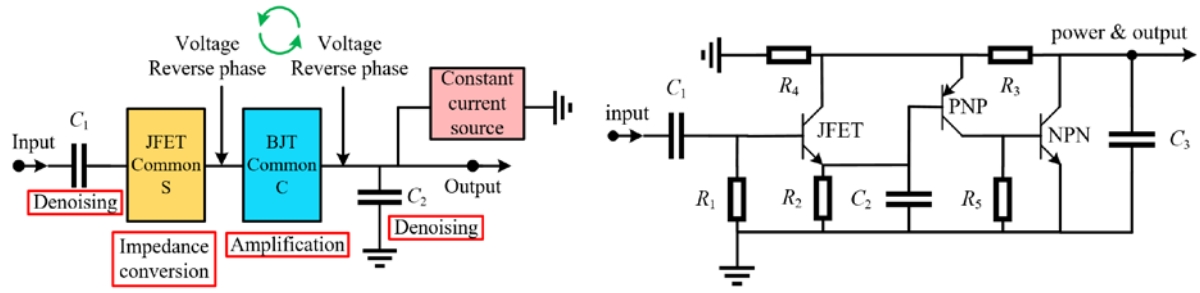

(a) (b)

Figure 2-18 Built-in PCB design. (a) Processing circuit topology. (b) Processing circuit diagram.

The schematic diagram of the designed built-in PCB is shown in Figure 2-18 (a) and (b). A JFET is used to convert the high impedance of PZT-5 to low due to its excellent impedance conversion characteristics, while a BJT is employed to amplify the signal from the JFET. Both the JFET (common-source) and BJT (common-collector) circuits exhibit an inverting voltage output characteristic, ensuring that the PCB output signal remains phase-consistent with the input signal. Additionally, capacitors C_1 and C_2 are used to suppress low-frequency and high-frequency noise, respectively. The PCB is powered by a constant current source providing 4 mA, which has a low output impedance. As a result, the output signal consists of both the preprocessed signal and a DC bias voltage (typically 7–12 V). This design allows the power supply and signal output to share a single wire, simplifying the circuit design[129]. Furthermore, the output signal is processed in PC using filters to

separate vibration and AE signals. The specific PCB component parameters are listed in Table 2-11, where the JFET can be replaced with an equivalent MOSFET.

Table 2-11 Component parameters of the built-in PCB

Component	Value	Component	Value
R_1	1 MΩ	JFET	J201
R_2	1 kΩ	PNP	9012
R_3	39 kΩ	NPN	3904
R_4	10 kΩ	C_1	10 uF
R_5	1 MΩ	C_2	0.1 uF
Constant current power	4 mA		

Figure 2-19 (a) shows the designed built-in PCB for the fusion sensor, with eight grounding vias arranged around its perimeter to ensure grounding with the sensor housing. Figure (b) presents the measured signal amplification spectrum. The input and output signals are sinusoidal, with a frequency sweep range set from 100 Hz to 100 kHz, a step size of 1 kHz, it can be seen the amplification is around 10.

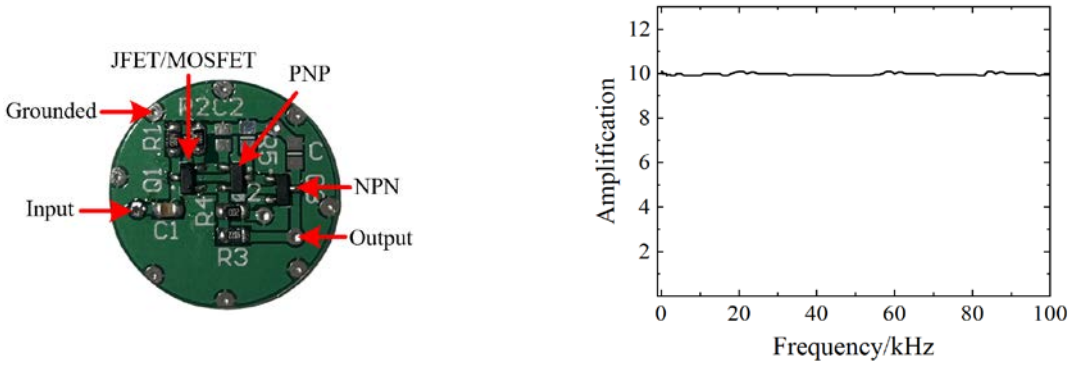

(a) (b)

Figure 2-19 Built-in PCB of the fusion sensor. (a) The PCB. (b) Signal amplification spectrum.

(a) (b) (c)

Figure 2-20 Vibration-AE fusion measurement device. (a) Structure of the fusion sensor. (b) Prototype of the fusion sensor. (c) A set of measurement device.

Finally, the designed PCB is connected to the piezoelectric module and installed inside the sensor housing. The assembly structure and the physical image of the fusion sensor are shown in Figure 2-20 (a) and (b). To ensure proper operation of the sensor, a 4 mA constant

current source, a data acquisition card, and a host PC are required. Figure (c) shows the developed measurement device, where the constant current source is integrated in the acquisition card.

2.4.2 Calibration of the Fusion Sensor Measurement Performance

1) AE calibration

An AE sensitivity calibration platform is established based on the GB/T 19801-2005 standard to evaluate the AE measurement performance of the fusion sensor[130]. With the reference sensor (RS) calibrated by absolute calibration, the sensitivity response of the sensor under test (SUT) in the target frequency band can be calculated.

The AE calibration platform is shown in Figure 2-21 (a). The steel block has a diameter of 42 cm and a height of 21 cm, with a lead break source mounted at the center of its surface to generate Rayleigh pulses. The SUT and the RS are placed symmetrically on opposite sides of the source, both at a distance of 10 cm from the excitation point. AE coupling agent is applied to enhance signal transmission efficiency by minimizing attenuation caused by air gaps. Due to the symmetrical sensor arrangement, the surface displacements at the RS and SUT positions are identical. Signals from both sensors are simultaneously recorded using an oscilloscope and subsequently processed by a PC. Figure 2-21 (b) illustrates the AE calibration setup. When the pencil lead breaks, the excitation pulse propagates through the steel block, scattering within the material. The first wavefront reaches both sensors via the steel block's surface, while the second wavefront arrives after reflecting off the bottom surface of the block. Since the reflected wave reaches the sensors from an unintended calibration direction, it should be eliminated from the recorded waveform. Therefore, the second-arrival wave and all subsequent signals should be truncated or zero-filled to remove unwanted reflections.

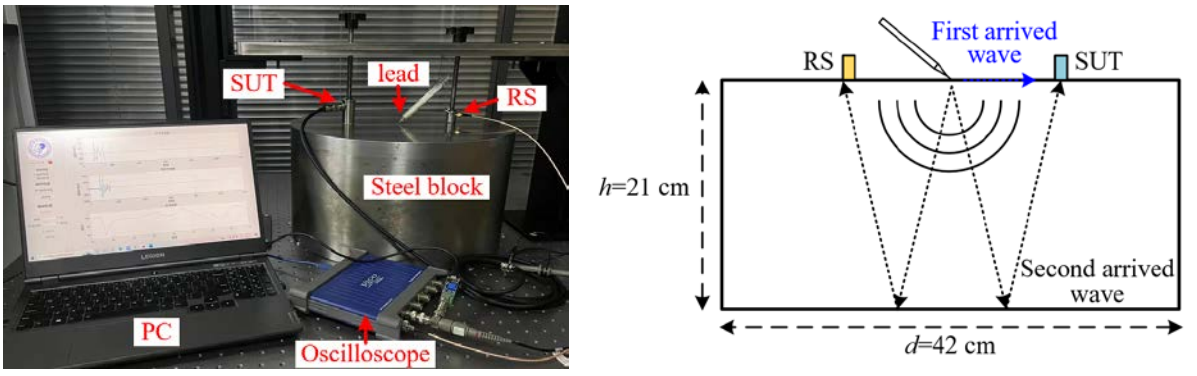

(a) (b)

Figure 2-21 AE calibration. (a) Experimental platform. (b) Calibration diagram.

The arrival time t of the wave can be calculated with Equation (2-31), where v=5165 m/s is the acoustic velocity of steel block, and x is the distance. Thus, the arrival times of the first two waves are around 19.36 μs and 83.6 μs, respectively, with a difference of about 64.24 μs. In this study, the second-arrival wave and its subsequent signals are zero-padded.

$$t = \frac{x}{v} \tag{2-31}$$

The signals of RS and SUT are shown in Figure 2-22 (a). After FFT on both signals, the AE sensitivity response of the SUT can be calculated using the following equation:

$$S_2(f) = 20 \times \log_{10} \frac{U_2(f)}{U_1(f)} + S_1(f) \tag{2-32}$$

where $S_1(f)$ and $S_2(f)$ represent the voltage sensitivity of the RS and the SUT, respectively, in dB (referenced to 1V/(m/s)), while $U_1(f)$ and $U_2(f)$ are the frequency-domain output voltages of the two sensors. $S_1(f)$ is provided by the manufacturer of the RS. The AE sensitivity responses of the SUT (fusion sensor) and the RS are shown in Figure 2-22 (b). The resonance frequency of the fusion sensor (with the built-in PCB) is 54 kHz, with a sensitivity exceeding 90 dB in the range of 20 kHz to 100 kHz and an average sensitivity of approximately 101 dB. The sensitivity curve of the fusion sensor exhibits slight fluctuations, which are attributed to calibration uncertainties, including RS performance and aperture effects. Generally, such uncertainties may cause minor local variations in frequency response but do not significantly affect the overall results. R3a, developed by Physical Acoustics Corporation (PAC), is used as the RS for AE calibration, and the relevant information of R3a is shown in Table 2-12.

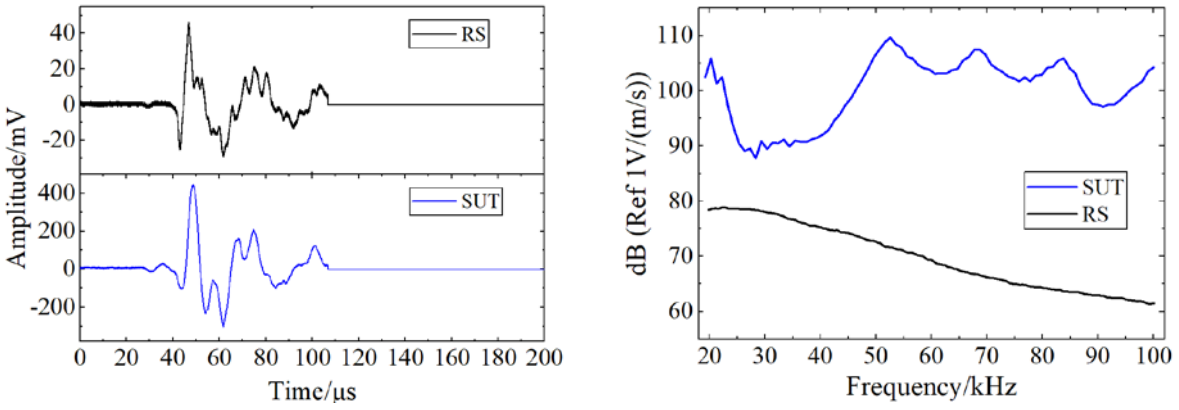

(a) (b)

Figure 2-22 AE calibration results. (a) Time domain signals. (b) Sensitivity responses.

Table 2-12 The relevant information of R3a (RS)

Item	Value	Item	Value
Peak Sensitivity/ dB Ref V/(m/s)	80	Resonant Frequency/ kHz	29
Temperature Range/°C	-65 to 175	Directionality/dB	+/-1.5
Frequency Range/kHz	20~100	Shock Limit/*g*	500

2) Vibration acceleration calibration

The vibration measurement performance of the fusion sensor is calibrated according to the ISO-16063-21:2003 standard[131]. The principle of vibration calibration is similar to that

of AE calibration. By simultaneously exciting an adjustable vibration source acting on both the SUT and the RS, the sensitivity of the SUT can be calculated. The vibration calibration experimental platform is shown in Figure 2-23 (a).

The RS and the SUT are mounted face-to-face on a standard vibration exciter to ensure both experience the same vibration. The vibration exciter is driven by a sine wave power amplifier that performs a frequency sweep from 100 Hz to 4 kHz in 100 Hz increments. The voltage sensitivity of the SUT, $S_2(f)$ (mV/g), can be calculated using the following equation, where $S_1(f)$ represents the voltage sensitivity of the RS, and $U_1(f)$ and $U_2(f)$ are the output voltage amplitudes of the two sensors, respectively.

$$S_2(f) = \frac{U_2(f)}{U_1(f)} \times S_1(f) \tag{2-33}$$

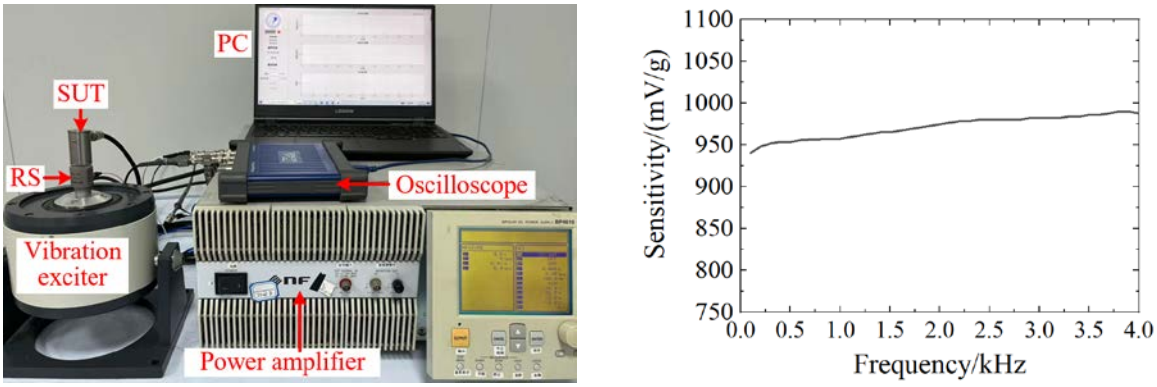

(a) (b)

Figure 2-23 Vibration calibration. (a) Experimental platform. (b) Vibration sensitivity calibration result.

The vibration calibration result of the fusion sensor (with the amplification circuit) is shown in Figure 2-23 (b). Within the frequency range of 100 Hz to 4 kHz, the vibration sensitivity is approximately 950 mV/g.

2.5 Brief Summary

To overcome the limitations of current sensor technologies for detecting mechanical and insulation defects in power equipment, namely their independent operation and diagnostic constraints, this chapter proposes a development approach for a vibration-AE fusion sensor that enables synchronized and co-located measurement of mechanical vibration and partial discharge AE signals. The measurement theory of the fusion sensor is formulated, and the basic sensing structure is designed. A finite element simulation model is established, focusing on three primary components: the matching layer, piezoelectric element, and mass backing block. The influence of structural parameters on measurement performance is investigated, and a data expansion algorithm optimization-based method is proposed to achieve intelligent structural optimization. Based on the optimized parameters and a multifunctional embedded processing circuit, the fusion sensor is assembled. The calibration platforms for vibration and AE meansurements are built, and the sensor’s measurement performance is validated. The main conclusions are as follows:

1) An equivalent electro-acousto-mechanical circuit model of the piezoelectric vibration-AE fusion sensor is established, and the theoretical transfer function is derived. A fusion sensing structure is designed, and finite element simulations are conducted to analyze the correlation between six key structural parameters, covering the matching layer, piezoelectric element, and mass backing block, and the sensing sensitivity.

2) Based on simulation data, curve-fitting algorithms are applied to extend the sensitivity characteristics in both the frequency and structural parameter domains, enriching the simulation database. A neural network model is then constructed to map the relationship between structural parameters and sensor performance indices. Furthermore, an optimization criterion is defined, and PSO is employed to determine the optimal structural parameters of the fusion sensor.

3) The sensor configuration is finalized based on the above analysis, and the assembly structure is designed accordingly. A built-in PCB signal processing circuit is developed, powered by phantom power and coupled with a 4 mA constant current source, to perform impedance transformation, noise filtering, and signal amplification. The fusion sensor is assembled, and a complete measurement device is developed. The calibration experiments show, the developed fusion sensor exhibits a vibration sensitivity of 950 mV/g and an average AE sensitivity of 101 dB within the target frequency band, enabling synchronous detection of vibration and AE signals.

3 Intelligentization of the Vibration-AE Fusion Sensor

Currently, sensors for power equipment detection suffer from low intelligence and poor operational efficiency. Traditional wired piezoelectric vibration and AE sensors are limited in the number of sensing nodes and rely heavily on manual assessment. To improve defect detection efficiency and advance the intelligence level of equipment monitoring, this chapter focuses on the comprehensive enhancement of the autonomous capabilities, covering sensing, storage, processing, and transmission of the vibration-AE fusion sensor. An intelligent framework is constructed by integrating features of advanced sensing technologies, including low-power wireless communication, edge computing, and self-calibration. A multifunctional embedded wireless module is designed and implemented. An edge computing strategy for fusion signal processing is proposed, and embedded algorithms are developed and validated through feasibility experiments. A rapid calibration method for piezoelectric sensor sensitivity and impedance based on pseudo-random M-sequence excitation is also presented, with both simulations and experiments verifying its feasibility and efficiency. These developments achieve a global optimization of the fusion sensor's intelligent performance.

3.1 Intelligent Framework of the Fusion Sensor

Intelligent sensors represent a key development trend in the field of perception and measurement, driven by advancements in sensor technology, electronics, and computer networks. Currently, there is no universally accepted scientific definition of intelligent sensors, but their core concept remains consistent. According to the description of intelligent sensors in IEEE 1451 by the International electrical and electronics engineering institution, an intelligent sensor integrates physical signal perception, data processing, network communication, and autonomous capabilities[132]. It not only performs high-precision measurements of environmental variables such as temperature, pressure, and vibration but also features an embedded computing unit for signal processing, data analysis, and pattern recognition. Moreover, it has the ability to communicate and collaborate with other sensors, edge computing devices, or cloud systems. Main features are as follows:

1) Low power consumption and energy management

Low-power design and energy management are crucial for the long-term stable operation of smart sensors, typically involving optimization across four aspects: sensing, computing, communication, and power management. At the sensing level, strategies such as low-power sensor materials, event-triggered acquisition, and adaptive sampling rates help reduce energy consumption. In computing, edge computing, low-power AI accelerators, and dynamic voltage and frequency scaling minimize processing power consumption. For wireless communication, low-power protocols (BLE, Zigbee, LoRa), data compression, and sleep-wake mechanisms optimize transmission energy efficiency. Additionally, smart sensors

rely on dynamic power management (DPM) and energy harvesting technologies (e.g., solar power and vibration energy recovery) to enhance self-sustaining capabilities, while ultra-low-power power management chips further optimize energy utilization.

2) Wireless communication and sensor networking

The development of wireless communication technology has significantly accelerated the networking of sensors, enabling smart sensors to achieve efficient data acquisition, transmission, and processing in complex environments. Traditional wired sensor networks, with their complex wiring, high maintenance costs, and limited scalability, struggle to meet the demands of modern Industrial Internet of Things (IIoT) and intelligent sensing systems. Wireless sensor network (WSN), employing low-power, distributed, and self-organizing network architectures combined with wireless communication protocols such as BLE, Zigbee, LoRa, and WiFi, enable efficient data exchange and remote monitoring capabilities.

3) Edge computing

Edge computing is a computational paradigm that shifts computing and data processing tasks from remote cloud servers to the network edge. By utilizing edge devices such as smart sensors, gateways, and edge servers for local data processing, edge computing reduces network latency, alleviates cloud computing loads, and enhances system real-time performance and reliability. Compared to traditional cloud computing architectures, edge computing employs distributed computation, data pruning, and intelligent collaboration to maintain computational capabilities while minimizing data transmission demands. This makes it particularly advantageous in resource-constrained IoT and IIoT environments. Furthermore, with AI-optimized edge computing frameworks such as TinyML and federated learning, edge devices can locally perform deep learning inference, enabling real-time anomaly detection and adaptive control.

4) Self-calibration

Self-calibration is a key feature of intelligent sensors, aiming to automatically compensate for environmental drift, component aging, and measurement errors through autonomous algorithms, built-in reference benchmarks, or collaborative calibration mechanisms. Compared to traditional manual calibration methods, self-calibration enables sensors to dynamically adjust system parameters after deployment, reducing maintenance costs and enhancing data reliability. This capability makes self-calibrating sensors highly valuable in applications such as industrial IoT, smart grids, and environmental monitoring.

This paper proposes an intelligent framework for the developed vibration-AE fusion sensor, as shown in Figure 3-1. The intelligent sensing unit (sensor node) consists of the vibration-AE fusion sensing module, analog signal processing circuit, power supply, System-On-Chip (SOC) chip, and its support circuit. Four main intelligent functions are implemented through the SOC chip: wireless communication, by designing a wireless PCB, assembling the sensor, and establishing and testing the WSN; low-power operation, achieving low-power operation of the chip through programming based on the energy management unit (EMU); edge computing, by designing algorithms for vibration, AE, and fusion features extraction according to the characteristics of the fusion signal; and

self-calibration, proposing a rapid calibration method for the piezoelectric sensor based on M-sequence signal. Additionally, the embedded storage system provides efficient data access and management, while also enabling the Transducer Electronic Data Sheet (TEDS) function. The AI/ML accelerator enhances computation speed, reduces power consumption, optimizes data processing, and strengthens advanced edge computing capabilities.

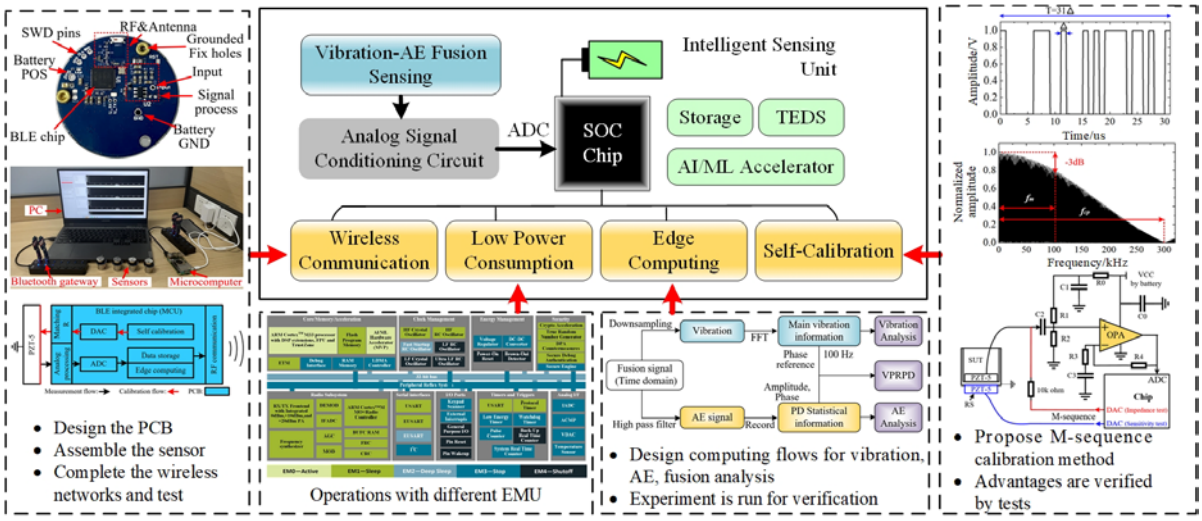

Figure 3-1 Intelligent framework of the fusion sensor.

3.2 Intelligent Built-in Module of the Fusion Sensor

Choosing the appropriate wireless transmission technology is the primary consideration in the development of the intelligent embedded module. The subject of this study is the vibration-AE intelligent fusion wireless sensor for GIS in substation, which requires good throughput, low power consumption, and low latency characteristics. Although Bluetooth Low Energy (BLE) has a limited transmission range, this issue can be addressed by increasing the number of client nodes. BLE 5.3 has the ability to switch flexibly between throughput, transmission range, and connection modes. The 2M PHY mode supports high-speed transmission, the LE Coded PHY mode is suitable for long-distance communication, while the 1 M PHY mode can balance transmission rate and range, and the Mesh mode can achieve mesh networking similar to Zigbee. In addition, BLE has a large user base and a comprehensive development ecosystem, with efficient connectivity to smart electronic devices, further enhancing its practicality and popularity. Therefore, compared to other technologies, BLE is a mature and comprehensive low-power wireless technology.

3.2.1 Wireless Low-Power Design of the Intelligent Built-in Module

The design of the integrated PCB should focus on reasonable layout to ensure that the fusion sensor can achieve wireless and intelligent functions. The design process should follow three principles: low power consumption, high efficiency, and lightweight.

The technical framework of the sensor-integrated PCB is shown in Figure 3-2. The core component of the circuit is the BLE SoC chip (EFR32MG24, Silicon Labs), which provides the sensor node with several key functions, including data acquisition and storage,

impedance calibration, edge computing, and wireless RF communication based on the BLE 5.3 protocol. The EFR32MG24 chip integrates high-performance ADC and DAC peripherals while offering extremely low power consumption and strong computational capabilities, making it an ideal choice for high-performance sensoring applications. During the measurement process, the output analog signal from PZT-5 is first preprocessed and then converted into a digital signal via the ADC. After computing and storage, these digital signals are transmitted to the target device through the BLE transceiver. In addition, for impedance self-calibration, the DAC generates excitation signal on the PZT-5 through matching resistor, while the response signal from PZT-5 is collected through the measurement chain and further analyzed and processed by the MCU.

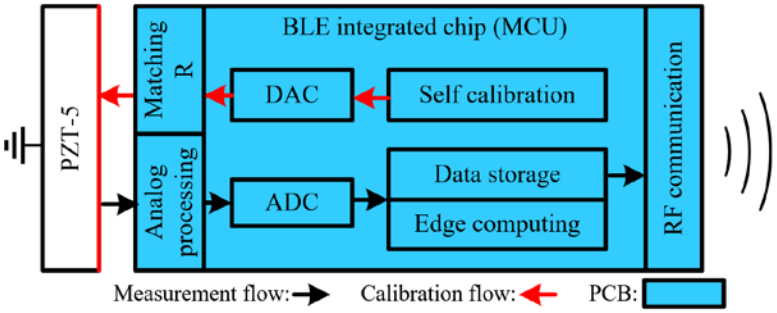

Figure 3-2 Wireless PCB Functional Framework.

Figure 3-3 (a) shows the designed integrated PCB with a diameter of 33 mm, where the BLE SoC chip serves as the core component of the PCB. The sensor is powered by a 3 V coin cell battery (CR 2477) with a unipolar supply voltage. Therefore, the static input signal of the ADC needs to be biased to half of the supply voltage (around 1.5 V) to receive the bipolar signal from the PZT-5. Additionally, to improve signal acquisition efficiency, the high impedance of the PZT-5 sensor needs to be converted to low impedance, and signal amplification is an essential functional requirement. To meet these needs, an analog signal conditioning circuit based on an operational amplifier is designed (as shown in Figure 3-3 (b)) to preprocess the signal before it is sampled by the ADC.

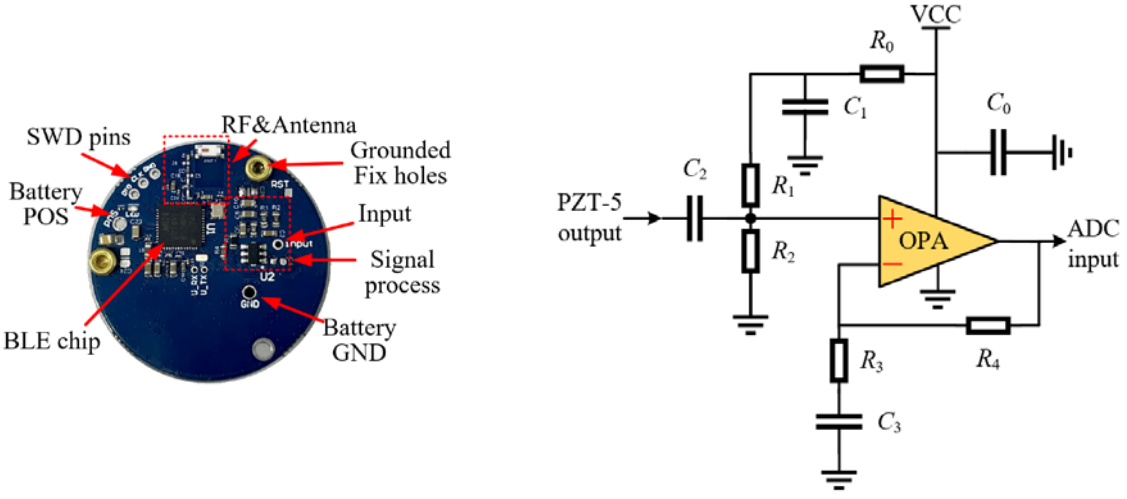

(a) (b)

Figure 3-3 The designed integrated PCB. (a) the PCB. (b) Analog signal processing circuit.

Specifically, in Figure 3-3 (b), R_0 and C_1 are used to stabilize the power supply voltage VCC. The voltage divider formed by resistors R_1 and R_2 generates the required DC bias for the input signal. C_2 is used to eliminate ultra-low-frequency components from the input signal (such as handheld vibrations or earthquakes). R_4 and R_3 determine the gain of the output signal (set to 10 in this paper). The gain A_{gain} is calculated as follows. Additionally, the BLE chip includes a programmable gain amplifier with five gain settings: 0.5, 1, 2, 3, and 4. Combined with the analog gain from the amplifier, a total of five adjustable amplification levels (5, 10, 20, 30, and 40 times) can be programmed. Furthermore, the operational amplifier OPA-363 features both active and shutdown modes, and its mode transition can be controlled by the MCU chip to further decrease power consumption. The values of the circuit components are listed in Table 3-1.

$$A_{gain} = \frac{R_3 + R_4}{R_3} \tag{3-1}$$

Table 3-1 Analog signal processing circuit parameters

Component	Value	Component	Value
R_0/kΩ	1	OPA	opa-363
R_1/MΩ	10	C_0/μF	200
R_2/MΩ	10	C_1/μF	100
R_3/kΩ	50	C_2/μF	10
R_4/kΩ	450	C_3/μF	10

The comparison between the input and output signals of the above analog signal processing circuit is shown in Figure 3-4. The input signal is a 50 Hz sine wave with an amplitude of 0.071 V, while the output signal is a 50 Hz sine wave with an amplitude of 0.71 V, superimposed with a 1.5 V DC bias.

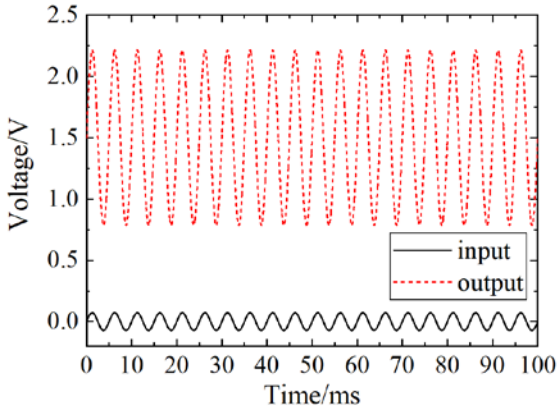

Figure 3-4 Input and output of the analog signal processing circuit.

The main information of the EFR32MG24 chip is shown in Table 3-2. It integrates a low-power MCU and a high-performance wireless transceiver. The MCU provides various peripherals and strong computing power, enabling the sensor to perform data sampling, storage, computation, and processing. On the other hand, through the wireless transceiver, its matching circuits, and the ceramic antenna, the sensor can communicate wirelessly with the

client. In addition, the chip supports a wide range of protocols, providing more expansion possibilities for future development. Its comprehensive hardware and software security framework offers strong data protection, secure operating environment, and anti-attack capabilities for IoT devices.

Table 3-2 Main information of EFR32MG24 chip

Component	Description
MCU	32-bit ARM® Cortex®-M33 core with DSP instruction and floating-point unit for efficient signal processing
ADC	12-bit @ 1 Msps or 16-bit @ 76.9 ksps. High Speed Mode (up to 2 Msps)
DAC	fully differential, DAC clock frequency up to 1 MHz, 12-bit
Flash	Up to 1536 kB flash program memory
RAM	Up to 256 kB RAM data memory
Radio Performance	-97.6 dBm sensitivity @ 1 Mbps GFSK -94.8 dBm sensitivity @ 2 Mbps GFSK TX power up to 19.5 dBm
Energy Consumption	4.4 mA RX current (1 Mbps GFSK) 5 mA TX current @ 0 dBm output power
Protocol Supports	Matter, OpenThread, Zigbee, Bluetooth Low Energy (BLE 5.3), Bluetooth Mesh, Proprietary 2.4 GHz, Multiprotocol, Direction finding using AoA, AoD
Secure Vault	Hardware Cryptographic Acceleration; True Random Number Generator; ARM® TrustZone®; Anti-Tamper, etc.

The low-power characteristics of the sensor are mainly reflected in the effective use of the Energy Management Unit (EMU) in the EFR32MG24, which is responsible for managing the power mode transitions of the device. As shown in Figure 3-5, there are five power modes ranging from active (EM0) to off (EM4). Each mode defines the available peripherals and functionalities. Most functions can be achieved in the low-power modes EM1-EM4. For example, in the EM3 shutdown mode, the key functions needed for the fusion sensor, such as IADC, VDAC, and LDMA transmission, can still be performed. In the EM1 sleep mode, timer, serial communication (USART), and wireless transmission functions can operate. Only the core processor and machine learning hardware accelerator need to run in the EM0 active mode. When the chip is in EM1-EM4 modes, the power consumption is in the microampere range, while in the EM0 mode, the power consumption is in the milliampere range. By effectively adjusting the available resources to meet the application requirements, the power consumption can be kept at the lowest level. The EMU enables chip to do specific functions at the lowest power consumption, thereby saving energy and extending the battery life of the coin cell used in the fusion sensor.

The main hardware design of the fusion sensor builds upon the content of Chapter 2, incorporating slight modifications to accommodate wireless functionality. Specifically, the original built-in PCB is replaced with an intelligent wireless embedded PCB powered by a coin cell battery. To ensure durability and prevent wireless signal shielding, the outer cover is made of PEEK plastic. The fully assembled wireless fusion sensor is shown in Figure 3-6:

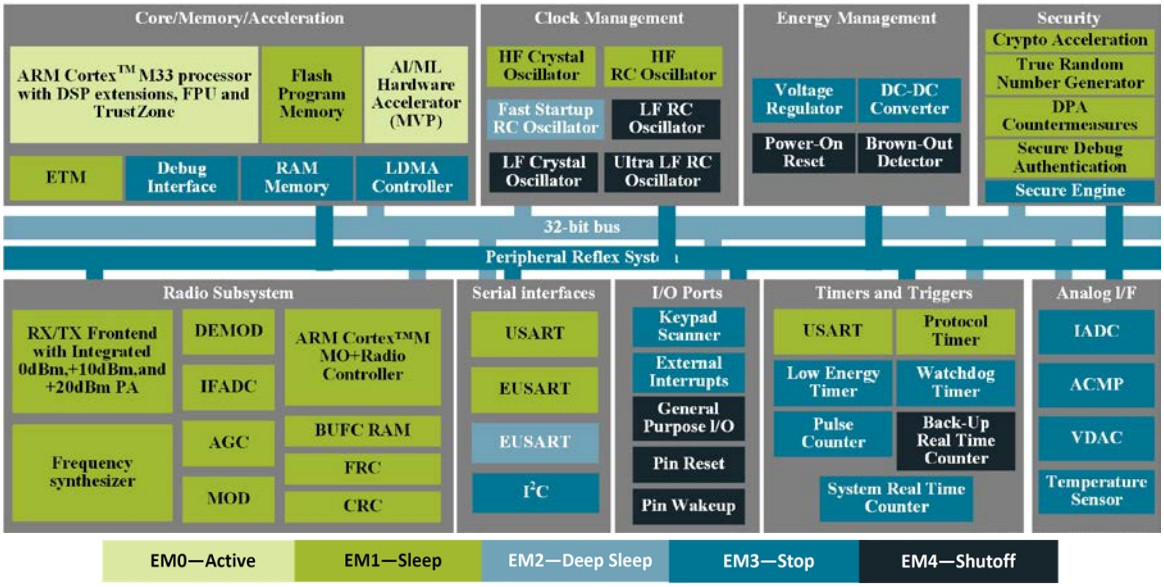

Figure 3-5 EFR32MG24 Energy management unit architecture.

(a) (b)

Figure 3-6 Intelligent wireless fusion sensor.

3.2.2 Wireless Function Tests of the Intelligent Built-in Module

1) BLE wireless transmission

Data transmission rate is a crucial performance indicator in wireless transmission, especially in real-time measurement applications, as it directly affects transmission speed and reliability. Several factors influence the data transmission performance of wireless sensors, with four key factors being the environment, distance, transmission parameter settings, and the number of sensors. Regarding transmission parameters, larger packet sizes can increase data rates but may lead to packet loss, while wider bandwidth supports higher data rates but also increases interference. In this paper, to achieve a good and stable data rate, the packet size is set to 240 bytes and the bandwidth to 2 MHz. For a point-to-multipoint mode (multiple sensor nodes to one client), as the number of sensors increases, data rates decrease due to the sharing of communication resources by the client. Therefore, Chapter 5 discusses the design of a many-to-many transmission mode. Additionally, device power, performance, and signal interference also affect data rates. The wireless chip in the fusion sensor supports BLE 5.3 with a 2 Mbps data transmission rate and a transmission frequency of 2.4 GHz, utilizing GFSK (Gaussian Frequency Shift Keying) to enhance wireless transmission efficiency. This section presents experimental studies on the transmission rate of fusion wireless sensor in different environments and distances. Tests are conducted

indoors, outdoors, and in a real GIS substation, with the distance between the sensor and the client varying from 1 meter to 20 meters. The test environments are shown in Figure 3-7.

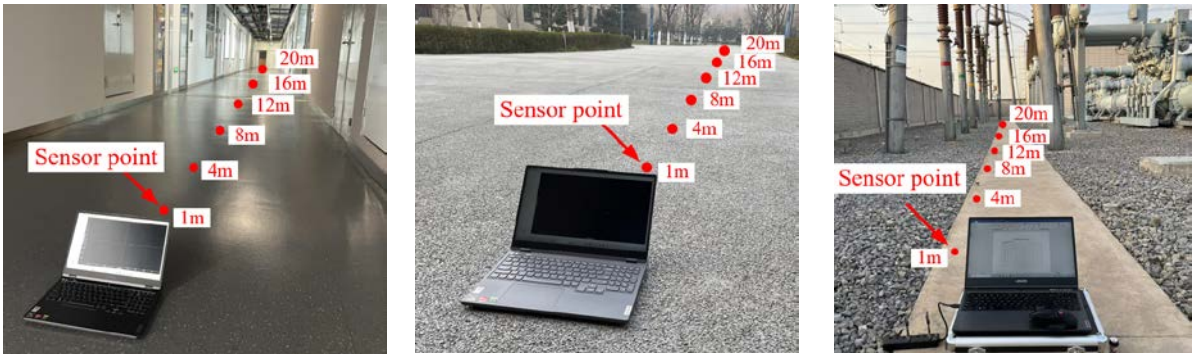

(a) (b) (c)

Figure 3-7 Data transmission test environment. (a) Indoors. (b) Outdoors. (c) In substation.

The data transmission rate results for the sensor are shown in Table 3-3. The results indicate that the data transmission rate decreases with distance, whether in indoor, outdoor, or actual GIS substation environments. In the indoor environment, the data transmission rate reaches 1.35 Mbps at a distance of 1 meter, and decreases to about 1.1 Mbps as the distance increases to 8 meters. A similar trend is observed in the outdoor environment, although the overall data rate is slightly lower. In the actual substation, the transmission rate is essentially the same as in the outdoor environment, indicating that the 2.4 GHz transmission frequency used by the fusion sensor is relatively unaffected by electromagnetic interference from the substation environment. Additionally, when the distance between the sensor node and the client is less than 8 meters, the sensor is able to transmit data at a rate above 1 Mbps. The sensor's sampling rate is set to 500 kHz. Therefore, a measurement dataset of 50,000 samples (2 bytes per sample) is transmitted at a rate of 1 Mbps in theoretically about 0.8 seconds. Considering the 0.1-second measurement duration and potential interference, the total time for a complete measurement is slightly more than 1 second.

Table 3-3 Results of data transmission test

Environment \Distance	Indoors/Mbps	Outdoors/Mbps	In substation/Mbps
1 m	1.35	1.31	1.285
4 m	1.17	1.05	1.12
8 m	1.1	1.01	1.03
12 m	1.058	0.8875	0.924.4
16 m	0.653.2	0.545.2	0.505.8
20 m	0.565.7	0.344.8	0.370.3

2) Power consumption

The EFR32MG24 chip provides technical support for low-power operation in wireless sensors. However, the actual power consumption of the sensor depends on the specific operation type and its duration, which is crucial for evaluating the device's lifetime.

Firstly, the operating mode of the wireless sensor needs to be clarified. In powered state,

the chip spends most of its time in a low-power sleep mode, so it consumes almost no power. The chip periodically wakes up from sleep mode to perform BLE broadcasting operations (microsecond level), generating current pulses of about 10 mA. When the client finds the sensor and initiates a connection request, communication is established through periodic connection events, during which brief current pulses (similar to the broadcasting events) occur. In connection mode, the sensor can receive commands and perform various operations, including data transmission, sampling, edge computing, etc. Once the connection ends, the sensor returns to sleep mode and periodically broadcasts.

In summary, the core operations of the wireless sensor include BLE connection, broadcasting, data transmission, ADC/DAC operations, and edge computing functions. To quantify the power consumption, this study employs a direct current measurement method, as shown in Figure 3-8. A 1 Ω resistor is placed in series between the battery and the PCB. By measuring the voltage change across the resistor, the sensor's current consumption can be determined. Figure 3-9 shows the currents consumption of five main operations.

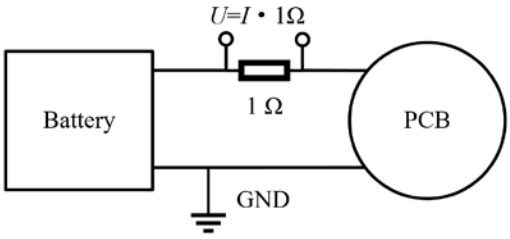

Figure 3-8 Current measurement diagram.

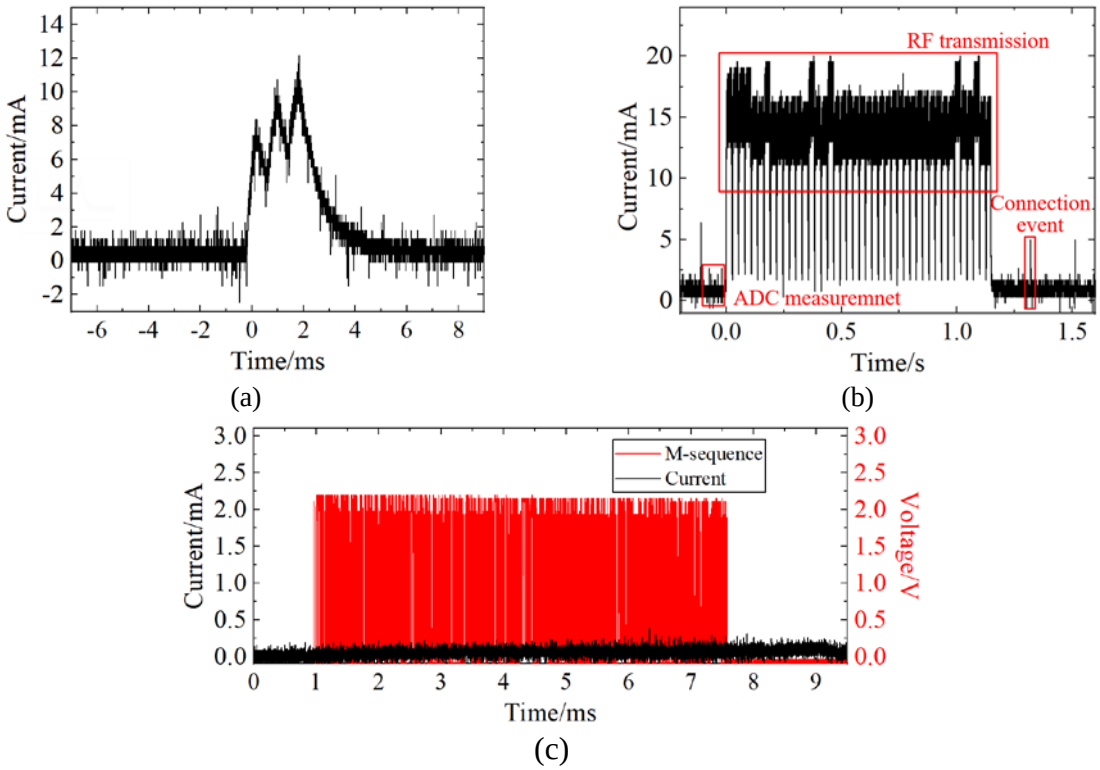

Figure 3-9 Currents of the five main operations. (a) Advertisement. (b) ADC measurement, RF data transmission, and connection event. (c) DAC.

The charge consumed by each operation is described in terms of charge quantity, which

can be calculated using the following equation:

$$Q = \int_0^t i dt \tag{3-2}$$

The amount of charge consumed by different operations is shown in Table 3-4.

Table 3-4 Power consumption of main operations

Operation charge	Description	Value
Q_{adv}/μC	Charge of each advertisement event	24
Q_{Con}/μC	Charge of each connection event	2
Q_{adc}/μC	Charge of each ADC measurement (50 k samples, sampling rate=500 kHz)	0.1
Q_{dac}/μC	Charge of each DAC generation (2047 samples, clock frequency=300 kHz)	0.6
Q_{RF}/mC	Charge of each data transmission (50 k samples=100 kB=800 kb)	17.25
Q_{edg}/μC	Charge of edge computing	0.5

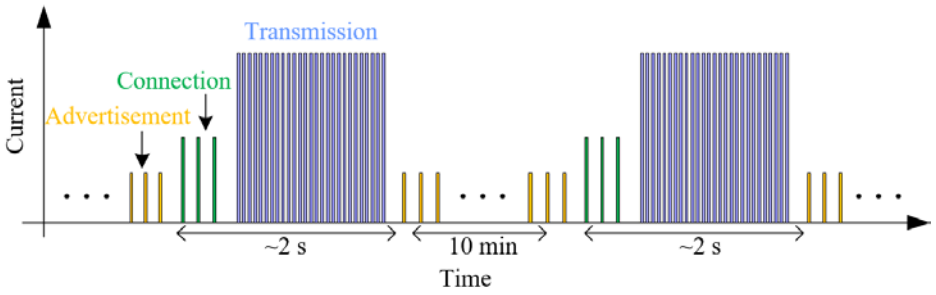

Figure 3-10 Typical operating timing diagram

The typical operating timing diagram is described in Figure 3-10. The sensor broadcasts every 10 seconds and performs a measurement (500 kHz, 0.1 s) every 10 minutes. The total charge consumption per hour, Q_{1h} can be calculated using the following equation:

$$Q_{1h} = n_{adv} \times Q_{adv} + n_{Con} \times Q_{Con} + 6 \times Q_{RF} \tag{3-3}$$

where, n_{adv} and n_{Con} represent the number of broadcast events and connection events per hour, respectively. Therefore, Q_{1h} is approximately 112.26 mC. Given that the CR 2477 battery has a capacity of 1 Ah (3600 C), the theoretical operational lifetime is about 4 years. However, considering the impact of battery self-discharge and environmental factors on battery capacity in practical applications, the actual operational lifetime of the sensor is typically shorter than the theoretical 4 years.

3.3 Feature Extraction of the Fusion Signal Based on Edge Computing

The time-domain signal for a single measurement of the fusion sensor is set to 50,000 measurement samples (100 kB), with a sampling frequency of 500 kHz. If edge computing is used to preprocess the data and extract key features, the effective information in the measurement data can be extracted and transmitted to the client, significantly reducing the

data transmission volume, latency, and power consumption. With the integration of AI machine learning algorithms, the sensor node can achieve preliminary self-diagnosis.

3.3.1 Edge Computing Framework Design

The built-in wireless PCB module described in this chapter uses the low-power wireless SoC from the EFR32MG series. Its core processing unit is a 32-bit ARM Cortex®-M33 processor with a working frequency of 78 MHz, and it integrates a digital signal processing (DSP) instruction set and a floating-point unit (FPU) to enhance computational capabilities and signal processing performance. This chip is equipped with 1536 kB of flash memory and 256 kB of RAM, enabling efficient data processing in low-power modes, making it suitable for energy-sensitive embedded applications. However, due to the relatively limited RAM capacity (which could be extended in the future), there are certain constraints when handling large-scale data processing tasks. Therefore, in the system design, the implementation of edge computing needs to follow principles of efficiency and light-weight design to reduce memory usage and enhance computational efficiency. Furthermore, this optimization direction is not only applicable to the sensor system in this study but also aligns with the design trends of most embedded devices with low-power and high-performance requirements. Based on the characteristics of the fusion signals of mechanical vibration (<4 kHz) and PDAE (>20 kHz) measured by the fusion sensor in this study, the proposed edge computing basic architecture is shown in Figure 3-11.

First, the time-domain fusion signal is downsampled and separated into vibration signals and AE signals processed by a high-pass filter. The vibration signal, after FFT transformation, provides the main vibration information in the frequency domain, including amplitude and phase, which can then be used to calculate vibration features (refer to Chapter 5 for details). On the other hand, the AE signal can be used to record statistical information such as the number, amplitude, and time points of the PD pulses, which can be used for PDAE analysis. Furthermore, by combining the 100 Hz vibration phase reference and PD information, Vibration-Phase-Resolved Partial Discharge (VPRPD) patterns can be plotted.

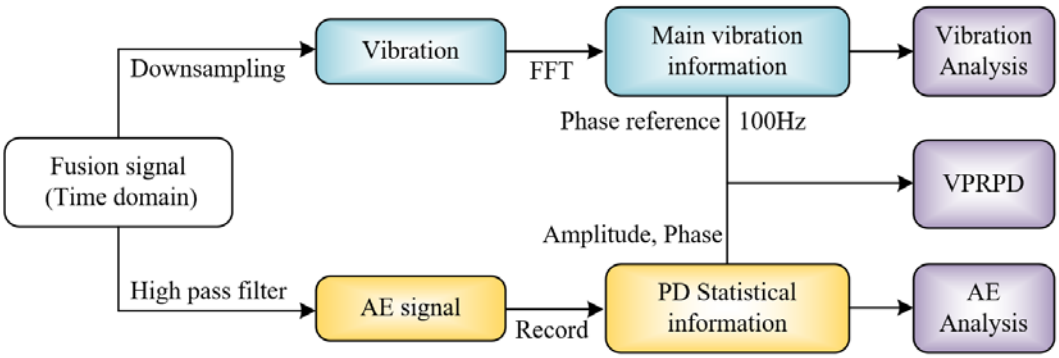

Figure 3-11 Fundamental architecture of edge computing.

1) FFT calculation of the vibration signal

KISS FFT (Keep It Simple, Stupid FFT) is a lightweight FFT library. Its intuitive structure and ease of integration make it popular in embedded systems and resource-constrained environments. It uses a radix-2 divide-and-conquer algorithm that

decomposes the input data into even and odd parts to reduce multiplication operations. The butterfly operation efficiently combines frequency components with a complexity of $O(N \cdot \log N)$. KISS FFT allows for efficient implementation of FFT calculations.

In this study, the sampling frequency of the fusion sensor is set to 500 kHz, with each measurement containing 50 k samples, and each sample being 2 bytes (16 bits). Therefore, the data size for each measurement is 100 kB, with a measurement time of 100 ms. After performing the FFT, the frequency spectrum ranges from 0 to 250 kHz, with a frequency resolution of 10 Hz. However, the spectral analysis is mainly used for low-frequency (<4 kHz) vibration signals, and processing large amounts of data introduces computational redundancy. To address this, a downsampling approach is applied: one sample is extracted from every 10 original samples, resulting in a simplified dataset with a total of 5 k samples. This reduces the sampling frequency to 50 kHz, which, according to the Nyquist theorem, is sufficient for vibration analysis. After FFT, the frequency spectrum ranges from 0 to 25 kHz, and the frequency resolution remains 10 Hz. This method provides the necessary vibration frequency-domain information without affecting the frequency resolution and alleviates computational pressure.

Taking a 1 kHz sine wave signal with an amplitude of 100 mV as an example, Figure 3-12 shows the results of edge-computing FFT: (a) the downsampled and simplified time-domain signal, with the data reduced to 5,000 samples, while the duration remains 100 ms; (b) the amplitude spectrum after FFT transformation, where the amplitude at 1 kHz is 100 mV, reflecting the amplitude of different frequency components; and the phase spectrum after FFT transformation, where the phase at 1 kHz is -90° (cosine phase). The entire FFT computation time is very short (millisecond level), and can be neglected.

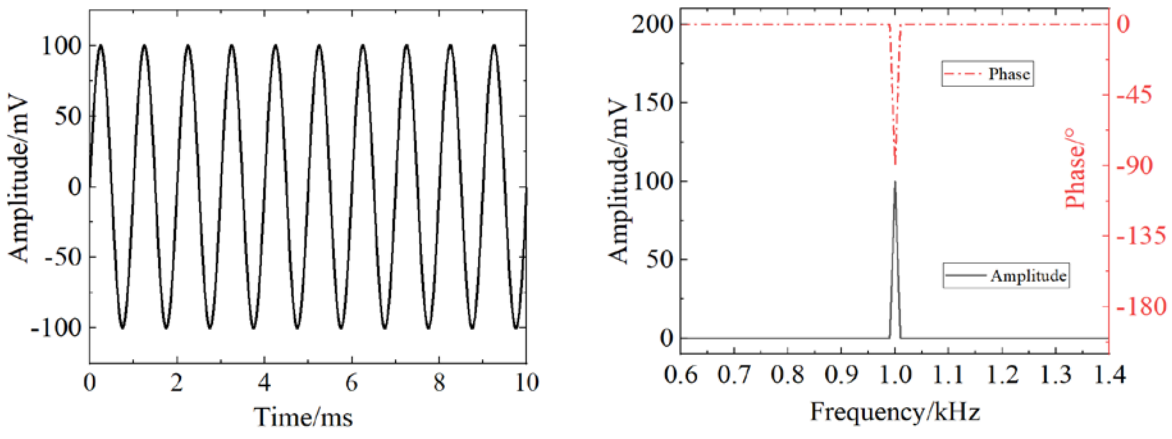

Figure 3-12 The results of FFT by edge computing. (a) Downsample. (b) Phase and amplitude information.

2) High-pass filtering and PD statistical information

PD manifests as pulse-decaying oscillations in the time domain, and a high-pass filter is a reliable method for extracting PD pulse signals from the vibration-AE fusion signal. Common filters include the moving average filter, Butterworth high-pass filter, and Chebyshev high-pass filter, each with its own characteristics. The moving average filter is

simple and easy to understand, but due to its smoothing characteristics, it may introduce lag in signal response, making it difficult to accurately capture rapidly changing signals. The Butterworth high-pass filter offers a flat passband and a gradual transition band, making it suitable for general signal processing. However, its transition band is not steep enough and may fail to effectively suppress lower-frequency interference. On the other hand, the Chebyshev-II high-pass filter, with its relatively constant stopband ripple, very flat passband, and steep transition band, can more accurately extract PD pulses. Moreover, the Chebyshev-II high-pass filter can be efficiently implemented with lightweight code, meeting the basic computational resource requirements of embedded systems.

The parameters of the designed 5th-order Chebyshev-II filter are shown in Table 3-5. This filter has a minimum attenuation of at least 40 dB in the stopband, with a stopband cutoff frequency of approximately 11 kHz.

Table 3-5 5th-order Chebyshev-II filter parameters

Parameters	Value					
Denominator	1	-4.575771	8.402231	-7.737786	3.573210	-0.661832
Numerator	0.813531	-4.057378	8.104507	-8.104507	4.057378	-0.813531

The normalized frequency response of the designed filter is shown in Figure 3-13 (a), the amplitude remains at 1 for frequencies above 10 kHz, while it is approximately 0 for frequencies below 6 kHz. The filtering effect on a 1 kHz sine wave with an amplitude of 100 mV is shown in Figure (b), the filtered signal almost has no sinusoidal component.

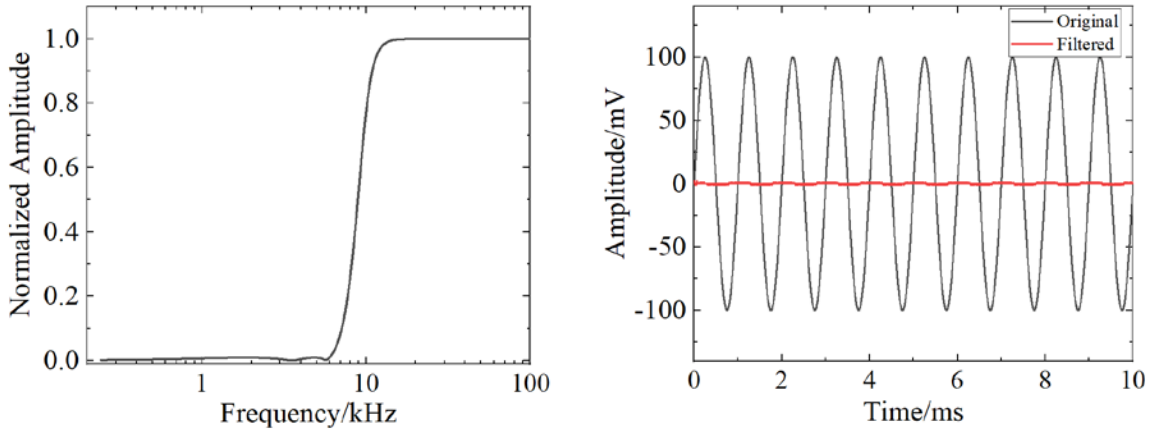

(a) (b)

Figure 3-13 The results of filtering by edge computing. (a) Normalized frequency response. (b) Time domain filtering.

3) $\triangle T$-A pattern

Under the AC electric field, the metal micro-particles inside the GIS generate an electric field force due to their own charge, causing them to continuously jump on the inner wall. When the particles fall back onto the wall, collisions and self-discharge generate AE signals, which are detected by the AE sensors as a series of PD signals. The time interval between two adjacent discharge signals corresponds to the flight time $\triangle T$ (x-axis), while the discharge amplitude reflects the strength of the AE signal (y-axis), as shown in Figure 3-14

(a). By plotting multiple discharge points on a two-dimensional coordinate, a △*T-A* flight pattern is obtained, which reflect the motion characteristics of metal particles.

The process of obtaining the AE flight pattern from the sensor is shown in Figure 3-14 (b). After high-pass filtering, AE pulses can be recorded to acquire PD statistical information, which consists of the quantity, amplitude, time, and density of the events. Since each single measurement of the wireless fusion sensor contains only 100 ms of data, the recorded PD information is insufficient to generate a flight pattern. Therefore, a measurement cycle criteria (the number of measurements or recorded PD events) should be set, and multiple measurements should be performed to collect enough PD information.

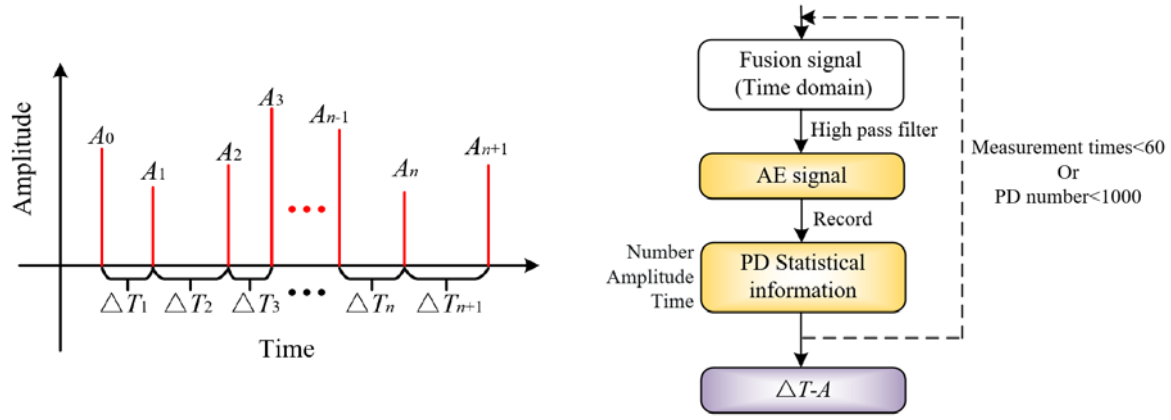

(a) (b)

Figure 3-14 △*T-A* flight pattern. (a) Data recording. (b) Acquisition process.

4) VPRPD pattern

Phase-resolved partial discharge (PRPD) is a PD statistical map based on the 50 Hz AC voltage phase. Different types of PD exhibit distinct PRPD characteristics, which are commonly used to assess insulation conditions. Similarly, based on the 100 Hz vibration phase of power equipment, the vibration phase-resolved partial discharge (VPRPD) pattern proposed in this study can be used to analyze the relationship between PD and mechanical vibration. The data recording for the VPRPD pattern is shown in Figure 3-15 (a), where both the mechanical vibration steady-state signal (blue) and the PDAE pulse signal (red) are recorded. It can be seen that the amplitude (y-axis) and occurrence time of the AE pulse, along with the initial phase of the 100 Hz frequency component in the vibration signal, are recorded. The phase of the 100 Hz vibration at the time of each AE pulse is then calculated and used as the x-axis information. Finally, all the discharge point data are plotted in a 2D coordinate to generate the VPRPD pattern. The edge computing process for VPRPD is shown in Figure 3-15 (b), with the following steps: First, the threshold is checked to determine whether PD pulses exist in the high-pass filtered fusion signal. If detected, the time, amplitude, and quantity of the pulses are recorded. The fusion signal is then transformed via FFT to obtain the initial phase of the 100 Hz vibration component, from which the corresponding 100 Hz vibration phase at the time of each PD pulse is calculated. After multiple measurement cycles, a large number of discharge points are collected to plot the VPRPD pattern. The stopping criteria for the measurement cycle is the attainment of

sufficient PD events and measurement repetitions.

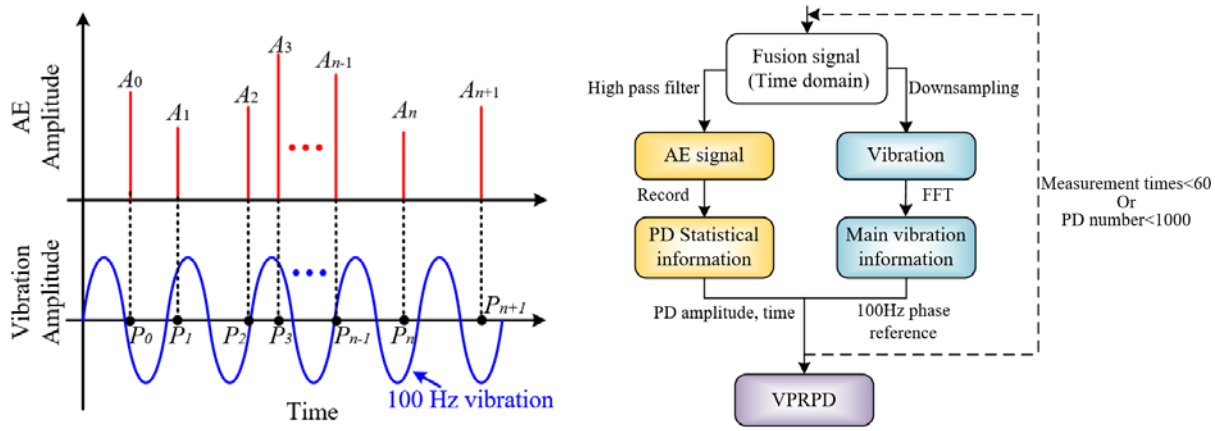

(a) (b)

Figure 3-15 VPRPD pattern. (a) Data recording. (b) Acquisition process.

3.3.2 Experimental Verification of Edge Computing

A combined experiment of metal particle discharge superimposed with sinusoidal vibration is conducted in the laboratory to validate the edge computing performance of the fusion sensor. The experimental setup is shown in Figure 3-16 (a), designed to simulate the discharge characteristics of particles in a high electric field environment with superimposed sinusoidal vibration. The system includes a chamber with high-voltage electrodes and a grounded platform, with a 50 Hz AC high-voltage source (7 kV) connected to the high-voltage electrode to create the electric field environment. A vibration exciter generates 0.5 *g*, 100 Hz sinusoidal vibration to simulate GIS vibration induced by current. Additionally, the chamber is filled with SF_6 gas at 0.4 MPa, and a 2 mm diameter metal particle is placed inside to simulate defect. The fusion sensor is positioned on the grounded platform of the chamber to measure. Figure 3-16 (b) shows the flight pattern obtained under the 0.5 *g* vibration amplitude, where the particle flight time ranges from 5 ms to 28 ms, exhibiting a unimodal feature, indicating a relatively low degree of particle jumping.

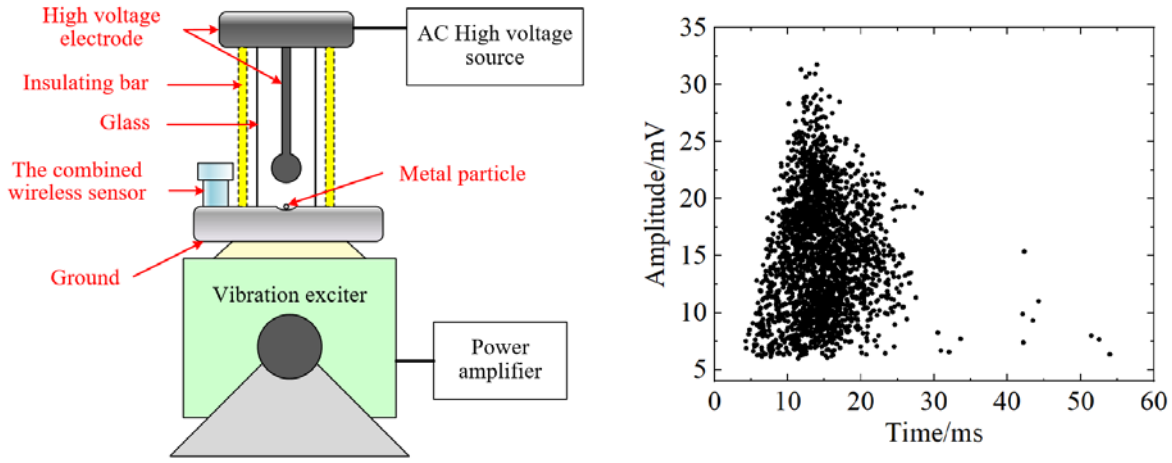

(a) (b)

Figure 3-16 Metal particle discharge experiment under AC high voltage with superimposed sinusoidal vibration. (a) Experimental platform. (b) Flight pattern.

To compare the correlation between particle discharge and vibration under different vibration conditions, the voltage (AC 7 kV) is kept constant, and sine vibration of 0.5 *g* and 1 *g* are applied through the vibration exciter. Figure 3-17 shows the VPRPD patterns under the two vibration amplitudes.

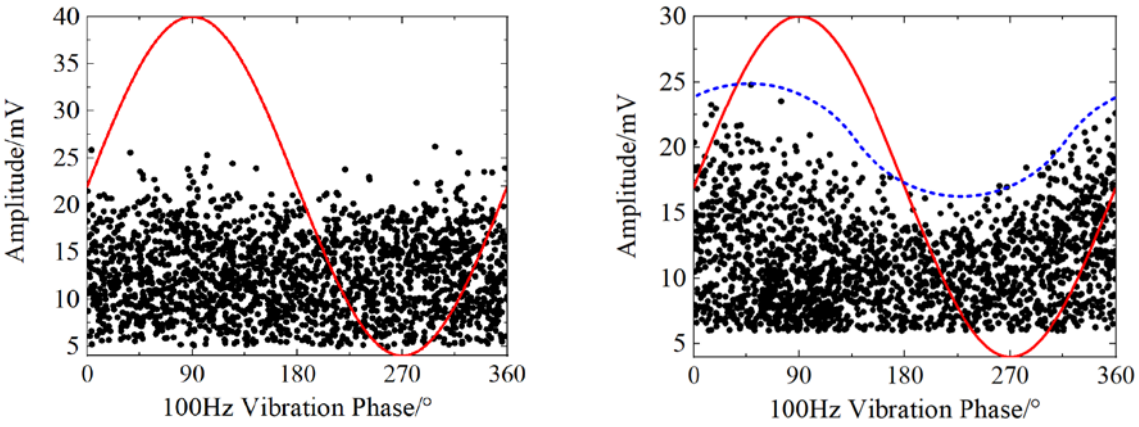

Figure 3-17 VPRPD patterns. (a) Under 0.5 *g* vibration. (b) Under 1 *g* vibration.

In the Figure 3-17, black dots represent the amplitude of the PDAE pulses. It can be observed that when the vibration is small (0.5 *g*), the maximum discharge amplitude is about 21 mV, and the discharge points are evenly distributed with little correlation to the 100 Hz vibration phase. However, when the vibration is larger (1 *g*), the distribution of discharge points shows a certain pattern. The envelope formed by the discharge points exhibits an around 45° phase difference with the 100 Hz sinusoidal vibration phase, and the maximum particle discharge amplitude reaches around 25 mV (at phase 45°). On the other hand, at the vibration trough, the discharge amplitude decreases to about 16 mV (at phase 235°). This indicates that vibration has an impact on the particle discharge, with a certain correlation between the two, reflected in the different distributions in the VPRPD pattern. However, it should be noted that when the particle motion is more active, its influence by the ground vibration is minimal, and relevant features are hard to observe in the VPRPD pattern.

3.4 Fast Calibration Method for Piezoelectric Sensor Based on Pseudo-Random M-Sequence Excitation

This section proposes a rapid calibration method based on a pseudorandom Maximum-length linear feedback shift register (M-sequence) for excitation. The method allows for the efficient measurement of the impedance and sensitivity response curves of piezoelectric sensor. Through theoretical analysis, the key parameters of the excitation signal are determined, and the feasibility of the method is validated using circuit simulation and FEA simulation. Additionally, the method has been applied to commercial AE sensor as well as the developed intelligent wireless sensor. Experimental results show that the method demonstrates significant advantages in terms of cost, time, and efficiency, making it highly suitable for field calibration of distributed multi-sensor systems. Moreover, this method is also applicable to other impedance and sensitivity response calibration scenarios.

3.4.1 Calibration Principle and Simulation Verification

1) Sensing Principle of Piezoelectric Sensors

The piezoelectric transducer can convert between electrical energy and mechanical energy. If the input is a mechanical variable, the output will be a voltage variable, and vice versa[133]. The equivalent circuit of a piezoelectric sensor is shown in Figure 3-18. In this circuit, R_m, L_m, and C_m represent the mechanical branch that reflects the sensitivity curve, while R_e and C_e represent the electrical branch that reflects the impedance curve. These two curves are essential for characterizing the performance of the sensor.

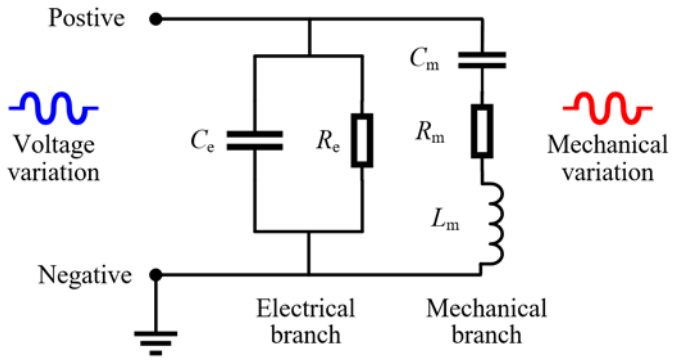

Figure 3-18 The equivalent electrical circuit of a typical piezoelectric sensor.

2) Pseudorandom M-sequence

Although white noise is an ideal calibration excitation signal due to its power spectral density being uniformly distributed across the entire frequency band, its generation process is complex and requires expensive and bulky equipment. However, the pseudorandom binary M-sequence, as a periodic sequence, possesses statistical properties similar to discrete binary white noise, making it highly suitable for rapid calibration of frequency response curves[134]. The advantages of M-sequences are significant: they can be designed using a linear feedback shift register (LFSR) and generated by low-cost digital-to-analog converter (DAC), offering good repeatability; the measurement frequency band can be easily adjusted by varying the clock frequency of the M-sequence; and, most importantly, the entire measurement process takes only a few milliseconds with very low power consumption, making it ideal for field applications and resource-constrained environments.

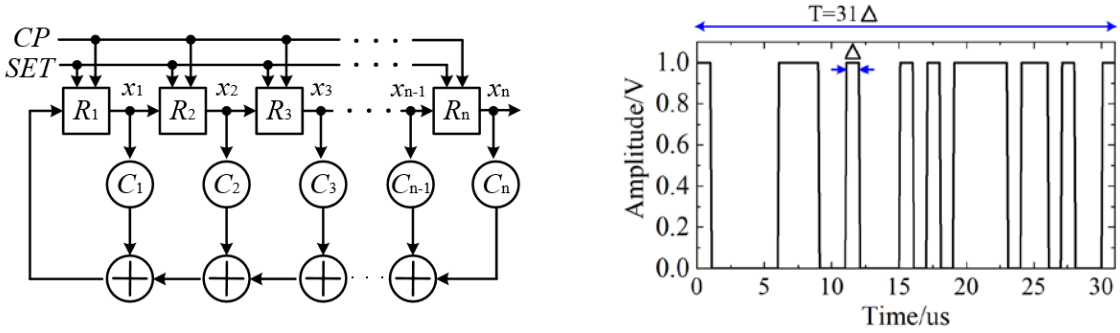

(a) (b)

Figure 3-19 The generation of M-sequence. (a) Binary linear feedback topology for generating M-sequence. (b) Example of a period of 5-stage M-sequence signal.

The M-sequence can be designed using a set of binary linear feedback shift registers (R_i, where i = 1, 2, ..., n) that are operated with an XOR (exclusive OR) logic, as shown in Figure 3-19 (a). The values of C_i are set to 1 or 0 to control whether the register R_i participates in the feedback process, which will determine the structure and links of the sequence. Additionally, x_i represents the state of the register R_i.

The feedback function of the M-sequence can be described by the following equation:

$$F(x_1, x_2, \cdots x_n) = C_1 x_1 \oplus C_2 x_2 \oplus \cdots \oplus C_n x_n \tag{3-4}$$

where $\oplus$ represents the XOR operation. Except for the all-zero state, an n-stage shift register has a total of $N_p=2^n$ - 1 states, which form a specific periodic sequence. If the duration of one stage is considered, the maximum period of the M-sequence should be $T=N_p \cdot \Delta$. One period of a 5-stage M-sequence is shown in Figure 3-19 (b). The characteristic polynomial of C_i should be:

$$f(x_1, x_2, \cdots, x_n) = C_0 + C_1 x^1 + C_2 x^2 + \cdots C_n x^n = \sum_{i=0}^{n} C_i x^i \tag{3-5}$$

where $C_0 = C_n = 1$ and x has no practical significance. To generate an M-sequence similar to white noise, the characteristic polynomial must be an irreducible polynomial to ensure the generated sequence is a maximum-length sequence with good random characteristics[135]. Furthermore, N_p should be sufficiently large. Studies have found that an 11-stage M-sequence signal is suitable for calibration testing, so N_p is 2047. The minimal primitive polynomial and the corresponding feedback function are:

$$f(x_1, x_2, \cdots, x_n) = 1 + x^2 + x^{11} \tag{3-6}$$

$$F(x_1, x_2, \cdots, x_n) = x_2 \oplus x_{11} \tag{3-7}$$

The measurement bandwidth f_m of the M-sequence can be calculated by the equation (3-8), where f_{cp} is the clock pulse frequency Δ.

$$f_m \approx \frac{f_{cp}}{3} = \frac{1}{3 \cdot \Delta} \tag{3-8}$$

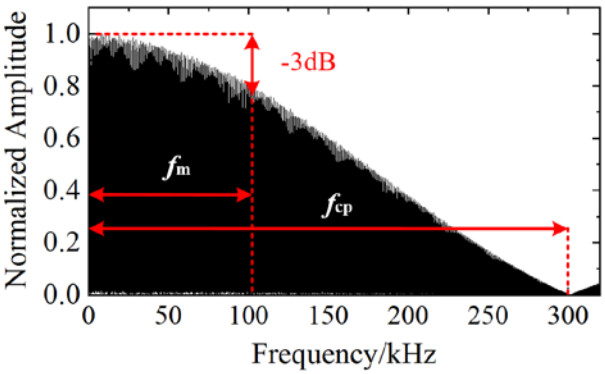

Figure 3-20 The power spectrum (normalized) of 11-stage M-sequence in frequency domain when f_m equals 100 kHz.

As mentioned earlier, the AE measurement band of the fusion sensor in this paper ranges in 20 kHz ~ 100 kHz. Therefore, the clock pulse frequency f_{cp} should be 300 kHz ($\Delta \approx 0.33\mu s$), resulting in a period of the M-sequence signal of only 6.823 ms. Figure 3-20 shows the normalized power spectrum of the 11-stage M-sequence signal when f_m =100 kHz and f_{cp}=300 kHz.

3) Simulation verification

Although the calibration measurement principles for impedance and sensitivity response curves are similar, there are some differences in their measurement topologies. Figure 3-21 (a) and (b) show the two main measurement topologies:

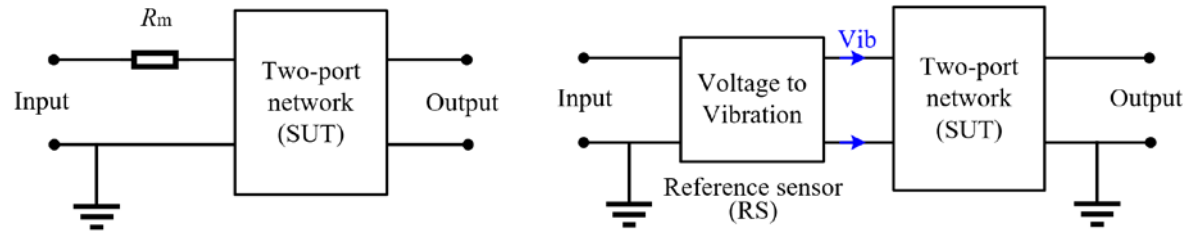

(a) (b)

Figure 3-21 Measurement topologies. (a) Impedance response measurement topology. (b) Sensitivity response measurement topology.

where the sensor under test (SUT) is treated as a two-port network, and the input signal can be either an M-sequence or a sweep signal. In impedance calibration, the SUT is connected in series with a matching resistor R_m (10 kΩ). In contrast, in sensitivity measurement, the input signal induces a mechanical response in the reference sensor (RS) via the piezoelectric effect, and this mechanical change is directly applied to the SUT. This requires the SUT and RS to be mounted face-to-face with a coupling agent to achieve mechanical coupling. In both cases, the measurement process involves recording the voltage signal at the output of the SUT.

Finally, the impedance and sensitivity response curves $Z(f)$ and $S_{SUT}(f)$ can be calculated from equations (3-9) and (3-10), respectively, where f is the frequency, R_m is the matching resistor, $U_{out}(f)$ and $U_{in}(f)$ represent the output and input voltage values in the frequency domain, while $T_{RS}(f)$ is the emission sensitivity response of the RS, provided by the RS manufacturer.

$$Z(f) = R_m \frac{U_{out}(f)}{U_{in}(f) - U_{out}(f)} \tag{3-9}$$

$$S_{SUT}(f) = 20 \times \log_{10} \frac{U_{out}(f)}{U_{in}(f)} + T_{RS}(f) \tag{3-10}$$

The equivalent circuit for the impedance curve simulation is shown in Figure 3-22 (a). The values of R_e and C_e are 5 MΩ and 8 nF, respectively, based on the equivalent impedance of actual piezoelectric ceramics. The signal source can be either an M-sequence signal or a sweep signal. The comparison results are shown in Figure 3-22 (b). The variance analysis factor (VAF), also known as the correlation factor R^2, is used to describe the similarity

between the results of the two methods and can be obtained using the following formula:

$$\begin{cases} SS_{\text{tot}} = \sum_i (y_i - \bar{y})^2 \\ SS_{\text{res}} = \sum_i (y_i - z_i)^2 \\ R^2 = 1 - \dfrac{SS_{\text{res}}}{SS_{\text{tot}}} \end{cases} \tag{3-11}$$

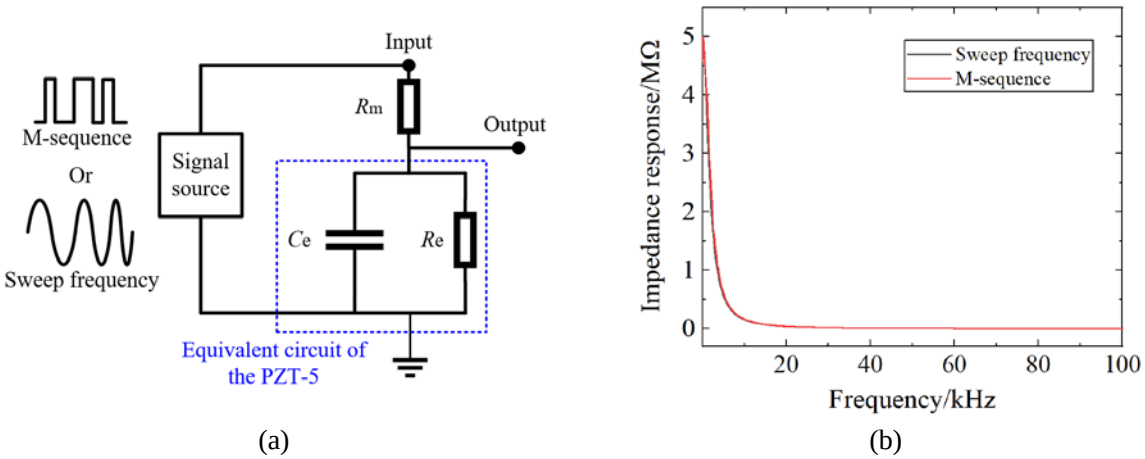

(a) (b)

Figure 3-22 Electrical circuit simulation for impedance calibration. (a) Simulation circuit. (b) Impedance curves measured by M-sequence and sweep frequency methods.

where SS_{tot} and SS_{res} represent the total sum of squares and the residual sum of squares, respectively, y_i and z_i are the i-th samples of the two arrays, and $\bar{y}$ is the mean value of the y-array. The closer R^2 is to 1, the more similar the two arrays are. In this case, R^2 equals 0.9997, indicating that the impedance results obtained using the M-sequence method are highly similar to those obtained using the sweep signal method.

Table 3-6 The FEA simulation setup for sensitivity calibration.

Item	Description
Material & Dimension	PZT-5: 4 mm height, 20 mm diameter Copper: 4 mm height, 24 mm diameter
Input voltage	M-sequence or Sweep frequency signal with the same 1 V amplitude.
Static and solid mechanics modules	PZT-5, Copper
Piezoelectric coupling module	PZT-5

The calibration of the sensitivity response curve is essentially the calibration of the electromechanical response (piezoelectric effect), so FEA is more suitable than circuit simulation. The simulation setup is shown in Figure 3-23 (a). The piezoelectric coupling module is applied to PZT-5, while static and solid mechanics modules are applied to both PZT-5 and metal. The bottom PZT-5 element is used as the RS, converting the input voltage signal (M-sequence or sweep signal) into vibration as the excitation source. The upper PZT-5 element and the intermediate metal layer are considered as the SUT, with the metal layer acting as a matching layer or base, and the metal layer is grounded. Finally, after completing

the simulation, the output voltage of the upper PZT-5 is obtained. The simulation using the M-sequence method is conducted in transient analysis (Time domain), while the sweep signal method simulation is performed in frequency-domain analysis. Table 3-6 shows the simulation setup.

According to Equation (3-10), the sensitivity response curves obtained by the two methods can be calculated, as shown in Figure 3-23 (b). The results are highly consistent, with a variance factor R^2 of 0.9929.

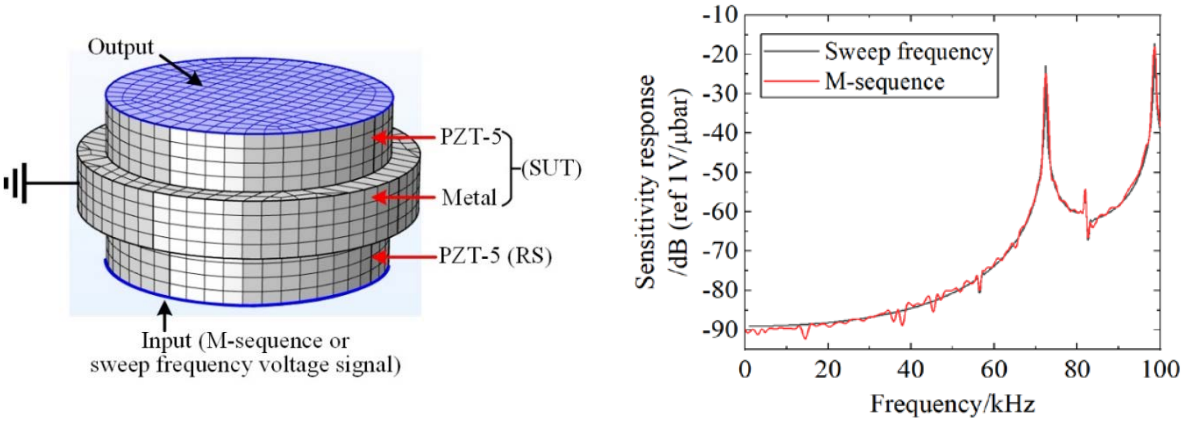

(a) (b)

Figure 3-23 FEA simulation. (a) FEA simulation set up. (b) Sensitivity response curves measured by M-sequence and sweep frequency methods.

3.4.2 M-sequence Excitation for Fast Calibration Experiment

The simulation results of the impedance and sensitivity response curves theoretically verify that the M-sequence method has the same effectiveness as the sweep method. However, the former requires only a few milliseconds and extremely low power consumption, making it highly suitable for on-site and embedded calibration. Additionally, the proposed method does not require expensive or bulky equipment. In this section, the M-sequence signal is generated and its characteristics are analyzed. The proposed method is then applied to both commercial sensors and the wireless sensor developed in this study.

1) The generation of M sequence signal

The M-sequence signal can be simultaneously generated and measured through a virtual oscilloscope (PicoScope 3206D). Figure 3-24 shows the generated M-sequence signal. Among them, Figures (a) and (b) and Figures (c) and (d) represent the time-domain and normalized power spectrum of two sets of 11th-order M-sequence signals, respectively. The measurement bandwidths are 100 kHz and 200 kHz, with clock frequencies of 300 kHz and 600 kHz, respectively. It can be observed that the time duration of a single M-sequence signal period for the two measurement bandwidths is 6.823 ms and 3.411 ms, respectively. The process is short and exhibits good repeatability (binary signal). Therefore, continuously measuring several periods of the M-sequence signal and averaging the results can reduce calibration deviation. The larger the measurement bandwidth f_m of the M-sequence, the shorter the time required for the M-sequence method. However, this also imposes higher performance requirements on the DAC and ADC.

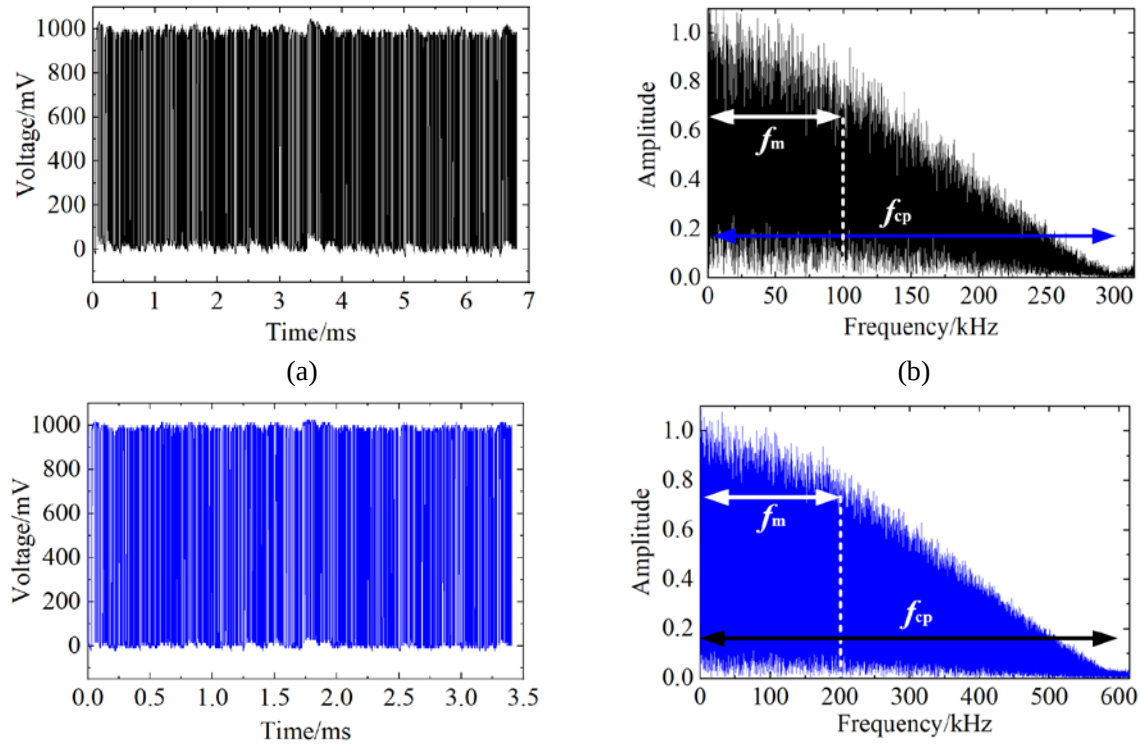

Figure 3-24 The generated M-sequence signal. (a) The M-sequence when f_m=100 kHz. (b) The normalized power spectrum. (c) The M-sequence when f_m=200 kHz. (d) The normalized power spectrum.

2) Application on commercial AE sensor

The experimental setup is shown in Figure 3-25. The virtual oscilloscope, controlled by a PC, is used to generate both M-sequence and sweep signals while simultaneously measuring signals from the SUT and the reference sensor RS. The calibration setup employs a fixture to secure the sensors, with sponges placed on both sides for protection. A coupling agent is used in the experiment to enhance the transmission efficiency of AE signals. Additionally, to comprehensively verify the accuracy of the results, the experimental data is compared with measurements obtained from an impedance analyzer and the reference data provided in the sensor product datasheet.

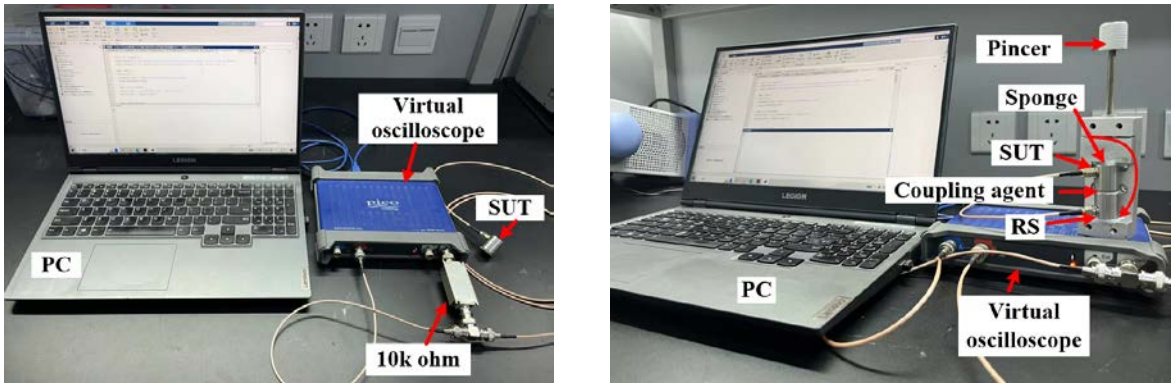

Figure 3-25 The calibration experiment setup of commercial AE sensor. (a) Impedance response calibration. (b) Sensitivity response calibration.

The experimental results are shown in Figure 3-26. Since the piezoelectric element in the AE sensor can be approximated as a parallel-plate capacitor, the impedance curve gradually decreases from approximately 23 kΩ to 3 kΩ. The correlation factor R^2 between the impedance curves obtained using the M-sequence method and the impedance analyzer is 0.9977, while the R^2 between the sweep method and the impedance analyzer is 0.9951. On the other hand, the sensitivity response curves overlap well above -90 dB. Below -90 dB, the sensitivity values are relatively small, which may introduce errors, leading to deviations in the curve. The R^2 between the sensitivity curve obtained using the M-sequence method and the product datasheet is 0.956, while the R^2 between the sweep method and the product datasheet is 0.995.

Table 3-7 compares the M-sequence method and the traditional sweep method in terms of accuracy, power consumption, and complexity. Accuracy is represented by the correlation factor R^2, while power consumption is analyzed based on a single calibration process. Specifically, power P and energy consumption E can be calculated using the following equations:

$$P = \frac{1}{T}\int_0^T \frac{u^2(t)}{Z(f)}\mathrm{d}t = \frac{1}{T \cdot Z(f)}\int_0^T u^2(t)\mathrm{d}t \tag{3-12}$$

$$E = \int_0^T \frac{u^2(t)}{Z(f)}\mathrm{d}t = \frac{1}{Z(f)}\int_0^T u^2(t)\mathrm{d}t \tag{3-13}$$

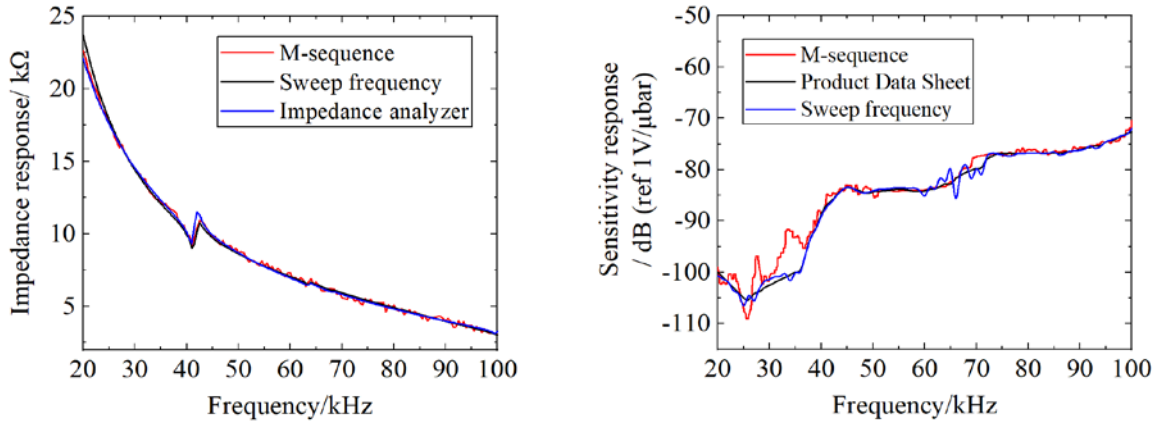

(a) (b)

Figure 3-26 The calibration results. (a) Impedance response curve. (b) Sensitivity response curve.

where T represents the time required for a single calibration process, $Z(f)$ denotes the sensor impedance, and $u(t)$ is the voltage excitation signal applied to the sensor. In this section, the amplitude of both the M-sequence signal and the sweep signal is set to 1 V.

It can be seen that the R^2 values of both methods are above 0.95, indicating high accuracy. The M-sequence method requires only 6.823 ms for a single calibration. Given a sampling frequency of 1 MHz, the frequency resolution is approximately 147 Hz. For comparison, the frequency resolution of the sweep method is also set to 147 Hz, covering the range from 20 kHz to 100 kHz. Considering the signal generation performance of the virtual

oscilloscope, each frequency signal requires at least 1 ms of duration for stable output, resulting in a total calibration time of approximately 780 ms. Therefore, although both methods have the same average power consumption, their energy consumption differs significantly. The sweep method consumes 390/$Z(f)$ mJ of energy, which is 114 times that of the M-sequence method.

Table 3-7 The comparison between the M-sequence and sweep frequency methods for single calibration.

Items\methods	M-sequence	Sweep frequency
Accuracy/R^2 factor	Impedance:0.9977 Sensitivity: 0.956	Impedance: 0.9951 Sensitivity: 0.995
Time cost/ms	6.823	780
Average power cost/W	0.5/$Z(f)$	0.5/$Z(f)$
Energy cost/mJ	3.41/$Z(f)$	390/$Z(f)$
Generating complexity	Binary signal (0 or 1)	Continuous signal

In addition, another significant advantage of the M-sequence calibration method is the ease of signal generation. The M-sequence signal can be directly generated using a binary pulse generator, such as by utilizing the GPIO (General-Purpose Input/Output) pins of a chip to produce binary pulse signals. In contrast, the sweep signal requires a DAC for generation.

3) Application on intelligent wireless fusion sensor

Based on the advantages of the proposed M-sequence calibration method, this section applies the method to the developed vibration-AE wireless fusion sensor. The designed analog signal processing circuit for calibration is shown in Figure 3-27, where the red line represents the impedance curve calibration loop, and the blue line represents the sensitivity response curve calibration loop. Operational amplifiers and related components in the circuit are used to achieve signal amplification, impedance matching, and measurement voltage range adjustment, ensuring that the output signal of the piezoelectric ceramic can be accurately acquired by the on-chip ADC.

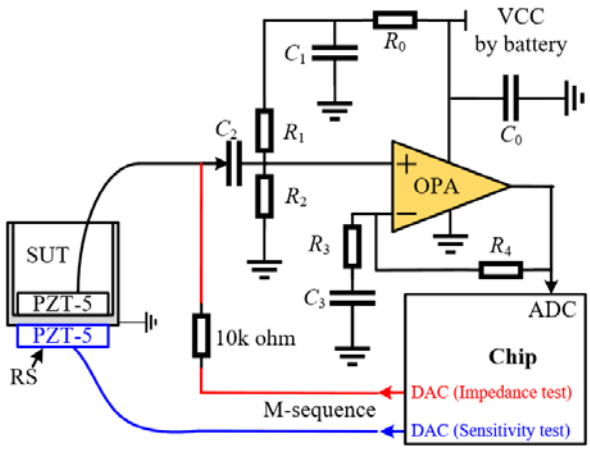

Figure 3-27 The self-calibration circuit applied in wireless sensor.

The M-sequence signal is generated by the DAC integrated into the microcontroller. According to the technical manual of the chip used in this study, the estimated power

consumption of the DAC is only 10 mW. Additionally, since the clock frequency of the M-sequence f_{cp} is 300 kHz, according to the Nyquist sampling theorem, the ADC sampling rate should be set to at least 600 kHz. To ensure the accuracy and reliability of the signal sampling, the ADC sampling rate is set to 1 MHz in this study.

To compare the results of the M-sequence method and the standard calibration method, the impedance curve of the sensor is calibrated using an impedance analyzer (sweet frequency), and the sensitivity response curve of the sensor is obtained through the AE calibration platform established in Chapter 2. Figure 3-28 (a) shows the impedance curves measured by the standard measurement method and the M-sequence method. Although the latter exhibits slight fluctuations, the overall trend of both curves is very similar, with the impedance value decreasing from 6 kΩ to 500 Ω. The correlation factor R^2 calculated for the impedance curves obtained by both methods is 0.99. Figure 3-28 (b) compares the sensitivity response curves obtained by the standard measurement method and the M-sequence method. Overall, both curves match closely, but slight differences exist at certain resonance frequencies, mainly due to the different experimental conditions (the M-sequence method used face-to-face calibration without steel blocks). The correlation factor R^2 calculated for the sensitivity response curves obtained by both methods is 0.986.

The experimental results demonstrate that the M-sequence method is feasible for impedance and sensitivity response calibration, with the added benefits of low energy consumption and test times of only a few milliseconds. Additionally, since the method utilizes the integrated ADC and DAC on the microcontroller, no additional hardware is required, further reducing the cost and size of field calibration for smart sensors. This method holds significant potential for application and can be used for distributed measurements in intelligent wireless sensors.

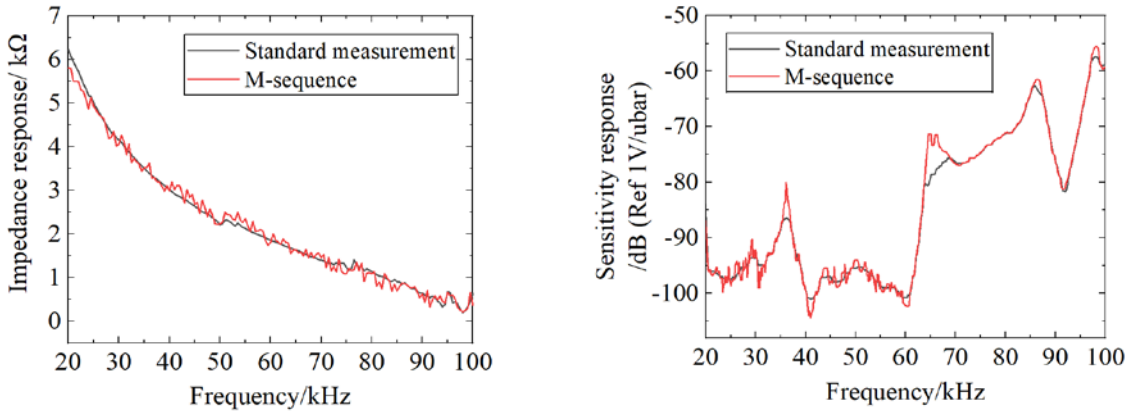

(a) (b)

Figure 3-28 The calibration results of M-sequence and standard measurement. (a) Impedance response curve. (b) Sensitivity response curve.

3.5 Brief Summary

Based on the research in Chapter 2, this chapter conducts a study on the intelligent upgrading of the vibration-AE fusion sensor. In response to practical detection requirements,

an intelligent wireless PCB module is developed based on the BLE SoC, and the basic architecture for edge computing of the fusion sensor is established. Additionally, a novel method for the rapid calibration of the impedance and sensitivity of the piezoelectric sensor, based on M-sequence signal excitation, is proposed for the first time. The specific conclusions are as follows:

1) An intelligent framework for the fusion sensor is proposed, and an intelligent wireless PCB module is designed and assembled. The module integrates functions such as wireless transmission, edge computing, measurement and storage, analog signal processing, and calibration circuits. Wireless functionality testing is conducted, and the results indicate that within an 8-meter range, the sensor data transmission rate remains above 1 Mbps, with the theoretical operating lifetime of a single battery estimated to be 4 years.

2) For the characteristics of vibration-AE fusion signals, a basic edge computing architecture based on MCU is proposed, covering feature extraction of AE, vibration, and fusion signals. The KISS FFT algorithm is used in embedded programming to efficiently extract vibration spectral features, while a Chebyshev-II filter is employed to extract AE pulse signals. Subsequently, the flight spectrogram, VPRPD diagram, and other analytical spectrograms are generated through statistical analysis.

3) A method for calibrating the impedance and sensitivity curves of piezoelectric sensors based on M-sequence signal excitation is proposed. The generation and calibration principles of the M-sequence are introduced, and the feasibility of the method is validated through circuit and finite element simulations. The method is applied to both commercial sensors and the developed wireless fusion sensors. The results show that the M-sequence method offers good calibration accuracy and stability. The M-sequence calibration process takes only a few milliseconds and consumes approximately 10 mW of power. It can be directly generated from binary pulse signals, with simple and rapid operation, providing reliable and stable results. This method offers a novel and efficient solution for the self-calibration of piezoelectric sensors.

4 Motion and PD Characteristics of Metal Particles Under PF Voltage and Mechanical Vibration

Metal particle defect inside GIS is a typical type of insulation defect associated with mechanical vibration. However, existing studies on particle detection have not adequately considered the combined effects of operational vibration and voltage. This chapter investigates the motion behavior and PD characteristics of metal particles in GIS under power-frequency voltage superimposed with mechanical vibration, reflecting actual operation conditions. A scaled 330 kV GIS experimental platform is designed and constructed to enable synchronous application of vibration and voltage excitations. Simulations and experiments verify the consistency of the model GIS with actual GIS in terms of vibration response and electric field distribution. Using the developed vibration-AE fusion sensor and a PD detector, measurements are conducted under power-frequency voltage alone and in combination with sinusoidal mechanical vibration, capturing both PD and vibration signals of particles with varying shapes, masses, and quantities. PRPD patterns, flight patterns, and discharge repetition rates are statistically analyzed. Finally, based on theoretical calculations, experimental results, and spectral characteristics, the motion behavior and PD characteristics of metal particles in GIS under combined voltage and vibration conditions are elucidated.

4.1 GIS Experimental Platform with PF Voltage and Mechanical Vibration Combined Excitation

1） Experimental GIS model

A scaled-down model of a 330 kV GIS is constructed for experiment, with a scale ratio of 4.4:1. Table 4-1 presents the structural and material parameters of the GIS model. Figure 4-1 (a) illustrates a schematic of the scaled model, which includes the filling/venting gas valve, GIS enclosure, barometer, glass insulator (for observation), busbar, and insulator. Figure (b) shows a physical image of the GIS model.

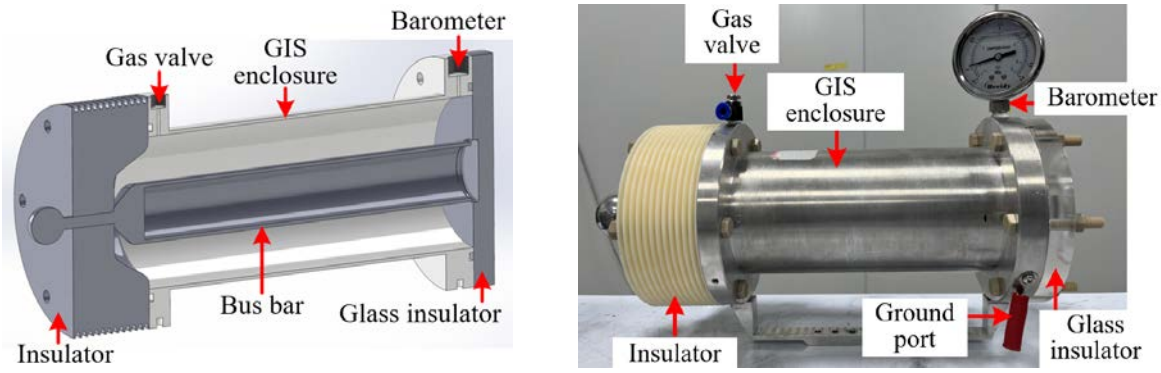

(a) (b)

Figure 4-1 GIS scaled-down model (a) The model diagram (b) The model photograph.

Table 4-1 Basic parameters of the GIS model

Name	value	Name	value
Inner radius/mm	49.32	GIS length/mm	200
Outer radius/mm	51.36	Busbar outer radius/mm	19.32
Scale ratio	4.4：1	SF_6 pressure/MPa	0.45
Metal material	Aluminum alloy	Insulator material	ABS and PMMA

2） Comparison of electric field distribution between the model and actual GIS

The line voltage of actual 330 kV GIS is 330 kV (effective value), corresponding to phase voltage and its peak of 190.5 kV and 269.4 kV. Therefore, the corresponding phase voltage and peak voltage of the scaled-down GIS model are 43.3 kV and 61.24 kV. Under 61.24 kV, the electric field distribution of the GIS model is as shown in Figure 4-2. The maximum field strength of 5.43 kV/mm occurs at the edge of the busbar end, exceeding the breakdown field strength of 3 kV/mm in air. In SF_6 gas at 0.45 MPa, the breakdown voltage is typically several times higher than in air, placing this value within the safe testing range[136]. The central region of the scaled model serves as the experiment area, with metal particles positioned on the inner wall below the central conductor.

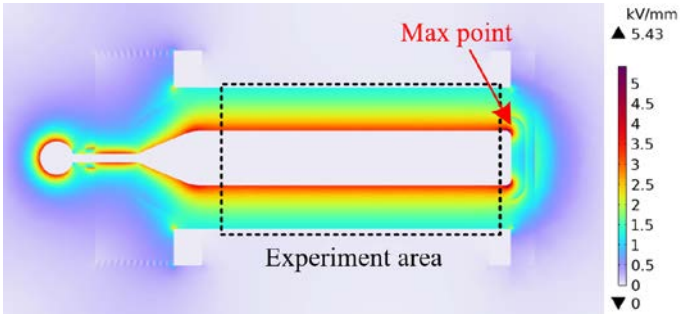

Figure 4-2 Electric field strength distribution of the GIS model under 61.24 kV voltage

Regarding the experiment area of the scaled GIS model, in order to verify that the model exhibits the same electric field distribution under 61.24 kV (phase voltage peak) as the actual 330 kV GIS does under 268.4 kV (phase voltage peak), simulations are conducted for both cases. Figure 4-3 (a) and (b) display the cross-sectional electric field strength of the scaled model and the actual GIS, indicating that the maximum field strength is at the surface of the central conductor, measuring 3.46 kV/mm and 3.44 kV/mm, respectively. The field strength decreases continuously from the central conductor surface to the inner wall of the GIS enclosure, with the minimum field strength at the inner wall of the cylinder being 1.3 kV/mm. This value is the maximum field strength experienced by metal particles on the inner wall of the GIS when they are stationary during operation. Figure 4-3 (c) and (d) show the radial field strength distribution curves of the scaled model and the actual GIS, where the horizontal axis represents the distance from the central conductor surface to the inner wall of the GIS enclosure. The field strength decreases rapidly starting from the central conductor, with a gradual decrease in the rate of field strength reduction as the distance increases. The two radial field strength distribution curves are almost identical.

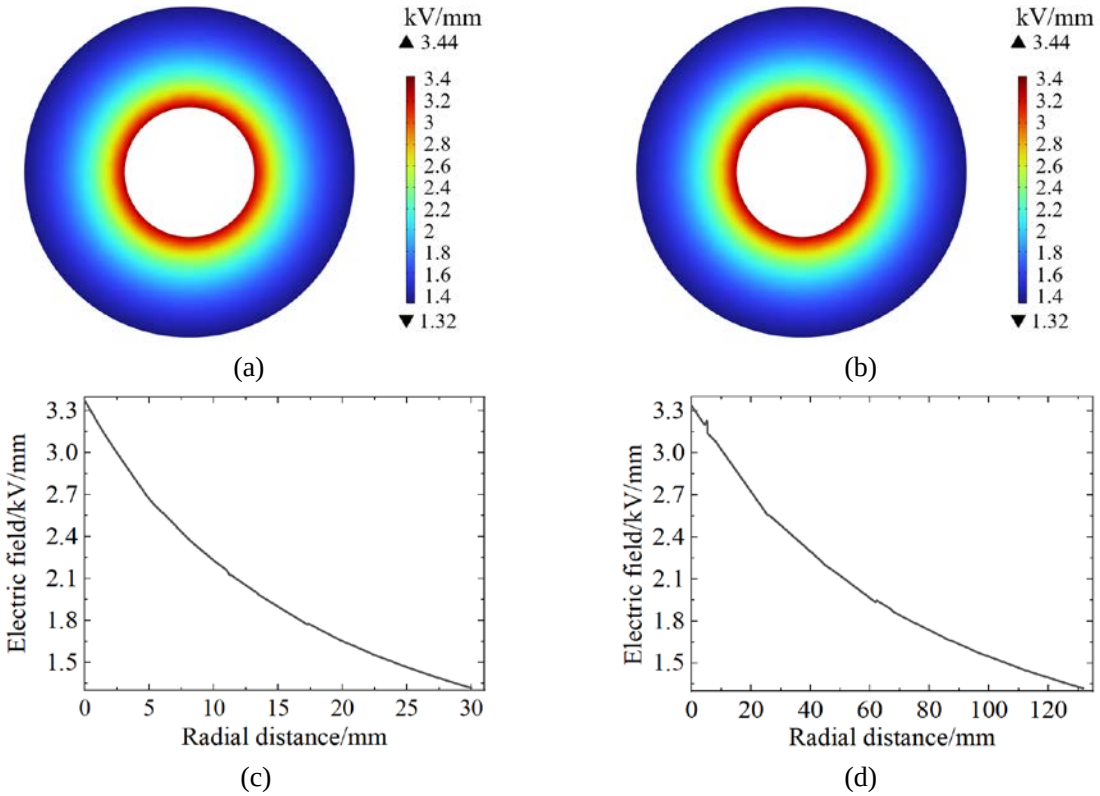

Figure 4-3 Comparison of field strength between the model and the actual GIS (a) Scaled-down model (b) Actual GIS (c) Radial distribution of field strength inside the model GIS (d) Radial distribution of field strength inside the actual GIS

3） Vibration mechanism of GIS and vibration loading on the GIS model

Currently, there is a preliminary consensus both domestically and internationally on the vibration mechanism of GIS. The prevailing view is that vibration is primarily caused by the contraction force of the contact surface current, the electromagnetic force of the enclosure's induced current within its own magnetic field, and magnetostrictive effects on the enclosure, all resulting from the current flowing through the central conductor. Additionally, GIS equipment includes coil-like components (such as PT, CT, etc.) that also generate vibration, mainly comprising winding vibration and core vibration. However, this aspect is not the focus of this study and will not be discussed herein.

(1) The contraction force of the contact surface current

In GIS equipment, the conductive circuit is not a single integral unit but rather assembled from multiple conductive structures. Within this setup, isolation switches, circuit breakers, and other switching devices have breaking contacts. These contact surfaces are not perfectly smooth, leading to point contact between the contacts. The current density of the conductor increases at the contact point, and the direction of the current lines is not perpendicular to the contact surface (but at an angle to its own magnetic field). Therefore, within the magnetic field generated by the central conductor, the deviation of the contact point from the current lines and the locally higher current density (current contraction) result in the generation of contraction forces, as shown in Figure 4-4.

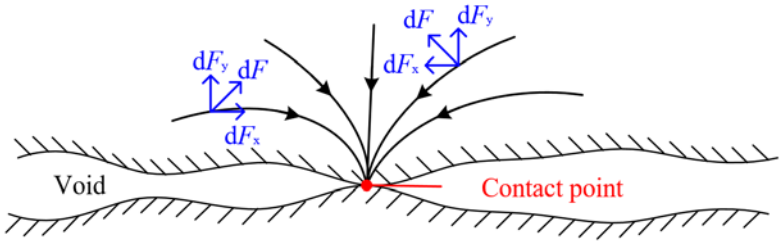

Figure 4-4 Contraction force at the point of the contact

The contraction force $\boldsymbol{F}$ can be represented by equations (4-1) and (4-2) as follows:

$$\boldsymbol{F} = \frac{\mu_0 I_0^2 \cos^2(wt)}{4\pi} \ln(\frac{d}{2r}) \tag{4-1}$$

$$r = \sqrt{\frac{\boldsymbol{F}_j}{\pi \xi H_b}} \tag{4-2}$$

where d is the diameter of the contact surface, μ_0 is the permeability of vacuum, r is the radius of the contact spot, $\boldsymbol{F}_j$ is the preloading force acting on the contacts, ξ is the material deformation coefficient, H_b is the Brinell hardness of the material. The magnitude of the electromagnetic force is directly proportional to the square of the current, independent of the current direction. Therefore, under power frequency current, contraction force varies at twice the power frequency (100 Hz).

(2) Electromagnetic force acting on the enclosure

The GIS equipment can be approximated as a hollow toroidal electromagnetic current transformer, with the central conductor as the primary side (one turn) and the enclosure as the secondary side (one turn). Therefore, when a large current flows through the central bus, a comparable level of induced current is generated on the enclosure with a certain thickness. Around the central conductor's current, there exists an alternating magnetic field. The induced current on the enclosure, under the influence of this magnetic field, experiences electromagnetic force, leading to regular vibration. Figure 4-5 illustrates the analysis of electromagnetic force acting on the enclosure of a three-phase segregated GIS cylinder.

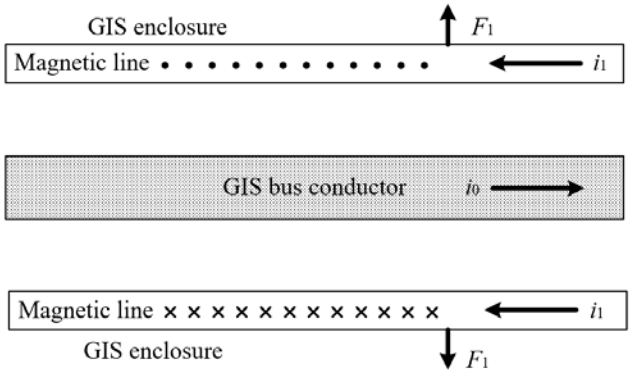

Figure 4-5 Direction of electromagnetic force on the three-phase separate GIS

Assuming the central conductor current is $i_0 = I_0 \cos(wt)$ and i_1 represents the eddy current in the enclosure (which is proportional to i_0), with the GIS enclosure radius being r,

and since the thickness of the enclosure is much smaller than the enclosure radius, the magnetic field at the enclosure can be considered uniform. Its value B_r can be expressed as:

$$\boldsymbol{B}_r = \frac{\mu_0 i_0}{2\pi r} = \frac{\mu_0 I_0 \cos(wt)}{2\pi r} \tag{4-3}$$

Subsequently, the electromagnetic force F acting on the unit area of the enclosure can be represented as:

$$\boldsymbol{F} = \boldsymbol{B}_r I_0 L = \frac{(\mu_0 \mu_r I_0)^2 SwL}{4\pi R_{\text{eq}} r} \sin(2wt) \tag{4-4}$$

where, R_{eq} is the equivalent resistance of the conductor, S is the unit area, μ_{r} is the permeability of vacuum. It is known that the GIS enclosure will undergo sinusoidal deformation (vibration) under the influence of electromagnetic force, with a vibration frequency of twice the power frequency (100 Hz).

(3) GIS enclosure magnetostriction

The phenomenon of magnetostriction is a mechanical deformation that occurs in materials under the influence of a magnetic field. When certain materials (usually ferromagnetic materials) are exposed to a magnetic field, their internal magnetic domains (small regions with consistent magnetic orientation) realign, resulting in minor changes in the material's length or volume. This change can be elongation, contraction, or others, depending on the material properties and the direction and intensity of the magnetic field. Research indicates that magnetostriction causes the GIS enclosure to vibrate at twice the power frequency, similar to the magnetostrictive vibration in transformer cores. In practice, transformer cores are typically made of highly ferromagnetic silicon steel sheets, whereas GIS equipment is made of aluminum alloy, which has lower ferromagnetic properties. Therefore, magnetostriction is considered a secondary cause of vibration in GIS enclosure.

In summary, according to relevant literature, it is evident that under normal condition, vibration are primarily at 100 Hz[137] (fundamental frequency). Mechanical defects can lead to an increase in the fundamental frequency amplitude and the appearance of harmonics at multiples of 100 Hz. The vibration amplitudes on the busbar section typically range from 0.5 μm to 10 μm, and with the severity of mechanical defects, the vibration amplitudes may be even larger[138].

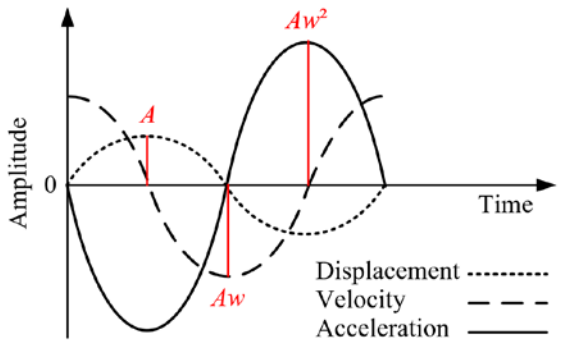

Figure 4-6 Relationship between GIS vibration displacement, velocity, and acceleration.

The relationship between vibration displacement y, velocity v, and acceleration a is illustrated in Figure 4-6, and can be represented by the following equation:

$$\begin{cases} y = A\sin(wt) \\ v = Aw\cos(wt) \\ a = -Aw^2\sin(wt) \end{cases} \tag{4-5}$$

where, w represents the angular frequency, A is the amplitude. It can be observed that when A=10 μm, the maximum amplitude of acceleration a reaches around 3.94 m/s² (which is 0.4 g). In this experiment, the vibration amplitudes are set at 0.1 g, 0.25 g, and 0.4 g.

In this research, a scaled-down GIS model is mounted on a vibration exciter to simulate the actual vibration of the GIS enclosure by applying controlled excitation. To validate the consistency of this method with the vibration of actual GIS, the vibration of both the actual GIS enclosure and the laboratory-scaled GIS model enclosure is measured and compared. Three-axis vibration sensors are placed on the GIS busbar section enclosure, and five measurement points are selected clockwise from top to bottom for vibration measurement. The comparison of the three-axis vibration signals from the five measurement points of the actual GIS equipment and the scaled model is shown in Figure 4-7.

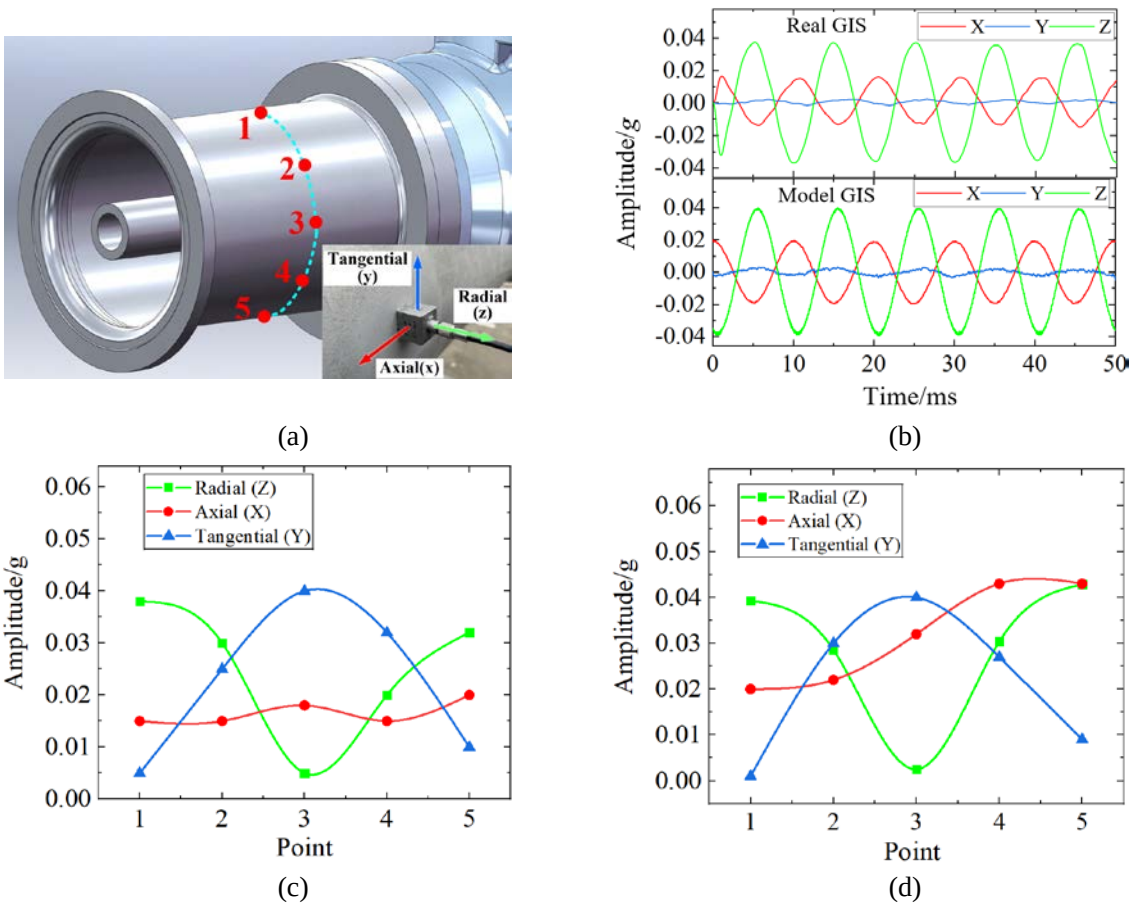

Figure 4-7 Comparison of vibration between the model GIS and the actual GIS (a) Vibration measurement points on the GIS enclosure (b) Vibration signals at point P1 (c) 100 Hz vibration at measurement points on the actual GIS enclosure (d) 100 Hz vibration at measurement points on the model GIS enclosure

Figure (a) illustrates the positions of 5 measurement points for the vibration of the GIS enclosure, where X, Y, and Z denote the axial, tangential, and radial vibrations on the surface of the GIS enclosure, respectively. In Figure (b), the comparison of the time-domain vibration signals at measurement point 1 between the actual GIS and the scaled model reveals that the predominant vibration in all three axes is a 100 Hz sine wave. Figures (c) and (d) show the variations in vibration amplitudes at the 5 measurement points on the enclosures of the actual GIS and the scaled model, demonstrating similar trends between the two. As the measurement points move downward, the radial vibration amplitude of the actual GIS enclosure decreases from 0.04 *g* to 0.05 *g* and then increases to 0.032 *g*. The axial amplitude gradually increases from 0.015 *g* to 0.02 *g*, while the tangential amplitude rises from 0.005 *g* to 0.04 *g* before decreasing to 0.01 *g*. In the model GIS, the radial vibration amplitude decreases from 0.04 *g* to 0.002 *g* before increasing to 0.043 *g*. The axial amplitude slowly rises from 0.02 *g* to 0.043 *g*, and the tangential amplitude increases from 0.001 *g* to 0.04 *g* before dropping to 0.01 *g*. This indicates the model GIS and the actual GIS enclosure exhibit similar vibration, confirming the feasibility of the vibration simulation in experiment.

4） Experimental platform

During the operation of actual GIS, the central bus conductor bears high voltage and large current. The high voltage creates high electric field strength inside the GIS, increasing the insulation performance requirements. The electromagnetic forces generated by the large current result in significant mechanical vibration of the enclosure.

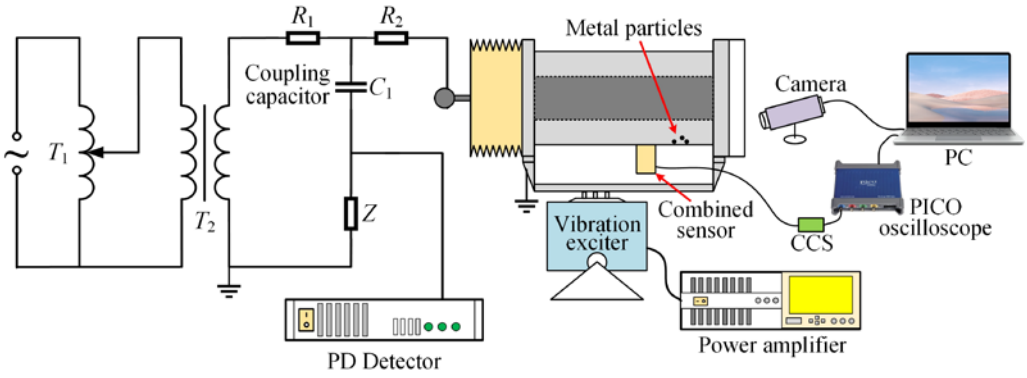

(a)

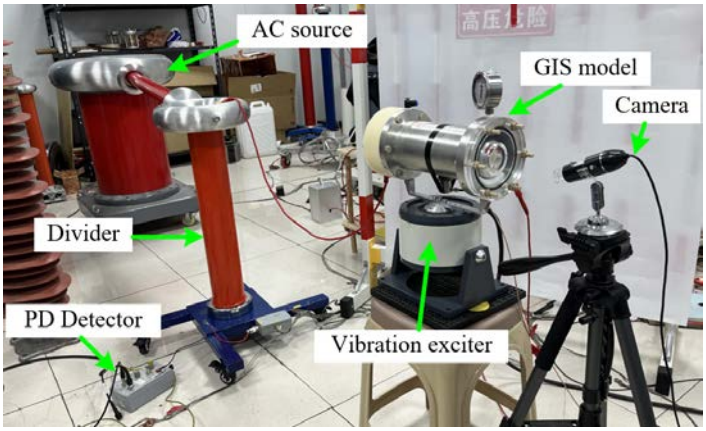

(b)

Figure 4-8 GIS model experimental platform. (a) Schematic diagram. (b) Physical image.

Figure 4-8 (a) depicts a schematic diagram of the GIS experimental platform with superimposed sinusoidal vibration of power frequency voltage (CCS means constant current source), and Figure (b) shows a physical image of the platform. The high-voltage AC power supply applies a variable amplitude sinusoidal high voltage (effective value 0 to 43.3 kV) to the bus conductor. The PD Detector detects PD on the platform with impedance measurement. The vibration exciter applies variable amplitude and frequency sinusoidal vibration to the entire GIS through a power amplifier, fixed beneath the center of gravity of the GIS model. The fusion sensor is fixed directly below the GIS model and connected to a PICO oscilloscope via a constant current source. A camera, aligned from the outside of the glass plate, captures images of the metal particle. A PC controls data acquisition from the oscilloscope and camera. Metal particles are put near the bottom area of the GIS enclosure close to the glass insulator to simulate particle defect. Additionally, the GIS is filled with SF_6 gas at a pressure of 0.45 MPa during the experiment.

To ensure vertical vibration, the vibration exciter should be fixed at the center of gravity of the model. The gravity center of the GIS model can be determined using the suspension method, as illustrated in Figure 4-9. One end of the GIS model is suspended using a line, allowing it to naturally hang down. The extension of this line is labeled as red line A. The other end of the test model is then suspended with a line, and the extension of this line is labeled as blue line B. The intersection point of lines A and B represents the model's gravity center. A line perpendicular to the support frame is drawn through this point, and the intersection point is identified as the supporting point C, which is the fixed point for the vibration exciter.

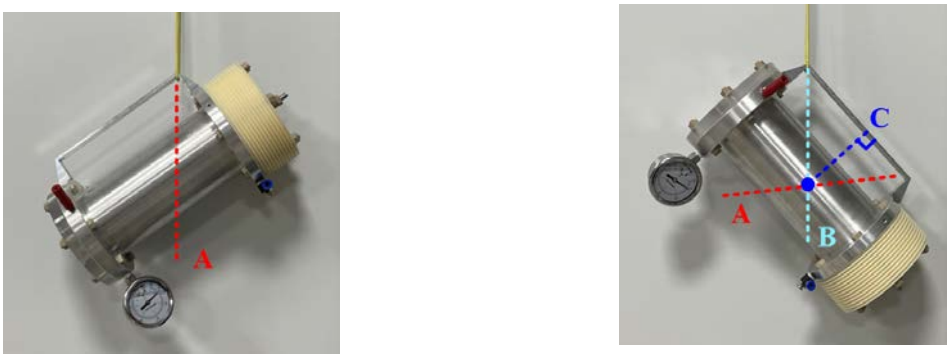

(a) (b)

Figure 4-9 Determination of the gravity center of the GIS model by suspension method. (a) First record. (b) Second record.

Theoretical force analysis of the motion characteristics of metal particle under the superposition of power frequency voltage and mechanical vibration is as follows: Figure 4-10 (a) and (b) depicts the force diagrams of metal particle inside the GIS when it is at rest and in flight. When stationary, the particle experiences the following forces: the support force from the GIS enclosure ($\boldsymbol{F}_S$), the electric field gradient force ($\boldsymbol{F}_{grad}$), the electric field force ($\boldsymbol{F}_q$), the combined force of gravity and buoyancy ($\boldsymbol{G}_1$), and the gas viscous drag force ($\boldsymbol{F}_{visc}$). When the particle is in motion, it no longer experiences the supporting force ($\boldsymbol{F}_S$).

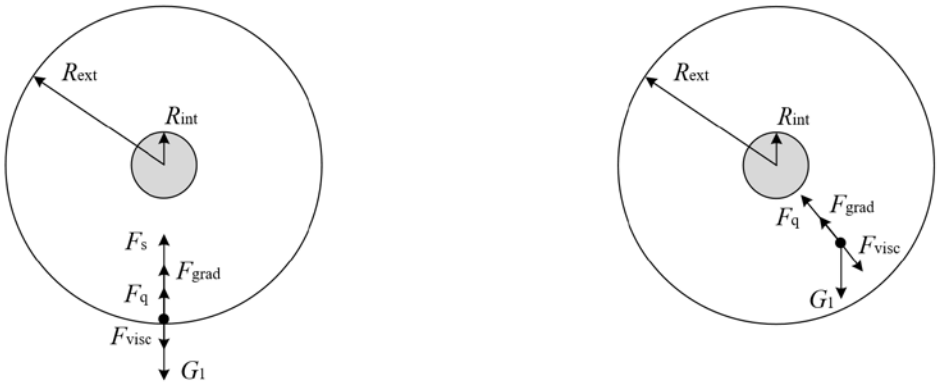

(a) (b)

Figure 4-10 Force analysis diagrams of metal particle in GIS. (a) Stationary particle. (b) Flying particle.

The combined force $\boldsymbol{G}_1$ of buoyancy $\boldsymbol{F}_\mathrm{f}$ of SF_6 gas on the metal particle and the particle's own gravity $\boldsymbol{G}$ can be represented as:

$$\boldsymbol{G}_1 = \boldsymbol{G} - \boldsymbol{F}_\mathrm{f} = \frac{4}{3}\pi r^3(\rho_\mathrm{AL} - \rho_{\mathrm{SF}_6})g \tag{4-6}$$

where, r stands for the particle radius, ρ represents density.

The most significant force acting on particles within GIS is the electric field force $\boldsymbol{F}_\mathrm{q}$, which is also the primary reason for particle jumping. The electric field force is dependent on the charge carried by the particle itself and the electric field strength at its position. The calculation method for the charge of particles of different shapes will be specifically elaborated in the following sections. The electric field strength E inside the GIS cylinder can be calculated with the following equation:

$$E = \frac{u}{r_x \ln(R_\mathrm{ext} / R_\mathrm{int})} \tag{4-7}$$

where, R_ext and R_int represent the inner radius of the GIS enclosure and the outer diameter of the bus conductor, respectively, r_x is the distance to the axis of the GIS; when calculating the field strength at inner wall, r_x equals R_ext; u is the function of the power frequency voltage.

Consequently, the electric field force F_q acting on the particle can be determined as:

$$\boldsymbol{F}_\mathrm{q} = kq_\pm E = kq_\pm \frac{u}{R_\mathrm{ext} \ln(R_\mathrm{ext} / R_\mathrm{int})} \tag{4-8}$$

where, k is the mirror charge correction factor. When the particle is far from the electric machine, k is 1; when the particle contacts the electrode or approaches a motor of the same polarity, k is 0.832. $q_\pm$ represents the charge of the particle, with the detailed calculation equations provided in the subsequent text.

The electric field gradient force is a force that acts on an electric dipole or a charged particle when these particles are in a non-uniform electric field. This force is related to the spatial variation (gradient) of the electric field. Specifically, when a particle is in a non-uniform electric field, the electric field strength varies at different positions. The electric

field gradient force will propel charged particles towards regions of stronger or weaker electric field strength (depending on the charge properties and polarity of the particles). For an electric dipole, the electric field gradient force guides it towards the position that maximizes the stability of the dipole. GIS enclosure is coaxial cylinder, with an uneven distribution of electric fields, radial gradient changes, and the electric field direction pointing towards the axis. The electric field gradient force $\boldsymbol{F}_{\text{grad}}$ acting on a particle on the inner surface of the GIS enclosure can be expressed as:

$$\boldsymbol{F}_{\text{grad}} = \frac{1}{2}\alpha \nabla E^2 \tag{4-9}$$

where α is the particle's polarizability, ∇E^2 represents the gradient of the square of the electric field strength. Typically, the electric field gradient force is related to the distribution of the electric field strength and the size of the particle. When the particle size is small, the electric field gradient force acting on it is generally very small.

Gas viscous drag is a resistance experienced by gas molecules on the surface of an object due to the shear stress applied to the object. It originates from the viscosity of the gas and the viscous forces between the object and surrounding gas molecules. This resistance is related to the gas viscosity and is a result of interactions between gas molecules and the surface of the object. It can be represented by the following equation:

$$\boldsymbol{F}_{\text{visc}} = 6\pi\eta r v \tag{4-10}$$

where η is the gas viscosity coefficient, v is the particle velocity, and the direction of $\boldsymbol{F}_{\text{visc}}$ is opposite to the direction of the particle's motion.

In conclusion, when the particle is at rest, it is in force equilibrium, and during the process of moving with the GIS enclosure, it satisfies the mechanical equation (4-11), where A_{p} is the vibration acceleration amplitude of the GIS enclosure. The condition for the particle to jump is when the support force $\boldsymbol{F}_{\text{s}}$ from the enclosure on the particle is zero. Once the particle jumps, the force equilibrium of the particle is disrupted. At this point, the particle itself has a certain velocity v, making the motion process more complex, and the fundamental mechanical equation becomes (4-12). Since the gas drag force $\boldsymbol{F}_{\text{visc}}$ and the electric field gradient force $\boldsymbol{F}_{\text{grad}}$ are relatively small compared to gravity, buoyancy, and electric field forces, these two values are omitted in the subsequent calculations.

$$\boldsymbol{G}_1 + \boldsymbol{F}_{\text{s}} + \boldsymbol{F}_{\text{q}} + \boldsymbol{F}_{\text{visc}} + \boldsymbol{F}_{\text{grad}} = mA_{\text{p}} \sin(wt + \varphi_0) \tag{4-11}$$

$$\boldsymbol{G}_1 + \boldsymbol{F}_{\text{q}} + \boldsymbol{F}_{\text{visc}} + \boldsymbol{F}_{\text{grad}} = m\boldsymbol{a} \tag{4-12}$$

The typical metal particles inside actual GIS equipment are shown in Figure 4-11. Research indicates that the predominant material of these metal particles found inside GIS is aluminum alloy. These particles are primarily linear, flaky, and irregularly shaped quasi-spherical particles with sizes (lengths) mainly concentrated within 8 mm. Under identical conditions, metal particles of different shapes exhibit variations in size structure,

resulting in differences in their charge amounts, electric field forces acting upon them, and viscous drag forces, leading to distinct PD characteristics. The vibration of GIS enclosure can influence the motion behavior of these particles and the characteristics of PD. Therefore, this study focuses on aluminum particles of linear, flaky, and spherical shapes with sizes under 8 mm. The research analyzes the differences in characteristics during the processes of particle jumping (initiation), stopping (cessation), and motion development from both the perspectives of mass and quantity.

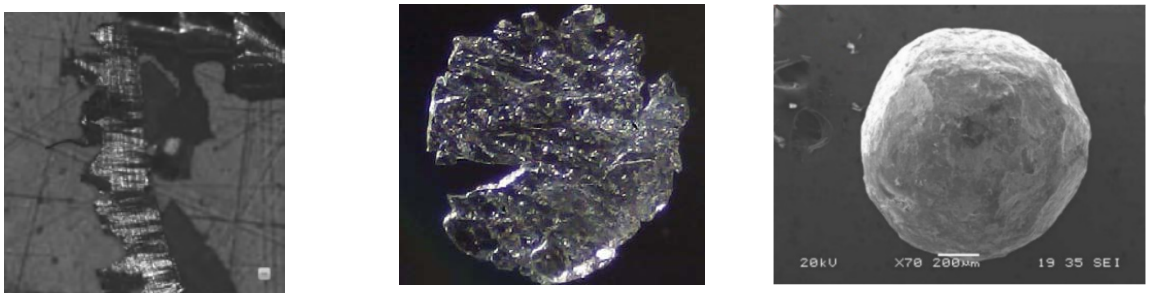

(a) (b) (c)

Figure 4-11 Typical particle shapes in practical GIS. (a) Linear. (b) Flaky. (c) Spherical.

The mass of metal particles is directly related to their size. Metal particles of the same shape but different masses exhibit variations in their motion states and discharge characteristics. They are also influenced differently by vibration. Focusing on the three types of particles mentioned above, this section selects particles with masses ranging from 1 to 16 mg in steps of 3 mg, totaling 6 different masses for research. The specific size information is shown in Table 4-2, and the experimental particles are shown in Figure 4-12.

Table 4-2 Sizes of the three types of particles in the experiment

Number	1	2	3	4	5	6
Mass/mg	1	4	7	10	13	16
Sphere *d*/mm	0.891	1.4144	1.7044	1.9196	2.0950	2.2452
Flake L*W/mm, Thickness=0.25mm	4.87*0.3	4.87*1.12	4.87*2.1	4.87*3	4.87*3.96	4.87*4.87
Line *l*/mm, *l*/*d*=6	2.5701	4.0798	4.9164	5.5371	6.0432	6.4762

*The diameters of the lines are 0.4283 mm, 0.68 mm, 0.82 mm, 0.92 mm, 1 mm, 1.08 mm, respectively.

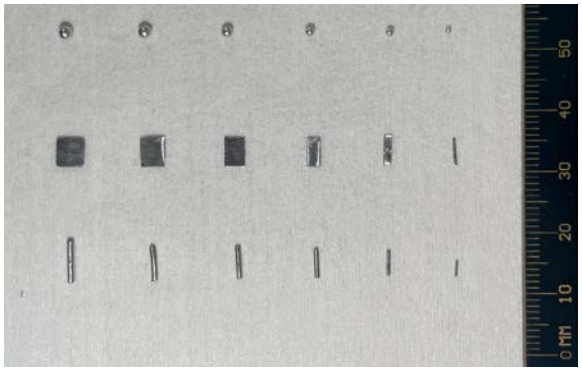

Figure 4-12 Three types of particles in the experiment.

The states of metal particles in GIS mainly include stationary and stable jumping. The vibration of the enclosure and the bus conductor voltage affect these two motion states of the particles. The electric field force acting on the particles is primarily and directly determined by the electric field strength, which is influenced by the applied voltage and the internal structure of the GIS. In this chapter, the electric field strength at the inner wall bottom of model GIS enclosure is taken as the descriptor of the electric excitation variable. Since it is an alternating current (AC) mode, the peak value of the alternating field strength is recorded.

4.2 Motion and PD Characteristics of Spherical Particles

4.2.1 Mass Effect on Motion and PD of Spherical Particles

1) The initiation and cessation characteristics of jumping

The jumping-stopping behavior of spherical particles in GIS typically adheres to the pattern illustrated in Figure 4-13. In this figure, the vertical axis represents the peak electric field strength on the bottom inner wall of the GIS enclosure. The voltage increase and decrease processes are carried out gradually in a step-wise way. When the field strength reaches the value of E_i (jumping initiation field strength), the spherical particle begins stable jumping. This field strength marks the minimum value required for the particle to take off from a stationary condition. As the field strength decreases, the particle, being in a state of stable jumping, sustains this state due to its inherent energy until the field strength drops to E_c (jumping cessation field strength), at which point the particle comes to a complete stop. This phenomenon represents the delayed cessation of hopping due to energy maintenance. Moreover, when the particle is stationary and the field strength lies between E_i and E_c, external impact vibration (such as circuit breaker or disconnector operations, etc.) may induce the particle to start jumping.

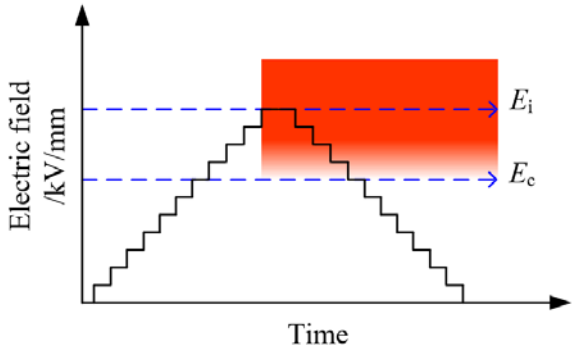

Figure 4-13 Pattern of initiation and cessation of jumping in spherical particles

Under different vibration conditions, the electric field strength for the jumping and stopping of spherical particles with varying masses inside GIS is depicted in Figure 4-14. As the vibration amplitude increases from 0 to 0.4 g, both the E_i and E_c of the spherical particles decrease. The E_i of S-2 to S-6 generally decrease by around 0.05 to 0.08 kV/mm with the increase in vibration. The E_i of S-1 without vibration is approximately 0.57 kV/mm. After applying a 0.2 g vibration, this value decreases to around 0.42 kV/mm and then gradually decreases to 0.39 kV/mm, showing the most significant drop. The E_c of all the spherical

particles are lower than their corresponding E_i, with the difference typically ranging between 0.05 to 0.08 kV/mm, showing a similar pattern of change as the E_i. From a mass perspective, for the heaviest particles, S-5 and S-6, which experience the relatively great gravitational force, a higher electric field force is required to induce jumping, resulting in the highest E_i. Conversely, the lightest particle, S-1, exhibits the lowest E_i. Overall, the magnitude of the E_c is lower than the E_i, with changes similar to those observed in the E_i.

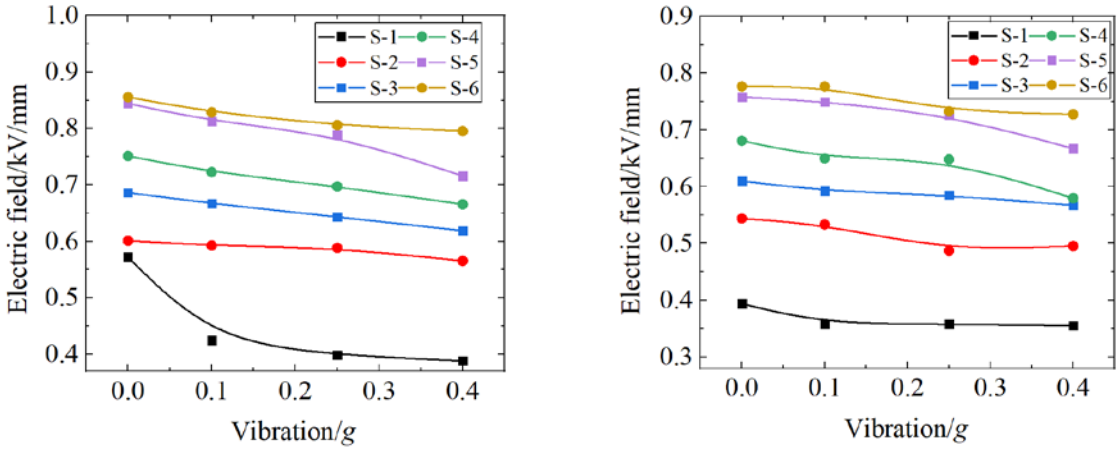

Figure 4-14 Jumping initiation and cessation field strengths of spherical particles with different masses. (a) Initiation field strength E_i. (b) Cessation field strength E_c.

The GIS vibration causes a decrease in the E_i and E_c of spherical particles, this can be calculated through force analysis. The force analysis for the jumping of spherical particles is illustrated in Figure 4-15 (a). The condition for a particle to jump is when the supporting force from the GIS enclosure is zero. When there is no vibration on the GIS, the particle's combined force ($\boldsymbol{G}_1$) of gravity and buoyancy equals to the supporting force, and the condition for the particle to jump is when the peak AC electric field force is greater than or equal to the $\boldsymbol{G}_1$, as shown in formula (4-13). When there is vibration in the GIS, the supporting force for the particle varies. According to the previous analysis, the particle is mainly influenced by the vibration force of the GIS enclosure $\boldsymbol{F}_{\text{GIS-V}}$, the electric field force $\boldsymbol{F}_q$, and combined force $\boldsymbol{G}_1$. The enclosure vibration frequency is 100 Hz, and the electric field force frequency is also 100 Hz, so the GIS enclosure vibration and the electric field force direction may be either parallel or opposite. When they are parallel, if the GIS vibrates upward along with the electric field force, the condition for the particle to jump is when the sum of the electric field force amplitude and the vibration force amplitude is greater than or equal to the weight. When they are in opposite directions, as the GIS vibrates downward until the peak, due to the inertia, the particle is in a weightless state as it is not connected to the GIS enclosure. The inertia causes the particle to have an upward acceleration relative to the GIS enclosure, and at this point, the electric field force is upwards. Therefore, the condition for the particle to jump is still when the sum of the electric field force amplitude and the vibration acceleration amplitude is greater than or equal to the weight, as shown in Equation (4-14).

This characteristic can also be analyzed from an energy perspective. When the particle

is stationary, the vibration force of the GIS $\boldsymbol{F}_{\text{GIS-V}}$ enclosure imparts a certain initial velocity to the particle, giving it a specific momentum. When the electric field force (providing potential energy) reaches a certain level, the particle's energy reaches the jumping energy, requiring less potential energy than when there is no vibration. In conclusion, the presence of GIS vibration leads to a decrease in the electric field force $\boldsymbol{F}_{\text{q}}$ required for the particle to jump, resulting in a decrease in the jumping electric field strength. Similarly, the stopping electric field strength of the particle also decreases.

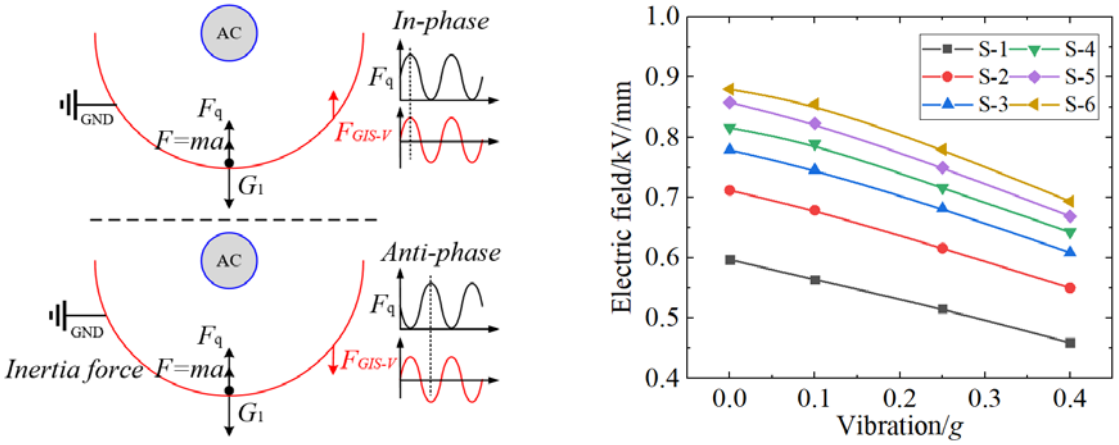

(a) (b)

Figure 4-15 Theoretical calculation of spherical particle E_{i}. (a) Force analysis for jumping. (b) Calculation result of E_{i} under different vibration.

Equation (4-15) can be used to acquire the electric field strength in coaxial cylindrical structures (GIS enclosure), where U is the electrode voltage, R_1 and R_2 are the outer diameter of the GIS bus conductor and the inner diameter of the enclosure, and x is the distance from the center. In this thesis, x=R_2 is used for calculating the electric field strength on the inner wall of the GIS enclosure. Equation (4-16) describes the calculation formula for the charge of spherical particles, where r represents the radius of the sphere, ε_0 and ε_{r} are the vacuum permittivity and the relative permittivity of SF_6, respectively. Equation (4-17) represents the vibration acceleration of the GIS, where A is the amplitude, taking values of 1 m/s^2, 2.5 m/s^2, and 4 m/s^2 (0.1 g, 0.25 g, and 0.4 g, respectively), with a frequency f of 100 Hz.

$$\boldsymbol{F}_{\text{q}} = kE_0 q_{\text{Sphere}} = \boldsymbol{G}_1 \tag{4-13}$$

$$\boldsymbol{F}_{\text{q}} + m_{\text{Sphere}}\boldsymbol{a} = \boldsymbol{G}_1 \tag{4-14}$$

$$E_0 = \frac{U\sin(100\pi t)}{x\ln(\frac{R_2}{R_1})} \tag{4-15}$$

$$q_{\text{Sphere}} = \frac{2}{3}\pi^3 r^2 \varepsilon_0 \varepsilon_r E_0 \tag{4-16}$$

$$\boldsymbol{a} = A\sin(2\pi ft) \tag{4-17}$$

Figure 4-15 (b) shows the theoretical calculation results of the variation in the jumping

initiation field strength E_i of spherical particles with GIS vibration. As the vibration amplitude increases, the E_i of the particles decreases. Additionally, with a decrease in the mass of the sphere, the E_i also decreases. This pattern of change aligns closely with the experimental results.

2) Development characteristics of jumping

After the spherical particle jumps, the jumping state is depicted in Figure 4-16. They stably jump back and forth in regions 1, 2, and 3 along the enclosure wall. The sphere initiates the jump from region 1, where vertical jumping is most active, resulting in the highest jumping height within this region. As the sphere jumps to regions 1 and 3, vertical jumping becomes less active, while horizontal jumping becomes more prominent. This phenomenon is attributed to the conversion of kinetic energy into potential energy. From force perspective, the horizontal component of the normal electric field force pulls the sphere back towards the center position, thus reducing the vertical component of the normal electric field force.

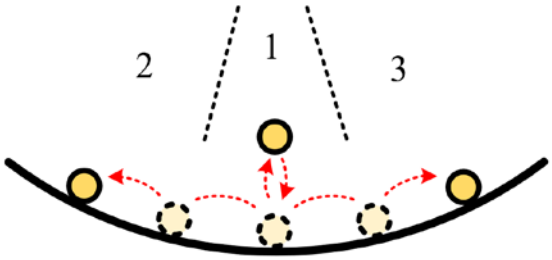

Figure 4-16 Motion modes of spherical particle

The discharge repetition rate of particles refers to the number of discharges per unit time. A higher value indicates higher PD density, resulting in less time spent airborne for each particle jump. It also to some extent reflects the particle's jumping height. After the particles jump, under low voltage conditions (peak electric field strength on the inner wall surface of GIS is approximately 0.9 kV/mm), the relationship between the discharge repetition rate of particles with different masses and the applied vibration is shown in Figure 4-17 (a). As the vibration magnitude increases from 0 to 0.4 *g*, the discharge repetition rates of particles S-1 to S-5 decrease gradually from 68, 65, 61.5, 56, 53 times per second to 58.9, 56.2, 52.5, 46, 40 times per second. Particle S-6, being a sub-millimeter particle, exhibits the lowest discharge repetition rate, ranging around 20-23 times per second.

These results indicate that particles with larger mass or size have slightly higher discharge repetition rates and lower jumping heights. This phenomenon occurs because particles are primarily influenced by both electric field forces and gravity. Under the same low electric field conditions, particles with greater mass experience a shorter duration of upward resultant force, leading to minimal jumping heights. The frequent collisions between vibrating GIS and particles increase the particles' kinetic energy, resulting in a slight increase in their flight height. Consequently, the flight time increases, causing a decrease in the discharge repetition rate compared to no vibration. Particles with smaller mass experience a longer duration of upward resultant force, showcasing more active motion, higher flight heights, and longer flight times. This implies fewer contacts with the GIS enclosure, making

the influence of GIS vibration on their motion almost negligible.

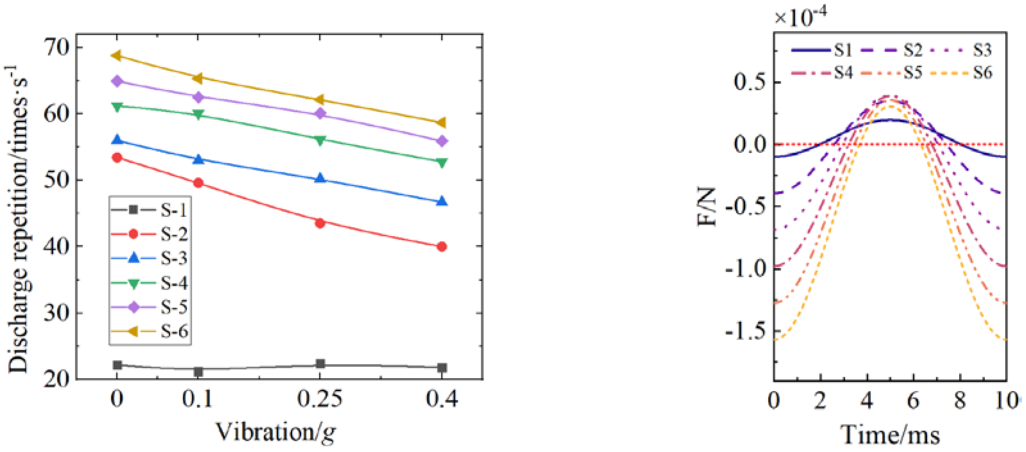

(a) (b)

Figure 4-17 Relationship between particle discharge repetition rate and GIS vibration. (a) Discharge repetition rate. (b) Resultant force.

Figure 4-17 (b) displays the resultant force on spherical particles of different masses during a single cycle (100 Hz). The positive direction indicates the force towards the GIS bus conductor, with an area denoted as A1, while the opposite direction represents the force towards the GIS enclosure, with an area denoted as A2. These two areas are approximately used to represent the time the particles spend in flight and in contact with the ground. Using Equation (4-18), the proportion of flight time to total time, denoted as r_{flight} (flight time ratio) for particles of each mass, can be calculated. The results are shown in Table 4-3.

$$r_{\text{flight}} = \frac{\text{A1}}{\text{A1} + \text{A2}} \tag{4-18}$$

Table 4-3 Flight time ratio r_{flight} of spherical particles with different masses

Item	S-1	S-2	S-3	S-4	S-5	S-6
r_{flight}	0.749	0.457	0.295	0.19	0.12	0.072

It is known that particle S-1 has the highest flight time ratio, at 0.749, followed by decreasing values for the subsequent particles, with S-6 having the smallest value at only 0.072. This indicates that under the same electric field strength, particles with smaller mass have longer flight times, lower discharge repetition rates, and exhibit more intense motion.

When the alternating voltage increases to the rated operating voltage, the alternating electric field strength within the GIS rises, reaching an peak value of 1.3 kV/mm on the inner wall. This results in particles experiencing greater resultant forces, leading to active motion states for spherical particles of all masses. Flight pattern can be used to describe the motion characteristics of particles, with a typical distribution showing multiple triangular peaks. Figure 4-18 illustrates the flight patterns of spherical particles S-2, S-4, and S-6 under the rated field strength. It is observed that for S-2, the maximum flight time is around 80 ms, displaying a tri-peak pattern with an AE signal peak of approximately 60 mV. For S-4, the maximum flight time is about 60 ms, showing a semi-bimodal pattern with an AE signal

peak of around 90 mV. S-6 exhibits a maximum flight time of 40 ms, displaying a bimodal pattern with an AE signal peak of approximately 120 mV. It is evident that under the same conditions, particles with larger mass carry more charge, resulting in larger AE signals generated by collision discharge, albeit with shorter flight times.

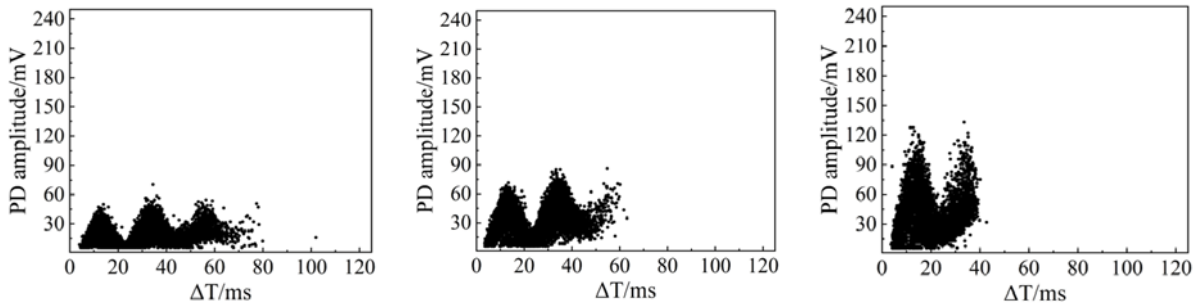

Figure 4-18 Flight patterns of spherical particles under rated field strength. (a)S-2. (b)S-4. (c)S-6.

In the jumping process of particles, the electric field strength plays a primary role as it is the fundamental cause of jumping. As the electric field strength continues to increase, the flight time of particles will prolong; however, there exists a limiting value. This limit is associated with the size of the GIS, where a closer distance between the bus conductor and the enclosure implies a lower limit for the flight height of the particles.

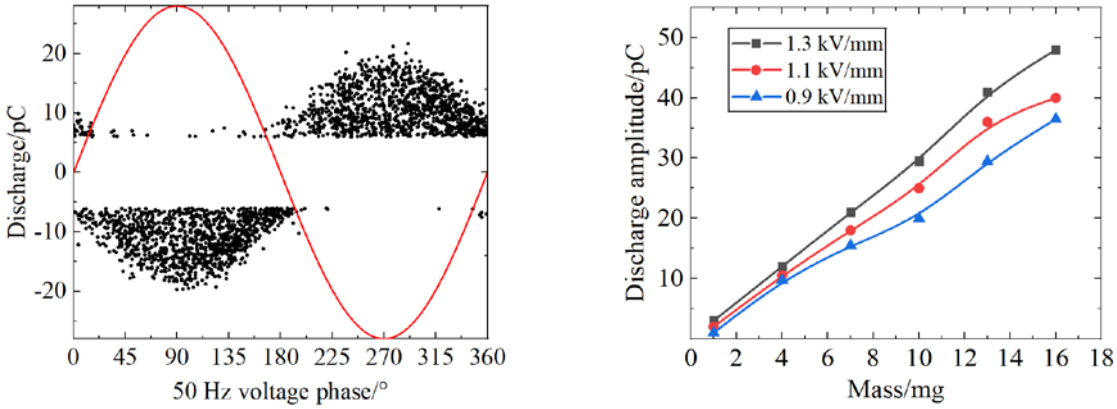

Figure 4-19 Discharge statistics of spherical particles.(a) PRPD pattern of spherical particles. (b) Maximum apparent discharge quantities of spherical particles with different masses.

Figure 4-19 (a) shows the PRPD pattern of a 10 mg spherical metal particle under an electric field strength of 0.9 kV/mm, measured using the PD detection device. The pattern exhibits a sinusoidal banded envelope with strong symmetry and full-phase discharge distribution. As the particle carries induced charges, its discharge polarity is opposite to the voltage polarity of the GIS busbar, and the amplitude is proportional to the amplitude of the sinusoidal voltage. PRPD patterns of spherical particles with different masses under different field strengths show similar distributions, but the maximum apparent discharge varies. For ease of analysis, the maximum apparent discharge from the spectra is taken as the statistical value. The maximum apparent discharge, Q_{amax}, for particles of different masses is depicted in Figure 4-19 (b). With mass increasing from 1 mg to 16 mg, at 0.9 kV/mm, Q_{amax} gradually

rises from 1.2 pC to 36.5 pC; at 1.1 kV/mm, Q_{amax} increases from 2.1 pC to 40 pC; and at 1.3 kV/mm, Q_{amax} increases from 3 pC to 48.5 pC. Additionally, the difference in discharge quantities caused by the field strength variation also increases. The relationship between spherical particle mass and maximum apparent discharge approximates a linear trend.

4.2.2 Quantity Effect on Motion and PD of Spherical Particles

This section takes S-4 as an example to illustrate the motion characteristics and PD features of spherical particles under the superposition of sinusoidal vibration with the power frequency voltage, with particle quantities set at 1, 5, and 9 in the experiment.

The experiment shows that as the electric field strength approaches the threshold for particle jumping, the influence of mechanical vibration caused a single particle to move first. When this particle approaches the others, it distorts the electric field, resulting in electrostatic repulsion due to carrying similar charges. Additionally, it might collide with other particles, initiating their movement. This avalanche-like phenomenon indicates the occurrence of the short-board effect in particle jumping when multiple particles are involved. The particle with the lowest jumping threshold triggers the jumping of other particles upon collision. Similarly, in this case, the stopping threshold requires all particles to come to a halt for the system to stabilize. This leads to an increase in the system's instability.

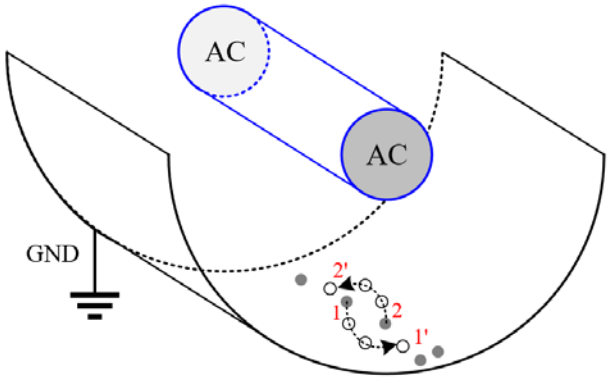

Figure 4-20 Motion characteristics of multiple spherical particles.

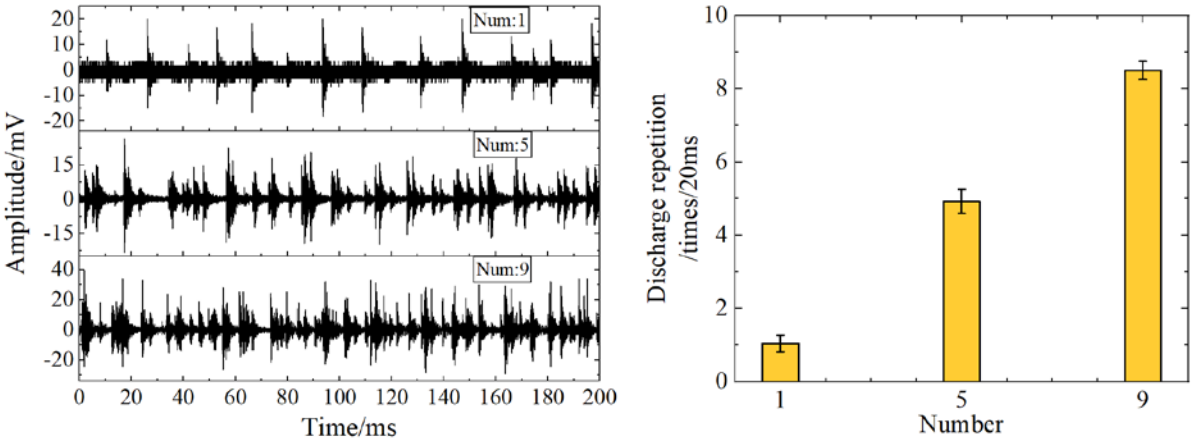

(a) (b)

Figure 4-21 PDAE of multiple spherical particles. (a) Time-domain signals. (b) Discharge repetition rate.

At rated voltage, all particles stably jump. It is observed that when two particles

approach each other, there is a noticeable repulsive force that separates them, as illustrated in Figure 4-20. For instance, spheres 1 and 2 will move around each other to positions 1' and 2', respectively. This behavior arises because during the jumping process, all particles carry the same polarity charge, leading to mutual repulsion due to like charges. As a result, the probability of pairwise particle collisions is not high, although there remains a certain likelihood of collisions occurring.

The time-domain signal and discharge repetition rates of spherical particles with different quantities are depicted in Figure 4-21. Since the jumping state is primarily influenced by the 50 Hz alternating voltage (field strength), the time unit is set at 20 ms. It can be observed that as the number of spherical particles increases, the discharge repetition rate significantly rises. For quantities of 1, 5, and 9 particles, the corresponding average discharge repetition rates are 1.04, 4.92, and 8.5 times per 20 ms, respectively, which are approximately proportional to the number of particles.

4.3 Motion and PD Characteristics of Flaky Particles

4.3.1 Mass Effect on Motion and PD of Flaky Particles

1) The initiation and cessation characteristics of jumping

The jumping and stopping characteristics of flaky particles essentially follow the pattern shown in Figure 4-22, which is similar to that of spherical particles, but with some differences. When a flaky particle is stationary and lying flat, it has a larger contact area with the GIS grounded enclosure, resulting in a more stable structure. Compared with a spherical particle in the same condition, a greater electrostatic force is required to make it take off, and the stable jumping initiation field strength E_i is higher. When the field strength reaches E_i, the flaky particle takes off and stands upright completely. At this point, it is closer to the busbar conductor, so its own charge increases rapidly. During the jumping process, the flaky particle has a higher self-charge than the spherical particle and experiences a greater electrostatic force. Therefore, it can maintain the jumping state more effectively, and its jumping cessation field strength E_c is slightly lower than that of the spherical particle.

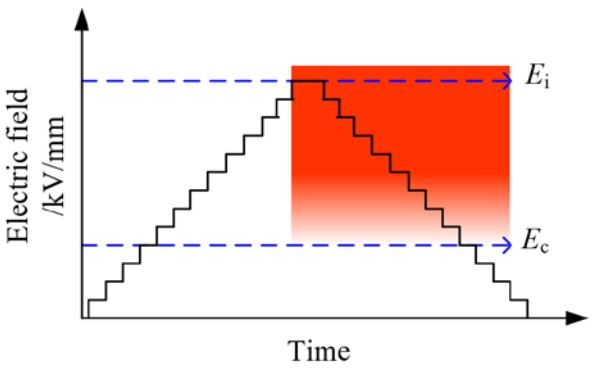

Figure 4-22 Pattern of initiation and cessation of jumping in flaky particles.

Figure 4-23 shows the changes in E_i and E_c of flaky particles with different masses and thickness of 0.25 mm under various GIS vibration conditions. The shape of the flaky

particles has a certain influence on the E_i and E_c field strengths. The width-to-length ratios of sheet 3 to sheet 6 range from 0.44 to 1. Within this range, the particles are in the shape of squares or relatively wide rectangles, which have better stability, making it more difficult for them to take off and resulting in greater dispersion. The E_i values are basically distributed between 0.8 and 1.1 kV/mm. The width-to-length ratios of F-2 and F-1 are 0.23 and 0.062, respectively, gradually approaching the shape of linear particles. The E_i values decrease progressively, being around 0.7 kV/mm and 0.55 kV/mm, respectively.

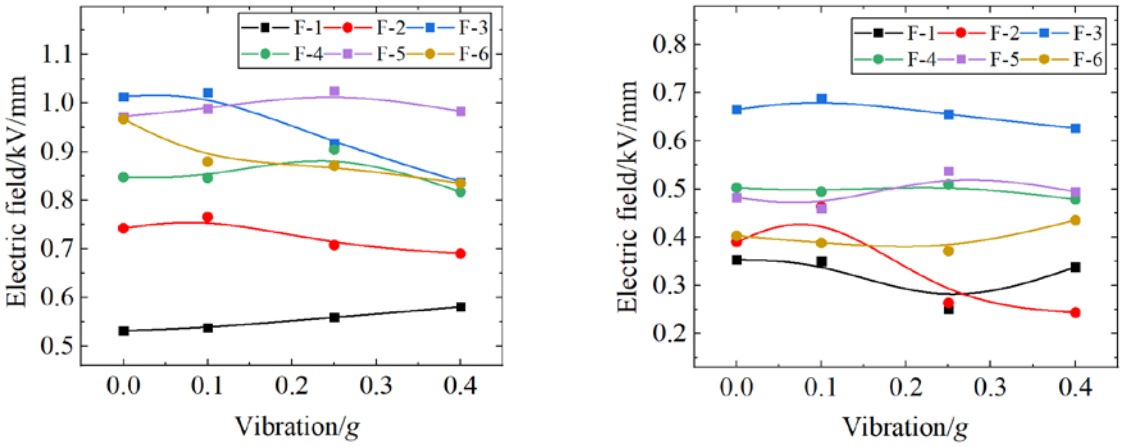

Figure 4-23 Jumping initiation and cessation field strengths of flaky particles with different masses. (a) Initiation field strength E_i. (b) Cessation field strength E_c.

When a flaky particle is stationary and lying flat, the amount of charge it carries under the influence of an electric field can be calculated using Equation (4-19). When calculating the take-off field strength, the shape factor of the flaky particle must be considered. This is because the flaky particle has a larger area (compared to spherical and linear particles), resulting in a relatively higher adsorption force (or static friction) with the GIS enclosure. Meanwhile, the electric field force has a lower density of action, making it more difficult for the localized unit area to generate enough tensile force (electric field force) to overcome the resistance. Geometric shape factor is commonly used to quantitatively describe the shape characteristics of objects, measuring their compactness or symmetry. The shape factor can affect the behavior of objects in various physical processes. In this paper, as the mass of the flaky particles decreases, their shape gradually changes from a square to a quasi-linear form. Therefore, a geometric shape factor *ks* is introduced to characterize the influence of the shape of the flaky particles, as shown in Equation (4-20), where *W*, *L*, and *D* represent the width, length, and thickness of the flaky particle, respectively. When the particle is a square plate, k_s=1; when the shape is close to a line, k_s≈0. Equation (4-21) describes the charge carried by the flaky particle when it is standing upright and jumping. Equations (4-22) and (4-23) represent the take-off conditions for a flaky particle when GIS enclosure is stationary and vibrating, respectively.

$$q_{\text{Flake}} = -\varepsilon_0 \varepsilon_r W L E_0 \tag{4-19}$$

$$k_s = \frac{4WL}{(W+L)^2} \tag{4-20}$$

$$q'_{\text{Flake}} = \frac{\pi\varepsilon_0\varepsilon_r L^2 E_0}{\ln\left(\frac{2L}{\sqrt{WD/\pi}}\right)-1} \tag{4-21}$$

$$\boldsymbol{F}_q / k_s = \frac{kq_{\text{Flake}}E_0}{k_s} = \boldsymbol{G}_1 \tag{4-22}$$

$$\boldsymbol{F}_q / k_s + (1-k_s)\times m_{\text{Flake}}\boldsymbol{a} = \boldsymbol{G}_1 \tag{4-23}$$

Figure 4-24 (a) shows the theoretical calculation results of the jumping initiation field strength E_i of flaky particles with different masses (shapes) as a function of vibration. It can be seen that the E_i of F-3 to F-6 are basically in the range of 0.83–0.96 kV/mm, and the effect of vibration on them is almost negligible. The E_i of F-2 is slightly lower, gradually decreasing from 0.73 kV/mm to 0.68 kV/mm with increasing vibration. The E_i of F-1 is the lowest, decreasing from 0.45 kV/mm to 0.39 kV/mm with increasing vibration. The experimental results of the E_i of flaky particles are generally consistent with the calculated results in terms of trends, but the former are slightly higher. This is because in practice, there are small and difficult-to-quantify adsorption forces, static friction forces, and gas resistances. These resistances can cause the practical E_i to be slightly higher than the calculated results. Moreover, in the experimental results, the take-off field strengths of F-3 to F-6 have large dispersion and unordered changes (as shown in Figure 4-24 (b)). This is due to the complex conditions in the experiment, where the force states of the particles are constantly changing. When the field strength reaches around the E_i value, the force imbalance occurs randomly. Once it occurs, the particles may take off.

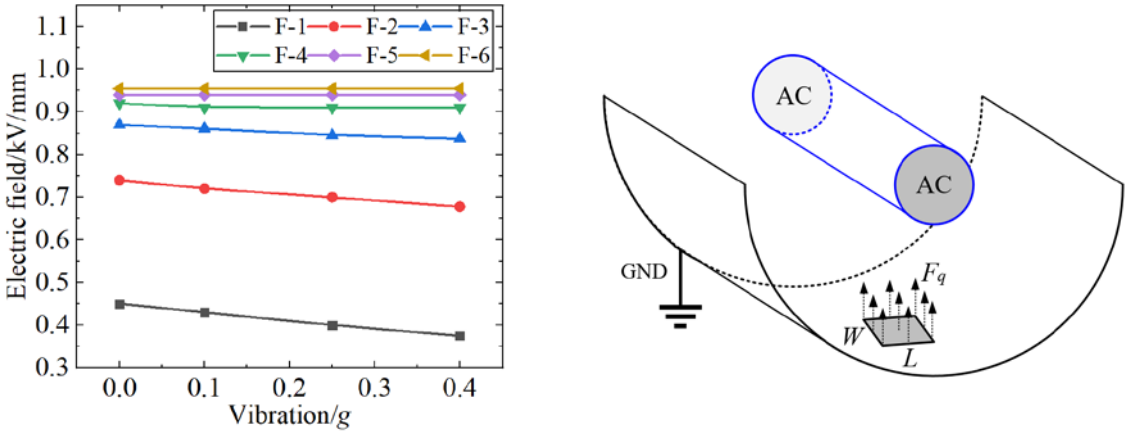

(a) (b)

Figure 4-24 Theoretical calculation of the jumping initiation field strength of flaky particles. (a) Jumping initiation field strength E_i. (b) Force analysis for jumping.

2) Development characteristics of jumping

After the flaky particles take off, their jumping states are shown in Figure 4-25, and there are mainly three states depending on the magnitude of the applied voltage. For State-1,

when the voltage is low, the flaky particles stand upright and jump slightly at the bottom of the GIS inner wall, accompanied by rotational motion along their own normal direction. This is because during the jumping process, the charge on the particles tends to accumulate at the sharp edges of the flaky particles. The different charges at these locations result in uneven electric field forces, causing the particles to rotate continuously. For State-2, as the voltage increases, the flaky particles begin to jump through the space between the ground and the busbar conductor. When the voltage continues to rise, State-3 occurs, where the particles occasionally jump near the busbar conductor. Discharge signals generated at the busbar conductor can easily be detected by PD detector as extremely large discharge signals (reaching hundreds or even thousands of pC). However, since PDAE signal needs to propagate through SF_6 gas or insulators to reach the fusion sensor, and both materials cause attenuation of AE signal, the fusion sensor on the outer surface of the GIS enclosure have difficulty detecting discharge signals near the busbar conductor. The reasons for State-2 and State-3 are that the electric field force acting on the flaky particles is much greater than their own weight. The time during which the resultant force on the particles points towards the conductor occupies a large proportion of the entire sinusoidal period (as indicated by the red line in Figure 4-25 (b)), which is sufficient to attract the particles to the vicinity of the conductor and cause discharge. When the resultant force points towards the ground for a short time (as indicated by the black line in Figure 4-25 (b)), the particles return to the GIS inner wall, which is the reason for the State-2. When the electric field force is even greater, the particles do not have enough time to return to the GIS inner wall during the time when the resultant force points towards the ground and are instead attracted back to the conductor repeatedly, which is the reason for State-3.

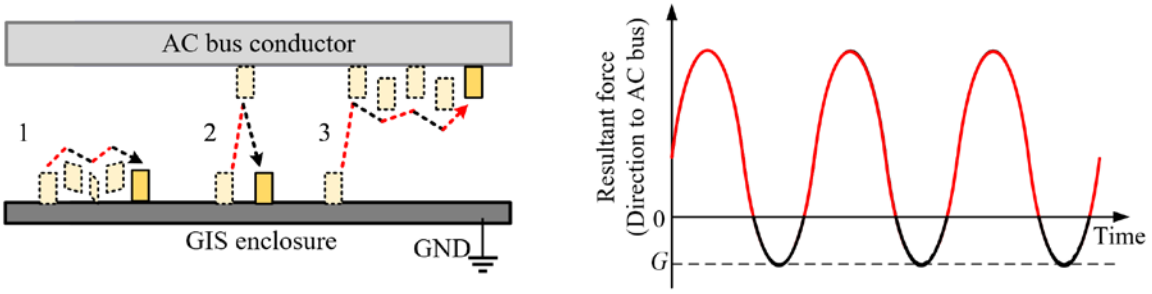

(a) (b)

Figure 4-25 Three jumping stages of flaky particles. (a) Three motion modes of flaky particles. (b) Schematic diagram of resultant force.

At a lower electric field strength of 0.9 kV/mm, the variation in discharge repetition rate of flaky particles with different masses as GIS vibration increasing is shown in Figure 4-26 (a). It can be seen that the discharge repetition rates of F-1 and F-2 remain almost unchanged with vibration, stabilizing at around 18 and 24, respectively. The discharge repetition rate of F-3 decreases slightly from 31 to 27. For F-4, the discharge repetition rate drops significantly from 41.5 to 32. The discharge repetition rates of F-5 and F-6 are nearly the same, decreasing from around 43 to around 37. The discharge repetition rate, which reflects the frequency of particle jumping and discharge, indicates the intensity of

the jumping state. A higher repetition rate suggests that the particle has a smaller jumping amplitude and less active motion, while a lower repetition rate implies a larger jumping amplitude and more intense motion. As the GIS vibration increases, the originally less active particles F-4 to F-6 become more active, with a noticeable decrease in discharge repetition rate. In contrast, the originally more active particles F-1 and F-2 are less or not affected by the vibration. On the other hand, under the same conditions, the discharge repetition rate increases with the increase in particle mass, indicating a decrease in the resultant force on the particles, which is similar to spherical particles. From the perspective of shape, F-4 to F-6 have similar shapes, all being square plates with a width-to-length ratio above 0.6, and their discharge repetition rates are close. In contrast, F-1 and F-2 have a width-to-length ratio below 0.4, with shapes gradually approaching that of linear particles, resulting in increased intensity of motion.

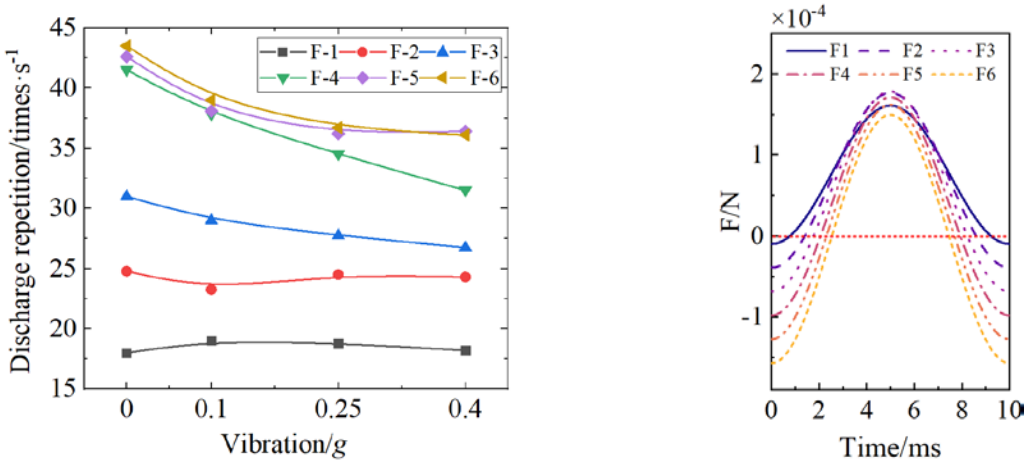

(a) (b)

Figure 4-26 Relationship between particle discharge repetition rate and GIS vibration. (a) Discharge repetition rate. (b) Resultant force.

Figure 4-26 (b) shows the comparison of the resultant forces on flaky particles with different masses within a single sinusoidal period (10 ms). The calculated results of the ratio r_{flight} are shown in Table 4-4. The value for F-1 is the highest at 0.984, and it decreases with increasing particle mass, with the value for F-6 being the lowest at 0.48.

Table 4-4 The flight time ratio r_{flight} of flaky particles with different masses

Item	F-1	F-2	F-3	F-4	F-5	F-6
r_{flight}	0.984	0.913	0.815	0.705	0.59	0.48

Under the rated field strength (peak value 1.3 kV/mm at bottom of the GIS inner wall), the flight patterns of flaky particles F-2, F-4, and F-6 are shown in Figure 4-27. There are some scattered points of discharge near the busbar conductor in the figure. However, since the actual GIS is large in size and it is difficult for such scattered points to appear, the influence brought by these scattered points is ignored here. It can be seen that the longest flight time of F-2 is about 105 ms, presenting an approximately five-peak characteristic, with the AE signal peak being about 90 mV; the maximum flight time of S-4 is 90 ms, presenting

a four-peak characteristic, with the AE signal peak being about 145 mV; the maximum flight time of S-6 is about 70 ms, presenting an approximately three-peak characteristic, with the AE signal peak being about 190 mV. It is known that under the same conditions, the larger the mass (and thus the area) of the flaky particles, the greater the charge they carry, and the larger the AE signal generated by collision discharge. However, the flight time is shorter. The overall trend is similar to that of spherical particles, but the changes are more pronounced and the motion is more intense.

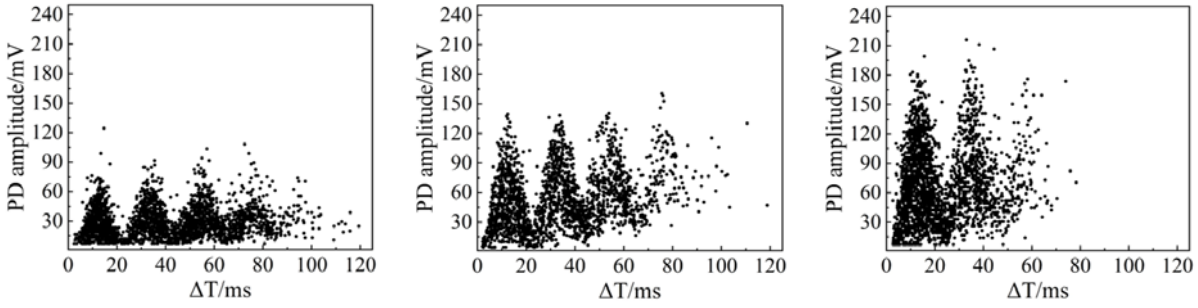

Figure 4-27 Flight patterns of flaky particles under rated field strength. (a) F-2. (b) F-4. (c) F-6.

Figure 4-28 (a) shows the PRPD pattern of a 10 mg flaky metal particle under an electric field strength of 0.9 kV/mm, it is similar to that of the spherical particle, also exhibiting a banded distribution with a phase opposite to the voltage. The maximum apparent discharge quantity Q_{amax} of flaky particles with different masses under different electrical field strength is shown in Figure 4-28 (b). The trend of the maximum apparent discharge quantity varying with the mass of the flaky particles is basically the same under the three different field strengths. As the mass increases from 1 mg to 16 mg, Q_{amax} gradually rises from 110 pC to 450 pC at 0.9 kV/mm, from 128 pC to 515 pC at 1.1 kV/mm, and from 160 pC to 580 pC at 1.3 kV/mm. Moreover, the difference in discharge quantity caused by a field strength change of 0.2 kV/mm is essentially constant (about 30 pC) for particles of different masses, except for the square flaky particle with a mass of 16 mg, where the difference is the largest (about 50 pC). The relationship between the mass of the flaky particles and the maximum apparent discharge quantity is approximately linear.

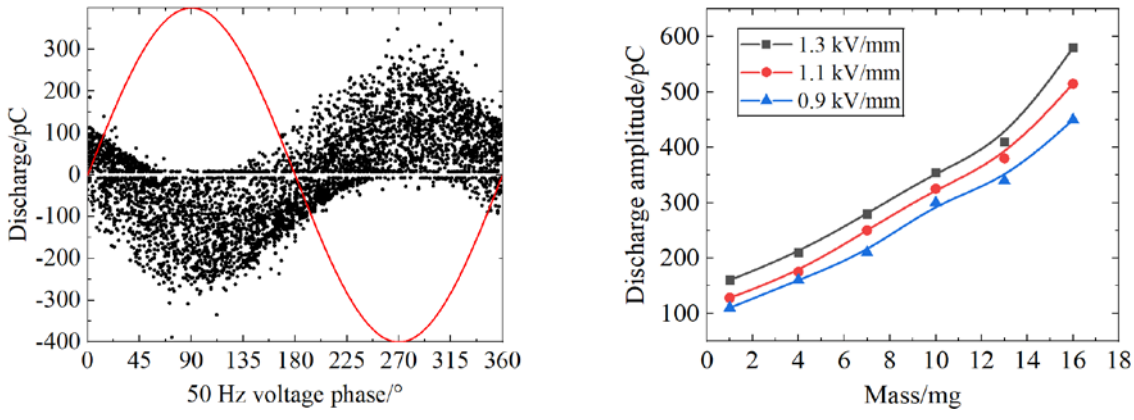

Figure 4-28 Discharge statistics of flaky particles.(a) PRPD pattern of flaky particles. (b) Maximum apparent discharge quantities of flaky particles with different masses.

4.3.2 Quantity Effect on Motion and PD of Flaky Particles

This section takes F-4 as an example to illustrate the motion and PD characteristics of flaky particles under power-frequency voltage and sinusoidal vibration conditions, with the number of particles set at 1, 5, and 9. When flaky particles move inside the GIS, they could adhere to the surface of the basin insulator. This can lead to local field strength distortion and charge accumulation on the surface, which physically reduces the insulation strength of the insulator and makes it highly susceptible to surface discharge. Due to electrostatic induction, when the busbar conductor is positively charged, negative charges accumulate on the side of the particle closer to the busbar; when the busbar conductor is negatively charged, negative charges accumulate on the side of the particle closer to the GIS grounded enclosure. Therefore, the particle can be approximately regarded as a dipole. It is known that regardless of the polarity of the conductor rod voltage, it exerts an attractive force (electric field force) on the particle, although the magnitude varies with the AC field strength. This also explains that the frequency of the electric field force (100 Hz) is twice that of the power frequency. The motion of multiple flaky particles inside the GIS is shown in Figure 4-29:

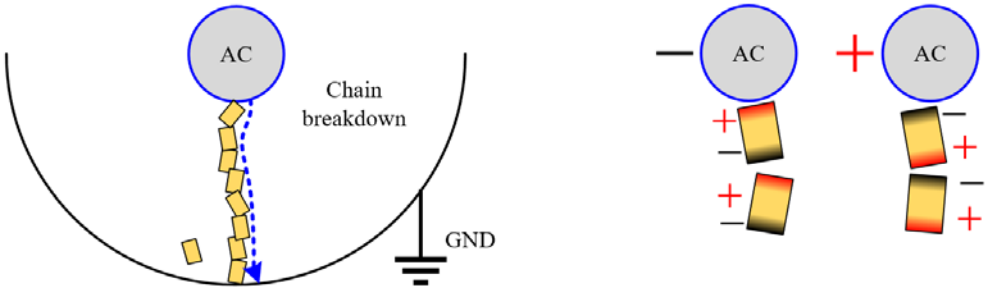

(a) (b)

Figure 4-29 Motion characteristics of the multiple flaky particles. (a) Chain breakdown. (b) Charge distribution.

where particles at the same horizontal level exert repulsive forces on each other, while particles at different heights exert attractive forces. Therefore, when the number of particles reaches a certain level, they move very actively under high field strength. At this time, multiple particles have a probability of forming a chain-like breakdown by connecting end-to-end, leading to a short circuit, which is dangerous to the safety of the equipment.

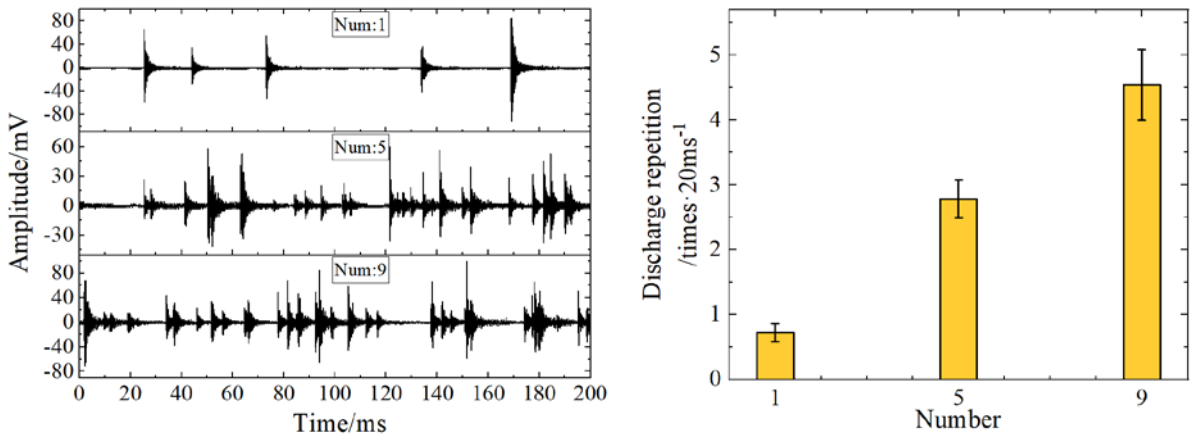

(a) (b)

Figure 4-30 PDAE of multiple flaky particles. (a) Time-Domain signals. (b) Discharge repetition rate.

The time-domain discharge signals and statistics of the discharge repetition rates for different numbers of flaky particles are shown in Figure 4-30. As the number of particles increases, the discharge pulses become gradually denser. Statistics show that the discharge repetition rates for 1, 5, and 9 flaky particles are 0.7, 2.78, and 4.54 per 20 ms, respectively. The number of particles is approximately twice the discharge repetition rate.

4.4 Motion and PD Characteristics of Linear Particles

4.4.1 Mass Effect on Motion and PD of Linear Particles

1) The initiation and cessation characteristics of jumping

Figure 4-31 illustrates the fundamental jumping and stopping characteristics of linear particles. When a linear particle is stationary and lying flat, it makes line contact with the GIS grounded enclosure, which provides a certain degree of stability. Therefore, under the same conditions, its jumping initiation field strength E_i is slightly higher than that of spherical particles (point contact) but slightly lower than that of flaky particles (surface contact). After taking off, the linear particles jumps vertically, similar to flaky particles, and its charge increases sharply comparing to lying state. When the field strength is reduced, the linear particle's contact with the GIS enclosure is only at one end, making it less stable than flaky particles. When the voltage drops to the $E_{i\text{-}c}$ value, there is a probability that the particle will fall over. At this field strength, the particle cannot take off from its lying position, leading to premature stoppage. However, there is also a probability that it will continue jumping until the field strength decreases to jumping cessation field strength E_c, at which point the electric field force is no longer sufficient to support the linear particle to jump. Whether a linear particle falls or continues jumping at the $E_{i\text{-}c}$ field strength depends on the condition of the particle's end surface and the rate at which the voltage decreases. The smoother the end surface and the faster the voltage drop, the more likely the particle is to fall over. Conversely, a rougher end surface and a slower voltage decrease make the particle less likely to fall.

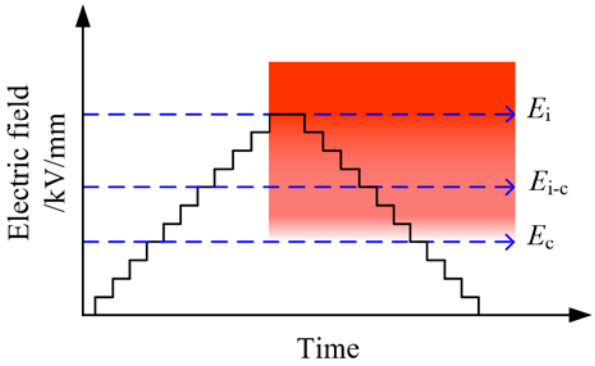

Figure 4-31 Patterns of initiation and cessation of jumping in linear particles.

Figure 4-32 (a) shows the changes in E_i and E_c of linear particles with different masses under various GIS vibration conditions. As vibration increases, the E_i of linear particles continuously decreases. The E_i of L-6 is the highest, decreasing from 0.97 kV/mm to 0.84

kV/mm, with the most significant drop. L-3, L-4, and L-5 all experience a decrease of about 1.1 kV/mm. L-2 decreases from 0.785 kV/mm to 0.7 kV/mm, while L-1 has the lowest E_i, dropping from 0.635 kV/mm to around 0.51 kV/mm. From the perspective of particle mass, the E_i increases with the increase in mass (size) of the linear particles. The E_i of the heaviest L-6 is about 1.65 times that of the lightest L-1, indicating that smaller linear particles are easier to take off.

Figure 4-32 (b) illustrates the variations of $E_{i\text{-}c}$ and E_c for linear particles. The upper six lines correspond to the $E_{i\text{-}c}$, which is generally lower than the E_i and has a similar trend. The higher the particle mass, the higher the E_c value, but it slightly decreases with vibration. This is because as GIS vibration increases, it imparts a certain amount of kinetic energy to the linear particles, making them more likely to maintain the "slight and stable jumping" before stopping. When the field strength continues to decrease to a level that cannot sustain the slight and stable jumping state, the particles lies down. The lower six curves correspond to the E_c, which is generally in the range of 0.32–0.48 kV/mm. The trend is not obvious, but it indicates that linear particles have a probability of maintaining continuous motion at lower field strengths, and GIS vibration could decrease E_c.

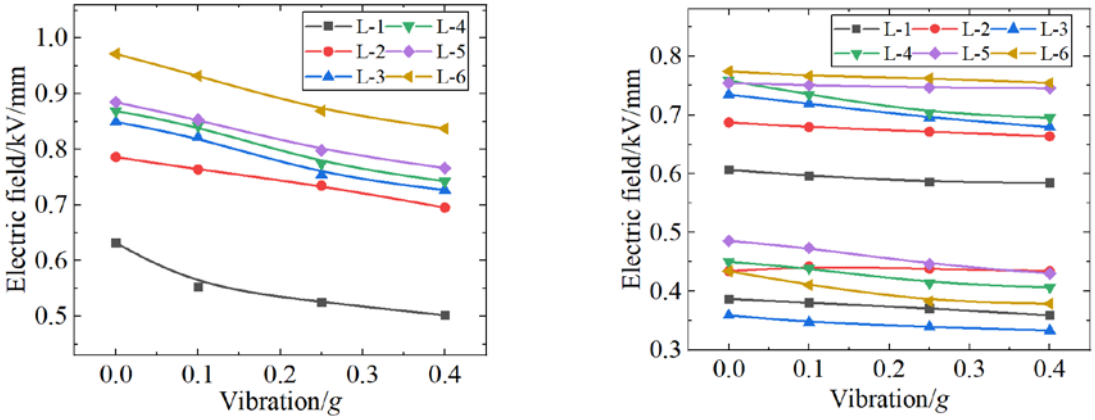

Figure 4-32 Jumping initiation and cessation field strengths of linear particles with different masses. (a) Initiation field strength E_i. (b) Cessation field strength E_c.

The above phenomena are related to the shape of the linear particles. The take-off process of linear particles is shown in Figure 4-33 (a). Initially, they lie flat on the GIS enclosure, with a distance to the busbar similar to that of spherical particles. As the electric field strength increases, the charge accumulation on the linear particles can be expressed by Equation (4-24), similar to spherical particles. The GIS vibration reduces the E_i of linear particles. When the electric field force is sufficient, one end of the line particle starts to rise first. During the standing process, the charge accumulation rate gradually increases until the particle stands upright and begins to jump. When standing upright, the charge on the linear particles can be expressed by Equation (4-25), where r_L is the radius of the linear particles and L is its length, the other variables refer to the Equation (4-16) of spherical particles. Calculations show that for the same linear particles, the charge and the electric field force when standing upright are about three times those when lying flat and stationary. Similar to

spherical particles, the E_i of linear particles in the absence and presence of GIS vibration can be calculated by Equations (4-26) and (4-27), respectively.

Figure 4-33 (b) shows the calculated E_i of linear particles, which has a trend and magnitude that are approximately the same as the experimental results.

$$q_{Line} = 2\pi\varepsilon_0\varepsilon_r r_L L E_0 \tag{4-24}$$

$$q'_{\mathrm{Line}} = \frac{\pi\varepsilon_0\varepsilon_r L^2 E_0}{\ln(\frac{2L}{r_L}) - 1} \tag{4-25}$$

$$\boldsymbol{F}_q = kq_{\mathrm{Line}}E_0 = \boldsymbol{G}_1 \tag{4-26}$$

$$\boldsymbol{F}_q + m_{\mathrm{Line}}\boldsymbol{a} = \boldsymbol{G}_1 \tag{4-27}$$

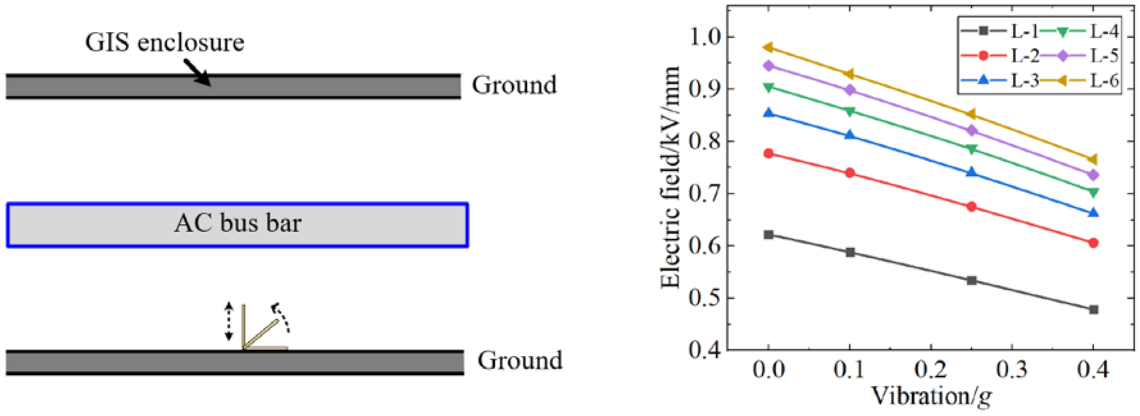

(a) (b)

Figure 4-33 Theoretical calculation of the jumping initiation field strength of flaky particles. (a) Force analysis for jumping. (b) Jumping initiation field strength.

2) Development characteristics of jumping

As shown in Figure 4-34, the jumping behavior of linear particles is similar with that of flaky particles, following three stages.

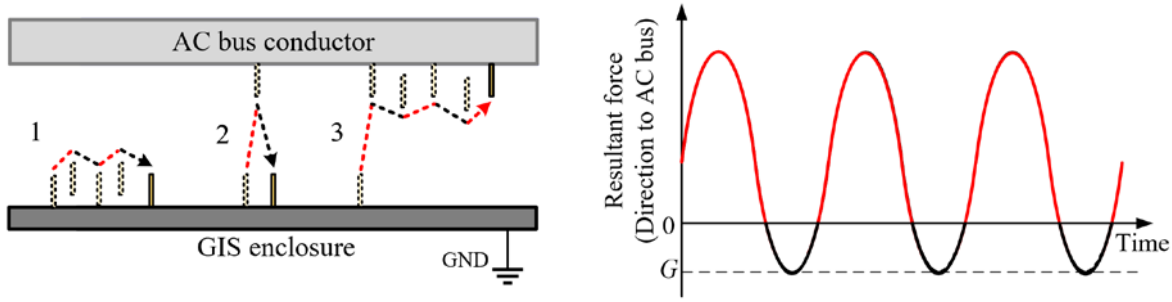

(a) (b)

Figure 4-34 Three jumping stages of linear particle. (a) Motion modes of linear particle. (b) Schematic diagram of resultant force.

Stage-1: At low voltage, the resultant force is low, and the particles jump slightly at the bottom of the GIS inner wall. Stage-2: As the voltage increases, the resultant force increases,

and the jumping amplitude of the particles increases until they jump through the space between the busbar conductor and GIS enclosure. Stage-3: At high voltage, the resultant force is large, and the particles often jump around the conductor, exhibiting a "firefly" phenomenon similar to flaky particles. At this time, due to the attenuation effect of SF_6 gas and insulators on AE signals, the PDAE signal of particles near the conductor attenuate significantly when propagating to the GIS enclosure, making it difficult for the fusion sensor to detect them.

Figure 4-35 (a) shows the discharge repetition rate statistics of linear particles at a lower field strength (0.9 kV/mm). The repetition rates of linear particles of various masses are basically in the range of 21~30 times per second, which is more intense than the jumping of spherical particles. This is because the electric field force is greater when linear particles jump vertically, resulting in a larger resultant force (see Figure 4-35 (b)).

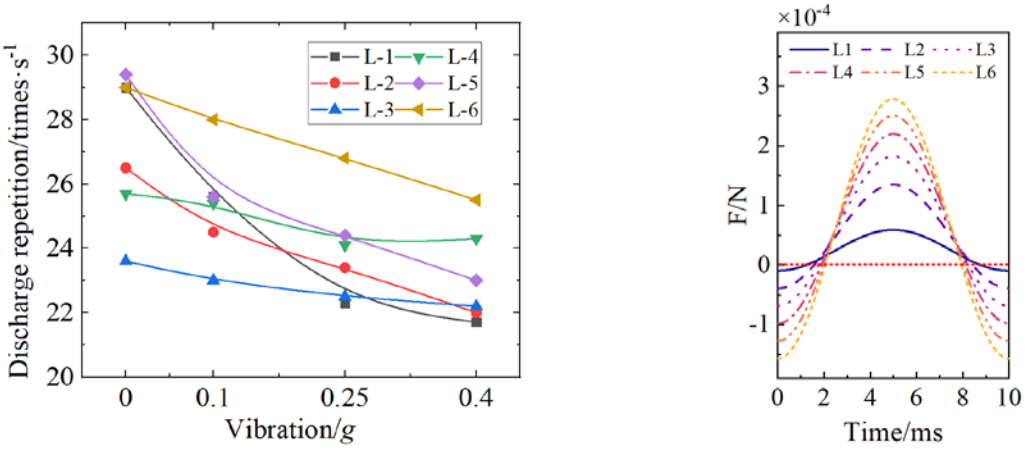

(a) (b)

Figure 4-35 Relationship between particle discharge repetition rate and GIS vibration. (a) Discharge repetition rate. (b) Resultant force.

The calculation results of the flight time ratio r_{flight} are shown in Table 4-5. The ratio for L-1 is the highest at 0.941, and it gradually decreases with decreasing mass, with the ratio for L-6 being the lowest at 0.709. However, it is still higher than the ratio for all spherical particles (see Table 4-3). This indicates when the flight time ratio is above around 0.6, the discharge repetition rate is relatively low, generally around 25 times per second. Besides, at lower field strengths, the vibration of the GIS slightly reduces the discharge repetition rate of linear particles.

Table 4-5 The flight time ratio r_{flight} of linear particles with different masses

Item	L-1	L-2	L-3	L-4	L-5	L-6
r_{flight}	0.941	0.872	0.818	0.78	0.742	0.709

Figure 4-36 shows the flight patterns of linear particles L-2, L-4, and L-6 under the rated field strength. It is known that the longest flight time of L-2 is about 105 ms, with an approximate five-peak distribution and an AE signal peak of about 80 mV. The longest flight time of L-4 is about 90 ms, presenting a four-peak characteristic and an AE signal peak of about 120 mV. The longest flight time of L-6 is about 70 ms, presenting a three-peak

characteristic and an AE signal peak of about 180 mV. The overall trend is similar to that of flaky particles, but the AE amplitude is slightly smaller.

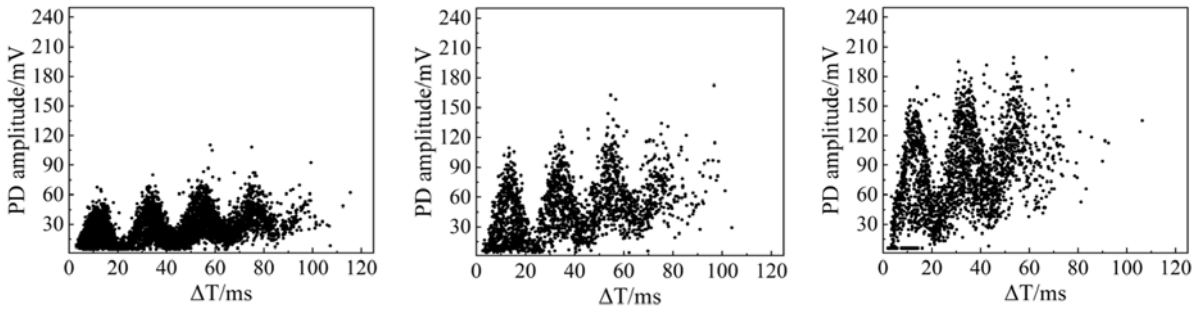

Figure 4-36 Flight patterns of linear particle under rated field strength. (a) L-2. (b) L-4. (c) L-6.

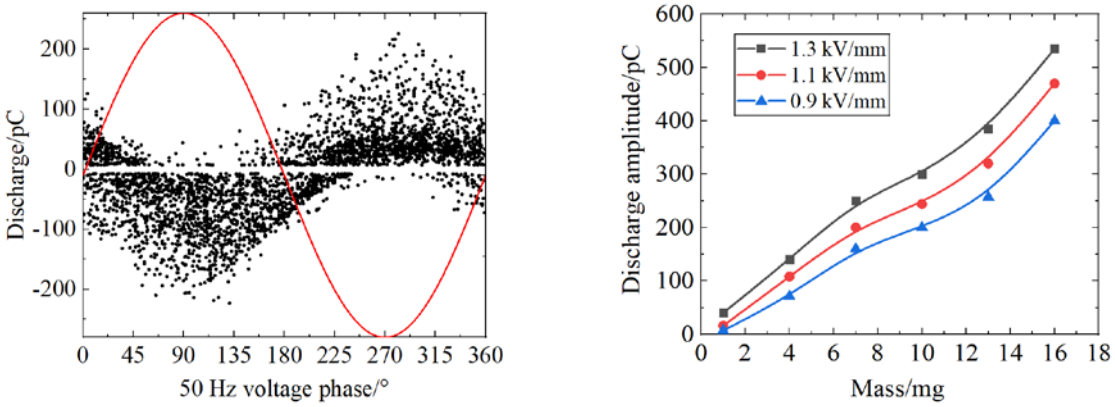

Figure 4-37 Discharge statistics of linear particles.(a) PRPD pattern of linear particles. (b) Maximum apparent discharge quantities of linear particles with different masses.

Figure 4-37 (a) shows the PRPD pattern of a 10 mg linear metal particle under an electric field strength of 0.9 kV/mm, it is similar to that of the spherical particle, also exhibiting a banded distribution with a phase opposite to the voltage. Figure 4-37 (b) shows the relationship between the maximum apparent discharge quantity and the mass of linear particles under different field strengths. The trend of the maximum apparent discharge quantity varying with the mass of linear particles is basically the same under the three different field strengths. As the mass increases from 1 mg to 16 mg, the maximum apparent discharge quantity Q_{amax} increases linearly from 7 pC to 400 pC at 0.9 kV/mm, from 16 pC to 470 pC at 1.1 kV/mm, and from 40 pC to 535 pC at 1.3 kV/mm. In addition, as the particle mass increases, the difference in discharge quantity caused by changes in field strength also increases. The relationship between the mass of linear particles and the maximum apparent discharge quantity gradually shifts from a linear to an exponential relationship.

4.4.2 Quantity Effect on Motion and PD of Linear Particles

This section takes L-4 particles as an example to study the motion and PD characteristics of different numbers of linear particles under power-frequency voltage and sinusoidal vibration. Under the rated field strength, when the number of linear particles is

small, they jump inside the GIS and may be adsorbed onto the surface of the basin insulator. At this time, the discharge distance along the surface of the insulator is shortened, which makes it easier to trigger surface flashover, accelerate the deterioration of the insulator, and form a discharge hazard. When the number of linear particles is large, experiments observe that linear particles inside the GIS may form chain breakdown, that is, multiple linear particles are connected end-to-end between the bus conductor and the grounded enclosure, as shown in Figure 4-38. This phenomenon significantly increases the risk of GIS equipment failure, and can further cause hidden dangers such as short-circuit tripping, reduction of gas insulation strength, deformation and deterioration of the equipment's mechanical structure. Moreover, after short-circuit tripping, the particles scatter to the inner wall of the GIS, and the discharge chain disappears. Therefore, it is difficult to identify the specific cause of the failure later on, which increases the difficulty of detection and diagnosis.

Under the rated field strength, the time-domain AE signals and discharge repetition rates from different numbers of linear particles are shown in Figure 4-39: It is known that compared with spherical particles, linear particles, which jumps vertically, are closer to the GIS bus conductor and carry more charge than the spherical particles. Therefore, the AE signal amplitude is slightly larger, but the discharge repetition rate is lower and the flight time is slightly longer, which means more intense jumping. Specifically, when the number of linear particles is 1, 5, and 9, the average discharge repetition rates are 0.543, 2.57, and 4.95 times per 20ms, respectively. It is observed that the number of linear particles is approximately twice their discharge repetition rate.

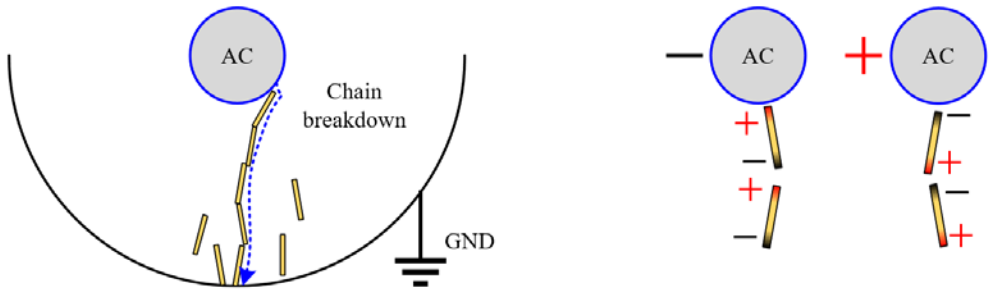

(a) (b)

Figure 4-38 Motion characteristics of the multiple linear particles. (a) Chain breakdown. (b) Charge distribution.

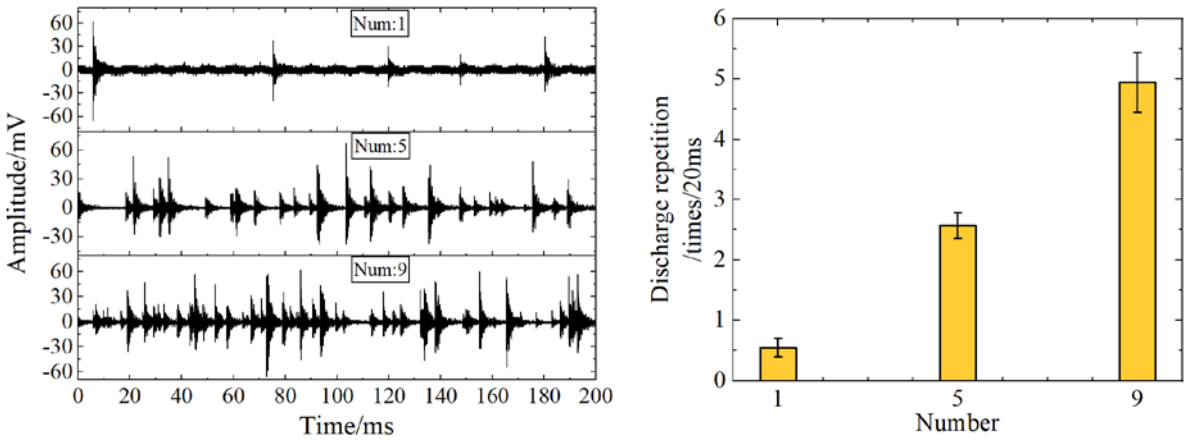

(a) (b)

Figure 4-39 PDAE of multiple linear particles. (a) Time-Domain signals. (b) Discharge repetition rate.

4.5 Brief Summary

Given that current studies on metal particle defect detection have not adequately considered the combined effects of operational voltage and mechanical vibration in GIS, this chapter establishes a scaled 330 kV GIS experimental platform capable of synchronously applying power-frequency voltage and mechanical vibration. The motion behavior and PD characteristics of metal particles under combined excitation are investigated. Defect scenarios are configured based on particle mass, shape, and quantity. Mechanical vibration signals, AE signals, and apparent discharge levels are measured under various conditions. The influence of electric field strength and mechanical vibration on different types of particle defects is identified. Based on experimental results and theoretical analysis, the motion behaviors and PD characteristics of three typical types of particles are analyzed. The main conclusions are as follows:

1) The electric field strengths required for the jumping initiation E_i and cessation E_c in spherical particles increase with particle mass. Mechanical vibration on GIS reduces both the E_i and E_c, with greater vibration amplitudes leading to more significant reductions. Under the same electric field, lighter particles exhibit more active motion but generate lower discharge magnitudes, whereas heavier particles show less motion activity but produce higher discharge levels. When lightly vibrating, particles demonstrate a slight increase in motion activity due to the influence of GIS vibration. When multiple particles jump simultaneously, mutual repulsion occurs as a result of the same charge polarity.

2) The E_i and E_c for flake particles are significantly affected by their mass and dimensions but are largely insensitive to GIS vibration. Flake particles with strip-like shapes and lower mass are more likely to initiate motion, whereas square-shaped and heavier flakes are more difficult to jump. Once airborne, flake particles exhibit vigorous motion and generate high discharge magnitudes, which increase with particle mass. Under high electric field, luminous "firefly" phenomena are observed. When multiple flakes are in motion, head-to-tail chain breakdown may be triggered, potentially leading to short-circuit fault.

3) For linear particles, the E_i and E_c increase with particle mass. GIS mechanical vibration reduces both thresholds, with greater vibration leading to more pronounced decreases. In some cases, linear particles may cease motion prematurely due to tipping or falling before decreasing to the E_c. Once initiated, linear particles exhibit active motion, are minimally affected by vibration, and produce large discharges, which increase with particle mass. Under high field strength, firefly phenomena may also occur. Simultaneous motion of multiple fiber particles may induce head-to-tail chain breakdown, posing a risk of short-circuit fault.

5 Vibration-AE Fusion Detection Technology and Application for GIS Equipment

Based on the research background and practical engineering needs, this chapter proposes a fusion detection technique for GIS to further enhance the level of mechanical vibration–PDAE fusion detection, aiming to enable the effective application of the sensing device. A fusion detection approach for GIS equipment is proposed and applied in substation field testing. Building on the experimental results in Chapter 4, evaluation methods for metal particle shape, mass, and quantity are summarized, along with signal processing and feature extraction methods for vibration, AE, and fusion signals. Considering the full sensing chain of sensing, storage, computation, and transmission, a distributed intelligent detection architecture for GIS in substation is proposed. Finally, an intelligent wireless fusion detection system integrating vibration and AE sensing is developed and successfully applied in practical GIS substation.

5.1 Evaluation Method for Metal Particle Defect in GIS

5.1.1 Inference of Metal Particle Shape

The differences in the shapes of spherical, flaky, and linear metal particles lead to variations in their motion and discharge characteristics, allowing the particle shape to be inferred based on these differences. As described in Chapter 4, the motion characteristics of metal particles vary with shape. Due to its low height and greater distance from the high-voltage electrode, a spherical particle carries a lower charge and exhibits the least active motion, jumping slightly on the ground electrode surface. In contrast, flaky and linear particles, having a certain length and being closer to the high-voltage electrode, carry more charge and move more actively, with longer time intervals between successive collisions with the ground electrode. As a result, the flight pattern of spherical particles exhibits lower amplitude and fewer peaks (typically only 2–3), whereas that of flaky and linear particles shows higher amplitude and more peaks (more than 3).

Figure 5-1 presents the flight patterns of three different particle shapes, each with a mass of 10 mg, under a field strength of 1.3 kV/mm (normal operating conditions). The spherical particle spectrum has only two peaks with an amplitude around 80 mV, while both flaky and linear particles exhibit four peaks with amplitudes around 120 mV. On the other hand, due to their lower jumping height, spherical particles exhibit a higher discharge frequency per unit time than flaky and linear particles. The discharge repetition rates of the three particle shapes under a field strength of 1.3 kV/mm are compared in Table 5-1. Spherical particles have the highest discharge repetition rate, exceeding 50 discharges per second. Flaky particles have a slightly lower rate, generally ranging between 20 and 40 discharges per second, while linear particles exhibit the lowest rate, around 25 discharges per second. The relatively high discharge repetition rate of flaky particles is attributed to their

larger surface area, which results in greater aerodynamic resistance compared to linear particles. In summary, particle shape can be roughly identified based on AE flight spectra and discharge repetition rate characteristics.

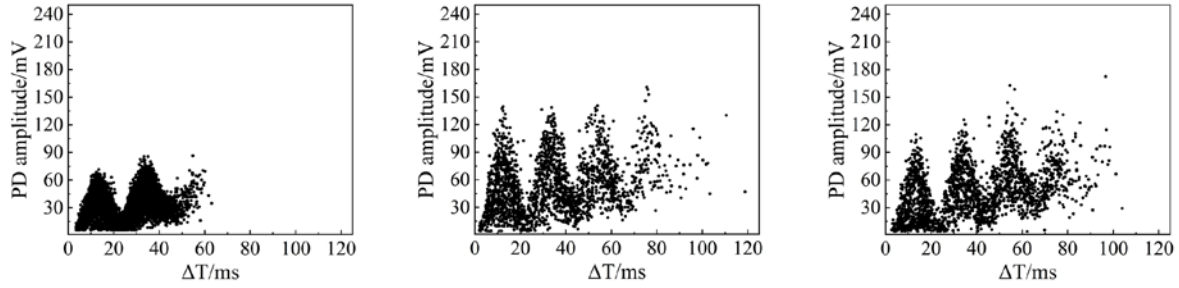

Figure 5-1 Flight patterns of different particle shapes. (a) Sphere. (b) Flake. (c) Line.

Table 5-1 Discharge repetition rate (/second)

Masses\Shapes	Sphere	Flake	Line
4 mg	50	24	25
10 mg	59	35	26
16 mg	66	38	28

5.1.2 Estimation of Metal Particle Mass

For particles of the same shape, differences in mass (size) lead to variations in charge amount, resulting in distinct motion and discharge characteristics. According to the electrostatic force equations in Chapter 4, the charge amount of a metal particle is related to its size: for spherical particles, it depends on the radius; for flaky particles, on the length and width; and for linear particles, on the length and radius. Analysis of the flight spectra for the three particle shapes (Figure 5-2 (a)-(i)) shows that, under the same field strength, larger-mass particles carry more charge but experience a smaller net force, making their motion less active. Conversely, smaller-mass particles exhibit higher motion activity. Additionally, the flight spectra tend to show an upward trend over time, indicating increasing flight height with time.

Figure 5-3 presents an analysis of the particle jumping process. During airborne motion, the particle trajectory consists of ascent and descent phases. In the ascent phase, the electric field force dominates, while in the descent phase, gravity becomes the dominant force. When the field strength is sufficiently high, the particle initially ascends to a certain height. If, by the end of the descent phase, it does not collide with the enclosure, it ascends again to a height slightly exceeding the previous peak before eventually descending and colliding. This entire process spans two power-frequency cycles and corresponds to the second peak in the particle’s flight pattern. Similarly, the formation of the third, fourth, fifth, and subsequent peaks follows the same pattern, with the particle undergoing repeated cycles of ascent and descent.

The light blue line in Figure 5-3 (b) corresponds to the light blue line in Figure 5-2 (i), indicating that at this moment, the electric field force cancels out gravity, resulting in a net

force of zero and the minimal force acting on the particle. Studies have shown that the amplitude of the AE signal generated by particle collisions is proportional to the instantaneous momentum of the particle[139]. The particle velocity can be estimated using the free-fall equation, given by Equation (5-1).

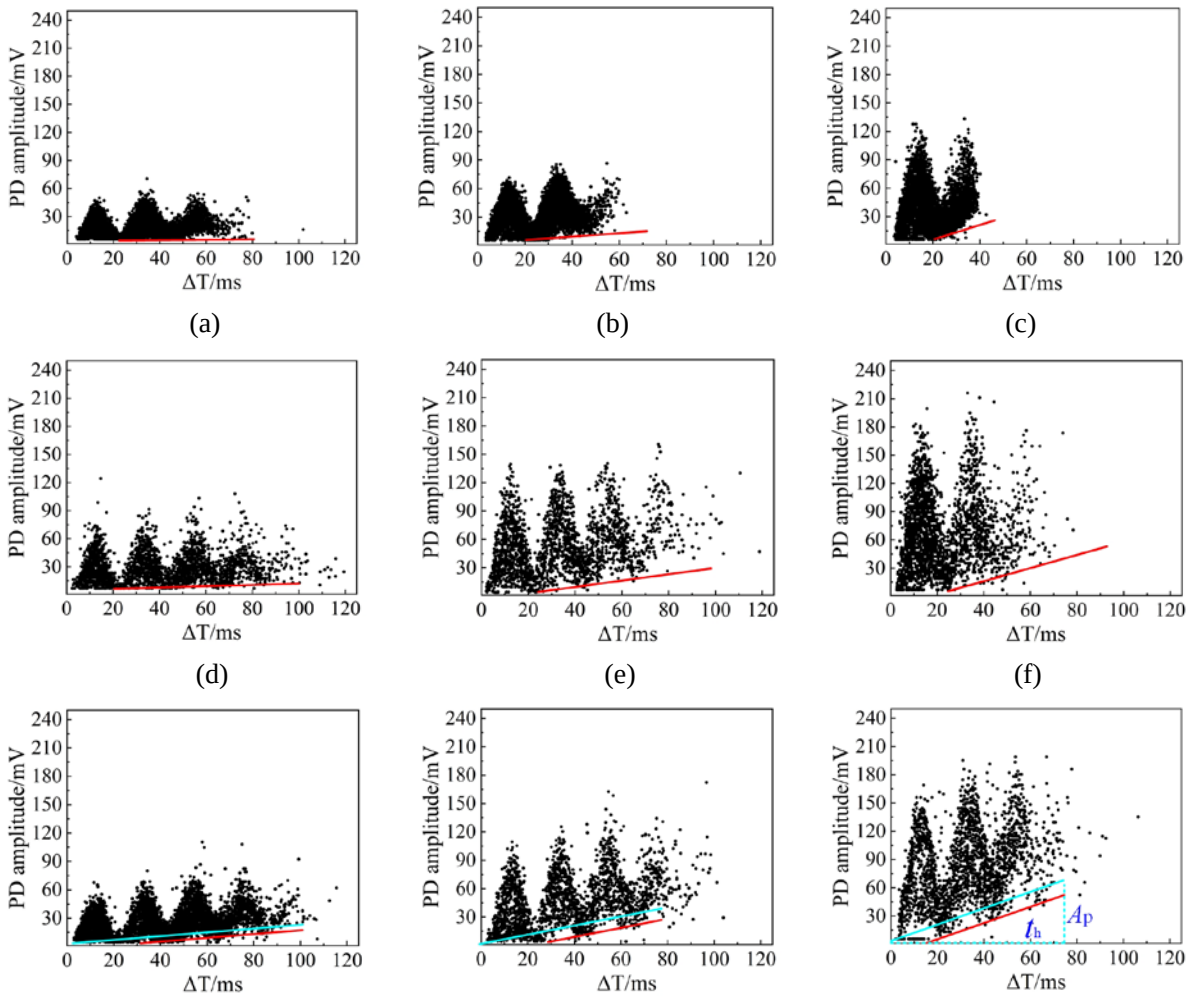

Figure 5-2 Flight patterns of different particle shapes and masses. (a) S-2. (b) S-4. (c) S-6. (d) F-2. (e) F-4. (f) F-6. (g) L-2. (h) L-4. (i) L-6.

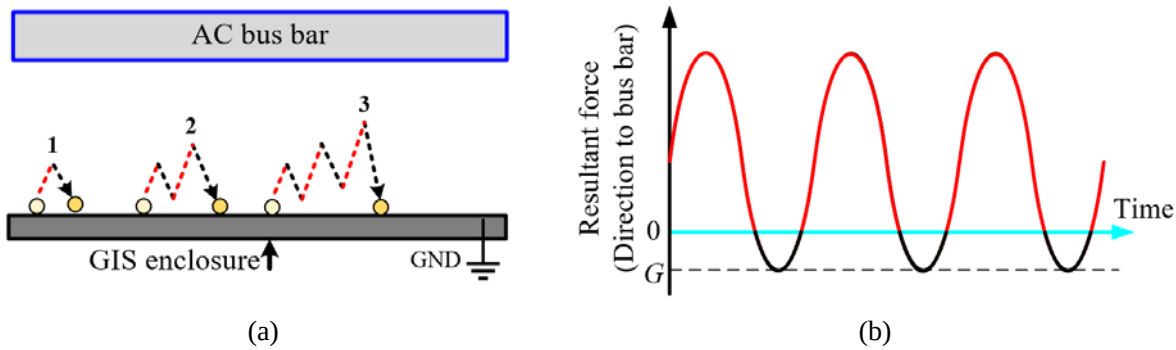

Figure 5-3 Analysis of the particle jumping process. (a) The jumping process. (b) The resultant force on the particle.

$$\begin{cases} A_{\mathrm{p}} = kmv_{\mathrm{p}} \\ v_{\mathrm{p}} = \dfrac{gt_{\mathrm{h}}}{2} \end{cases} \tag{5-1}$$

where A_{p} is the AE signal amplitude, m is the particle mass, k is the proportionality factor between the AE signal amplitude and the collision momentum, which depends on the AE measurement performance of the sensor, v_{p} is the particle velocity at the moment of collision, and $t_{\mathrm{h}}/2$ is the flight descent time. Thus, the following equation can be derived:

$$mk = \frac{2A_{\mathrm{p}}}{gt_{\mathrm{h}}} \tag{5-2}$$

When the value of k is known (requiring calibration of the proportionality between AE amplitude and particle momentum), the particle mass m can be calculated. From the flight pattern, it can be observed that $A_{\mathrm{p}}/t_{\mathrm{h}}$ corresponds to the slope (red line) in the figure. Since k and g are constants, the particle mass m is proportional to the slope $A_{\mathrm{p}}/t_{\mathrm{h}}$. This explains why the flight pattern distribution exhibits an upward trend for larger-mass particles.

Taking the flight pattern of flaky particles in Figure 5-2 (g)~(i) as an example, calibration yields a k value of approximately 0.0107. Using Equation (5-2), the calculated particle masses and their actual masses are shown in Table 5-2. The results indicate that the calculated values closely match the actual masses. The slight deviations for L-2 and L-4 particles may be due to statistical errors in measuring A_{p} and t_{h} from the flight pattern.

Table 5-2 Comparison of the actual mass of particles with the estimated results

Item	L-2	L-4	L-6
Actual/mg	4	10	16
Calculated/mg	4.67	9.35	16.02

5.1.3 Assess of Metal Particle Quantity

When using AE sensors to detect the jumping discharge of multiple particles, a detection issue arises. The AE signal generated by particle discharge typically lasts for several milliseconds, and when multiple particles discharge simultaneously, their pulses and sustained signals overlap, making it difficult to distinguish the signals detected by the sensor. Therefore, an effective signal processing method is required to differentiate the overlapping discharge pulses. The energy variation of the AE pulses generated by particle jumping discharge follows a pattern: it first increases sharply and then gradually decreases. Additionally, instantaneous signals like these should be processed using a signal windowing method to capture time-varying results. Based on this pattern, this study applies the Root Mean Square (RMS) envelope method to process the acquired PDAE signal. RMS represents the energy level of the signal per unit time, while envelope analysis reduces high-frequency interference, providing clearer pulse resolution. Through windowing, a time-domain energy map of the signal can be obtained. This method can effectively differentiate two non-fully synchronized discharge pulses based on their energy variation.

The principle of calculating the RMS envelope of a signal is as follows: First, a sliding

window W is defined. The larger the window, the smoother the envelope, but the finer details may be lost. Next, the RMS is calculated within the sliding window to reflect the instantaneous energy magnitude, and the resulting smooth envelope curve is obtained. To account for potential DC component effects in the actual signal, the upper and lower envelopes are averaged to form the final envelope curve. Experiments have shown that the PDAE pulses generated by particle discharge typically last between 2 ms and 5 ms. To ensure the envelope is smooth and clear without losing too much detail, this study sets the window size to 0.4 ms. The calculation results are shown in Figure 5-4. It can be seen that the signal inside Frame 1 is a standard single particle discharge pulse, with its RMS energy value increasing sharply and then gradually decreasing to near zero. The original time-domain signal inside Frame 2 makes it difficult to determine how many discharge pulses are present, but the RMS energy envelope clearly shows three local peaks, corresponding to three discharge pulses.

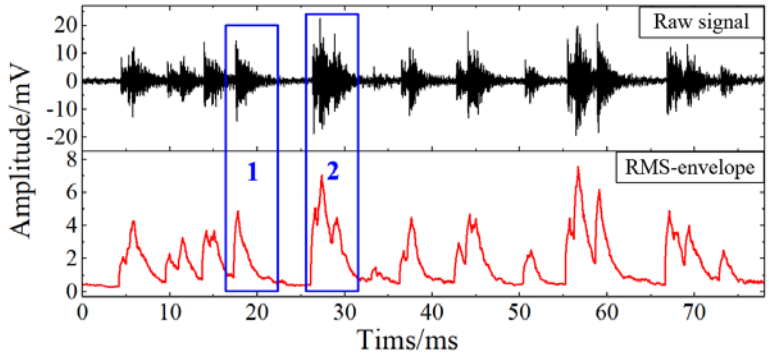

Figure 5-4 Comparison of the time-domain signal and RMS envelope of PDAE for five spherical particles.

A direct and effective method to estimate the number of particles is by statistically counting the discharge frequency per unit time. First, statistics are performed on the experimental results from Chapter 4, yielding the discharge repetition rate of individual particles per 20 ms at the rated field strength of 1.3 kV/mm, as shown in Table 5-3. It can be seen that, as mass increases, the discharge repetition rate for spherical particles rises from 0.4434/20 ms to 1.376/20 ms, the discharge repetition rate for flaky particles increases from 0.36/20 ms to 0.87/20 ms, and the discharge repetition rate for linear particles remains around 0.55/20 ms.

Table 5-3 Discharge repetition rate of a single particle per 20 ms under rated field strength of 1.3 kV/mm

Masses\shapes	Spherical	Flaky	Linear
1 mg	0.4434	0.36	0.58
4 mg	0.82	0.4956	0.53
7 mg	0.95	0.62	0.472
10 mg	1.02	0.73	0.534
13 mg	1.298718	0.852	0.588
16 mg	1.376	0.87	0.58

At the rated field strength of 1.3 kV/mm, the discharge repetition rate per 20 ms for a large number of 10 mg particles is statistically analyzed, as shown in Table 5-4. By analyzing the variation in the discharge repetition rate of 10 mg particles with the number of particles, and combining the discharge repetition rate of individual particles with other masses, a pattern of how the discharge repetition rate changes with the number of particles for other masses can be indirectly derived.

Table 5-4 Discharge repetition rate per 20 ms for multiple particles (10 mg) under rated field strength (1.3 kV/mm)

Number\Shapes	Spherical	Flaky	Linear
1	1.02	0.73	0.534
5	4.92	2.78	2.57
9	8.5	4.54	4.95

It can be observed that an increasing number of particles leads to a rise in discharge repetition rate, but due to randomness, the increase is not entirely linear, and there is a certain margin of error. Therefore, the estimation of particle quantity can currently only provide an approximate range. This study defines the particle quantity levels as small, medium, and large, corresponding to the ranges of 1~5, 5~9, and more than 9 particles, respectively. Based on the two tables above, the discharge repetition rates for different particle masses at quantities of 1, 5, and 9 particles are estimated using proportional coefficients, as shown in Table 5-5.

Table 5-5 Discharge repetition rate of particles with different masses at quantities of 1, 5, and 9

Number	Mass/mg					
Sphere	1	4	7	10	13	16
1	0.4434	0.82	0.95	1.02	1.3	1.376
5	2.139	3.955	4.58	4.92	6.264	6.6365
9	3.7	6.83	7.92	8.5	10.82	11.47
Flake	1	4	7	10	13	16
1	0.36	0.4956	0.62	0.73	0.852	0.87
5	1.368	1.88328	2.356	2.774	3.2376	3.306
9	2.2392	3.082632	3.8564	4.5406	5.29944	5.4114
Line	1	4	7	10	13	16
1	0.58	0.53	0.472	0.534	0.588	0.58
5	2.791366	2.550731	2.271594	2.569982	2.829868	2.791366
9	5.3766	4.9131	4.37544	4.95018	5.45076	5.3766

Based on the above table, the relationship between the discharge repetition rate and the particle quantity for different particle masses is plotted in Figure 5-5. In the three graphs, the blue, red, and black lines represent the discharge repetition rate per 20 ms for particles with quantities of 9, 5, and 1, respectively. Therefore, the region above the blue line corresponds

to a particle quantity greater than 9, the region between the blue and red lines corresponds to a particle quantity between 5 and 9, the region below the red line corresponds to a particle quantity less than 5, and the region below the black line corresponds to a particle quantity equal to 1. This allows for an approximate assess of the particle quantity range.

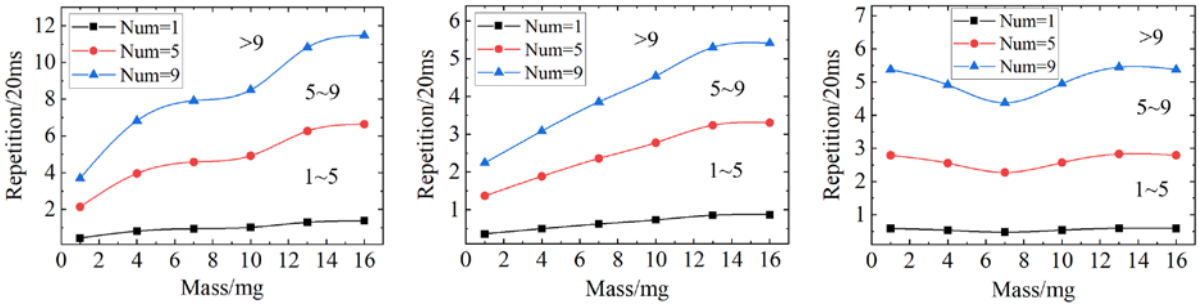

Figure 5-5 Relationship between discharge repetition rate and particle quantity for different particle masses under rated field strength. (a) Spherical. (b) Flakey. (c) Linear.

5.2 Vibration-AE Fusion Detection Method in Substation Field

5.2.1 Denoising and Separation of the Fusion Signal Based on VMD

The electromagnetic and mechanical environment in substations is complex. During on-site measurements, fusion sensor signals are easily affected by noise from both the environment and the sensors themselves. This noise mainly includes ultra-low-frequency vibration noise and high-frequency electromagnetic noise. Low-frequency vibration noise is caused by vibrations from external sources, such as seismic activity or vibrations from external equipment, as well as structural vibration noise from the power equipment itself. These noises have relatively low frequencies, typically ranging from a few Hz to several tens of Hz[140]. High-frequency electromagnetic noise originates from high-frequency electromagnetic interference coupled through the sensor's internal circuits or signal lines, as well as the induced voltage on the surface of the power equipment. This noise has higher frequencies, usually in the MHz range[141]. On the other hand, the fusion sensor's measurement signal consists of steady-state low-frequency sinusoidal mechanical vibration signals superimposed with transient high-frequency PDAE pulse signals. The frequency range of these signals primarily spans from 100 Hz to 100 kHz. The superposition of these two types of signals makes further analysis difficult. Therefore, denoising and effectively separating the fusion measurement signals of the sensor is a crucial step in achieving accurate signal measurement and data fusion analysis.

Currently, various signal processing techniques, such as wavelet transform, FFT, local mean decomposition (LMD), empirical mode decomposition (EMD), and others, are widely used for data preprocessing, denoising, and analysis. Each method has its pros and cons. Wavelet transform is effective for non-stationary signals and high-frequency noise but involves complex parameter selection and large computation. FFT is efficient for periodic signal analysis but unsuitable for non-stationary signals. LMD handles nonlinear and non-stationary signals well but can be noise-sensitive and computationally complex. EMD

decomposes signals into stationary modes but suffers from mode mixing and instability in long sequences. Among these, Variational Mode Decomposition (VMD), proposed by K. Dragomiretskiy and D. Zosso in 2014[142], has gained attention for its strong noise resistance, adaptability, and ability to avoid mode mixing. VMD decomposes signals into Intrinsic Mode Functions (IMFs) by optimizing a penalty factor to narrow the bandwidth of each mode. This method offers better robustness and stability, making it ideal for analyzing nonlinear and non-stationary signals in applications like denoising, feature extraction, and fault diagnosis.

Figure 5-6 Noise sources in vibration-AE detection of GIS equipment

1) Principle of VMD algorithm

The objective function of the classical VMD variational model can be represented by equation (5-3), and the constraint condition is given by equation (5-4).

$$\min_{\{u_k\},\{\omega_k\}}\left\{\sum_k\left\|\partial_t\left[\left(\delta(t)+\frac{\mathrm{j}}{\pi t}\right)*u_k(t)\right]e^{-\mathrm{j}\omega_k t}\right\|_2^2\right\} \tag{5-3}$$

$$f(t)=\sum_{k=1}^{K}u_k(t) \tag{5-4}$$

where ∂_t represents the time derivative operator used to measure bandwidth, $f(t)$ is the original signal, K is the number of modes obtained after the VMD decomposition of the original signal, $u_k=\{u_1,u_2,\ldots u_k\}$ and $\omega_k=\{\omega_1, \omega_2,\ldots\omega_k\}$ represent the mode components and their corresponding center frequencies, * denotes the convolution operator, and $\delta(t)$ is the impulse function.

To solve the optimization problem, a quadratic penalty term and Lagrange multipliers are introduced to transform the constrained variational problem into an unconstrained variational problem. The resulting augmented Lagrangian Equation is:

$$L\left(\{u_k\},\{\omega_k\},\lambda\right)=\alpha\sum_k\left\|\partial_t\left[\left(\delta(t)+\frac{\mathrm{j}}{\pi t}\right)*u_k(t)\right]e^{-\mathrm{j}\omega_k t}\right\|_2^2+\left\|f(t)-\sum_k u_k(t)\right\|_2^2+\left\langle\lambda(t),f(t)-\sum_k u_k(t)\right\rangle \tag{5-5}$$

where α is the penalty factor that controls the bandwidth limitation, and $\langle\cdot\rangle$ represents the inner product. Finally, the Alternating Direction Method of Multipliers (ADMM) is used to solve the problem, updating the modal components u_k, the center frequencies ω_k, and the Lagrange multipliers:

$$u_k^{n+1}(\omega)=\frac{\hat{f}(\omega)-\sum_{i\neq k}\hat{u}_i(\omega)+\frac{\hat{\lambda}(\omega)}{2}}{1+2\alpha(\omega-\omega k)^2} \tag{5-6}$$

$$\omega_k^{n+1}=\frac{\int_0^\infty \omega\left|\hat{u}_k(\omega)\right|^2 d\omega}{\int_0^\infty \left|\hat{u}_k(\omega)\right|^2 d\omega} \tag{5-7}$$

$$\hat{\lambda}^{n+1}(\omega)=\hat{\lambda}^n(\omega)+\gamma\left(\hat{f}(\omega)-\sum_k \hat{u}_k^{n+1}(\omega)\right) \tag{5-8}$$

where *n* represents the iteration count, and $\hat{u}_k^{n+1}(\omega)$, $\hat{\lambda}(\omega)$, $\hat{f}(\omega)$ are the Fourier transforms of $u_k^{n+1}(\omega)$, $\lambda(\omega)$, $f(\omega)$, respectively. ω denotes the frequency value, and γ is the noise tolerance. Finally, the IMFs are obtained by performing the IFFT on the extracted modes.

2) Fusion signal denoising and separation based on the VMD method

In the VMD input parameters, the penalty factor α and the number of modes K are two important input parameters. For different input signals, setting appropriate parameters can significantly improve the processing effect of VMD. The number of modes K determines the number of decomposed modes. Too many modes can lead to over-decomposition, while too few modes can cause mode mixing. The penalty factor α controls the bandwidth of the modes. When the value is large, the mode bandwidth is narrow, suitable for separating high-frequency components; when the value is small, the mode bandwidth is wide, suitable for low-frequency components. In this study, the frequency range of the fusion signal in 100 Hz~100 kHz. Considering the transition segment at the boundaries, the working frequency range for signal separation is set to 40 Hz to 120 kHz, with noise frequencies below 40 Hz and above 120 kHz. The frequency range distribution is shown in Figure 5-7. The penalty factor α and the number of modes K are set to 3000 and 7, respectively.

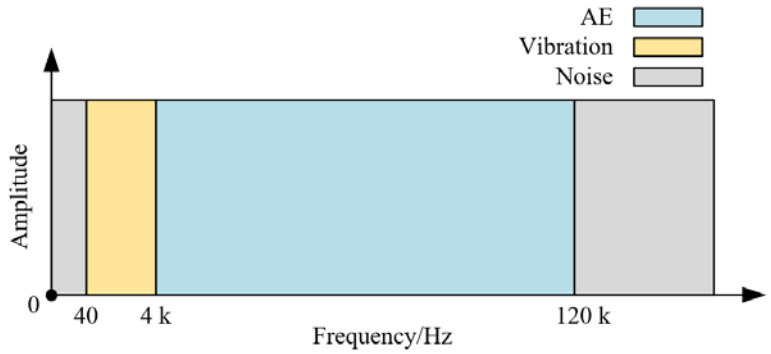

Figure 5-7 Noise and the fusion measurement bands.

After performing VMD decomposition on the signal, a set of IMFs distributed from high to low frequency bands is obtained, as shown in Figure 5-8 (a). Among them, IMF 1~6 correspond to PDAE signals, while IMF 7 represents low-frequency vibration signals. The FFT results for each IMF, shown in Figure 5-8 (b), indicate that the center frequency of IMF 7 is 100 Hz, while the center frequencies of IMF 6~1 are 17 kHz, 27 kHz, 41 kHz, 55 kHz, 63.7 kHz, and 106.6 kHz, respectively. IMFs with center frequencies within the working

frequency range (40 Hz~120 kHz) are selected as the denoised signal. Finally, IMFs with center frequencies below 4 kHz correspond to vibration signals, while those above 4 kHz are linearly summed to obtain the AE signal, as shown in Figure 5-8 (c).

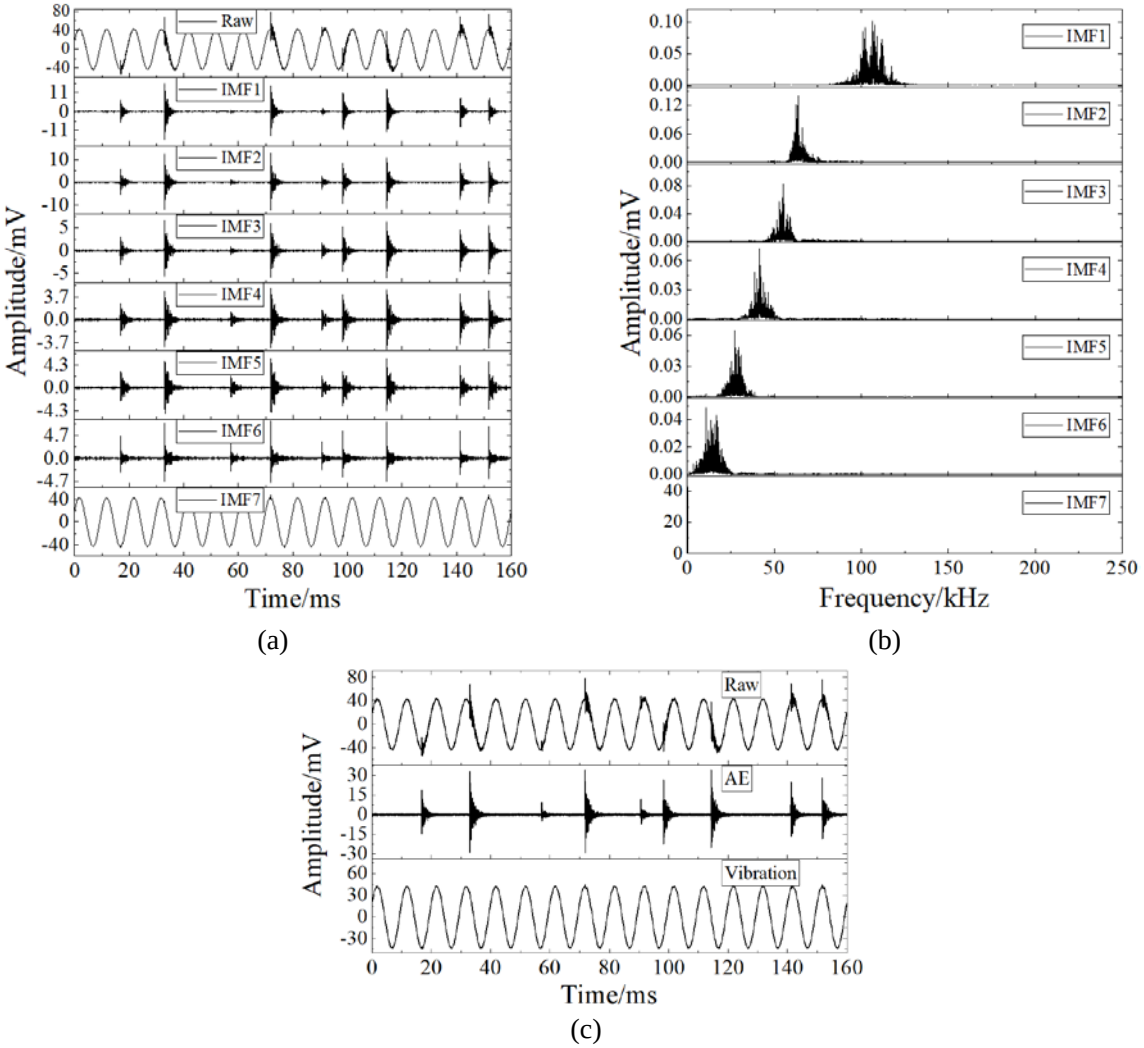

Figure 5-8 Signal separation based on VMD. (a) VMD decomposition of the fusion signal. (b) FFT calculation of the IMFs. (c) Separated fusion signal.

5.2.2 Feature Extraction of the Fusion Signal

1) PDAE features extraction

The extraction approach for PDAE signal features is illustrated in Figure 5-9 (a), where time-domain and time-frequency features are first extracted, followed by statistical feature computation based on time-domain characteristics. A typical PDAE signal, after denoising and separation, is shown in Figure 5-9 (b).

In time-domain features, duration refers to the total time interval during which the AE signal exceeds a predefined pulse threshold. It is closely related to the ring count and is commonly used for AE signal detection and identification. AE amplitude represents the peak value of the pulse signal, indicating the signal strength and serving as a measure of the AE energy captured by the sensor. AE energy refers to the accumulated signal energy, often represented by the area under the AE signal envelope (shown as the light green region in the

figure). This feature provides a comprehensive reflection of both the signal intensity and duration. Ring count denotes the total number of oscillation cycles that exceed a predefined threshold in the received signal—a higher count suggests slower signal attenuation or stronger oscillations.

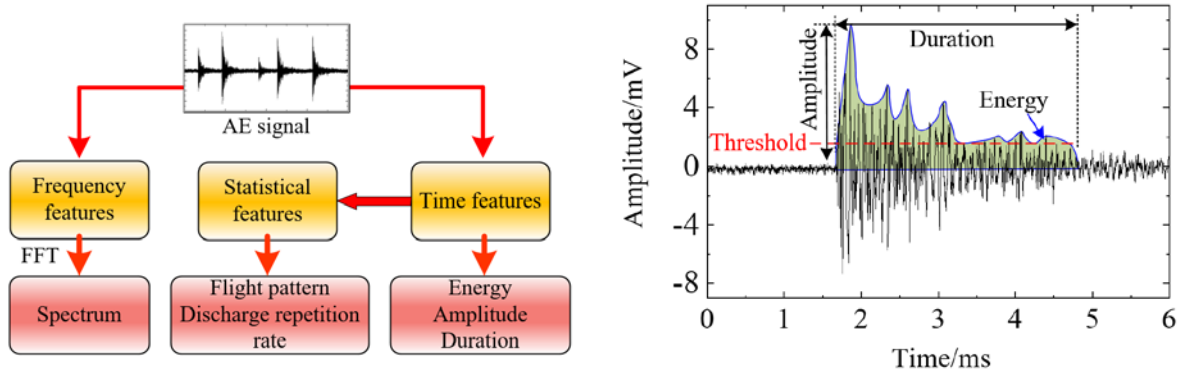

(a) (b)

Figure 5-9 Features extraction of the PDAE signal. (a) Extraction process. (b) Time-domain features.

In statistical features, the PDAE repetition rate (pulse density) refers to the number of AE pulses per unit time, reflecting the severity of PD in terms of quantity. The PRPD pattern describes the relationship between PDAE signal and the phase of the power frequency voltage. It is a crucial method for evaluating PD patterns in power equipment, with the horizontal axis representing the power frequency voltage phase and the vertical axis representing the PDAE amplitude. However, in practice, it is often difficult to synchronize the fused sensor signal with the power frequency voltage, requiring the use of a virtual phase to generate the PRPD pattern[143].

The frequency-domain distribution of AE pulse signals can, to some extent, reflect the type and intensity of PD. By applying the FFT, the spectral characteristics of the signal can be obtained, including key parameters such as dominant frequency and spectral centroid. These frequency-domain features play a crucial role in analyzing discharge mechanisms, identifying different PD patterns, and assessing the energy distribution of discharges.

2) Mechanical vibration features extraction

Mechanical vibration signal features are extracted in the time and frequency domains. The main time-domain features are listed in Table 5-6.

For frequency-domain feature extraction, VMD is used to decompose the vibration signal into multiple IMFs, followed by FFT analysis. This approach effectively separates frequency components, improves frequency resolution, reduces mode mixing, and enhances time-frequency localization. It also suppresses noise interference, highlights key frequency features, and improves signal quality.

Due to electrodynamic force, the fundamental frequency of GIS mechanical vibration is 100 Hz. Mechanical defects alter the frequency components of the vibration signal, primarily by enhancing or attenuating amplitudes of specific frequencies. Different defects cause distinct frequency variations, enabling the characterization of GIS mechanical conditions based on these changes. Accordingly, this study extracts the following features from GIS

vibration signal: energy ratio, vibration entropy, phase difference-amplitude plot, and odd-even harmonic ratio.

Table 5-6 Time-domain features extraction of vibration signal

Time-domain features	Formulas	Physical meaning
RMS	$\mathrm{RMS}=\sqrt{\frac{1}{N}\sum_{i=1}^{N}x_i^2}$	Measure of the signal's energy or intensity
Peak: Pk & Pk factor	$\max(\lvert x_i\rvert)$, $\frac{\max(\lvert x_i\rvert)}{\mathrm{RMS}}$	Describes the extreme vibrations and impulsiveness of the signal
Standard Deviation: σ	$\sqrt{\frac{1}{N}\sum_{i=1}^{N}(x_i-\bar{x})^2}$	Describes the degree of fluctuation or dispersion of the signal
Skewness: Sk	$\frac{\frac{1}{N}\sum_{i=1}^{N}(x_i-\bar{x})^3}{\sigma^3}$	Describes the symmetry of the signal
Kurtosis: Ku	$\frac{\frac{1}{N}\sum_{i=1}^{N}(x_i-\bar{x})^4}{\sigma^4}$	Reflects the sharpness of the signal, suitable for detecting impulsive vibrations

The energy ratio p_f at a specific frequency f is calculated as follows, where A_f represents the amplitude corresponding to frequency f.

$$p_f=\frac{A_f^2}{\sum_{i=100}^{i=4000}A_i^2} \tag{5-9}$$

The vibration entropy H reflects the complexity of the signal's frequency distribution. When the energy in the frequency domain is concentrated at a few frequencies (such as a single frequency or narrow band), the signal is orderly, and the vibration entropy is low. Conversely, when the energy distribution spans a wide frequency range with complex and diverse frequency components, the vibration entropy is high. The calculation formula for vibration entropy H is:

$$H=\left|\sum_{f=100}^{f=4000}p_f\log_2 p_f\right| \tag{5-10}$$

When mechanical defects occur in GIS, the odd and even harmonic components of the fundamental frequency (100 Hz) will increase differently. The odd-even harmonic ratio $R_{+\infty}$ represents the proportion of odd and even harmonic components, it can be expressed as:

$$R_{+\infty}=\sqrt{\sum_{i=1}^{N/2}A_{2i-1}^2}\Big/\sqrt{\sum_{i=1}^{N/2}A_{2i}^2} \tag{5-11}$$

where A_{2i} is the amplitude of the even harmonics, $A_{2i\text{-}1}$ is the amplitude of the odd harmonics, N is the total number of harmonic frequencies within the calculated frequency range of the vibration.

In addition, this paper proposes using the phase difference-amplitude diagram to characterize vibration signal features. After performing FFT on each IMF mode of the vibration signal, the corresponding frequency amplitude and phase can be obtained. The x-axis represents the corresponding frequency, the y-axis represents the phase difference with respect to the fundamental frequency of 100 Hz (using the 100 Hz phase as reference), and the z-axis represents the amplitude corresponding to that frequency. If a specific GIS vibration state corresponds to a specific vibration signal (steady signal), which also corresponds to a specific phase difference-amplitude diagram.

3) Vibration-AE fusion features

The extraction of fusion signal features includes time-frequency domain features and statistical features. Obtaining the time-frequency representation of AE signals is key for time-frequency feature extraction. PDAE signals consist of numerous transient pulses (non-stationary signals) with a wide frequency range. Compared to FFT and traditional wavelet analysis, wavelet packet transform captures the instantaneous features of PDAE pulses and provides fine decomposition across the entire frequency band. It offers significant advantages in processing complex non-stationary signals, improving time-frequency resolution, suppressing noise, and identifying PD signal features. Therefore, wavelet packet transform can be used to extract the time-frequency representation of PDAE pulses.

Figure 5-10 illustrates the feature extraction process of vibration-AE fusion signals. After performing wavelet packet analysis on the AE signal, the time-frequency representation of the AE signal is obtained. The vibration signal is decomposed using VMD, and then Hilbert-Huang Transform (HHT) is applied to obtain the vibration time-frequency representation. By aligning both signals in time and frequency domains and linearly superimposing them, the time-frequency representation of the fusion signal is acquired. Additionally, for statistical feature, the 100 Hz signal obtained from the VMD decomposition is selected, its phase information is extracted via FFT, and then the VPRPD pattern can be obtained after combining it with the AE signal in time domain.

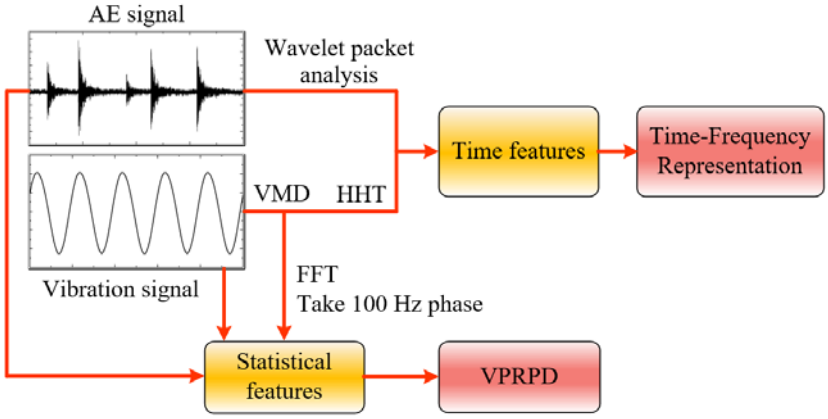

Figure 5-10 Features extraction process of the vibration-AE fusion signal

5.2.3 Intelligent Distributed Detection Architecture for GIS substation

Distributed measurement refers to the deployment of sensor nodes at multiple physical locations, working collaboratively to gather comprehensive information about a target

system or environment. This approach is commonly applied in large-scale monitoring tasks, such as in smart grids, industrial production, and condition monitoring. By collecting data from various locations, distributed measurement enables comprehensive sensing and real-time monitoring of complex systems, overcoming the limitations of single sensors confined to a local area, and providing more accurate global information[144]. Distributed measurement systems efficiently transmit sensor data via wireless or wired networks to central processing units or edge computing nodes, enabling data fusion and analysis for effective data processing, intelligent decision-making, and anomaly detection. It is widely used in fault diagnosis, health monitoring, real-time control, and plays a crucial role in enhancing system reliability, responsiveness, and flexibility. The intelligent distributed measurement and computing architecture for GIS substations proposed in this study includes fusion measurement and communication, as well as cloud-edge collaborative computing.

1) Fusion measurement and communication

The proposed fusion measurement and communication approach is shown in Figure 5-11. The hardware components include wired and wireless vibration-AE fusion sensing devices, data relay devices with built-in acquisition cards, and inspection robots. The wireless communication protocols primarily consist of short-range, efficient BLE and high-speed, stable WiFi.

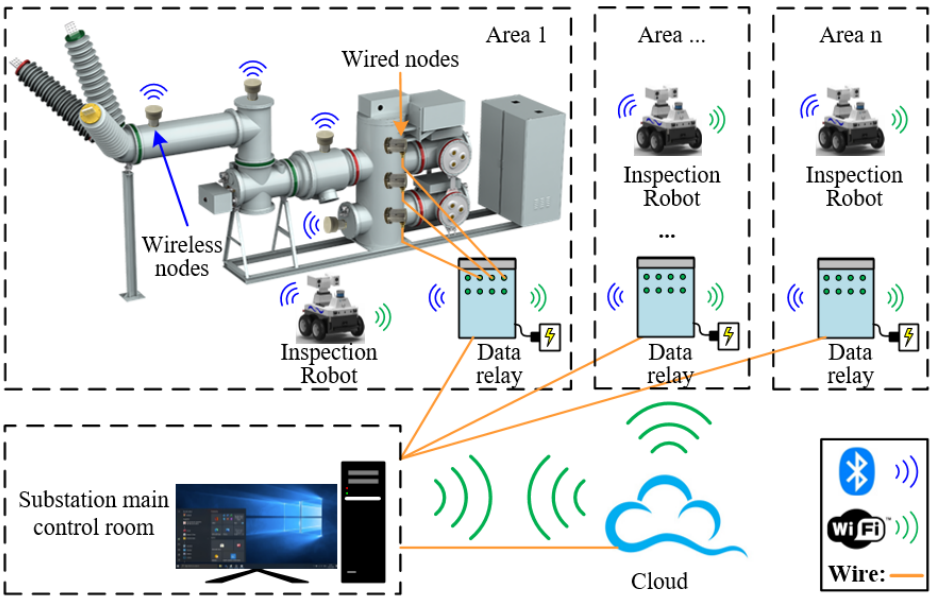

Figure 5-11 Fusion measurement and communication architecture.

In terms of measurement, sensor nodes are deployed in critical areas of the GIS substation for key electrical equipment. Wired nodes are installed in particularly important components (transformers, CTs, PTs, disconnectors, etc.) for real-time monitoring, and signals are collected by the data relay devices. For sensitive areas (such as bus sections, circuit breakers, etc.), wireless nodes are installed for periodic monitoring, with data transmitted via BLE to the data relay devices. In cases where there are too many wireless nodes or where the distance is too long, inspection robots are used to periodically collect signals and transmit them to the data relay devices. Both the robots and data relay devices

are equipped with backup power supplies that can last for more than one day to ensure continuous monitoring of critical equipment during power outages.

In terms of communication, wireless Bluetooth technology is used for low-power, efficient signal transmission between regional nodes, while WiFi and wired communication are employed for stable data transmission between regions and the central system. Both inspection robots and data relay devices are equipped with Bluetooth and WiFi for communication with sensors, while maintaining regular communication with the substation control room via wired connections. In special cases, communication with the cloud can be established via WiFi (as a backup). Additionally, multiple data relay devices provide stable and wide-area communication support for the inspection robots, ensuring reliable control. Both the data relay devices and the substation control room can locally store data. The substation control room is also connected to the regional power department network, enabling real-time monitoring of substation equipment status across the entire region.

2) Cloud-Edge collaborative computing

Cloud-edge collaborative computing leverages the computational power of both cloud and edge devices to optimize resources, ensure real-time responses, and enhance reliability by appropriately allocating computing tasks and data processing. First, the application scenario must be defined, and tasks should be divided based on actual needs, considering the timeliness, size, and security of data. Tasks requiring high real-time performance should be processed at the edge, while computationally intensive or historical data analysis tasks are handled in the cloud. Next, the computing and storage capabilities of edge devices and cloud systems must be assessed, and appropriate hardware processors (e.g., GPU, CPU), communication interfaces, and cloud platforms should be selected to optimize hardware and network architecture. Additionally, software architecture (cloud-edge collaboration mechanisms) is essential, including data synchronization, model updates, and anomaly handling (e.g., alarm mechanisms), which are closely related to the fusion detection method. Finally, optimization deployment, security encryption, and collaborative testing should be carried out to ensure the stability and reliability of the entire computing framework.

Figure 5-12 illustrates the distributed computing model for vibration and AE fusion of GIS substation equipment proposed in this paper. From bottom to top, the components are sensor nodes, primary edge terminals, intermediate edge terminals, and the cloud.

Wireless sensor nodes are equipped with certain signal processing capabilities, allowing them to perform basic computational tasks such as filtering, FFT, and feature extraction in both time and frequency domains. These processing capabilities effectively reduce latency and power consumption during data transmission, thereby enhancing transmission efficiency. By performing preprocessing and data compression at the wireless node end, network bandwidth pressure can be significantly alleviated, optimizing the overall system's energy efficiency and response speed.

The primary edge terminal mainly collects data and environmental location information from the sensor nodes, performs format conversion for different signals (potentially from other types of sensors on-site), and implements feature extraction of vibration and AE signals

using algorithms.

The intermediate edge terminal is deployed in the substation control room and possesses real-time monitoring and analysis capabilities. It is responsible for displaying the real-time data collected by the sensors and the equipment's operating status. Using deep learning models, it diagnoses and analyzes the on-site data, comprehensively evaluating the equipment's operating condition and confirming the diagnostic results. Based on the analysis, the intermediate edge terminal can generate and issue operational commands to guide equipment operation adjustments or handle anomalies, ensuring the system's stability and efficient operation.

The cloud system uses historical and real-time monitoring data to implement equipment fault diagnosis and operational trend prediction using complex AI models. Additionally, the analysis algorithms used by edge devices are continuously trained and optimized, with the updated algorithms regularly deployed to the edge nodes to improve local computational efficiency and accuracy. Moreover, through global coordination of data from each substation, regional-level equipment status evaluation reports are generated, providing decision-making support for comprehensive understanding of equipment operation.

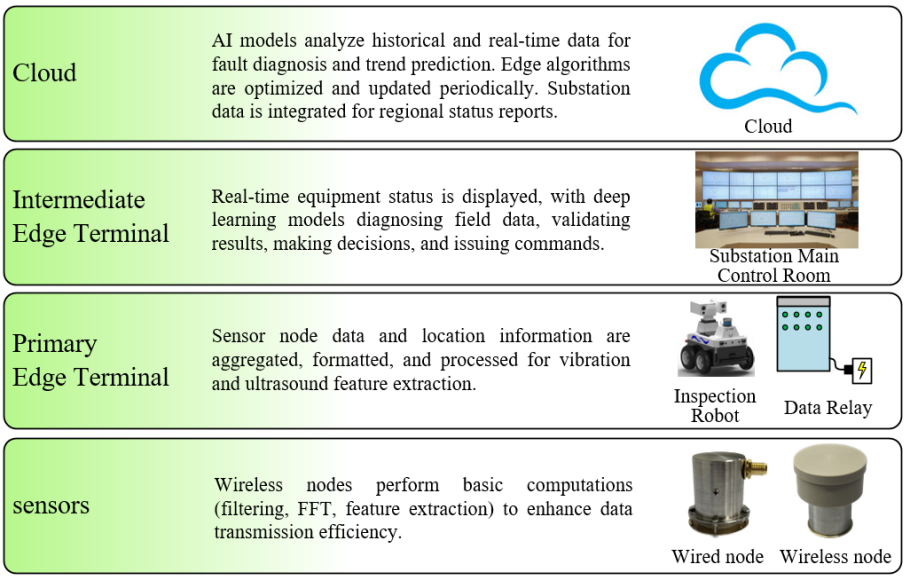

Figure 5-12 Cloud-edge collaborative computing model.

5.3 Vibration-AE Fusion Detection System and Field Application

5.3.1 Vibration-AE Fusion Detection System

The developed wireless vibration-AE fusion detection system consists of sensor terminals and client terminals. The sensor terminals, made up of multiple wireless vibration-AE fusion sensors, are key components of the measurement system responsible for collecting, processing, and transmitting data from specific locations of GIS equipment. However, the traditional BLE network architecture has limitations: a single BLE master can typically connect to no more than seven slave devices, restricting the scalability and functionality of the WSN. Additionally, when a BLE master connects to multiple slaves

simultaneously, data transmission blockages and unstable connections can reduce system efficiency. To address this issue, this paper proposes a one-to-one communication method: introducing multiple BLE masters into a single client terminal, each connected to an individual sensor node. This approach distributes the transmission load across multiple masters, increasing the number of connectable sensor nodes and enhancing the network's functionality and scalability.

Figure 5-13 (a) shows the designed Bluetooth gateway. This adapter wirelessly communicates with the sensor nodes via the integrated EFR32BG24 Bluetooth module, while it connects to the client terminal through an FT232 USB UART interface, enabling efficient data transmission and management. The design of the adapter balances communication stability and system flexibility, making it a key component in the wireless sensor network. Figure 5-13 (b) illustrates the network topology, where two sensor nodes are connected to two Bluetooth gateways controlled by a PC client, and another two sensor nodes are connected to two Bluetooth gateways controlled by a microcomputer. In this architecture, thanks to the Frequency-Hopping Spread Spectrum (FHSS) mechanism of BLE technology, multiple Bluetooth gateways can operate without interference in the same environment. This design ensures reliable synchronous communication and measurement between the client and multiple sensor nodes, providing solid technical support for multi-node collaborative detection in complex scenarios.

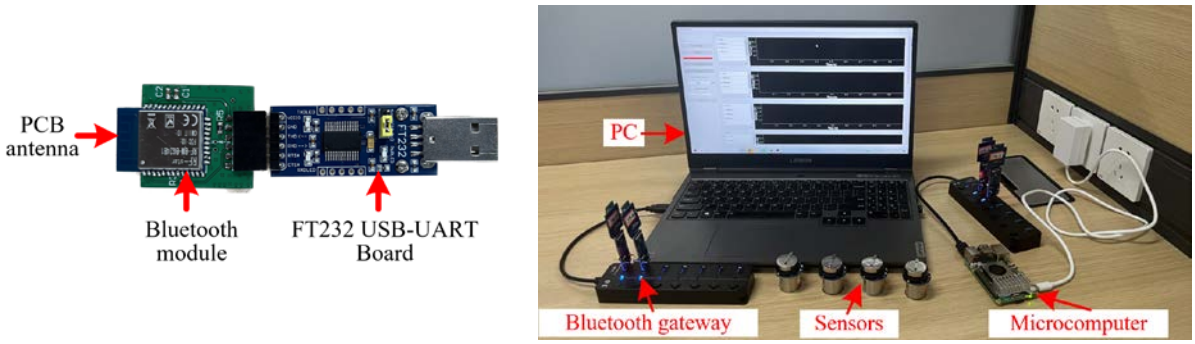

(a) (b)

Figure 5-13 The developed vibration-AE wireless sensor network. (a) Designed Bluetooth gateway. (b) Wireless sensor network prototype.

Additionally, the built-in flash memory can store the TEDS, which includes a unique identifier code (UIC) for each sensor. This UIC serves as the sole key to access the sensor’s dedicated cloud service account, ensuring that all data from the sensor is stored centrally in its cloud account. In the event of sensor damage or loss, a new sensor can be created as a replacement, inheriting its historical data. This design enhances the maintainability of the sensor and ensures continuity in data management.

The developed vibration-AE fusion detection software interface is shown in Figure 5-14. Figure (a) represents the main sensor measurement interface, consisting of four sections, numbered 1 to 4: Device initialization area, Operation control area, display area, and Vibration spectrum area. The device initialization area scans for nearby wireless devices, allowing the user to select, connect, display, or disconnect the device. The operation control

area allows the user to set sensor measurement parameters, issue action commands, and process data. This includes setting sensor sampling parameters (sampling frequency, number of sampling points), controlling sensor sampling and data transmission, configuring edge computing parameters (vibration or AE signal feature extraction), setting measurement modes (single measurement or multiple cycle measurements), and selecting spectrum plotting and data analysis options. The display area shows the raw signals from selected sensors, separated vibration and AE signals, signal spectra, and statistical spectra. It also displays the raw signals from all sensors simultaneously. The vibration spectrum area shows amplitudes of 100 Hz and its frequency multiplication components.

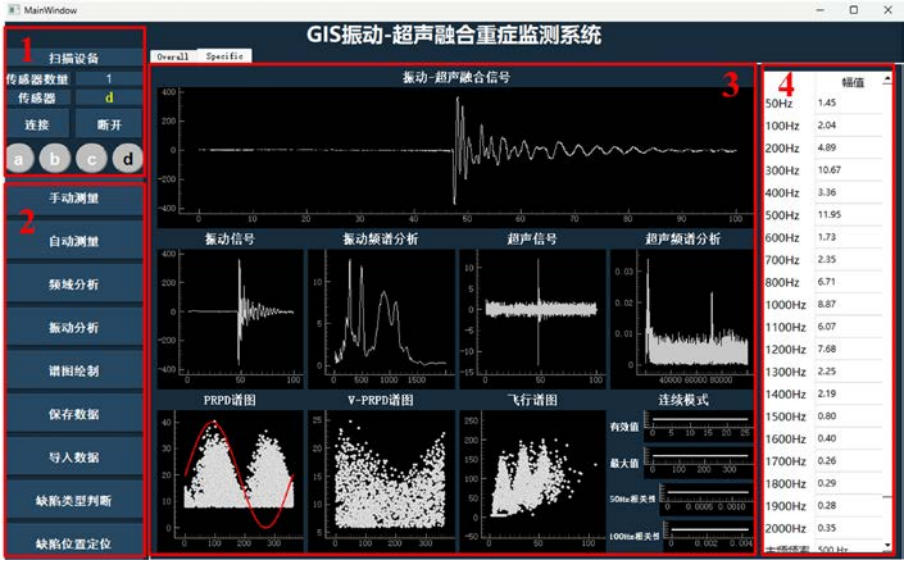

(a)

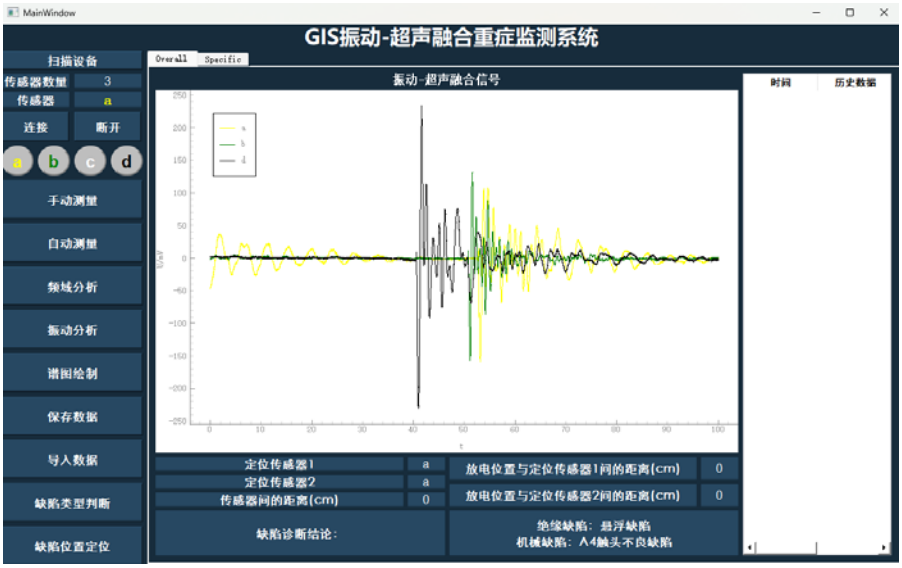

(b)

Figure 5-14 Vibration-AE fusion detection software (a) Measurement main interface (b) PDAE localization interface

Figure (b) shows the AE localization interface, used to laterally compare the PDAE signals detected by different sensors, thereby estimating the location of the PD source.

5.3.2 Field Application in GIS Substation

1) Field detection of GIS disconnector and busbar

The GIS disconnector in high-voltage power systems enables circuit switching operations, consisting of support insulators and fixed contacts to provide mechanical support and electrical connection. Its primary functions include isolating the power supply, separating energized equipment, and ensuring operational safety during maintenance. The busbar section serves as the conductive part within GIS equipment, facilitating power collection and distribution. This study focuses on the detection of a specific 220 kV GIS disconnector chamber and busbar section. The sensor installation and numbering details are shown in Figure 5-15.

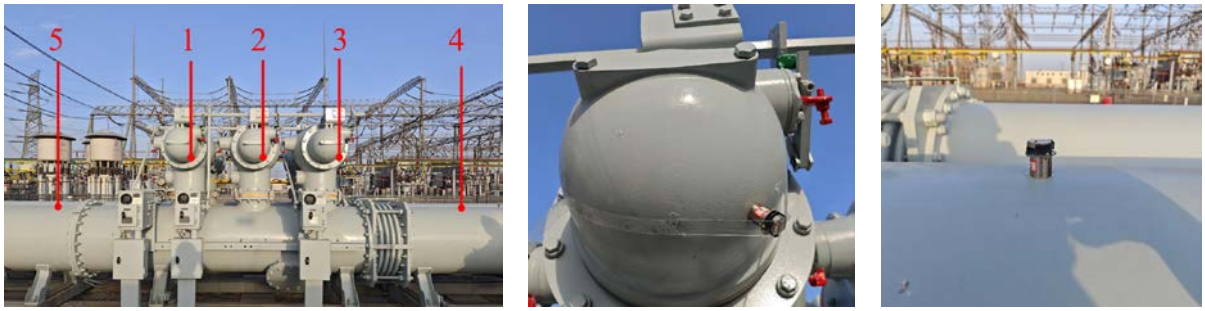

(a) (b) (c)

Figure 5-15 Experimental site. (a) Measurement positions, (b) Disconnector detection, (c) Busbar section detection.

The measurement results of five sensors are shown in Figure 5-16 (a). Sensors 1, 3, 4, and 5 exhibit a distinct 100 Hz vibration characteristic, while Sensor 2, which monitors the B-phase disconnector, detects not only the 100 Hz component but also additional high-frequency components.

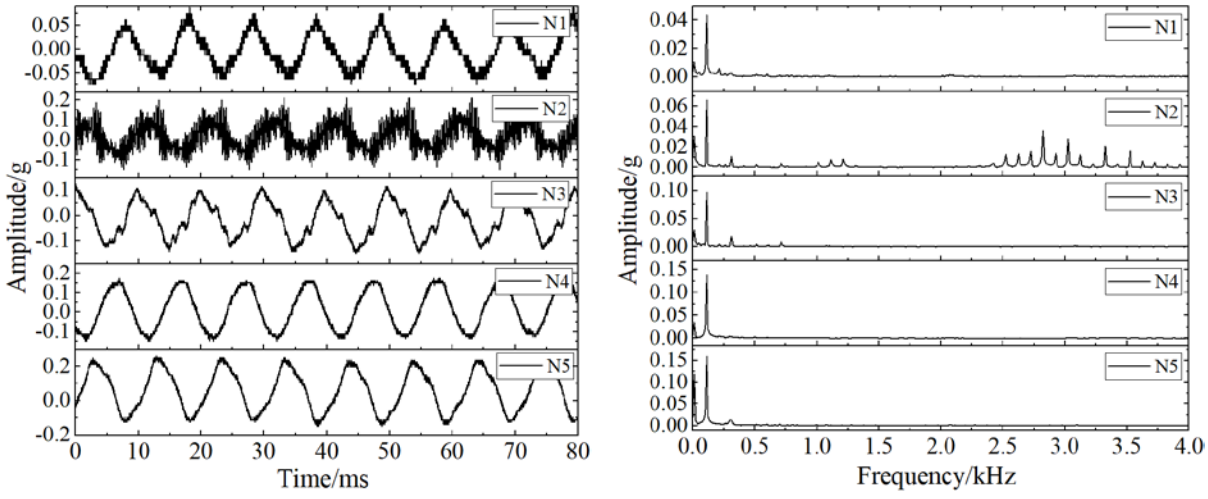

(a) (b)

Figure 5-16 Measured Signal. (a) Time-Domain Signal (b) Frequency-Domain Signal

Figure 5-16 (b) presents the corresponding frequency spectra of the five measurement signals. The primary frequency component of the A-phase and C-phase enclosure vibration signals is 100 Hz, with an amplitude ranging from approximately 0.06 *g* to 0.1 *g*, and no

significant abnormal spectral components, indicating normal operation. However, the B-phase disconnector measurement point exhibits abnormal vibration signals, with a dominant 100 Hz frequency component and additional spectral components in the 1000~1300 Hz and 2500~4000 Hz ranges, suggesting potential defects such as loose external bolts or small internal components. In the AE analysis, no significant PDAE signals are detected, or their amplitudes are too low. The vibration signals at both busbar ends also show a distinct 100 Hz primary frequency with an amplitude of approximately 0.15 *g*, without abnormal spectral components, indicating normal operation. No PDAE signals are detected.

2) GIS PT Gas Chamber Inspection

The PT chamber in GIS equipment is the metering and protection section, primarily comprising circuit breaker, disconnector, and potential transformer. Some operations may induce mechanical changes within the chamber, leading to defects such as loosening, poor contact, or winding deformation. The experimental setup is shown in Figure 5-17. The vibration-AE fusion detection is applied to the three-phase PT chamber (phases A, B, C) of a 220 kV GIS. Two fusion sensors are installed at the center of each phase chamber, measuring synchronously.

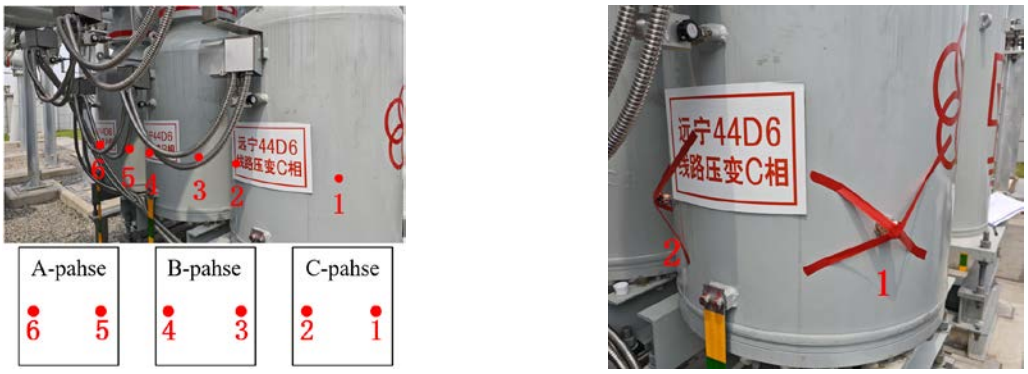

(a) (b)

Figure 5-17 Experimental setup: (a) Measurement positions on PT chamber three phases (b) Phase-C measurement positions

The measurement results from six sensors are shown in Figure 5-18 (a). The vibration signals of phases A and C exhibit a 100 Hz sinusoidal signal, whereas the vibration signal of phase B displays significant anomalies. Figure 5-18 (b) presents the frequency spectrum obtained via FFT. Sensors 1, 2, 5, and 6 primarily exhibit a 100 Hz vibration acceleration component with an amplitude of approximately 7×10^{-3} *g*. In contrast, sensor 3 detects 100 Hz and 200 Hz vibration components with amplitudes of 19×10^{-3} *g* and 28×10^{-3} *g*, respectively, while sensor 4 records 100 Hz and 200 Hz components with amplitudes of 12×10^{-3} *g* and 10×10^{-3} *g*, respectively. No PD is detected during the experiment..

Studies indicate that under normal condition, GIS exhibits periodic vibration with minimal interference, with a fundamental vibration frequency of 100 Hz, while vibrations at other frequencies are negligible. Additionally, the vibration characteristics of the three phases are similar, enabling cross-phase comparison and analysis. However, poor electrical contact results in harmonic frequencies of 100 Hz (e.g., 200 Hz, 300 Hz), with greater contact degradation leading to higher harmonic amplitudes. In this study, the phase-B sensor

detect clear 100 Hz and 200 Hz vibration components, suggesting a potential poor contact defect in the phase B gas chamber, which may further develop into floating discharge[145,146].

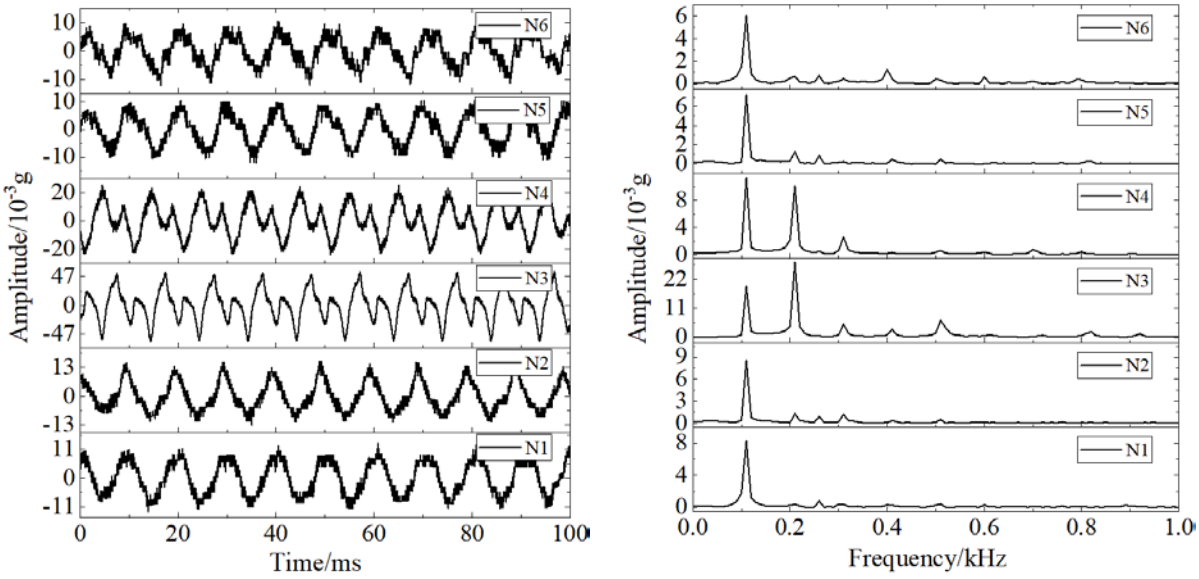

Figure 5-18 Measured signal. (a) Time-domain signal. (b) Frequency-domain signal.

5.4 Brief Summary

Based on the application background and practical engineering demands of this research, this chapter proposes a vibration-AE fusion detection method and carries out its field application in substation. Building upon the experimental studies in Chapter 4, an evaluation approach for metal particle defect in GIS is developed. The processing and feature extraction methods for fusion mechanical vibration and PDAE signals are summarized, and an intelligent distributed sensing–computation–diagnosis architecture for substation equipment detection is proposed. Finally, the developed vibration-AE fusion detection system is successfully applied to on-site condition detection of power equipment. The main conclusions are as follows:

1) Differences in metal particle shapes lead to variations in the amount of carried charge, resulting in distinct motion behaviors, which can be assessed using flight patterns and discharge repetition rates. The slope of the flight pattern distribution can be used to estimate the particle mass. The RMS envelope is effective in distinguishing PDAE pulses from multiple particles, and by analyzing discharge repetition rate trends with varying quantities of particles of different masses, the particle count can be estimated.

2) The VMD algorithm, with its strong adaptability and high resistance to modal aliasing, effectively denoises and separates fusion signal. Feature extraction methods for AE, vibration, and fusion signals are summarized. Besides, a vibration-AE fusion measurement and communication framework and a cloud-edge collaborative computing model are proposed, offering insight and strategy for intelligent distributed detection in substation.

3) The developed vibration-AE fusion detection system features efficient capabilities in signal measurement, data transmission, processing, and storage. Its many-to-many

communication model improves transmission efficiency, and the Python-based client software offers strong adaptability and scalability. The system has been applied to GIS equipment in substations, and experimental results verify its reliability.

6 Conclusions and Future Work

6.1 Conclusions

During operation, GIS equipment is subjected to the combined effects of mechanical stress and electric field, and there exists a correlated influence between its vibration and insulation conditions. Focusing on the challenge of simultaneous detection and efficient diagnosis of mechanical and insulation conditions in GIS substation, this study investigates vibration-AE fusion sensing technology. First, a development method for the vibration-AE fusion sensor is proposed to enable synchronous and co-located measurement of mechanical vibration and partial discharge AE signals. To enhance sensor efficiency, an intelligent framework based on global optimization is established, achieving autonomous performance in "sensing–storage–computation–transmission." Furthermore, to address the current gap in metal particle defect studies: the insufficient consideration of the combined effects of vibration and voltage during GIS operation, a GIS test platform with synchronized vibration and voltage excitation is developed. Experiments are conducted to investigate the motion behavior and discharge characteristics of metal particles under electromechanical coupling. Finally, a GIS fusion detection technique is proposed, and on-site detection in substations is carried out. The main conclusions are as follows:

1) A piezoelectric vibration-AE fusion sensing device is developed, enabling synchronous and co-located detection of mechanical vibration and PDAE signals. An electromechanical-acoustic equivalent model for the piezoelectric fusion measurement is established, and a fusion sensing structure is designed. Simulation analysis clarifies the correlation between structural parameters and both vibration and AE measurement performance. Furthermore, an intelligent optimization method based on data fitting expansion and algorithmic optimization is proposed to determine the optimal structural configuration of the fusion sensor. A built-in sensor circuit is designed using a two-wire (ground and power/signal) phantom power scheme, realizing impedance transformation, noise filtering, and signal amplification. Calibration experiments determined that the fusion sensor has a vibration sensitivity of 950 mV/g and an average AE sensitivity of 101 dB within the target frequency band, with a resonant frequency of 54 kHz, enabling synchronous measurement of vibration-AE fusion signal.

2) By comprehensively considering key features of intelligent sensor technology, including wireless communication, low power consumption, edge computing, and self-calibration, an intelligent framework for the fusion sensor is established, achieving autonomous performance enhancement across the sensing-storage-computation-transmission chain. A system-on-chip intelligent module is designed and integrated into the sensor, and wireless performance tests demonstrate stable low-power data transmission rates above 1 Mbps within an 8-meter range in substation environment, with a theoretical battery life of up to four years. An edge computing strategy tailored for vibration-AE fusion signals is

proposed, and embedded algorithms are implemented to enable signal feature extraction at sensor level. VPRPD is firstly proposed to analyze the correlation between PD and mechanical vibration. Additionally, an efficient calibration method for piezoelectric sensor sensitivity and impedance based on pseudo-random M-sequence excitation is proposed. Coupled electromechanical simulations verified the feasibility of the M-sequence approach. Application tests on both commercial and custom fusion sensors show correlation coefficients above 0.95 with the true values, confirming high accuracy and stability. The calibration process required only a few milliseconds and consumed merely a few milliwatts, demonstrating clear advantages in time efficiency, power consumption, cost, and precision. This work enhances the efficiency of fusion-based detection and lays foundation for practical distributed measurement in field application.

3) Considering the combined effects of voltage and vibration under actual GIS operating condition, this study investigates the motion and PD characteristics of typical metal particles through experiments and theoretical analysis. A test platform is built with synchronized power-frequency voltage and mechanical vibration excitation, and particle defects are configured with variations in shape, mass, and quantity. The mechanical vibration, AE signals, and apparent discharge are measured. Results show that for spherical particles, the jumping initiation and cessation field strengths, E_i and E_c, increase with mass, while GIS vibration reduces these thresholds; greater vibration leads to a greater reduction. Smaller particles move actively but produce PDs with lower amplitudes, whereas larger ones exhibit the opposite trend. For flaky particles, field thresholds depend on mass and size. Linear, lightweight flakes jump more easily than square, heavy ones. PD increases with mass, and firefly effect occurs under high field. Multiple flakes may cause chain breakdown, leading to short circuit. For linear particles, field thresholds also rise with mass and decrease with vibration. After jumping, motion remains active with little vibration influence. PD is strong and increases with mass; firefly effect also appears under high field. Multiple linear particles may induce chain breakdown and short-circuit fault. This study offers valuable experimental reference for GIS metal particle defect diagnosis.

4) Based on the research background and practical engineering demands, this work proposes a fusion detection approach for GIS equipment and demonstrates its application in field substation. Evaluation methods for metal particle shape, mass, and quantity are introduced: particle shape is identified through flight patterns and PD repetition rate; mass is estimated from the slope of the flight pattern distribution; quantity is assessed from the relationship between PD repetition rate and particle number across different masses. VMD is employed for denoising and separating fusion signals, and signal feature extraction methods are summarized. A vibration-AE fusion measurement and communication framework is proposed, along with a cloud-edge collaborative computing model, offering an innovative strategy for intelligent distributed sensing, processing, and diagnosis in substation. The developed fusion detection system supports efficient signal acquisition, data transmission, processing, and storage, and has been successfully applied to GIS equipment condition detection in substation.

6.2 Future Work

This study investigates the vibration-AE fusion detection technology for metal particle defects in GIS equipment under electromechanical coupling. However, the following aspects require further improvement:

1) The cache space of the core SoC chip in the vibration-AE fusion intelligent sensor is limited, making it difficult for the sensor to perform long-duration continuous measurements in a single session. Consequently, the advantages of high efficiency and autonomy in edge computing have not been fully realized. It is necessary to optimize the storage and computing capabilities of the embedded circuit in the fusion sensor and integrate AI diagnostic algorithms to further enhance its intelligence.

2) The current fusion sensor is primarily used for studying metal particle defects in laboratory GIS equipment. However, actual GIS systems also experience electromechanical coupling defects such as poor contact and looseness. The correlation and complementarity between mechanical vibration and PDAE signals for these typical defects require further investigation. Therefore, extensive experimental studies on typical GIS defects should be conducted to accumulate a large amount of valid data, establish the variation patterns of acoustic and vibration signals, and further deepen the data fusion analysis with AI algorithms.

3) Given the long distance, large volume, and complex structure of GIS equipment, a small number of sensors are insufficient for comprehensive monitoring. It is necessary to study distributed fusion detection method, understand the signal characteristics of mechanical vibration and PDAE, and refine diagnostic techniques for defect classification, severity assessment, and localization. Furthermore, on-site fusion detection and monitoring applications should be conducted in substations to obtain real defect diagnosis cases.

References

[1] Xiancai H, Hongjun Z. China's Ultra-High Voltage AC Transmission Projects (2006–2021) [J]. Contemporary Electric Power Culture, 2022, (04): 102.

[2] Dengming X, Yue D, Donghai H. GIS Technology in China's Ultra-High Voltage Transmission Projects [J]. High Voltage Engineering, 2006, (12): 115–117.

[3] Xiancai H, Xin S, Haibo C, et al. Overview of Technical Development of China's Ultra-High Voltage AC Transmission Projects [J]. Proceedings of the CSEE, 2020, 40(14): 4371–4386+4719.

[4] Yuanyuan G, Boyuan C, Chengyu W, et al. Development of 1100kV/63kA Gas-Insulated Metal-Enclosed Switchgear [J]. Power System Technology, 2011, 35(12): 20–25.

[5] Peng L, Jinzhong L, Boyuan C, et al. Latest Technological Developments in UHV AC Transmission and Transformation Equipment [J]. High Voltage Engineering, 2016, 42(4): 1068–1078.

[6] Yonghui D. Compilation of Typical Failure Cases of High Voltage Switchgear (2006–2010) [M]. Beijing: China Electric Power Press, 2013.

[7] Yangliu C, Hongzhong M, Taoyun W, et al. GIS Fault Analysis Based on Fault Tree Theory [J]. High Voltage Apparatus, 2015, 51(7): 125–129+135.

[8] Fangcheng L, Bo Z. Recognition of GIS partial discharge types based on S-Kohonen network [J]. Electrical Measurement & Instrumentation, 2014, 51(20): 21-24.

[9] Jian H, Xu L, Ziqi S, et al. Adaptive Diagnosis Method for Mechanical Vibration Defects of GIS Equipment Based on Multi-Graph Fusion Analysis and Load Current [J]. Proceedings of the CSEE: 1–12.

[10] Xiping J, Yongfu L, Yingkai L, et al. Study on Vibration Signal Feature Analysis Technology for Mechanical Defects in GIS Equipment [J]. High Voltage Apparatus, 2025, 61(2): 17–25+34.

[11] Chao G, Bo Z, Xuemin T, et al. Live Detection and Disassembly Analysis of Suspended Discharge Defects in GIS Disconnectors [J]. High Voltage Apparatus, 2021, 57(5): 168–174.

[12] Dong G, Yang T, Hongxun T, et al. Typical Fault Analysis of Insulation Breakdown in 500kV GIS Disconnector [J]. High Voltage Apparatus, 2020, 56(8): 261–267.

[13] Chong K, Xingwei L, Wei L, et al. Discharge Analysis and Treatment of Arc-Extinguishing Chamber in 500kV GIS Circuit Breaker [J]. High Voltage Apparatus, 2023, 59(8): 173–179.

[14] Dong W, Zhibin Q, Wei W, et al. Analysis and Treatment of Single-Phase Ground Fault in 220kV Substation GIS [J]. High Voltage Apparatus, 2020, 56(11): 259–265+274.

[15] Qingmin L, Jian W, Botao L, et al. Research Progress on Metal Particle Contamination in GIS/GIL [J]. High Voltage Engineering, 2016, 42(3): 849–860.

[16] Sabot A, Petit A, Taillebois JP. GIS insulation co-ordination: on-site tests and dielectric diagnostic techniques. A utility point of view[J]. IEEE Transactions on Power Delivery, 1996, 11(3): 1309-1316.

[17] Xiaoang L, Xiaoyu Y, Xiaoxiao L, et al. Jumping and Adsorption Behavior of Metal Particles and Surface Flashover Characteristics of Insulators under Live GIS Operation [J]. High Voltage Engineering: 1–13.

[18] Yulun C, Dingge C, Dingge Y, et al. Study on the Development Process of Surface Partial Discharge Induced by Metal Particles in GIS [J]. Electric Power Engineering Technology, 2021, 40(3): 153–158.

[19] Naifan X. Study on the Dynamics of Micro/Nano Particles and the Physical Mechanism of Multi-Mode Discharge in GIS/GIL [D]. North China Electric Power University (Beijing), 2024.

[20] Kang M. Research on the Dynamics and Mitigation Methods of Metal Particle Dust in DC GIS/GIL

[D]. North China Electric Power University (Beijing), 2023.
[21] Shuang Y, Ke Z. Analysis of a Busbar Discharge Fault in 1100kV Gas-Insulated Metal-Enclosed Switchgear [J]. Electrical Technology, 2021, 22(4): 94–97.
[22] Yongpeng M, Bo Z, Shenli J. Application and Development of Vibration Analysis in Condition Monitoring of Power Equipment [J]. High Voltage Apparatus, 2005(6): 461–465.
[23] Shengchang J, Fan Z, Yuhang S, et al. Review of Mechanical Condition Diagnosis Methods for Power Transformers Based on Vibration Signals [J]. High Voltage Engineering, 2020, 46(1): 257–272.
[24] Gang C, Chong G, Ping L, et al. Review on Reliability Improvement of Insulation in UHV/EHV GIS [J]. High Voltage Apparatus: 1–16.
[25] Shengchang J, Dehua Z, Yunfei J, et al. Research Status and Prospects of Discharge Characteristics and Detection Methods for Transformer Insulation Defects [J]. High Voltage Engineering, 2024, 50(10): 4297–4314.
[26] Junhao L, Xutao H, Zehui L, et al. Review of Partial Discharge Detection Technology for Power Equipment [J]. High Voltage Engineering, 2015, 41(8): 2583–2601.
[27] Weigen C, Zhixian Z, Jian L, et al. Intelligent Sensing Technology for Status Parameters of Electrical Equipment [J]. Proceedings of the CSEE, 2020, 40(S1): 323–342.
[28] Gehao S, Yong Q, Lingen L, et al. Key Technologies and Development Trends of Digital Power Equipment Oriented to New-Type Power Systems [J]. High Voltage Engineering, 2023, 49(5): 1765–1778.
[29] Xinghui Z, Wenzhi C, Fei D, et al. Research Progress on Multi-Feature Sensing of Partial Discharge in GIS [J]. High Voltage Apparatus, 2022, 58(4): 8–16.
[30] Guidong L. Piezoelectric Transducers and Transducer Arrays [M]. Peking University Press, 2005.
[31] Huifen Y, He Q, Xiaoniu T, et al. Research Progress on High-Temperature Piezoelectric Vibration Sensors and Piezoelectric Materials [J]. Acta Physica Sinica, 2025, 74(2): 182–211.
[32] Walter PL. Review: Fifty Years Plus of Accelerometer History for Shock and Vibration (1940–1996)[J]. Shock and Vibration, 1999, 6(4): 197-207.
[33] Mark Serridge, Bsc, Torben R. Licht MSc. Piezoelectric accellerometer and vibration preamplifier: Bruel&Kajaer[M]. 1987.
[34] T. R. Licht. Five Decades of Accelerometer Development at Bruel and Kjaer[C]//Proceedings of the 67th Shock and Vibration Symposium. SAVIAC, 1996.
[35] J. M. Kubler. Evolution of Miniaturized Piezoelectric Accelerometers at Endevco[C]//Proceedings of the 67th Shock and Vibration Symposium. SAVIAC, 1996.
[36] L. Maier. Evolution of Integrated Circuit Technology in the Accelerometer[C]//Proceedings of the 67th Shock and Vibration Symposium. SAVIAC, 1996.
[37] J. F. Lally. Evolution of Sensors for Modal Analysis[C]//Proceedings of the 67th Shock and Vibration Symposium,. SAVIAC, 1996.
[38] Fuxue Z. Impact and Vibration Acceleration Sensors [J]. Sensor Technology, 1983(Z1): 12–31.
[39] Yuanbo M. Research on Piezoelectric Vibration Sensors for Oil Pipeline Condition Monitoring [D]. Harbin Institute of Technology, 2021.
[40] Ruihao Z. Design and Fabrication of High-Temperature Piezoelectric Acceleration Sensors [D]. University of Electronic Science and Technology of China, 2019.
[41] Yiqiang C. Research on Noise Characteristics and Signal Processing Methods of Low-Frequency Piezoelectric Acceleration Sensors [D]. Yanshan University, 2016.
[42] Xueguang Q, Zhihua S, Weijia B, et al. Research Progress on Fiber-Optic Ultrasonic Sensors and Their Applications [J]. Acta Physica Sinica, 2017, 66(7): 128–147.
[43] Yuchen M, Jiandong S, Tao L, et al. Review of Passive Acoustics Based on Piezoelectric Ultrasonic

Transducers and Their Applications [J]. Piezoelectrics & Acoustooptics, 2024, 46(5): 617–633+643.
[44] Jie L, Quanfang C. Review of Fabrication Techniques for Capacitive Micromachined Ultrasonic Sensors [J]. Chinese Journal of Scientific Instrument, 2018, 39(8): 98–109.
[45] Shujuan W, Lei K, Zaixin Z, et al. Review of Research Progress on Electromagnetic Ultrasonic Transducers [J]. Instrumentation Technology and Sensor, 2006(5): 47–50.
[46] Jaffe B, Roth RS, Marzullo S. Piezoelectric Properties of Lead Zirconate-Lead Titanate Solid-Solution Ceramics[J]. Journal of Applied Physics, 1954, 25(6): 809-810.
[47] Rathod VT. A Review of Acoustic Impedance Matching Techniques for Piezoelectric Sensors and Transducers[J]. Sensors, 2020, 20(14): 4051.
[48] Desilets CS, Fraser JD, Kino GS. The design of efficient broad-band piezoelectric transducers[J]. IEEE Transactions on Sonics and Ultrasonics, 1978, 25(3): 115-125.
[49] Viera MAA, Gotz R, De Aguiar PR, et al. A Low-Cost Acoustic Emission Sensor based on Piezoelectric Diaphragm[J]. IEEE Sensors Journal, 2020: 1-1.
[50] Chongfu Y. Ultrasonics [M]. Beijing: Science Press, 1990.
[51] Rong L. Research on Ultrasonic-Based Detection and Diagnosis Technology for XLPE Power Cable Insulation Defects [D]. Northwestern Polytechnical University, 2015.
[52] Yu Y, Lulu Y, Ming W, et al. High-Sensitivity Flexible PZT Piezoelectric Ultrasonic Sensor for Partial Discharge Detection in Power Cables [J]. High Voltage Engineering: 1–9.
[53] Yan W, Chuan C, Jiayi Z, et al. Study on the Effects of Piezoelectric Material Properties and Device Dimensions on the Sensitivity of Piezoelectric Sensors for Transformer Partial Discharge Monitoring [J]. High Voltage Apparatus, 2025, 61(2): 63–72.
[54] Khan Q, Refaat SS, Abu-Rub H, et al. Partial discharge detection and diagnosis in gas insulated switchgear: State of the art[J]. IEEE Electrical Insulation Magazine, 2019, 35(4): 16-33.
[55] Hui X, Zhengyang L, Chuanxian L, et al. Study on Vibration Characteristic Differences of GIS Equipment under Operating Conditions [J]. High Voltage Apparatus, 2024, 60(6): 43–49+56.
[56] Jinggang Y, Yuan L, Siqi S, et al. Research on Vibration Detection Technology for Mechanical Defects in GIS Equipment [J]. High Voltage Apparatus, 2018, 54(11): 86–90.
[57] Jiushan W, Zhuangmin Z, Yueping Y, et al. Combined Vibration–Temperature Detection Method for Contact Status of GIS Disconnector [J]. High Voltage Engineering, 2023, 49(1): 207–214.
[58] Jizhong L, Tao J, Shu N, et al. Study on Diagnosis Method of GIS Mechanical Defects Based on EMD-FFT Feature Extraction [J]. Journal of Electric Power Science and Technology, 2023, 38(3): 216–223.
[59] Dengwei D, Liang H, Wei L, et al. Research on Vibration Mechanism and Detection Diagnosis Technology of GIS Equipment under Operating Conditions [J]. High Voltage Apparatus, 2019, 55(11): 93–99.
[60] Ying F, Xu L, Yao Z, et al. Research on Mechanical Defect Diagnosis Method of GIS Equipment Based on Multilayer Fusion Vibration Data Analysis [J]. Proceedings of the CSEE, 2024, 44(14): 5797–5810.
[61] Yao Z, Jian H, Yilin D, et al. Study on Nonlinear Vibration Behavior Characterization Parameters and Diagnosis Model for Typical Mechanical Defects in GIS Equipment [J]. Proceedings of the CSEE, 2022, 42(19): 7248–7260.
[62] Yanpeng H, Xuezhi L, Shenglong H, et al. Research Progress and Prospects on Ultrasonic Detection of GIS/GIL Insulators [J]. High Voltage Engineering, 2023, 49(9): 3596–3606.
[63] Wen-rong S, Hua H, Chen-zhao F, et al. Integrated Classification Technique for Typical Insulation Flaws in Gas Insulated Switchgear Based on Acoustic Detection[J]. 2011.
[64] Ilkhechi HD, Samimi MH. Applications of the Acoustic Method in Partial Discharge Measurement: A Review[J]. IEEE Transactions on Dielectrics and Electrical Insulation, 2021, 28(1): 42-51.

[65] Faizol Z, Zubir F, Saman NM, et al. Detection Method of Partial Discharge on Transformer and Gas-Insulated Switchgear: A Review[J]. Applied Sciences, 2023, 13(17): 9605.

[66] Stief A, Ottewill JR, Baranowski J, et al. A PCA and Two-Stage Bayesian Sensor Fusion Approach for Diagnosing Electrical and Mechanical Faults in Induction Motors[J]. IEEE Transactions on Industrial Electronics, 2019, 66(12): 9510-9520.

[67] Hao J, Ding Y, Li Y, et al. Comparative Analysis of Partial Discharge and Mechanical Vibration Characteristics under Loose Bus Base with Foreign Body Defect of GIS[C]//2022 IEEE International Conference on High Voltage Engineering and Applications (ICHVE). Chongqing, China: IEEE, 2022: 1-4.

[68] Ding Y, Zhong Y, Wang X, et al. Difference and Analysis of Mechanical Vibration Signal Characteristics between Mechanical Defects and Partial Discharge Defects of Gas Insulated Switchgear[C]//2021 IEEE 5th International Conference on Condition Assessment Techniques in Electrical Systems (CATCON). Kozhikode, India: IEEE, 2021: 211-214.

[69] Ruifeng Y, Yan W, Jinghui G, et al. Applications of Piezoelectric Materials and Devices in Electrical Engineering [J]. Transactions of China Electrotechnical Society, 2021, 36(7): 1324–1337.

[70] Tingwei G, Minghong T, Xiaodong S. Review on the Current Status and Development Trend of Intelligent Sensor Technology Applications [J]. Internet of Things Technologies, 2025, 15(1): 59–63.

[71] Peng L, Jiangang B, Hao Y, et al. Intelligent Sensing and State Perception Technology and Its Applications in Substation Equipment [J]. High Voltage Engineering, 2020, 46(9): 3097–3113.

[72] Tao Y, Minhang L, Qingquan L, et al. Key Technologies and Prospects of Dedicated Sensing and Edge Intelligence for New-Type Power Systems [J]. High Voltage Engineering, 2024, 50(8): 3324–3338.

[73] Qiang Z, Yugeng S, Ting Y, et al. Applications of Wireless Sensor Networks in Smart Grids [J]. Electric Power, 2010, 43(6): 31–36.

[74] Weigen C, Zhixian Z, Jian L, et al. Intelligent Sensing Technology for Equipment State Parameters [J]. Proceedings of the CSEE, 2020, 40(S1): 323–342.

[75] Jian L, Jin Z, Can W, et al. Research on Integrated Intelligent Monitoring Devices for Substation Equipment Based on the Internet of Things [J]. High Voltage Engineering, 2015, 41(12): 3881–3887.

[76] Junjie J, Jun H, Guoming M, et al. Application Requirements and Development Trends of Specialized Sensors for Digital Power Equipment [J]. High Voltage Engineering, 2024, 50(8): 3271–3307.

[77] Seferagić A, Famaey J, De Poorter E, et al. Survey on Wireless Technology Trade-Offs for the Industrial Internet of Things[J]. Sensors, 2020, 20(2): 488.

[78] Abderrahmane T, Nourredine A, Mohammed T. Experimental analysis for comparison of wireless transmission technologies: Wi-Fi, Bluetooth, ZigBee and LoRa for mobile multi-robot in hostile sites[J]. International Journal of Electrical and Computer Engineering (IJECE), 2024, 14(3): 2753.

[79] Boning Y, Ming R, Zhibin Z, et al. Implementation Methods of Distributed Partial Discharge Sensing Technology for Distribution Equipment [J]. High Voltage Engineering, 2020, 46(6): 1929–1938.

[80] Liccardo A, Bonavolonta F, Balato M, et al. Lora-Based Smart Sensor for PD Detection in Underground Electrical Substations[J]. IEEE Transactions on Instrumentation and Measurement, 2022, 71: 1-13.

[81] Shi D, Feng G, Du X, et al. The Design and Fabrication of an On-Rotor Sensing Wireless Vibration Node for Motor Condition Monitoring[J]. IEEE Transactions on Instrumentation and Measurement, 2024, 73: 1-11.

[82] Shi W, Cao J, Zhang Q, et al. Edge Computing: Vision and Challenges[J]. IEEE Internet of Things Journal, 2016, 3(5): 637-646.

[83] Klein L, Žmij P, Krömer P. Partial Discharge Detection by Edge Computing[J]. IEEE Access, 2023, 11: 44192-44204.

[84] Huan L, Tang B, Zhao C. Global Composite Compression of Deep Neural Network in Wireless Sensor Networks for Edge Intelligent Fault Diagnosis[J]. IEEE Sensors Journal, 2023, 23(16): 17968-17978.

[85] Zhao C, Tang B, Deng L. Missing-Measurements-Tolerant Compressed Sensing in Wireless Sensor Networks for Mechanical Vibration Monitoring[J]. IEEE Transactions on Instrumentation and Measurement, 2024, 73: 1-13.

[86] Luong P, Wang W. Smart Sensor-Based Synergistic Analysis for Rotor Bar Fault Detection of Induction Motors[J]. IEEE/ASME Transactions on Mechatronics, 2020, 25(2): 1067-1075.

[87] Yi J, Zhengyang L, Wenrui W, et al. Study on Multi-State Monitoring System for Substation Equipment Based on Edge-Cloud Collaboration [J]. Power System Protection and Control, 2021, 49(6): 138–144.

[88] Ji J, Shu Z, Li H, et al. Edge-Computing-Based Knowledge Distillation and Multitask Learning for Partial Discharge Recognition[J]. IEEE Transactions on Instrumentation and Measurement, 2024, 73: 1-11.

[89] Jiang X, Zhang X, Tang T, et al. Electromechanical impedance based self-diagnosis of piezoelectric smart structure using principal component analysis and LibSVM[J]. Scientific Reports, 2021, 11(1): 11345.

[90] Sukesha, Vig R, Kumar N. Variation of piezoelectric coefficient and dielectric constant with electric field and temperature: A review[C]//2014 Recent Advances in Engineering and Computational Sciences (RAECS). Chandigarh, India: IEEE, 2014: 1-6.

[91] Lan H, Yan L, Xiao D, et al. Surface-to-surface calibration of acoustic emission sensors[J]. Sensors and Actuators A: Physical, 2012, 174: 16-23.

[92] Zhang L, Yalcinkaya H, Ozevin D. Numerical approach to absolute calibration of piezoelectric acoustic emission sensors using multiphysics simulations[J]. Sensors and Actuators A: Physical, 2017, 256: 12-23.

[93] Pertijs M. Calibration and Self-Calibration of Smart Sensors[M]//Meijer G, Pertijs M, Makinwa K. Smart Sensor Systems. 1st ed. Wiley, 2014: 17-41.

[94] Yan T, Theobald P, Jones BE. A conical piezoelectric transducer with integral sensor as a self-calibrating acoustic emission energy source[J]. Ultrasonics, 2004, 42(1-9): 431-438.

[95] Manling D, Chunyan Z, Zhenyu Z, et al. Research Progress on Metal Particle Issues Inside GIL [J]. High Voltage Apparatus, 2024, 60(1): 1–14.

[96] Doepken HC. Compressed-Gas Insulation in Large Coaxial Systems[J]. IEEE Transactions on Power Apparatus and Systems, 1969, PAS-88(4): 364-369.

[97] Nitta T, Shibuya Y, Fujiwara Y, et al. Factors Controlling Surface Flashover in SF_6 Gas Insulated Systems[J]. IEEE Transactions on Power Apparatus and Systems, 1978, PAS-97(3): 959-968.

[98] Ronghui H, Xin Z, Yifan Q, et al. Influence of Metal Contaminants on Flashover Characteristics of Bowl Insulators in GIS under Lightning Impulse [J]. High Voltage Apparatus, 2016, 52(4): 111–116.

[99] Li X, Liu W, Xu Y, et al. Partial Discharge and Movement Characteristics of Micron-sized Metal Particles on Insulator Surface in Gas-Insulated Switchgear with Long-time AC Stress[J]. IEEE Transactions on Dielectrics and Electrical Insulation, 2021, 28(6): 2152-2160.

[100] You H, Zhang Q, Guo C, et al. Motion and discharge characteristics of metal particles existing in GIS under DC voltage[J]. IEEE Transactions on Dielectrics and Electrical Insulation, 2017, 24(2): 876-885.

[101] Dai L. Insulation Fault Analysis Caused by Internal Metal Particles in 330kV GIS[C]//2024 IEEE 7th Advanced Information Technology, Electronic and Automation Control Conference (IAEAC).

Chongqing, China: IEEE, 2024: 1722-1735.
[102] Sakai K, Labrado Abella D, Khan Y, et al. Experimental studies of free conducting wire particle behavior between non-parallel plane electrodes with ac voltages in air[J]. IEEE Transactions on Dielectrics and Electrical Insulation, 2003, 10(3): 418-424.
[103] ASANO K, YATSUZUKA K, HIGASHIYAMA Y. The motion of charged metal particles within parallel and tilted electrodes[J]. Journal of Electrostatics, 1993, 30(5): 65-74.
[104] Hongxin J, Chengrong L, Zhikai P, et al. Partial Discharge Characteristics of Freely Moving Flaky Particles in GIS [J]. Proceedings of the Chinese Society for Electrical Engineering, 2017, 37(24): 7367–7376 + 7451.
[105] Hongxin J, Chengrong L, Zhikai P, et al. Influencing Factors of Lift-off Voltage for Linear Particles in GIS [J]. Proceedings of the Chinese Society for Electrical Engineering, 2017, 37(1): 301–313.
[106] Hongzhong M, Lixian W, Feng D. Study on Motion Behavior and Discharge Characteristics of Metal Particle Contaminants in GIL [J]. Journal of Electrical Machines and Control, 2022, 26(3): 49–58.
[107] Hongxin J. Motion Behavior and Discharge Characteristics of Metal Particles in GIS under AC Operating Voltage [D]. North China Electric Power University (Beijing), 2017.
[108] Zhenyu Z. Key Technology Research on Surface Insulation Performance Enhancement of Support Insulators in Gas-Insulated Transmission Pipelines [D]. North China Electric Power University (Beijing), 2020.
[109] Kuwahara H, Inamura S, Watanabe T, et al. Effect of Solid Impurities on Breakdown in Compressed SF_6 Gas[J]. IEEE Transactions on Power Apparatus and Systems, 1974, 93(5): 1546-1555.
[110] COOKSON A H, BOLIN P C, DEOPKEN H, et al. Recent research in the United States on the effect of particle con- tamination reducing the breakdown voltage in compressed gas-insulated systems[C]//International Conference on Large High Voltage Electric Systems: Vol. 8. Materials and Emerging Test Techniques(D1), 1976: 1-10.
[111] Lundgaard LE, Runde M, Skyberg B. Acoustic diagnosis of gas insulated substations: a theoretical and experimental basis[J]. IEEE Transactions on Power Delivery, 1990, 5(4): 1751-1759.
[112] Lundgaard LE, Tangen G, Skyberg B, et al. Acoustic diagnoses of GIS; field experience and development of expert system[J]. IEEE Transactions on Power Delivery, 1992, 7(1): 287-294.
[113] Lundgaard LE. Particles in GIS characterization from acoustic signatures[J]. IEEE Transactions on Dielectrics and Electrical Insulation, 2001, 8(6): 1064-1074.
[114] Runde M, Aurud T, Ngkleby JE, et al. Risk assessment basis of moving particles in gas insulated substations[J].
[115] Schlemper H D, Feser K. Characterization of moving particles in GIS by acoustic and electric partial discharge detection[C]//10th International Symposium on HV Engineering: Vol. 2. Montreal, 1997: 13-18.
[116] Dajian L, Jinggang Y, Jizhong L, et al. Ultrasonic Signal Characteristics of Freely Moving Metal Particles Inside Gas-Insulated Switchgear [J]. Journal of Xi'an Jiaotong University, 2009, 43(2): 101–105.
[117] Xing L, Weidong L, Yuan X, et al. Motion of Metal Particles in GIS under Impact Vibration and Their Induced Surface Flashover Characteristics [J]. Proceedings of the Chinese Society for Electrical Engineering, 2023, 43(7): 2838–2848.
[118] Lv Y, Li X, Li J, et al. Simulation on Motion Characteristics of Free Metal Particles in GIS / GIL under Power Frequency Voltage and Vibration Superposition[C]//2020 IEEE International Conference on High Voltage Engineering and Application (ICHVE). Beijing, China: IEEE, 2020: 1-4.

[119] Jie L, Xiaoang L, Yufang L, et al. Motion Characteristics of Free Metal Particles inside GIS under Sinusoidal Vibration Excitation [J]. Journal of Electrical Engineering Technology, 2021, 36(21): 4580–4589+4597.

[120] Yiqiang C. Noise Characteristics and Signal Processing Methods of Low-Frequency Piezoelectric Accelerometers [D]. Yanshan University, 2016.

[121] Guoming T. Analysis and Application of Resonant Frequency for Piezoelectric Accelerometer Installation [D]. Huazhong University of Science and Technology, 2006.

[122] Jian Z. Study on the Effects of Matching Layer and Backing Materials on Ultrasonic Transducer Performance [D]. Changchun University of Science and Technology, 2021.

[123] Chunlong F. Development and Application of High-Frequency (≥100 MHz) Ultrasonic Sensors [D]. Wuhan University, 2015.

[124] Krimholtz R, Leedom DA, Matthaei GL. New equivalent circuits for elementary piezoelectric transducers[J]. Electronics Letters, 1970, 6(13): 398-399.

[125] Chunying W, Cong W. Design of Backing Parameters for High-Frequency Broadband Underwater Acoustic Transducers [J]. Journal of Harbin Engineering University, 2022, 43(10): 1471–1477.

[126] Vives AA. Piezoelectric Transducers and Applications[M]. Berlin, Heidelberg: Springer Berlin Heidelberg, 2008.

[127] State Grid Corporation of China. Q/GDW11304.9-2023. Technical Specification for Live Detection Instruments of Electric Power Equipment—Part 9: Ultrasonic Partial Discharge Detectors [S]. Beijing: China Electric Power Press, 2023.

[128] Iorgulescu M, Beloiu R, Popescu MO. Vibration monitoring for diagnosis of electrical equipment's faults[C]//2010 12th International Conference on Optimization of Electrical and Electronic Equipment. Brasov, Romania: IEEE, 2010: 493-499.

[129] Jianwen Z, Lei Z, Jianlong Q. Two-wire Built-in Charge Amplifier Circuit Based on Field Effect Transistor, CN106788297B [P]. 2019.

[130] General Administration of Quality Supervision, Inspection and Quarantine of the People's Republic of China; Standardization Administration of China. GB/T 19801-2005. Non-destructive Testing—Acoustic Emission Testing—Secondary Calibration of Acoustic Emission Sensors [S]. Beijing: China Standards Press, 2005.

[131] General Administration of Quality Supervision, Inspection and Quarantine of the People's Republic of China; Standardization Administration of China. GB/T 20485.21-2007. Calibration Methods for Vibration and Shock Sensors—Part 21: Calibration by Vibration Comparison Method [S]. Beijing: China Standards Press, 2007.

[132] IEEE Instrumentation and Measurement Society. IEEE Std 1451.1-1999, IEEE Standard for a Smart Transducer Interface for Sensors and Actuators—Network Capable Application Processor (NCAP) Information Model[S]. IEEE, 1999.

[133] Janů P, Bajer J, Dyčka P, et al. Precise experimental determination of electrical equivalent circuit parameters for ultrasonic piezoelectric ceramic transducers from their measured characteristics[J]. Ultrasonics, 2021, 112: 106341.

[134] Yanjun L, Ke Z. System Identification Theory and Applications [M]. Beijing: National Defense Industry Press, 2009.

[135] Luo Y, Gao J, Chen P, et al. A test method of winding deformation excited by pseudorandom M-Sequences — Part I: Theory and simulation[J]. IEEE Transactions on Dielectrics and Electrical Insulation, 2016, 23(3): 1605-1612.

[136] Zhang Y, Deheng Z. High Voltage Insulation Technology [M]. 3rd ed. Beijing: China Electric Power Press, 2015.

[137] Yuan L, Jinggang Y, Yongyong J, et al. Contact state detection technology of GIS disconnector

contacts based on vibration principle [J]. High Voltage Engineering, 2019, 45(5): 1591-1599.
[138] Hui X, Zhengyang L, Chuanxian L, et al. Study on vibration characteristic differences of GIS equipment under operating conditions [J]. High Voltage Apparatus, 2024, 60(6): 43-49+56.
[139] Li X, Li J, Ren J, et al. Acoustic Method for Multiple Free Metallic Particle Recognition in GIS/GIL[J]. IEEE Transactions on Power Delivery, 2022, 37(3): 2104-2111.
[140] Tu Jiayi, Guan Xiangyu, Zhao Junyi, et al. GIS vibration signal denoising algorithm based on SVD-IACMD [J]. Electric Power Engineering Technology, 2024, 43(6): 163-172.
[141] Zhiguo T, Tongtong J, Huisheng Y, et al. Statistical characteristics of electromagnetic interference in substation partial discharge detection [J]. High Voltage Engineering, 2017, 43(9): 2998-3006.
[142] Dragomiretskiy K, Zosso D. Variational Mode Decomposition[J]. IEEE Transactions on Signal Processing, 2014, 62(3): 531-544.
[143] Zhicheng W, Qiaogen Z, Jiajie S, et al. Partial discharge phase-resolved pattern of freely moving conductive particles defects inside GIS [J]. High Voltage Engineering, 2019, 45(6): 1995-2002.
[144] Peng Z, Tianjiao P, Xinying W, et al. Key technologies and prospects of power IoT for energy internet digital twin [J]. Proceedings of the Chinese Society for Electrical Engineering, 2022, 42(2): 447-458.
[145] Zhang J, Xu H, Wang X, et al. Mechanical Defect Field Detection for Operational GIS Equipment Based on Vibration Signal Analysis[C]//2021 6th Asia Conference on Power and Electrical Engineering (ACPEE). Chongqing, China: IEEE, 2021: 1244-1248.
[146] Wang H, Yang J, Wang X, et al. Feature Fingerprint Extraction and Abnormity Diagnosis Method of the Vibration on the GIS[C]//2020 IEEE International Conference on High Voltage Engineering and Application (ICHVE). Beijing, China: IEEE, 2020: 1-4.

Achievements

Publications：

[1] **Zhang ZY**, Wang HT, Chen H, et al. A novel IEPE AE-vibration-temperature-combined intelligent sensor for defect detection of power equipment[J]. IEEE Transactions on Instrumentation and Measurement, 2023, 72:1~9 (SCI: 000991806800028).

[2] **Zhang ZY**, Li JH, Song YF, et al. A Novel Ultrasound-Vibration Composite Sensor for Defects Detection of Electrical Equipment[J]. IEEE Transactions on Power Delivery, 2022, 37(5): 4477-4480 (SCI: 000857347300101).

[3] **Zhang ZY**, Shi TY, Lombardo L, et al. A Fast Self-Calibration Method for Piezoelectric Sensors Excited by Pseudorandom M-Sequence[J]. IEEE Transactions on Instrumentation and Measurement, 2024, 73: 1~9 (SCI: 001308263200014).

[4] **Zhang ZY**, Lombardo L, Shi TY, et al. A Smart Combined Wireless Sensor Network for Vibration and AE Signals Measurement[J]. IEEE Transactions on Instrumentation and Measurement, 2025, 74: 1~12 (SCI: 001455427800040).

[5] **Zhang ZY**, Hu YD, Song YF, et al. Development and Application of Mechanical Vibration-ultrasound Combined Sensor for Power Equipment[J]. Chinese Journal of Electrical Engineering, 2023, Vol. 43, No. 14, pp. 5713-5723. (EI: 20233214502994)

[6] **Zhang ZY**, Lombardo L, Shi TY, et al. A Smart Combined Wireless Sensor for Vibration and AE Signals Measurement[C]// IEEE International Instrumentation and Measurement Technology Conference (I2MTC), Glasgow, Scotland, 2024 (EI: 20242816682143)

Patents:

[1] Li JH, **Zhang ZY**, Song YF. Piezoelectric Ultrasonic–Vibration Acceleration Composite Sensor and Measurement Device [P]. Chinese Patent, CN113720390B. May 5, 2023.

[2] Li JH, **Zhang ZY**, Han XT, et al. Calibration Method for Piezoelectric Sensor Excited by Pseudo-Random M-Sequence [P]. Chinese Patent, CN118424361A. August 2, 2024.

[3] Li JH, Sun Y, **Zhang ZY**. Piezoelectric Ultrasonic–Transient Ground Voltage Composite Sensor and Measurement Device [P]. Chinese Patent, CN113702685B. 2022.

[4] Li JH, Song YF, **Zhang ZY**. Shear-type Vibration–Ultrasonic Composite Sensor and Measurement Device [P]. Chinese Patent, CN113654583B. 2022.